Carbon-Supported Copper for Gas-Phase Hydrogenation Catalysis

Doctoral thesis

Rolf Beerthuis

University Utrecht

PhD thesis, Utrecht University, the Netherlands, March 2020.

ISBN: 9789464021219

Printed by: Gildeprint
Cover concept: Rolf Beerthuis
Cover design: Ilse Modder, www.ilsemodder.nl

This work described in this thesis was performed in the Inorganic Chemistry and Catalysis group, part of the Debye Institute of Nanomaterials Science at Utrecht University.

Carbon-Supported Copper for Gas-Phase Hydrogenation Catalysis

Koolstof-gedragen koper voor gasfase-hydrogeneringskatalyse

(met een samenvatting in het Nederlands)

Proefschrift

ter verkrijging van de graad van doctor aan de Universiteit Utrecht op gezag van de rector magnificus, prof dr. H. R. B. M. Kummeling, ingevolge het besluit van het college van promoties in het openbaar te verdedigen op

maandag 30 november 2020 des ochtends te 09:15 uur

door

Rolf Beerthuis

geboren op 5 februari 1989
te Vlaardingen

Promotoren:
Prof. dr. P. E. de Jongh
Prof. dr. ir. K. P. de Jong

The research in this thesis was financially supported by BP.

Contents

Chapter 1

General Introduction

1.1 Copper

Copper (Cu) was amongst the first metals known to mankind.[1-3] The discovery that Cu could be alloyed with zinc (brass) and tin (bronze) to produce strong tools and weapons, strongly accelerated the development of human civilization in the Bronze Age around 10,000 years ago. Nowadays, Cu is predominantly used for electrical applications and heat exchangers, due to its high electrical (59 MS/m) and thermal conductivity (400 W/mK) as compared to other base metals such as Fe (10 MS/m, 80 W/mK) and Ni (14 MS/m, 91 W/mK).[4] Cu is a transition metal with $[Ar]4s^1 3d^{10}$ electronic configuration and situated above silver and gold in group 11 of the periodic table (Figure 1.1).[5] Cu, Ag and Au are traditionally used as coinage metals, due to their high resistance against corrosion, a characteristic for noble metals.[1-2] Cu is more easily oxidized than Ag and Au. Interestingly, when metallic Cu is exposed to air, only a thin layer of copper oxide is formed. This phenomenon is known as passivation and protects the underlying metal against further oxidation.

3	*4*	*5*	*6*	*7*	*8*	*9*	*10*	*11*	*12*
s^2d^1	s^2d^2	s^2d^3	s^2d^4	s^2d^5	s^2d^6	s^2d^7	s^2d^8	s^1d^{10}	s^2d^{10}
21 **Sc** Scandium	22 **Ti** Titanium	23 **V** Vanadium	24 **Cr** Chromium	25 **Mn** Manganese	26 **Fe** Iron	27 **Co** Cobalt	28 **Ni** Nickel	29 **Cu** Copper	30 **Zn** Zinc
39 **Y** Yttrium	40 **Zr** Zirconium	41 **Nb** Niobium	42 **Mo** Molybdenum	43 **Tc** Technetium	44 **Ru** Ruthenium	45 **Rh** Rhodium	46 **Pd** Palladium	47 **Ag** Silver	48 **Cd** Cadmium
57 **La** Lanthanum	72 **Hf** Hafnium	73 **Ta** Tantalum	74 **W** Tungsten	75 **Re** Rhenium	76 **Os** Osmium	77 **Ir** Iridium	78 **Pt** Platinum	79 **Au** Gold	80 **Hg** Mercury

Figure 1.1: *Position of the transition metals in the periodic table of the elements, indicating the group numbers (italic) for periods 4, 5 and 6 in descending order, and the electron configuration of the s and d atomic orbitals.*

Cu-based materials are also widely used as catalysts in the chemical industry, for numerous oxidation and hydrogenation reactions, *i.e.* reacting (organic) molecules with O_2 or H_2, respectively.[6-10] A catalyst is a compound which accelerates the rate of a reaction, without being consumed itself.[11] In heterogenous catalysis, a catalyst is used for conversion of reactants in a different phase (solid, liquid or gaseous) than the catalyst itself. The use of solid catalysts is vital for the efficient liquid- and gas-phase manufacture of fuels and chemicals, and for environmental technology. More than 85 % of all chemicals are synthesized through at least one catalyzed production step.[12] Since most chemical reactions only take place on the metal surface, the Cu catalysts are usually nanoparticles, with a size between 1 and 100 nm.[8, 13-17] The metal nanoparticles are generally stabilized on metal oxide support materials with a high surface area, such as silica (SiO_2), alumina (Al_2O_3) or titania (TiO_2), to prevent the loss of metal surface area due to particle growth during catalysis.[10, 18-21] In order to rationally design more efficient and stable catalysts, it is essential to understand the relationship between the catalyst structure and performance. In the following sections we shall introduce the catalyst materials and synthesis, catalyzed reactions and scientific questions related to this thesis.

1.2 Carbon

Carbon materials have been used for decades in heterogenous catalysis, either as catalysts or as support materials for metal nanoparticles.[22-24] For instance, carbon materials are applied as catalysts for the synthesis of phosgene and thionyl chloride,[25] removal of NO_x and SO_X pollutants from flue gas streams[26-27] and various oxidation reactions.[28-29] Examples of industrial applications of carbon as a support material include catalysts based on Ru for ammonia synthesis, and[30-31] Pd and Pt for various hydrogenation reactions, biomass conversion and fuel cell applications,[32-34] while carbon supports were also used in academic studies such as for catalysts based on NiMo in hydrodesulphurization reactions,[35-36] and Fe and Co for Fischer Tropsch synthesis.[37-39] Metal oxides are typically preferred over carbon supports in terms of catalyst processing, shaping and stability at elevated temperatures in atmospheres containing O_2 or H_2 However, carbon provide several distinct advantages[22-24, 40] such as high chemical resistance towards acids and bases, facile recovery of supported precious metals by combustion, and tunable structure, surface area and surface chemistry, as explained in the following paragraphs.

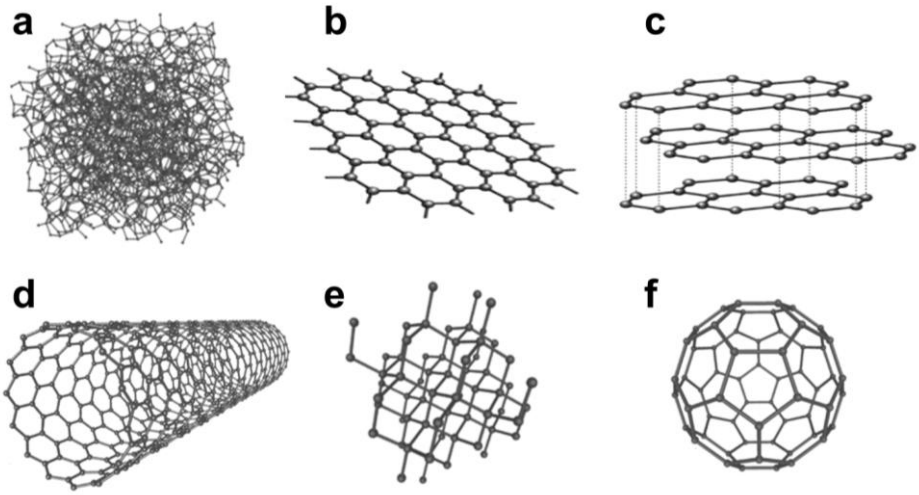

Figure 1.2: *Schematic illustration of several different carbon structures; a) Amorphous carbon; b) Graphene; c) Graphite; d) Single-walled carbon nanotube; e) Diamond; f) C_{60} buckminsterfullerene. Figure adapted from reference [41] with permission from The Royal Society of Chemistry, and reference [42] with permission from Springer-Verlag.*

Carbon materials are available in different structures, such as amorphous carbon, graphene, graphitic carbon, carbon nanotubes and nanofibers, diamond and fullerenes (Figure 1.2).[43-45] The various carbon structures exhibit different structural and chemical properties, such as surface area, porosity, electrical conductivity and presence of functional surface groups. Carbon atoms have the ability to bond with other carbon atoms in various ways (through hybridization of the s and p atomic orbitals)[46] which gives either planar or tetrahedral bonding arrangements. Most

carbon materials used in catalysis are mainly graphitic, such as activated carbon, carbon black, graphene, graphite and carbon nanotubes, with relatively inert surface properties and high electrical conductivity.[22-23, 44] The carbon materials used in this thesis are high surface area graphitic carbons, with approximately 500 m^2 g^{-1} surface area and 0.7 mL g^{-1} total pore volume. The graphitic carbons were prepared through recrystallization and ball-milling of acetylene-derived carbon black (<100 m^2 g^{-1}, <0.3 mL g^{-1}), providing significantly higher purity than for carbon materials which are produced from bio-organic sources.[47-48]

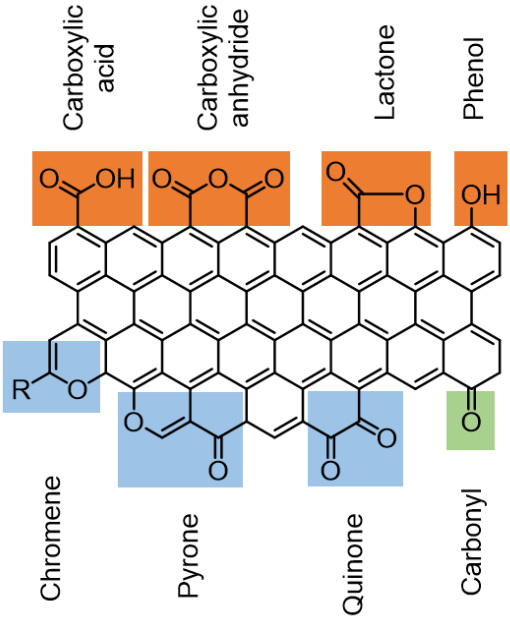

Figure 1.3: *Schematic representation of oxygen-containing surface groups on a graphitic carbon support, showing several acidic (red), neutral (green) and basic (blue) surface groups.*

The chemistry of the carbon surface can be modified to tune the polarity and hydrophobicity, using a variety of oxidation, amination or sulfidation techniques.[22, 40, 49-50] Carbon surface-oxidation by HNO_3 oxidation is a well-known method to introduce a range of oxygen-containing surface groups. These groups may be acidic such as carboxylic acid and anhydride, phenol and lactone groups, neutral like carbonyl groups, or basic such as quinone, chromene and pyrone groups (Figure 1.3).[51-53] Moreover, the π-electron density of the basal planes contributes (weakly) to the carbon basicity.[54] The point of zero charge (the pH at which the overall electrical charge of the surface is zero) may be tuned between pH=2 and pH=10, depending on the specific nature and amount of surface groups.[55] The control over structural and chemical properties makes carbon a versatile material to study supported metal catalysts. In Chapters 2, 3 and 4, we discuss the influence of

liquid-phase HNO_3 oxidation of the carbon surface on the Cu particle size during catalyst synthesis and catalysis.

1.3 Catalyst synthesis

Common methods to prepare supported metal catalysts include precipitation, impregnation and drying, ion adsorption and colloidal synthesis routes.[7, 18, 20] These synthesis routes typically rely on multiple steps to convert metal precursors in solution to supported metal particles. Deposition-precipitation is a method wherein a metal (or hydroxide/oxide/sulfide of a metal) is deposited onto the surface of a support material. The metal precursor is dissolved in the aqueous suspension of support material. A chemical reaction is carried out which changes the precursor solubility and leads to precipitation of the metal compound. Co-precipitation involves the concurrent formation of the metal compound and the support material, from a solution containing both metal and support precursors. An additional thermal decomposition or reduction treatment is typically required to obtain metal nanoparticles supported on the support. Precipitation routes are widely applied to prepare Cu-based catalyst with high Cu loadings (>30 wt%) on metal oxide supports, such as Cu/SiO_2,[56-58] Cu/Al_2O_3,[59-60] Cu/CeO_2,[61-62] Cu/Cr_2O_4,[63-64] $Cu/ZnO/Al_2O_3$[65-67] and $Cu/MnO/Al_2O_3$.[68-69]

Impregnation and drying is a method to deposit the metal precursor from solution in a porous support material, by either applying a large excess of solution (wet impregnation) or by filling only the support pores (incipient wetness impregnation). The solvent is evaporated by heating and/or applying vacuum, with subsequent heating at higher temperatures to decompose the metal precursor. If the interactions between the metal precursor and support are sufficiently strong, no metal redistribution occurs during the heating steps. A final treatment such as reduction, oxidation or sulfidation can be applied, depending on the desired phase for catalysis. Impregnation is widely applied to prepare catalyst with moderate Cu loadings (<20 wt%) on supports such as Al_2O_3,[70-71] SiO_2,[56, 71-73] CeO_2[71, 74] and TiO_2.[71, 75-76]

Electrostatic adsorption of metal ions from a precursor solution is a well-known synthesis route to obtain high dispersions of precious metals, such as Pd and Pt.[34, 77-78] The support is suspended in a large excess of precursor solution. The pH of the solution is adjusted with respect to the point of zero charge of the surface, to introduce an electrostatic interaction between the oppositely charged metal precursor and support material. The adsorption can be classified as either outer sphere complex formation which concerns mainly electrostatic or Coulombic interactions, or inner sphere complex formation in which the support surface groups become directly involved in binding the metal complex in solution.[55, 79-80] The adsorbed metal ion is subsequently reduced to obtain supported nanoparticles.

Colloidal synthesis offers accurate control over the metal particle size and shape. The colloids are commonly prepared by nucleation and particle growth from a precursor solution, while ligands are present to stabilize the nanoparticles against extensive growth. Highly mono-disperse particle size distributions were reported for Cu and $CuZnO_x$ colloids.[81-83] However, removal of the ligands often leads to particle growth and large scale use in catalysis is limited, with only few examples of industrial application.

Impregnation and precipitation are the most widely applied synthesis methods in industry, due to the relative simple procedures, low costs and efficient use of the metal precursors.[18, 20, 84] In this thesis, incipient wetness impregnation is applied to prepare well-defined Cu-based catalysts supported on graphitic carbon, using moderate Cu loadings (3–20 wt%). A schematic overview of the incipient wetness impregnation synthesis approach is given in Figure 1.4.

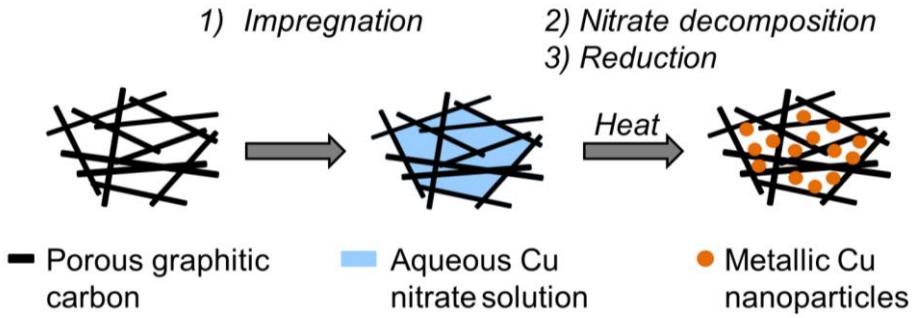

Figure 1.4: *Schematic overview for preparing carbon-supported Cu catalysts via incipient wetness impregnation of a graphitic carbon support, followed by thermal treatments to evaporate the solvent and decompose the metal precursor, and finally reduction to metallic Cu nanoparticles.*

It is well-known in the field of catalyst preparation, that small changes in the synthesis protocol may have a large impact on the properties of the final catalyst.[7, 15, 73, 85] The assembly of carbon-supported Cu catalysts is not trivial and synthesis protocols used for other supports such as SiO_2 or Al_2O_3[73, 86-87] cannot be used directly to obtain the same Cu nanoparticle sizes. Controlling the Cu particle size well below 10 nm was observed as a major constraint in literature to prepare carbon-supported Cu catalysts.[88-92] This limitation likely stems from the weak interaction between the Cu species and the carbon supports during catalyst synthesis. Moreover, the melting point of Cu (1,085 °C) is significantly lower than for noble metals such as Pd (1,555 °C) and Pt (1,768 °C).[19, 93] This implies that Cu species are prone to diffuse and coalesce into larger agglomerates. Surface-oxidation of the carbon support can enhance the density of oxygen-containing surface groups, which can act as an

anchoring point to adsorb metal ions from solution [41, 94] Van der Lee *et al*. previously investigated the deposition precipitation of $Ni(OH)_2$ onto (surface-oxidized) carbon nanofiber supports.[95] The presence of oxygen-containing surface groups was essential to produce small (8 nm) Ni particles, in contrast to the large Ni particles (500 nm) obtained in absence of functional surface groups. Suh *et al*. studied the influence of carbon surface-oxidation on the dispersion of Pd, using an alkali-assisted precipitation method for palladium chloride on activated carbon and carbon black supports.[96] They observed that the metal dispersion increased with an increasing density of oxygen-containing surface groups. To control the structural evolution of the carbon-supported Cu catalysts during synthesis, we will study the interactions between the Cu (precursor) species and carbon supports in Chapter 2.

1.4 Methanol synthesis

A major industrial applications of Cu-based catalysts is the production of methanol from CO_2-enriched synthesis gas (H_2, CO, CO_2).[97-99] More than 75 million tons of methanol are produced each year, providing synthetic routes to essential chemicals such as lower olefins, formaldehyde, dimethyl ether and acetic acid.[97] Methanol additionally shows potential as a sustainable fuel.[98] Synthesis gas can be produced from natural gas and coal, or from renewable biomass and solid municipal waste.[100-103] The benchmark catalyst for methanol synthesis is co-precipitated $Cu/ZnO/Al_2O_3$, with reactions operated at temperatures between 200 and 300 °C and pressures between 40 and 100 bar.[99, 104] The activity and stability of Cu-based catalysts for methanol synthesis have been important research topics over the last decades,[105-110] also in our research group with recent work by Van den Berg and Pompe *et al*.[56, 72, 86, 111-112]

$$CO_2 + 3\,H_2 \rightleftharpoons CH_3OH + H_2O \quad \Delta H_{298\,K,\,1\,bar} = -50\ kJ\ mol^{-1} \qquad \text{(Eq. 1.1)}$$
$$CO + 2\,H_2 \rightleftharpoons CH_3OH \quad \Delta H_{298\,K,\,1\,bar} = -91\ kJ\ mol^{-1} \qquad \text{(Eq. 1.2)}$$
$$CO + H_2O \rightleftharpoons CO_2 + H_2 \quad \Delta H_{298\,K,\,1\,bar} = -41\ kJ\ mol^{-1} \qquad \text{(Eq. 1.3)}$$

The mechanism for synthesis gas conversion to methanol is complex and consists of three concurring reactions, namely hydrogenation of CO (Eq. 1.1), hydrogenation of CO_2 (Eq. 1.2) and the water gas shift reaction (Eq. 1.3). The carbon selectivity towards methanol is higher than 99 %, so the overall reaction can be completely described by Eq. 1–3. Each of these reactions is reversible and thus limited by a thermodynamic equilibrium.[113-115] The conversion per pass through the reactor bed is typically low (<30 %) and unconverted reactant gasses hence need to be recycled. The hydrogenation reactions of CO and CO_2 are exothermic and proceed under volumetric contraction. Low temperatures and high pressures drive the equilibria to methanol. Fast kinetics and high catalyst activity are hence essential for process efficiency.[99, 109]

There is general consensus that CO_2 is the main carbon source for methanol,[106, 110, 116] while CO acts as an oxygen/water scavenger.[67, 99] The rate-determining step for the Cu-catalyzed methanol synthesis from CO_2 is generally believed to be hydrogenation of the formate reaction intermediate, since it is the most abundant carbon-containing surface species under reaction conditions.[99, 106, 117] However, the nature of the catalytic active site for the rate-determining step is still under debate, and likely different for hydrogenation of CO or CO_2.[86, 104-106, 108, 116-122] The advanced understanding of the exact nature of the active site and how its occurrence scales with particle size is crucial to design catalysts with improved performance. However, the high Cu loading (>50 wt%) and general complexity of the ternary component $Cu/ZnO/Al_2O_3$ catalyst hamper the establishment of structure-performance relationships. Fundamental studies are therefore facilitated by using well-defined model catalysts, supported on inert materials, and using moderate Cu loadings (<20 wt%). In Chapter 3, we present a synthesis method to tune the Cu and $CuZnO_x$ particle size supported on graphitic carbon, to investigate the particle size effects on methanol synthesis activity, under industrially-relevant temperature (260 °C) and pressure (40 bar).

1.5 Hydrogenation of ethyl acetate

The hydrogenation of short alkyl esters, such as methyl acetate (MeOAc) and ethyl acetate (EtOAc), is a promising route for the production of renewable ethanol *via* synthesis gas.[123-127] Ethanol is an essential chemical with applications as a fuel, solvent, and chemical building block for the production of *e.g.* acetaldehyde, ethylene, ethylene oxide and ethylene glycol.[128] Over 100 billion liters of ethanol were produced in 2017, mainly by fermentation of (edible) biomass.[129] The increasing demand for ethanol warrants research into sustainable production routes using heterogenous catalysis, which focus on utilizing $C_{1–4}$ oxygenates obtained from (renewable) synthesis gas.[130-131] Dehydration of synthesis gas-derived methanol gives dimethyl ether, which can be carbonylated to MeOAc.[123, 126-127, 132] Hydrogenation of MeOAc yields a mixture of ethanol and re-usable methanol, thus providing high carbon efficiency.[123, 125-126, 133-135] Alternatively, ethanol can be obtained by hydrogenation of EtOAc, which can be efficiently derived from synthesis gas *via* acetic acid.[10, 59, 123, 136]

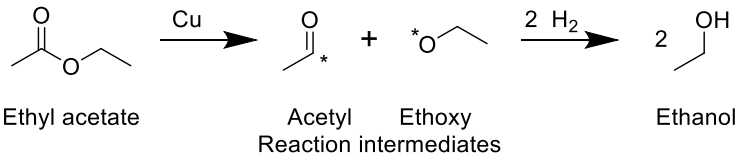

(Eq. 1.4)

$\Delta H_{298\ K,\ 1\ bar} = -75\ kJ\ mol^{-1}$

The industrial hydrogenation of esters is commonly performed using Cu-based catalysts. Cu provides advantages over other active hydrogenation metals, such as Pd, Pt, Ru, Rh and Ni, in the aspect that Cu is less expensive, abundantly available and exhibits superior selectivity towards C-O ester bonds while leaving C=C bonds intact when processing fatty acid alkyl esters.[6, 137-138] The reaction mechanism for the Cu-catalyzed hydrogenation of MeOAc and EtOAc are relatively well understood.[10, 59, 125, 133, 139-140] Both hydrogenation reactions proceed through dissociation of the C–O ester bond, yielding the acetyl and methoxy/ethoxy reaction intermediates (Eq. 1.4). Hydrogenation of the acetyl intermediate to acetaldehyde is generally considered to be the rate-determining step in both reactions, with subsequent hydrogenation of acetaldehyde to ethanol.[125, 133-134] Hydrogenation of EtOAc yields ethanol at more than 95 % selectivity.[133, 139, 141] Conversely, hydrogenation of MeOAc yields a mixture of ethanol and methanol, but also CO, CO_2 and water through the reverse methanol synthesis and water-gas shift reactions. In Chapters 4 and 5, we discuss the Cu-catalyzed hydrogenation of EtOAc under industrially-relevant temperatures (180–210 °C) and pressure (30 bar), as a general model reaction for Cu-based hydrogenation catalysis.

1.6 Selective hydrogenation of butadiene

The purification of olefin feedstocks is crucial to produce high quality plastics.[142-144] Olefins such as ethene, propene and butenes are mainly produced through steam cracking of naphtha and gas oil fraction, during which polyunsaturated impurities such as acetylene, propyne, butyne and butadiene are also formed in concentrations up to around 5 vol%.[142, 145] The presence of the alkyne and diene impurities is detrimental to the polymer quality and may poison the polymerization catalyst.[145-146] For instance, the presence of butyne was reported to poison the Ziegler-Natta $(cyclopentadienyl)_2$-Sc-methyl catalyst used for 2-butene polymerization, by formation of an unreactive $(cyclopentadienyl)_2$-Sc-butene complex.[147] The polyunsaturated impurities must hence be removed to concentrations well below 10 ppm.[143] The industrially-preferred removal method is by partial hydrogenation to the corresponding mono-olefins, while avoiding the formation of alkanes.[142]

The selective hydrogenation of alkynes and dienes is commonly operated using supported Pd-based materials, at temperatures between 30 and 150 °C and pressures between 1 and 30 bar.[85, 144, 148-153] Depending on the specific reactants and catalysts, the process may be carried out in either the gas- or liquid-phase. Un-promoted Pd catalysts are known to be very active, yet unselective with alkane formation rising above 10 % upon complete hydrogenation of the polyunsaturated impurity. Moreover, the Pd-based catalysts suffer from relatively fast deactivation by oligomer deposition, sometimes referred to as “green oil”.[154-155] Alloying Pd with a second metal, such as Ag,[155-156] Au[157] or Cu,[158-160] or adding catalyst poisons such

as Pb, S, or quinoline (Lindlar catalyst)[161], has been reported to increase the selectivity, albeit at lower overall activity, by avoiding the presence of extended Pd surfaces.[144]

Interestingly, supported Cu catalysts have been reported to be highly selective for the hydrogenation of various alkynes[162-166] and dienes.[75-76, 167-170] Nevertheless, the Cu catalysts in literature consistently showed poor stability, resulting in catalyst deactivation within several hours on stream. In our group, Masoud *et al.* recently showed that the support can have a major effect on the stability of supported Au catalysts for the hydrogenation of butadiene.[171] Significantly higher stability was observed when using SiO_2 compared to TiO_2, due to reduced oligomer formation on the support surface. Using carbon or SiO_2 as an inert support for monometallic Cu may provide relatively stable catalysts. In Chapter 6, we discuss the catalytic performance of monometallic Cu on carbon for the gas-phase hydrogenation of butadiene at atmospheric pressure, as a model reaction for selective hydrogenation catalysis (Eq. 1.5).

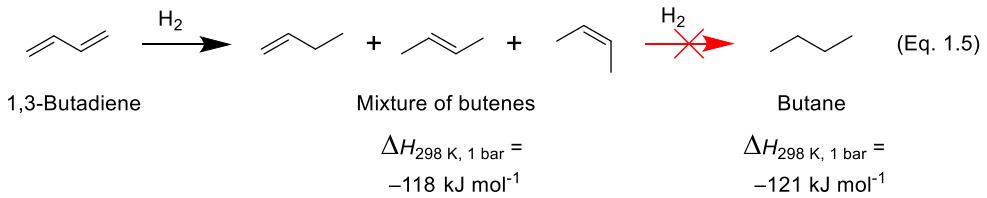

1.7 Promoter effects

The performance of supported metal catalysts is often enhanced by the addition of promoters, which are defined as species that exhibit little or no activity alone, but that boost the catalytic performance when added to a catalytically active phase.[172] Promoters are generally believed to change the electronic nature of the active phase, assist in reactant activation, stabilize reaction intermediates and/or prevent particle growth.[173-175] Metal oxide promoters have been studied in various high-pressure hydrogenation reactions, such as ZnO_x for Cu-catalyzed methanol synthesis,[86, 105, 108] ZnO_x and MnO_x for Cu-catalyzed hydrogenation of alkyl esters,[134-137, 176-178] MnO_x for Co-catalyzed Fischer-Tropsch synthesis,[174-175, 179-180] and MnO_x for Rh and Co catalysts for higher alcohols synthesis.[181-183] The promoters were mainly studied in literature using metal oxide supports, which can give thermodynamically highly stable spectator species such as mixed MnTi oxides.[174, 180, 184] Metal oxide supports may hence obscure the true nature of the promoters. In Chapter 3, we discuss ZnO_x for the Cu-catalyzed synthesis of methanol from CO and CO_2, and compare the promoter efficacy using SiO_2 and carbon supports. In Chapter 5, we apply graphitic carbon to investigate the nature of MnO_x for the Cu-catalyzed hydrogenation of EtOAc to ethanol.

1.8 Particle size effects

The reaction rate in catalysis generally depends on the activation energy for the rate-determining step, the amount and nature of the active sites, and the surface coverage with reactant, intermediates and products. The surface of metal nanoparticles is generally believed to consist of different surface sites, such as facets, corners and step sites.[8, 14, 17, 185] The fraction of the surface sites changes with increasing particle size. Each surface site exhibits a unique degree of coordination saturation and hence different adsorption strength and chemical reactivity. If the reaction intermediates are not adsorbed strongly enough, the reaction does not proceed. However, if the intermediates are too strongly adsorbed, the high adsorbate surface coverage may lead to poisoning of the active site.[110, 186] The metal particle size for supported catalysts can strongly affect the catalytic activity, such as for Co and Fe in Fischer-Tropsch synthesis,[187-190] Ni in CO and CO_2 methanation[13, 191-192] and Pd and Pt in various hydrogenation and oxidation reactions.[148, 192-193] The differences in catalytic activity for varying metal particle sizes may originate from changes in the particle shape, crystal structure, electronic effects and/or metal-support interactions.[8, 15, 190] To rationally design optimized supported metal catalysts, it is crucial to understand how the activity, selectivity and stability depend on the particle size.

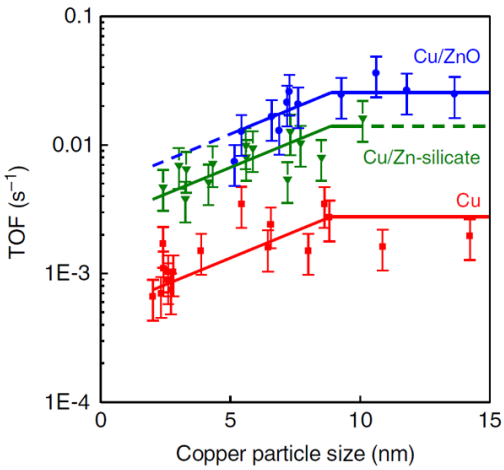

Figure 1.5: *Effect of copper particle size on the surface-specific activity (TOF) for the methanol synthesis reaction from CO_2-enriched synthesis gas, showing un-promoted Cu (red), Cu/Zn-silicate (green) and Cu/ZnO (blue) catalysts. Reaction conditions: H_2:CO:He:CO_2 = 60:23:10:7 vol%, 260 °C and 40 bar. Figure reproduced from reference [86] with permission from Springer Nature.*

Cu particle size effects for hydrogenation reactions are still not fully understood. Recent investigations of $CuZnO_x$-based catalysts for methanol synthesis suggest that the rate-determining step, *i.e.* hydrogenation of the formate intermediate, predominantly occurs on defects on the Cu surface which are stabilized by ZnO_x, yet also that the activation barrier was lowered by ZnO_x decoration on the Cu sites.[105, 108, 110, 194-197] Cu particle size effects and ZnO_x promoter effects are thus difficult to separate. Computational studies by Kuld *et al*. suggested that the catalytic activity was determined by the ZnO_x promoter efficacy, and that the Cu particle size only had an indirect effect *via* the ZnO_x coverage.[108] Alternatively, Van den Berg *et al.* in our research group proposed that the methanol synthesis reaction was intrinsically sensitive to both the Cu and $CuZnO_x$ particle size (Figure 1.5).[86] However, the particle size effects for the un-promoted Cu catalysts were possibly masked by comparing Cu catalyst on SiO_2, Al_2O_3 and carbon supports of varying morphologies. The presence of thermodynamically stable mixed metal oxides spectator species may conceal the intrinsic promoter and particle size effects. In Chapter 3, we investigate whether the particle size effects in methanol synthesis originate from structure sensitivity or from a particle size-dependent coverage of the ZnO_x promoter onto Cu. In Chapter 4, we study the Cu particle size effects on the activity for hydrogenation of EtOAc. Comparing the Cu particle size effects for the hydrogenation of CO, CO_2 and EtOAc may give general insight to design improved Cu-based catalysts for various hydrogenation reactions.

1.9 Scope of this thesis

The main aim of this thesis is to correlate the structural properties of carbon-supported Cu-based catalysts to their performance in various gas-phase hydrogenation reactions. A strong focus lies on intrinsic Cu particle size effects, and separating those from support and promoters effects. Synthesis method development was crucial to tune the Cu nanoparticle size, both the absence and presence of ZnO_x and MnO_x as promoters. State-of-the-art transmission electron microscopy, X-ray absorption spectroscopy and X-ray diffractometry techniques were applied to elucidate the collective structure-performance relationships for three industrially-relevant chemical processes, namely methanol synthesis from CO and CO_2, hydrogenation of EtOAc to ethanol and the selective hydrogenation of butadiene, as schematically summarized in Figure 1.6.

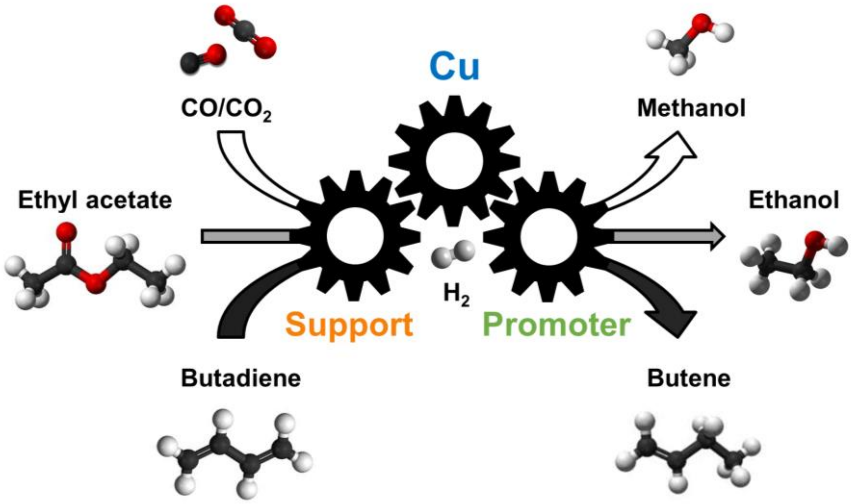

Figure 1.6: *Schematic illustration of the catalyst supports, Cu nanoparticles and metal oxide promoters for the various hydrogenation reactions as discussed in this thesis.*

In **Chapter 2** we discuss the synthesis of atomically dispersed Cu^{2+} ions supported on surface-oxidized graphitic carbon and carbon xerogel. These highly-dispersed Cu materials were used to investigate the formation and growth of Cu nanoparticles, using *in-situ* X-ray absorption and diffraction techniques, and *ex-situ* transmission electron microscopy. Thermal sintering was employed as a synthesis approach to tailor the Cu size from single ions to 10 nm particles. In **Chapter 3** we continue with the synthesis methods for carbon-supported Cu and $CuZnO_x$ catalyst, with tuning the particle sizes, by varying the Cu loading and thermal sintering temperature. The control over Cu and $CuZnO_x$ particle sizes between 3 and 14 nm allowed us to investigate whether the methanol synthesis reaction is intrinsically sensitivity to the Cu particle size, or whether the Cu size only indirectly affects the ZnO_x promoter efficacy.

In **Chapter 4** we discuss the impact of the Cu particle size on the catalytic performance in the gas-phase hydrogenation of EtOAc. The Cu particle size effects are compared to those for the methanol synthesis reaction in Chapter 3, suggested the presence of a common active site for both hydrogenation reactions, with a maximal Cu weight-normalized activity for Cu particles of around 6 nm. In **Chapter 5** we discuss the promoter effects of MnO_x for the Cu-catalyzed hydrogenation of EtOAc. A series of well-defined MnO_x-Cu catalysts was prepared, through co-impregnation of a high surface area graphitic carbon support with aqueous mixed Cu and Mn nitrate solutions. We deliberately kept the MnO_x-Cu particle size constant around 6 nm, while systematically varying the Mn loading. Advanced transmission electron microscopy and *in-situ* X-ray absorption studies were used to study the

catalyst structure and establish structure-performance relationships for the MnO_x-promoted Cu-based catalyst.

In **Chapter 6** we expand on the synthesis methods from Chapters 2 and 3 to tune the Cu particle size from 1 to 23 nm on graphitic carbon. The effects of Cu particle size and the carbon support are described on the catalytic activity, selectivity and stability in the gas-phase hydrogenation of butadiene.

In **Chapter 7** we summarize the results of this thesis and provide an outlook for future research.

Chapter 2

Atomically Dispersed Cu on Carbon and Growth into Cu Nanoparticles of Tailored Size

This chapter is based on the publication: "*Atomically Dispersed Cu on Carbon and Growth into Cu Nanoparticles of Tailored Size"* by R. Beerthuis, P. J. Dietrich, G. J. Sunley, K. P. de Jong and Petra E. de Jongh, Under review.

Abstract

In this chapter, a practical impregnation method to prepare atomically dispersed Cu^{2+} on surface-oxidized carbon was reported. The number of deposited Cu atoms was tuned with respect to the density of oxygen-containing carbon surface groups, to achieve a uniform distribution of isolated Cu^{2+} ions, in the absence of any nanoparticles. A combination of *in situ* X-ray absorption and diffraction techniques revealed that the Cu^{2+} ions could be reduced to Cu^{+}, with retention of the atomic dispersion. The complete reduction to Cu^{0} coincided with cluster formation. Thermal sintering was developed as an approach to tailor the Cu size from sub-nm clusters to 10 nm particles. This practical method to prepare either single Cu ions or Cu nanoparticles may facilitate fundamental studies in catalysis.

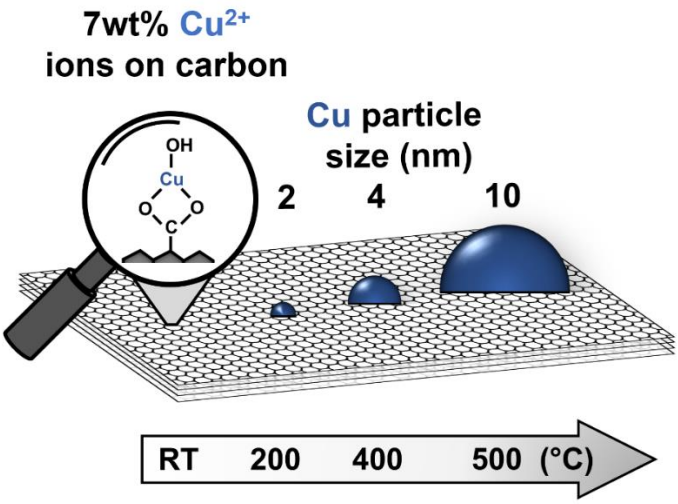

2.1 Introduction

Recent research in catalysis focuses on supported single metal atoms or ions.[8, 17, 198-199] Atomically precise materials may combine the beneficial characteristics of supported metal nanoparticles and single site metal complexes in solution. Most research is focused on the cost-efficient use of precious metals.[17, 21, 199] Yet sub-nm clusters of base metals, such as Cu, Co and Fe, are promising candidates for various important processes, such as the Cu-catalyzed oxidation of methane and selective reduction of nitrogen oxide (NO_x) pollutants.[200-203] However, most research is limited to using zeolites or reducible metal oxides as supports.[8] Only few reports for single Cu atom materials are found in literature based on other common support materials. Conductive carbon-based supports are particularly interesting for the electrochemical application of Cu-based materials.[204-207] For example, Li *et al.* recently reported the fabrication of single Cu atoms, supported between ultrathin nitro-doped carbon nanosheets, with remarkable efficiency in the electrocatalytic oxygen reduction reaction.[208] Yang *et al.* reported high CO_2 reduction efficiency using single Cu atoms, prepared *via* the pyrolysis of Cu-doped metal organic frameworks.[209] However, base metals generally interact only weakly with the inert sp2 hybridized carbon surface, hence limiting the control over the metal particle size[22, 84, 88, 90, 210] and synthesis techniques for single Cu atom on industrially applied non-zeolitic supports are not generally available.

Interestingly, high surface area carbons are commonly applied to remove metal ions from waste water streams, *via* ion adsorption onto oxygen-containing surface groups.[41] These surface groups can be efficiently introduced by various liquid or gas phase oxidation techniques.[22, 49, 211] The surface groups may also provide an anchoring point during the synthesis of supported Cu clusters. The strong electrostatic adsorption of metals from an excess of precursor solution, is a well-known synthesis route for the preparation of small metal nanoparticles (<5 nm) on metal oxide supports.[20] Regalbuto *et al.* demonstrated that electrostatic adsorption may also be combined with incipient wetness impregnation.[77] Van der Lee *et al.* previously investigated the adsorption of Ni species onto carbon nanofiber supports, during the deposition precipitation of $Ni(OH)_2$. The presence of oxygen-containing surface groups was essential to produce small (8 nm) Ni particles, compared to the large Ni particles (500 nm) obtained in absence of functional surface groups.[95] The metal particles were believed to form during the decomposition of precursor complexes. However, the mechanisms for metal ion adsorption and particle formation are generally complex and still not fully understood.[18, 20]

In this chapter, we report the synthesis of Cu ions dispersed over a carbon support, using incipient wetness impregnation. Tuning the ratio between the amount of deposited Cu atoms and carbon surface groups allowed us to prepare up to 9 wt% of atomically dispersed Cu^{2+} sites, as evidenced by X-ray absorption spectroscopy. We investigated the mechanism of Cu particle formation and growth, to tailor the Cu

size from single ions to 10 nm particles, by varying the heat treatment temperature and gas atmosphere. This practical synthesis approach may facilitate the study and application of single Cu atoms and Cu clusters in catalysis.

2.2 Experimental Methods

Carbon synthesis and functionalization

Two carbon support types were used in this chapter, namely turbostratic high surface area graphite and carbon xerogel. The pristine graphite support (HSAG–500, kindly provided by Timcal Ltd.) was referred to as PG. The carbon xerogel was prepared by adaptation of a published procedure.[212] Herein, resorcinol (17.3 g) and sodium carbonate (34 mg) were dissolved in deionized water (24.0 mL). Next, formaldehyde (23.6 mL; 37 % in H_2O, stabilized by 10–15 wt% methanol) was added while vigorously stirring. The resulting carbon gel was aged in a closed vessel for several days at different temperatures. First, the gel was kept for 24 h at room temperature, subsequently for 24 h at 60 °C and finally for 72 h at 90 °C. After cooling down to room temperature, the carbon gel was crushed and washed three times by soaking (1h, 1h and 16h) in acetone (500 mL), while decanting the solvent after each washing step. The gel was dried at room temperature for 72 h, to slowly evaporate the solvent. The dried gel was crushed and pyrolyzed by heating to 800 °C (5 °C min^{-1}) with 10 h isothermal hold at 800 °C, under Ar flow (10 mL min^{-1} g^{-1}). Finally, the pristine carbon xerogel was collected after cooling down to room temperature, and referred to as PX. The porosity of the turbostratic graphite support arises from stacking of the plate-like graphitic sheets, giving a broad pore diameter distribution, with most porosity exhibited below 30 nm pore diameter. The carbon xerogel is largely comprised of amorphous carbon, in which the porosity originates from the stacking of spherical carbon particles, with an average pore diameter of 23 nm. The BET surface areas of bare pristine graphite and bare pristine xerogel carbon were approximately 500 m^2 g^{-1} and 680 m^2 g^{-1}, respectively.

The pristine carbon supports were surface functionalized by liquid-phase oxidation using concentrated nitric acid. Herein, ~10 gram of the pristine carbon material was suspended in $HNO_{3\,(aq)}$ (65 %; 40 mL g^{-1}), inside a 1 L round-bottom flask fitted with a reflux condenser. The pristine graphite material was heated to 80 °C in approximately 25 min, and kept at 80 °C for 110 min. Alternatively, the pristine xerogel was heated to 120 °C in approximately 40 min, and kept for 55 min hold at 120 °C. Thereafter, the reaction was quenched by diluting the suspensions with ~1.6 L of cold deionized water (25 °C). The surface-oxidized carbons were allowed to sediment for 30 min and the supernatants were decanted. The solids were washed with deionized water until a pH of around 7 was reached. After the final washing step, the carbons were dried overnight at 120 °C and crushed into powders. Finally, all carbon supports were dried for 90 min at 170 °C, under dynamic vacuum, to remove traces of adsorbed water, and kept inside an Ar-filled glovebox (Mbraun LABmaster;

<1 ppm H_2O; <1 ppm O_2), The surface-oxidized carbon supports were referred to as OG for surface-oxidized graphite and OX for surface-oxidized xerogel.

Cu/C sample preparation

A series of carbon-supported Cu samples was prepared by impregnating of the (surface-oxidized) carbon supports to incipient wetness using $Cu(NO_3)_2$ precursor solutions. The metal concentration in the precursor solution was adjusted to control the metal loading, which was calculated as $\mathrm{Cu\ wt\%} = \left(\frac{\mathrm{mass\ Cu}}{\mathrm{mass\ CuO + mass\ support}}\right) * 100$. The metal precursor was dissolved in 0.1 M HNO_3 (aq) to yield a pH of ~1. The samples (8_Cu/PG, 3_Cu/OG, 7_Cu/OG and 9_Cu/OX) were labelled as *X*_Cu/*Y*, in which *X* shows the Cu wt% and *Y* indicates the surface-oxidized graphite (OG) or surface-oxidized xerogel (OX) support.

In a typical synthesis, ~2 g of the dried carbon support was impregnated, by adding the solution by syringe, in a round-bottom flask, under static vacuum. After the impregnation, the sample was first stirred for 24 h to homogenize the metal content, then dried for 24 h while stirring under dynamic vacuum, both steps at room temperature. In the preparation of the sample with 8 wt% Cu on pristine graphite (8_Cu/PG), the dried impregnated sample was first purged at room temperature for 30 min under N_2 flow (~100 mL min^{-1} g^{-1}) and subsequently heated to 230 °C (2 °C min^{-1}) under 20 vol% H_2/N_2 flow (~100 mL min^{-1} g^{-1}). Subsequently, the sample was left to cool down and was purged at room temperature for 5 h under N_2 flow (~100 mL min^{-1} g^{-1}). Next, the sample was treated, first for 1 h at room temperature using a flow of 5 vol% O_2/N_2 (~100 mL min^{-1} g^{-1}), followed by a heating step to 200 °C (1 °C min^{-1}), and finally for 1 h at 200 °C under a flow of 15 vol% O_2/N_2 flow (~100 mL min^{-1} g^{-1}). In the case of the 3_Cu/OG, 7_Cu/OG and 9_Cu/OX samples, the dried impregnated material was heated to 230 °C (0.5 °C min^{-1}) with 1 h hold at 230 °C, under a flow of pure N_2 (~100 mL min^{-1} g^{-1}). The Cu/C samples were transferred to an Ar-filled glovebox without exposure to air, and finally passivated by overnight exposure to air at room temperature.

The 3_Cu/OG and 7_Cu/OG samples were heated *ex-situ* to grow the sub-nm Cu species into Cu nanoparticles. The samples were loaded into a glass plug-flow reactor and first purged for 30 min under a flow of N_2 (~100 mL min^{-1} g^{-1}) and subsequently exposed to a flow of 20 vol% H_2/N_2 (100 mL min^{-1} g^{-1}). Next, the sample was heated to 150 °C (2 °C min^{-1}), followed by 120 min hold at 150 °C, and finally heated to 400 °C (2 °C min^{-1}), with 1 h hold at 400 °C. The materials were left to cool down to room temperature and passivated by exposing them overnight to air, and referred to as 3_Cu/OG_400 and 7_Cu/OG_400.

Cu/C characterization

The support porosity was characterized by N_2 physisorption (Micromeritics TriStar 3000 V6.08). Before the measurements, the samples were outgassed for 14 h at 150 °C under dynamic vacuum. Isotherms were measured at −196 °C, using Carbon Black STSA as reference. The specific surface area was calculated using the multi-point Brunauer-Emmet-Teller (BET) method, with P/P_0 between 0.05–0.25. The total pore volume was calculated as single point pore volume at P/P_0 of 0.995. The micropore area and volume were calculated using the t-plot method. The pore diameter distribution was determined using the Barrett-Joyner-Halenda method applied to the isotherm adsorption branches.

Potentiometric titration was performed using a TitraLab pH-meter. The amount of acidic and basic surface groups was determined in separate measurements. The sample was suspended in 65 mL of 0.1 M $KCl_{(aq)}$ solution, using ~25 mg for the PG and PX supports, and ~8 mg for the OG and OX supports. The carbon suspension was de-gassed for 5 min using a flow of N_2, under vigorous stirring. Next, the titrations were performed using solutions of either 0.01 M $NaOH_{(aq)}$ or 0.01 M $HCl_{(aq)}$, both prepared in 0.1 M $KCl_{(aq)}$. The density of the acidic and basic surface groups was calculated from the equivalence point of the titration curves, after subtraction of the value for a blank measurement to adjust for any dissolved CO_2.

Thermogravimetric analysis was performed on a PerkinElmer balance (Pyris 1), coupled to Pfeiffer mass spectrometer. The sample (5–10 mg) was first purged under a flow of Ar (20 mL min^{-1}) at 50 °C. Thereafter, the sample was heated to 600 °C (5 °C min^{-1}), either under a flow of either pure Ar or 5 vol% H_2/Ar (20 mL min^{-1}).

Temperature programmed reduction analysis was performed on a Micromeritics Autochem II ASAP 2920 apparatus. The H_2 consumption was determined using a thermal conductivity detector. Prior to the measurement, the sample was dried at 120 °C for 30 min under a flow of Ar (~1 mL min^{-1} mg^{-1}), and cooled down to 30 °C. All experiments were performed using a flow of 5% H_2/Ar (~1 mL min^{-1} mg^{-1}). Two methods were applied to study the reduction behavior for the Cu/C samples. In the first experiment, the sample was heated from 30 to 150 °C (2 °C min^{-1}), with 2 h isothermal hold at 150 °C, and subsequently heated to 350 °C (5 °C min^{-1}). In the second experiment, the sample was heated continuously from 30 to 400 °C (2 °C min^{-1}). The amount of H_2 consumption was calculated by integration of the TCD peak area.

Scanning transmission electron microscopy (STEM) in high-angle annular dark-field (HAADF) mode, coupled with energy-dispersive X-ray spectroscopy (EDX) was performed on an FEI Talos F200X microscope operated at 200 kV. The Cu/C materials were ground into a fine powder and directly deposited onto a holey carbon coated Ni grid (Agar 300 mesh). The surface-averaged Cu particle size (d_s) was

calculated as $d_s = \frac{\sum_{i=1}^{N} d_i^3}{\sum_{i=1}^{N} d_i^2}$. Herein, d_i is the diameter of the ith particle and N the number of counted particles. The standard deviation in width of the particle size distribution (σ_{ds}) represents the typical difference between d_i and d_s, and was calculated as $\sigma_{ds} = \sqrt{\left(\frac{1}{N-1}\right)\sum_{i=1}^{N}(d_i - d_s)^2}$.

In situ X-ray absorption spectroscopy was conducted at the MRCAT Sector 10 Insertion Device Beamline at the Advanced Photon Source, Argonne National Laboratory.[213] Samples were loaded into a single well of a 6-well sample holder, and placed in a 1 inch quartz tube, thus encompassing the *in situ* measurement cell. Ultra-torr fittings with welded Swagelok ball valves were used to supply gases and seal the tube environment. Kapton (polyimide) windows were present at both ends of the measurement cell. A thermocouple touching the sample holder was used to monitor temperature. All experiments were conducted in transmission mode. Sample amounts were calculated to give an absorbance (µx) of 2.0. This corresponded to 22 mg for 3_Cu/OG, 12 mg for 7_Cu/OG and 10 mg for 9_Cu/OX. Prior to scanning, the samples were pre-treated under a flow of 20 vol% O_2/He (50 mL min^{-1}) at room temperature. Following the pre-treatment, the sample was sealed under the 20 vol% O_2/He atmosphere and transferred to the beamline. The samples were purged with pure He to remove all O_2, then scanned initially under a flow of He (1.5 mL min^{-1} mg^{-1}). Thereafter, the gas composition and temperature profile was set according to the specific experiment.

The X-ray absorption spectra were normalized and background subtracted by standard methods in the Athena software package. XANES fitting was performed by linear combination fitting with reference spectra for Cu^{2+}, Cu^{+}, and Cu^{0} states, in Athena. Reference spectra for the linear combination fitting were the initial spectrum of 3_Cu/OG measured under He at room temperature (Cu^0), the spectrum of 3_Cu/OG measured under H_2/He at 162 °C (maximum intensity of the 8982 eV feature in the first derivative, and the point at which $CN_{Cu–O}$ was 2, parameters consistent with only Cu^+ species in the sample), and the spectrum of 3_Cu/OG after 120 min at 300 °C, where complete reduction was determined. Note that we chose to not only use bulk references (Cu foil, Cu_2O, CuO) as the specific geometry of the Cu atoms and their resulting cluster sizes can result in measurably different XANES spectra,[214] so it is best practice to use representative reference spectra.

The coordination numbers were calculated, by considering only the first Cu–O and Cu–Cu coordination spheres, using a FEFF quick first shell fit in the Artemis software package. Pathway parameters were determined by first fitting a Cu foil (for Cu–Cu path) and $Cu(OAc)_2$ (for Cu–O path). EXAFS fitting results were fitted with a temperature-corrected Debye-Waller factor (DWF), indicating that all CN are corrected for temperature effects. A correlation between DWF and temperature

(DWF is a function of temperature) was determined for the Cu–Cu path by fitting the spectrum for the 3_Cu/OG sample at 300 °C (under 3.5 vol% H_2/He atmosphere) and immediately after cooling to room temperature, and assuming that $N_{Cu–Cu}$ was the same for both (*i.e.* no growth during cooling). A DWF correlation for the Cu-O scattering pathway was similarly determined using the 3_Cu/OG sample compared at 150 °C (under 3.5 vol% H_2/He atmosphere) and room temperature. This allows for the CN to be corrected for temperature effects and directly compared.

The Cu–Cu coordination number from EXAFS was obtained after correcting for the fraction of oxide ($CN_{Cu–Cu}$ = CN_{raw}/Fraction Cu^0). In this approach, the coordination of the metal phase was estimated by assuming it were the only phase in the system. All fits were performed on the Fourier Transform (FT; 1<R<3) of the k^2 EXAFS, with FT taken between 2.6<k<11.8. Goodness of fit was determined by visual comparison of the magnitude and imaginary part of the FT, as well as considering the R-factor if multiple fits were compared. Absolute uncertainty in EXAFS fitting is generally regarded as ±10 % for estimated coordination numbers, ±0.01 Å for the bond distances. Uncertainty in the XANES fitting is regarded as <5 %, but that assumes perfect references, which is not necessarily the case here. Particle sizes were estimated from the coordination numbers from EXAFS using a correlation developed by Jeff Miller *et al*.[215] The uncertainty in particle sizes is approximately 0.5 nm.

Powder X-ray diffraction (XRD) was performed on a Bruker D8 diffractometer equipped with a Co-$K_{\alpha 1,2}$ radiation source (λ=1.79026 Å) and Lynxeye detector. The diffractometer was operated at 30 kV, 45 mA and using a V20 variable slit. The *in situ* measurement was performed using an XRK 900 Anton Parr insertion device, equipped with gas manifold to control the gas composition and flow rate. Diffractograms were recorded continuously from 40 to 67 °2θ during the experiment. The sample (~20 mg) was first purged for 30 min under a flow of pure He (200 mL min^{-1}). Next, the gas flow was changed to 10 vol% H_2/He (200 mL min^{-1}) and the sample was heated to 250 °C (2 °C min^{-1}). After 120 min isothermal hold at 250 °C, the temperature was increased to 510 °C (2 °C min^{-1}). The diffractogram of the bare surface-oxidized graphite support was subtracted as a baseline for each diffractogram. The Cu crystallite size was determined by applying the Scherrer equation to the Cu^0 (111) diffraction peak at 50.7 °2θ, using a shape factor *k* of 0.89 and a line broadening factor of 0.1. A trendline curve for exponential growth of the crystallite size with temperature was fitted using the formula $y = y_0 + A_1 * e^{((x-x_0)/t1)}$, which gave $y = 1.97 + 0.11 * e^{((x-139)/87.5)}$. The apparent activation energy (E_a) for Cu crystallite growth was calculated from the linear slope (between 300–460 °C) in the Arrhenius plot, by using the increase in crystallite size as a function of the reciprocal absolute temperature (K).

2.3 Results and Discussion

Atomically dispersed Cu on carbon. We first prepared a carbon-supported Cu sample via a standard impregnation method, using an aqueous $Cu(NO_3)_2$ solution (Figure 2.1).[56, 72-73, 86, 88, 134, 176, 216] The sample contained 8 wt% Cu on a pristine high surface area graphite support, and was labelled as 8_Cu/PG. In general, all samples discussed in the results section will be labelled as *X*_Cu/*Y*, where *X* signifies the Cu wt% and *Y* indicates the carbon support, *i.e.* pristine graphite (PG), surface-oxidized graphite (OG) or surface-oxidized xerogel (OX). All impregnated samples were heated to 230 °C to fully decompose the nitrate precursors , but the heating rate (0.5 or 2 °C min^{-1}) and gas composition 20 vol% H_2/N_2 or pure N_2 varied. In the case of the 8_Cu/PG sample, the heating rate was 2 °C min^{-1} and the gas atmosphere 20 vol% H_2/He, which gave a surface-averaged Cu particle size of 10.4±4.3 nm. The Cu particle size on carbon was much larger than Cu particle sizes on metal oxide supports as reported in literature.[56, 72, 86, 176, 216] For example, preparing a sample with 15 wt% Cu on SiO_2 previously yielded 2.4 nm Cu particles, using similar synthesis conditions.[86] Furthermore, we observed next to the Cu particles, also sub-nanometer Cu spread over the carbon support (Figure 2.1c). This indicated that small Cu species could be stabilized on the carbon support, likely by anchoring to oxygen-containing surface groups. However, the molar ratio of Cu atoms to oxygen-containing surface groups was around 11 for this sample, hence representing a large excess of Cu atoms (Table 1). We therefore increased the density of surface groups and lowering the Cu loading as a strategy to increase the Cu dispersion.

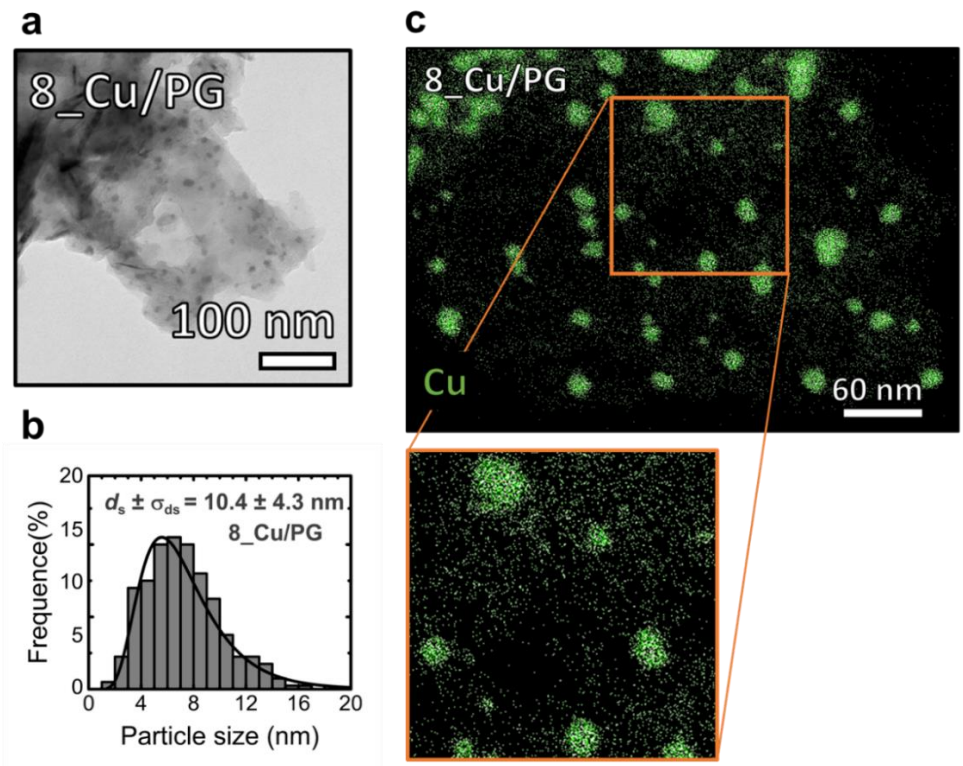

Figure 2.1: *Transmission electron microscopy analysis for the 8_Cu/PG sample, prepared by incipient wetness impregnation of a pristine graphite support, showing* ***a****) Micrograph in bright-field mode and* ***b****) corresponding particle size distribution fitted with a lognormal curve and the surface-averaged Cu particle size (d_s) with standard deviation in the particle size distribution (δ_{ds});* ***c****) Cu distribution map (green) by energy-dispersive X-ray spectroscopy, with enhanced magnification inset (orange square).*

Liquid-phase HNO_3 oxidation was applied to the graphite and carbon xerogel supports. We optimized the oxidation conditions to introduce a large density of surface groups, while minimizing the loss of support porosity (Figure 2.2a,b). The oxidation treatment resulted in a minor decrease in surface area from 500 to 440 m^2 g^{-1} for the graphite support, and from 680 to 590 m^2 g^{-1} for the xerogel support.The density of basic surface groups was negligible for carbon supports (Figure 2.2c), while the acidic surface groups increased from 0.14 to 0.65 nm^{-2} for the graphite support, and from 0.02 to 2.1 nm^{-2} for the xerogel support (Figure 2d). The surface-oxidized carbon supports were hence acidic in nature with a predominant surface coverage of carboxylic acid groups.[22, 40, 211]

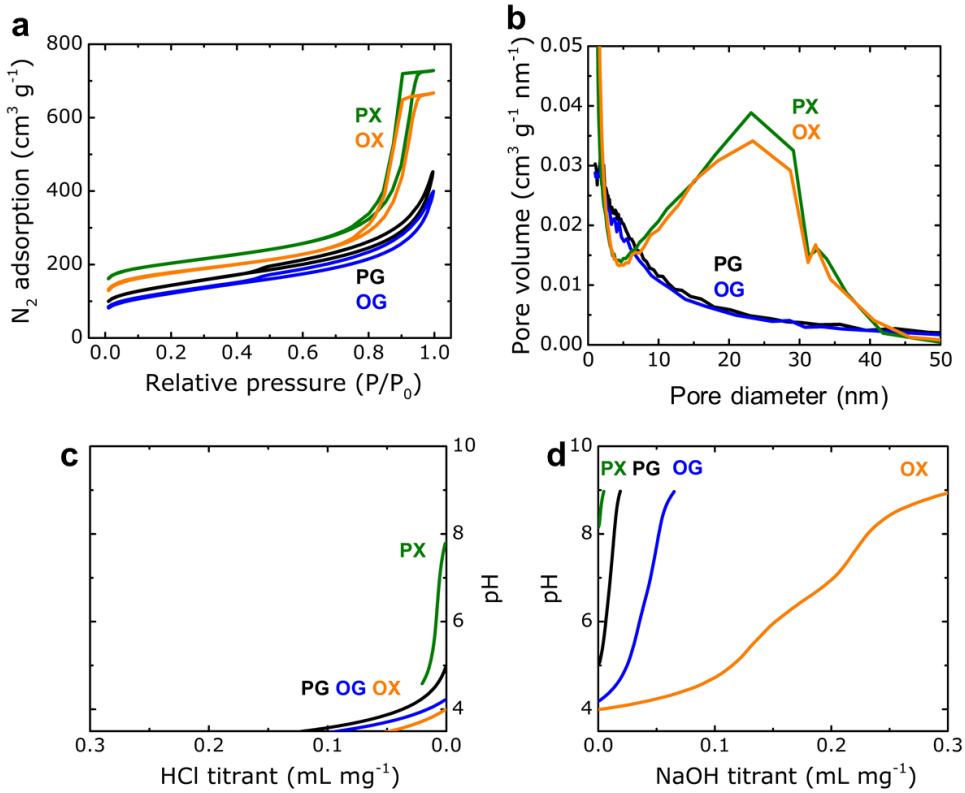

Figure 2.2: *Physicochemical characterization of the bare carbon support materials, for pristine graphite (PG; black), surface-oxidized graphite (OG; blue), pristine xerogel (PX; green) and surface-oxidized xerogel (OX; orange).* ***a****) N_2 physisorption isotherms;* ***b****) Pore diameter distribution determined using the Barrett-Joyner-Halenda method applied to the isotherm adsorption branches;* ***c*** *and* ***d****) Potentiometric titration curves using solutions of* ***c****) HCl and* ***d****) NaOH.*

The surface-oxidized carbon supports were used to prepare three Cu/C samples with varying Cu loadings (Table 1). We hence tuned the molar ratio between Cu atoms and oxygen-containing surface groups between 0.75 and 2.5 (Figure 2.3). Variations in the temperature profile and gas atmosphere during the precursor decomposition, strongly affected the final Cu particle size. For example, heating the 3_Cu/OG sample with 5 °C min^{-1} to 230 °C under a flow of 20 vol% H_2/N_2 yielded 5 nm Cu crystallites, as determined by XRD analysis. However, heating the 3_Cu/OG sample with 0.5 °C min^{-1} to 230 °C, under pure N_2 flow resulted in the absence of crystalline Cu. Remarkably, for all samples that were prepared on surface-oxidized carbon and heated (230 °C, 0.5 °C min^{-1}) under pure N_2 flow, no crystalline CuO_x nanoparticles were observed, and the sub-nanometer Cu was uniformly spread, as evidenced by STEM analysis.

Table 2.1: Chemical properties of the carbon-supported Cu (Cu/C) materials.

Sample	Cu loading (wt%)	Surface area (m^2 g^{-1})[a]	Pore volume (mL g^{-1})[a]	Density of surface group (nm^{-2})[b]	Cu/Surface group ratio (mol/mol)
8_Cu/PG	7.7	500	0.70	0.14	11.4
3_Cu/OG	3.0	440	0.63	0.63	1.00
7_Cu/OG	7.1	680	1.10	0.65	2.50
9_Cu/OX	8.7	590	0.93	2.10	0.75

***a**) BET surface area and total pore volume for the bare carbons, as determined by N_2 physisorption; **b**) Density of acidic surface groups for the bare carbons, as determined by potentiometric titration.*

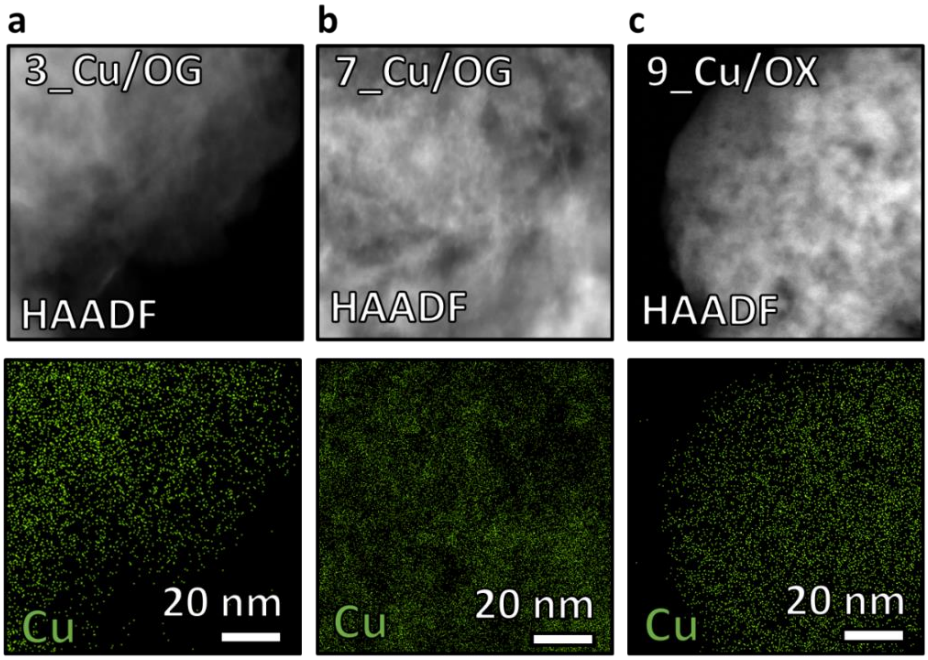

***Figure 2.3:** STEM micrographs in HAADF mode (above) with corresponding EDX Cu distribution maps (below). **a**) 3_Cu/OG; **b**) 7_Cu/OG and **c**) 9_Cu/OX. The carbon-supported Cu samples were prepared by incipient wetness impregnation of surface-oxidized graphite (OG) or surface-oxidized xerogel (OX) as the support material, and using 3 to 9 wt% Cu.*

The nature of the Cu species was investigated by X-ray absorption spectroscopy. Figure 2.4a shows the X-ray absorption near edge structure (XANES) spectra for the Cu/C materials, which were prepared by heating to 230 °C under N_2 flow and subsequently passivated in air at room temperature (3_Cu/OG, 7_Cu/OG and 9_Cu/Ox). The edge energies were located around 8,985 eV, with a characteristic white line feature around 8,997 eV, which proves that the Cu/C materials contained

predominantly Cu^{2+} species. While short range Cu-O scattering (R= 1–2 Å) was observed in the EXAFS spectra, no significant long-range scattering (R= >2 Å) was observed for any Cu/C material (Figure 2.4b). These results, when compared to the bulk Cu(II) oxide reference standard, strongly indicating the presence of either atomically dispersed Cu^{2+} ions or Cu-oxide clusters of at most a few atoms in size.

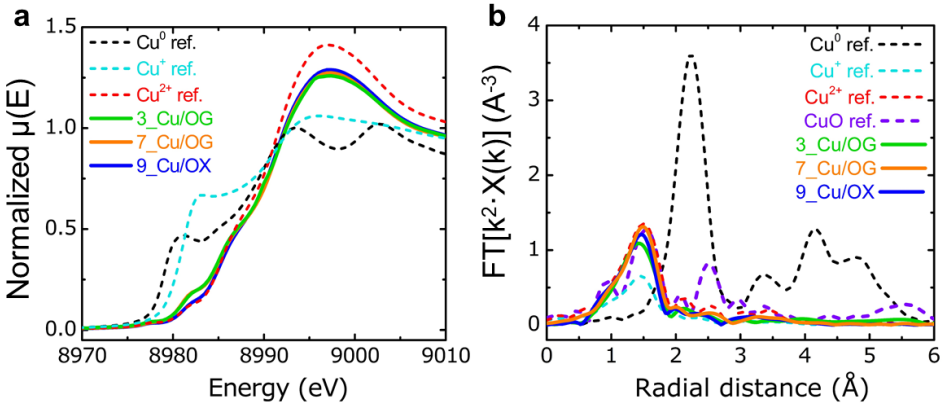

Figure 2.4: *X-ray absorption spectra for the passivated 3_Cu/OG (green), 7_Cu/OG (orange) and 9_Cu/OX (blue) materials, prepared by impregnation of surface-oxidized graphite (OG) or surface-oxidized xerogel (OX), with variation of the Cu loading between 3 to 9 wt%, including Cu^0 foil, bulk CuO, and isolated Cu^+ and Cu^{2+} references (dashed lines), spectra acquired at room temperature in He flow,* ***a****) Baseline-corrected and intensity-normalized spectra;* ***b****) k^2-weighted Fourier transforms in R-space.*

The Cu–O coordination number ($CN_{Cu–O}$) calculated from EXAFS fitting was 3.0 for the 3_Cu/OG and 9_Cu/OX samples. A Cu–carboxylate interaction would account for a $CN_{Cu–O}$ of 2, with Cu^{2+} binding to both oxygen atoms. The $CN_{Cu–O}$ of 3.0 shows that each Cu^{2+} ion is bound to another oxygen-species. Since the ratio between Cu atoms and carbon surface groups was 1.0 or less for these samples, the Cu^{2+} ions cannot on average bind to more than one carboxylate group, with an averaged distance of 1.25 nm between individual carboxylate surface groups. The third oxygen atom binding to the Cu^{2+} ions might be part of an extra ligand anion such as $–OH^–$, originating from the decomposition of the $Cu(NO_3)_2*(H_2O)_x$ precursor. Heating the samples for 1 h at 230 °C excludes the presence of NO_x ligands, as evidenced by thermogravimetric analysis. The 7_Cu/OG sample with a Cu atom to surface group ratio of 2.5 showed a $CN_{Cu–O}$ of around 3.5. This value is slightly higher than the 3_Cu/OG sample, and as it is unlikely that more coordinating ligands are present, we tentatively explain this by the presence of sub-nanometer Cu-oxide clusters. Tuning the Cu atom to surface group ratio to 1.0 or less, hence resulted in the coverage of the carbon surface groups with isolated Cu^{2+} ions, while applying excess Cu resulted in additional sub-nanometer CuO_x clusters. Strikingly, the Cu–carboxylate complex was thermally stable at 230 °C under N_2 flow.

Stability of the atomically dispersed Cu species. To assess the stability of the highly dispersed Cu^{2+} ions and sub-nanometer Cu-oxide clusters, we performed two sets of temperature-programmed reduction experiments under 5 vol% H_2/Ar flow (Figure 2.5). During a continuous temperature ramp from 30 to 400 °C (Figure 2.5a), the Cu^{2+} species were reduced in two discrete steps, first from Cu^{2+} to Cu^{+} and subsequently from Cu^{+} to Cu^{0}. A two-step reduction was earlier reported for the reduction of CuO particles supported on SiO_2 and Al_2O_3.[56, 70, 73, 217] The temperatures for the two reduction peaks were the lowest for the 7_Cu/OG sample (145 and 169 °C), intermediate for 3_Cu/OG (160 and 217 °C) and highest by 9_Cu/OX (194 and 217 °C). In the second experiment, we increased the temperature step-wise, first from 30 to 150 °C and subsequently to 350 °C (Figure 2.5b). The amount of hydrogen consumed during the isothermal stage at 150 °C, corresponded to the full reduction of all Cu^{2+} in the 7_Cu/OG sample to Cu^{0}. However, for the 3_Cu/OG sample the amount only corresponded to reduction Cu^{+}. The complexed Cu^{2+} ions were hence more stable than the sub-nanometer Cu-oxide clusters, in line with theoretical calculations on Cu clusters.[218-219]

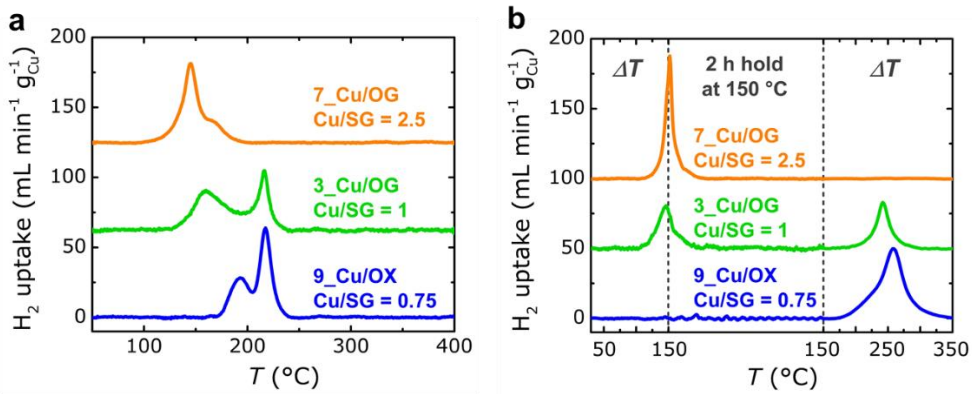

Figure 2.5: *H_2 temperature-programmed reduction profiles for the 3_Cu/OG (green), 7_Cu/OG (orange) and 9_Cu/OX (blue) materials. H_2 consumption is shown as a function of temperature during **a**) Continuous heating to 400 °C (2 °C min^{-1}); **b**) Step-wise heating, first to 150 °C (2 °C min^{-1}), followed by 2 h isothermal hold at 150 °C, and finally heating to 350 °C (5 °C min^{-1}).*

The structural changes upon reduction of the Cu^{2+} species were investigated by *in situ* X-ray absorption spectroscopy (Figure 2.6). The 3_Cu/OG sample was heated to 90 °C under a flow of 3.5 vol% H_2/He. This gave a decrease in the white line feature around 8,997 eV, with a concurrent increase in the 8,981 eV edge feature (Figure 2.6a), which confirms the reduction of Cu^{2+} to Cu^{+}. After 30 min at 150 °C, the sample contained only Cu^{+} species, while still no significant Cu–Cu scattering (R= >2 Å) was observed in the EXAFS spectra, even after 2 h at 150 °C (Figure 2.6b). A decrease in the Cu–O scattering intensity (R= <2 Å) and corresponding drop in $CN_{Cu–O}$ from approximately 3 to 2, in absence of either Cu–

Cu coordination or other long-range coordination, indicated that the Cu^+ ions were still atomically dispersed.

Upon heating the 7_Cu/OG sample to 150 °C, an extra feature appeared around 8,979 eV in the XANES spectra, corresponding with reduction to Cu^0 (Figure 2.6c). A significant decrease in the Cu–O scattering intensity (R= <2 Å) coincided with an increase in the Cu–Cu scattering intensity (R= >2 Å), as shown in Figure2. 6d. The estimated Cu-Cu coordination number (CN_{Cu-Cu}) from EXAFS fitting was 7.2, corresponding to an average Cu^0 particle size of 2 nm, according to the correlation published by Miller *et al*.[215] Finally, heating the 9_Cu/OX to 150 °C gave only minor reduction of Cu^{2+} to Cu^+, with no significant change in Cu–O scattering intensity. Even though the 9_Cu/OX sample had the highest Cu loading, it was prepared with the lowest Cu atom to surface group ratio (0.75), and showed the highest stability. Tuning the Cu atom to surface group ratio was an efficient tool to vary the Cu size and thermal stability on carbon.

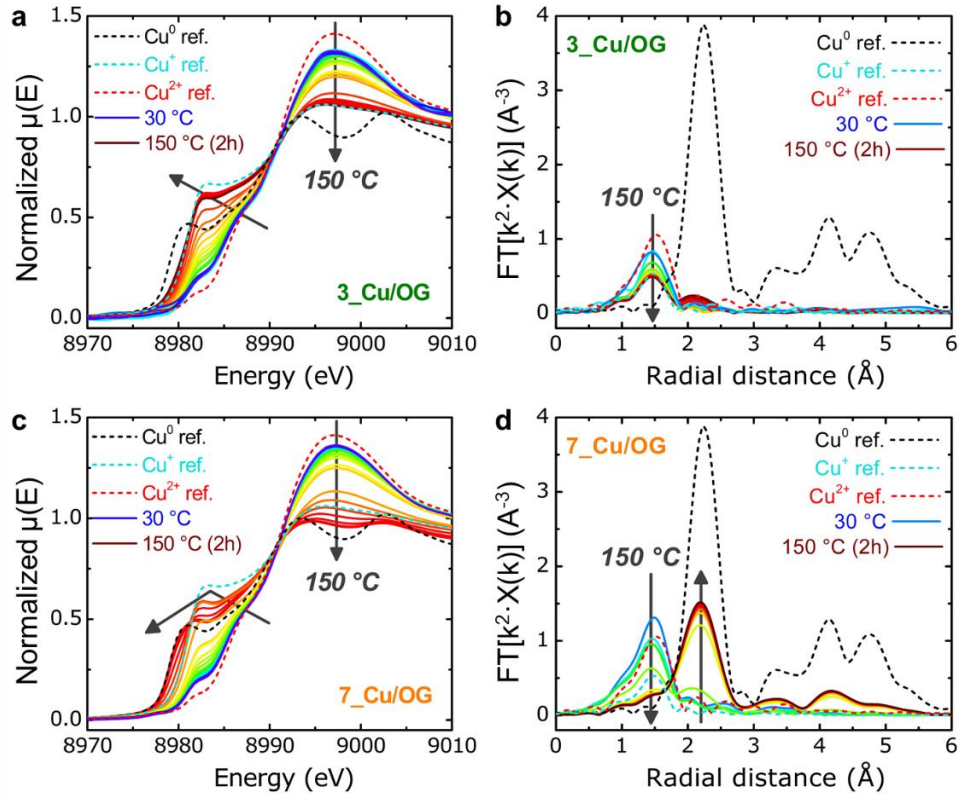

Figure 2.6: *In situ X-ray absorption spectra acquired during heating to 150 °C (2 °C min^{-1}) and 2 h isothermal hold at 150 °C, under a flow of 3.5 vol% H_2/He, for samples 3_Cu/OG (**a**,**b**) and 7_Cu/OG (**c**,**d**), showing the baseline-corrected and intensity-normalized spectra (**a**,**c**) and k^2-weighted Fourier transforms in R-space (**b**,**d**), including Cu^0, Cu^+ and Cu^{2+} reference spectra (dashed lines). Arrows indicate the direction of increasing temperature.*

Observing in situ Cu particle formation. The mechanism for Cu particle formation and growth was in more detail investigated by heating the 3_Cu/OG sample to 300 °C under 3.5 vol% H_2/He (Figure 2.7). The reduction of Cu^+ to Cu^0 coincided with a decrease in the $CN_{Cu–O}$ from around 2 to 0. Concurrently, the $CN_{Cu–Cu}$ increased from 0 to approximately 8. The estimated Cu^0 particle size from EXAFS analysis was approximately 4 nm at 300 °C, and did not significantly increase after 2 h isothermal hold at 300 °C. The Cu/C particles were hence found to be thermally stable. Intriguingly, the reduction of Cu^+ to Cu^0 also coincided with Cu agglomeration when heating under a pure He flow, albeit at higher temperatures. These findings suggest that mobile Cu species, for instance surface-bound Cu–H, Cu–OH or Cu–HCOO complexes,[220] facilitate the formation of larger Cu^0 nanoparticles. A tentative schematic representation for the particle formation mechanism is given in Figure 2.7c.

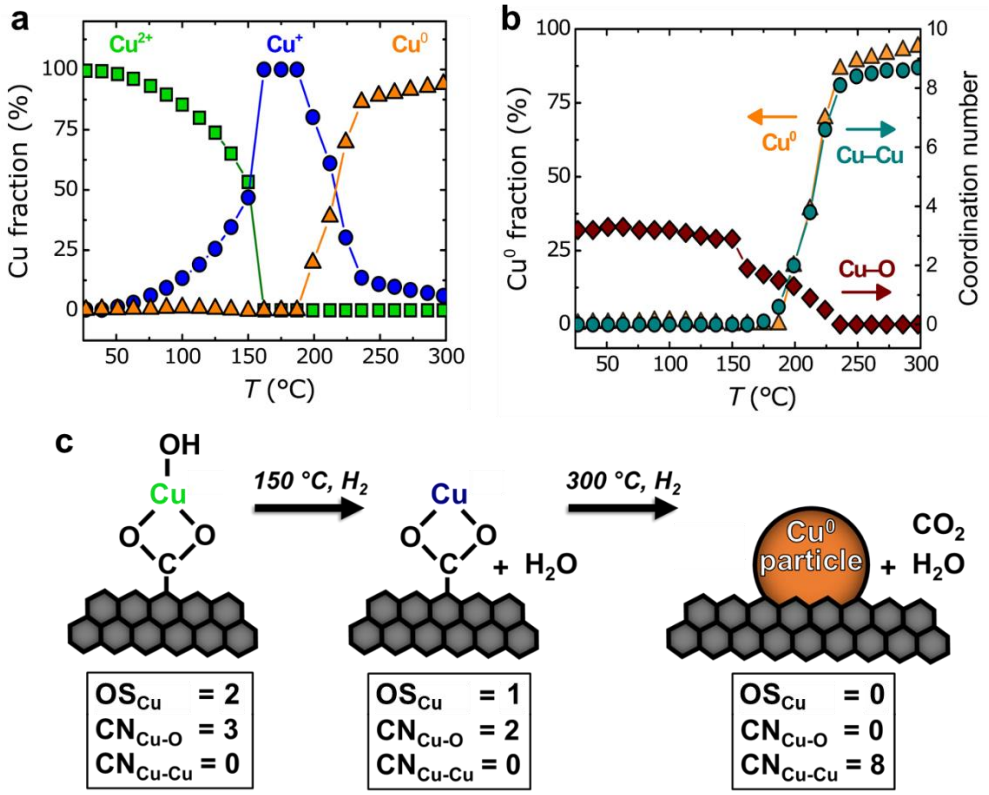

Figure 2.7: *In situ XAS analysis for the 3_Cu/OG sample during heating to 300 °C (2 °C min^{-1}).* ***a)*** *Evolution of the Cu oxidation state (OS_{Cu}) as a function of temperature, indicating fractions of Cu^{2+} (green squares), Cu^+ (blue circles) and Cu^0 (orange triangles) as measured by linear combination fitting of the XANES;* ***b)*** *EXAFS coordination numbers for Cu–O ($CN_{Cu–O}$, red diamonds) and Cu–Cu ($CN_{Cu–Cu}$, cyan circles);* ***c)*** *Schematic illustration of the Cu particle formation starting from complexed Cu^{2+} ions on surface-oxidized carbon.*

Cu particle growth by thermal sintering. The temperature-dependent particle growth of Cu was monitored for 7_Cu/OG by *in situ* XRD under 10 vol% H_2/He (Figure 2.8). No crystalline Cu was observed at room temperature, indicating that the Cu species were uniform and highly dispersed. Two broad Cu^0 diffraction peaks appeared around 170 °C (Figure 2.8a), corroborating the temperature for particle formation derived from the X-ray absorption spectroscopy experiments. Interestingly, the Cu^0 crystallite size only increased from 2.2 to 2.4 nm, when heating from 170 to 250 °C. Moreover, the size did not significantly increase during 2 h isothermal hold at 250 °C. Heating to 510 °C gave to 9.4 nm Cu^0 crystallites, with an exponential increase in the Cu^0 crystallite size as a function of temperature (Figure 2.8b). Van den Berg *et al*. previously reported the formation of Cu particles from a copper-phyllosilicates precursor. 5 nm Cu particles had formed after heating for 30 min at 250 °C under 1 mbar of H_2, which still grew to 8 nm during 2 h isothermal hold at 250 °C.[221] On carbon supports the reduction of Cu^+ to Cu^0 hence occurs at much lower temperatures than on oxide supports, which allows to prepare Cu particles as small as 2 nm, and tailor the particle size by varying the temperature.

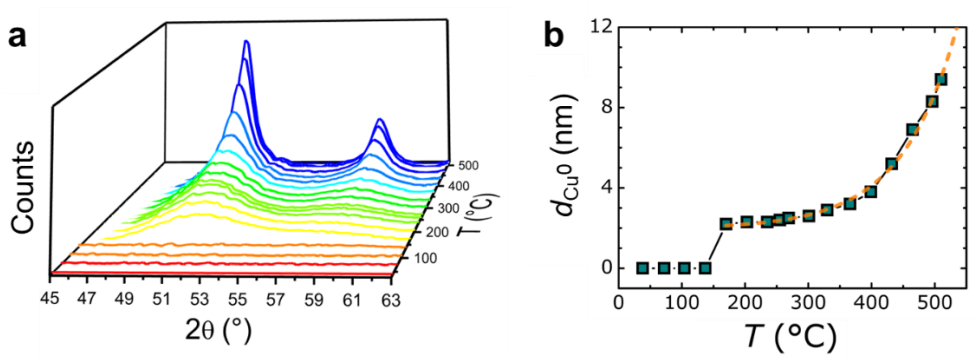

Figure 2.8: *In situ XRD for the 7_Cu/OG sample during heating to 510 °C (2 °C min^{-1}), under a flow of 10 vol% H_2/He.* ***a****) Carbon baseline-corrected diffractograms;* ***b****) Cu^0 crystallite sizes (cyan squares) as a function of temperature, including an exponential fit (dashed orange line).*

To better understand the Cu particle growth, we calculated the apparent activation energy (E_a) for particle growth from the Arrhenius plot. The value for E_a was 59 kJ mol^{-1} and thus in good agreement with previous studies on grain growth for nanocrystalline Cu materials (56–68 kJ mol^{-1}). Thermogravimetric analysis under H_2-containg flow indicates that the reduction to Cu^0 coincided with the decomposition of the carboxylate surface groups to CO_2. After removal of the carboxylate groups, the weak interaction between the mobile Cu species and graphite support likely led to Cu^0 agglomeration, while further particle growth may be diffusion limited.

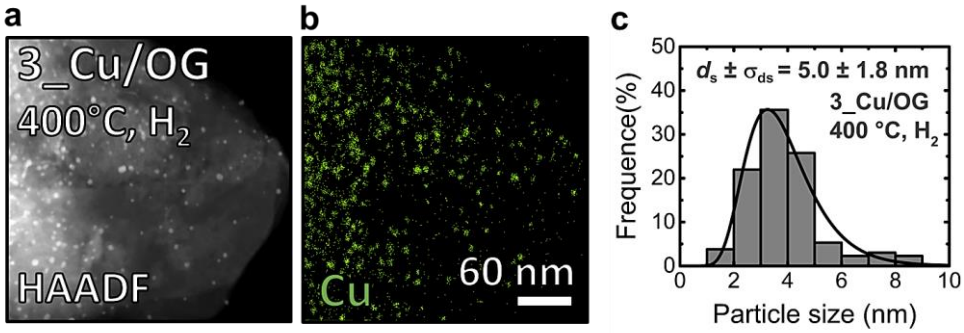

Figure 2.9: ***a****) STEM micrograph in HAADF mode for the 3_Cu/OG_400 sample, prepared by ex-situ heating of the 3_Cu/OG sample to 400°C under 20 vol% H_2/N_2;* ***b****) EDX Cu distribution map;* ***c****) Cu particle size distribution with lognormal fit, surface-averaged Cu particle size (d_s) and standard deviation in the width of the particle size distribution (σ_{ds}).*

The homogeneity of the thermally sintered Cu nanoparticles was evaluated by STEM (Figure 2.9). Heating the 3_Cu/OG and 7_Cu/OG samples *ex-situ* for 1 h at 400 °C under a flow of 20 vol% H_2/N_2 gave surface-averaged Cu particle sizes of 5.0±1.8 nm (3_Cu/OG_400) and 7.3±2.4 nm (7_Cu/OG_400), respectively. The homogeneous distribution of Cu^{2+} on the surface-oxidized carbon support hence gave a relatively narrow Cu particle size distribution after the thermal sintering treatment. This uniquely allowed us to tailor the Cu structure from single atoms to 10 nm particles on carbon.

2.4 Conclusions

In this chapter, a series of carbon-supported Cu samples on two different surface-oxidized carbon supports was prepared using incipient wetness impregnation. The ratio between Cu atoms and carbon surface groups was varied to tune the Cu size and stability. A combination of electron microscopy and X-ray absorption spectroscopy studies revealed the uniform distribution of either atomically dispersed Cu^{2+} ions and/or Cu-oxide clusters of a few Cu atoms, depending on the Cu atom to surface groups ratio. The carboxylate coordinated Cu^{2+} ions were reduced to Cu^{+} with retention of the dispersion. Upon complete reduction to Cu^{0}, the Cu species became mobile led to formation of Cu^{0} nanoparticles. Increasing the temperature gradually to 500 °C allowed us to tailor the Cu size from isolated atoms to 10 nm particles. This synthesis method opens up practical approaches to investigate atomically dispersed Cu in catalysis.

Acknowledgements

The authors acknowledge Peter Bramwell for N_2 physisorption, Wouter Lamme for STEM-HAADF-EDX imaging and Matthew Kulzick for assisting in the XAS measurements.

Chapter 3

Disentangling Promoter, Support and Particle Size Effects in Methanol Synthesis

This chapter is based on the publication: "*Disentangling Promoter, Support and Particle Size Effects in Methanol Synthesis"* by R. Beerthuis,[#] C. E. Pompe,[#] R. Dalebout, K. P. de Jong and P. E. de Jongh, Submitted (# authors contributed equally).

Abstract

The efficiency and energy requirement of many industrially processes strongly depends on the performance of nanoparticulate metal catalysts. Tuning the catalyst composition and metal particle size is a general strategy to boost the catalytic activity. However, the role of the copper (Cu) particle size in methanol synthesis from CO and CO_2 is still debated. In this chapter, we prepared carbon-supported catalysts with Cu particle size between 3 and 14 nm, both in the absence and presence of zinc oxide (ZnO_x) as a promoter. Under industrially relevant temperature (260 °C) and pressure (40 bar), the surface-normalized activity increased approximately 4-fold, with increasing Cu size from 3 to 10 nm and became size-independent for larger particles. Using carbon as a chemically inert support material revealed the intrinsic ZnO_x promoter and Cu particle size effects, proving that the methanol synthesis reaction is intrinsically sensitive to the Cu particle size below 10 nm.

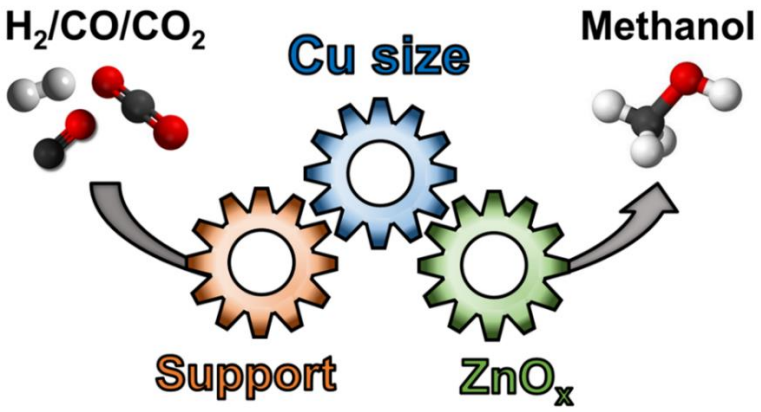

3.1 Introduction

Over 75 million tons of methanol are produced annually from CO_2-enriched synthesis gas (H_2, CO, CO_2), using co-precipitated Cu/Zn/Al_2O_3 catalysts.[98] The conversion of synthesis gas to methanol proceeds *via* three concurring reactions, namely hydrogenation of CO, hydrogenation of CO_2 and the water gas shift reaction, as described by Eq. 1.1–1.3 in Chapter 1 of this thesis. Although high specific surface areas were correlated to high activity,[99] the Cu and $CuZnO_x$ particle size effects are still not comprehensively understood, with uncertain consequences to the catalytic performance. Recent studies indicate that the rate-determining step in methanol synthesis, *i.e.* hydrogenation of the formate intermediate, predominantly occurred on Cu surface defect sites and that the activation barrier was lowered at ZnO_x decorated Cu sites.[105, 108, 110, 194-197] The effects of Cu particle size and ZnO promoter are hence often intertwined.

An important open question in literature is whether particle size effects in methanol synthesis originate from structure sensitivity or from a particle size-dependent coverage of the ZnO_x promoter onto Cu. Computational studies by Kuld *et al*. from Haldor Topsøe suggested that the catalytic activity was dictated by the ZnO_x promoter efficacy, and that the Cu particle size only affected the ZnO_x coverage.[108] Alternatively, Van den Berg *et al.* proposed that the methanol synthesis reaction is intrinsically sensitive to the $CuZnO_x$ particle size and surface structure,[86] originating from a size-dependent abundance of different surface sites with unique chemical reactivities.[185, 192] However, the particle size effects for the un-promoted Cu catalysts were likely masked by comparing Cu catalyst on SiO_2 and Al_2O_3 supports of varying morphologies.[86] Both Zn and Cu species can strongly interact with the metal oxide supports, forming thermodynamically highly stable mixed metal oxides such as Zn–silicate or Cu–aluminate compounds, which may conceal the intrinsic promoter and particle size effects.[20, 99, 105, 112, 222]

In this chapter, we report a methodology to tune the Cu and $CuZnO_x$ particle size between 3 and 14 nm on a graphitic carbon support, by varying the Cu loading, support functionalization and applying controlled thermal sintering. The approaches for metal particle size control may offer wide applicability in catalysis. By using carbon as a chemically inert support, we demonstrate that the methanol synthesis reaction is intrinsically sensitive to the Cu particle size below 10 nm, under industrially relevant temperature (260 °C) and pressure (40 bar). The particle size effects were observed both in the absence and presence of ZnO_x, suggesting that the size-dependence in $CuZnO_x$ activity originates from combined intrinsic Cu particle size effects and effective ZnO_x coverage onto the Cu particles. Disentangling the promoter, support and particle size effects may guide the rational design of catalysts with optimized performance.

3.2 Experimental methods

Catalyst assembly

All carbon-supported Cu and $CuZnO_x$ catalysts were prepared using turbostratic graphitic carbons as the catalyst support materials. High surface area graphite (HSAG–500, kindly provided by Timcal Ltd.) was used either pristine (as-received) or after surface-oxidation by liquid-phase HNO_3 treatment as described in Chapter 2. Both the pristine and surface-oxidized carbon supports were dried under dynamic vacuum at 170 °C for 1.5 h to remove residual absorbed water and finally stored in an Ar-filled glovebox (Mbraun LABmaster; <1 ppm H_2O; <1 ppm O_2) until further use.

The Cu and $CuZnO_x$ catalysts were prepared by incipient wetness impregnation of the dried powdered support, using mixed aqueous solutions of $Cu(NO_3)_2$ and $Zn(NO_3)_2$, in 0.1 M HNO_3, followed by drying and thermal treatment to decompose the metal precursors. Incipient wetness impregnation is one of the most reliable and scalable techniques for the industrial preparation of heterogeneous catalysts, allowing accurate regulation of the catalyst composition.[18, 20] In the case of the CuZnOx catalysts, a Cu:Zn molar ratio of 65:35 was applied. The Cu and Zn loadings were controlled by adjusting the concentration of their respective metal nitrate precursors in aqueous solution for impregnation. The final Cu and Zn weight loadings therefore correspond to the nominally added amounts, calculated as $\text{Cu wt\%} = \left(\frac{\text{mass Cu}}{\text{mass CuO+mass ZnO+mass support}}\right) * 100\ \%$ and $\text{Zn wt\%} = \left(\frac{\text{mass Zn}}{\text{mass CuO+mass ZnO+mass support}}\right) * 100\%$.

In a typical synthesis procedure, around 2 g of dried powdered carbon was impregnated to incipient wetness, in a round-bottom flask under static vacuum. The impregnated sample was stirred for 24 h under static vacuum to homogenize the metal content, and subsequently dried for 24 h while stirring under dynamic vacuum, at room temperature. The dried impregnated sample was transferred to a plug-flow reactor, without exposure to air, and subsequently heated to decompose the metal precursors.

In the case of the Cu and $CuZnO_x$ catalysts prepared using the pristine carbon support, the dried impregnate was heated to 230 °C (2 °C min^{-1}) with 1 h isothermal hold at 230 °C, under 20% H_2/N_2 flow (100 mL min^{-1} g^{-1}). The sample was left to cool down to room temperature and flushed with N_2 (100 mL min^{-1} g^{-1}). Next, the catalyst was heated to 200 °C (1 °C min^{-1}) with 3 h isothermal hold at 200 °C, under 5 vol% O_2/N_2 flow (100 mL min^{-1} g^{-1}). The gas flow was exchanged for 15 vol% O_2/N_2 flow (100 mL min^{-1} g^{-1}) with 1 h isothermal hold at 200 °C. After allowing to cool down to room temperature, the catalyst was collected.

In the case of the Cu and $CuZnO_x$ catalyst prepared using the surface-oxidized carbon support, the dried impregnated sample was heated to 230 °C (0.5 °C min^{-1})

with 1 h isothermal hold at 230 °C under N_2 flow (100 mL min^{-1} g^{-1}). The sample was left to cool down to room temperature and first flushed for 3 h with a flow of 20 vol% O_2/N_2 (100 mL min^{-1} g^{-1}) and subsequently flushed with for 30 min with a flow of pure N_2 (100 mL min^{-1} g^{-1}). Next, the sample was heated to 150 °C (2 °C min^{-1}) with 2 h isothermal hold at 150 °C, under 5 vol% H_2/N_2 flow (100 mL min^{-1} g^{-1}). The temperature was increased at 2 °C min^{-1} to the final heat treatment temperature (250–400 °C) with 1 h isothermal hold at the final temperature. The $CuZnO_x/C$ catalyst was heated for 1 h at the final temperature of 250 °C. After allowing to cool down to room temperature and flushing for 30 min under N_2 flow (100 mL min^{-1} g^{-1}), the catalyst was transferred in a closed vessel to an Ar-filled glovebox (Mbraun LABmaster; <1 ppm H_2O; <1 ppm O_2). Finally, the sample was passivated by overnight exposure to air at room temperature.

The Cu/SiO_2 and $CuZnO_x/SiO_2$ catalysts were prepared by adaption of previously reported methods by Van den Berg *et al.*[86] and Pompe *et al*.[56] The Cu/SiO_2 catalyst was prepared using a SiO_2 gel with 805 m^2 g^{-1} BET surface area and 0.56 mL g^{-1} total pore volume (Grace-Davison). The $CuZnO_x/SiO_2$ catalyst was prepared using a SiO_2 gel with 520 m^2 g^{-1} BET surface area and 0.82 mL g^{-1} total pore volume (Merck). Prior to the impregnation, the SiO_2 gels were dried for 2 h at 170 °C under dynamic vacuum. The SiO_2 gels were impregnated to incipient wetness using aqueous solutions of $Cu(NO_3)_2$ and $Zn(NO_3)_2$ in 0.1 M HNO_3, subsequently dried under dynamic vacuum for 48 h, and finally heated to 250 °C (2 °C min^{-1}) with 90 min isothermal hold at 250 °C, under 20 vol% H_2/N_2 flow (28 mL min^{-1} g^{-1}).

Catalyst characterization

The support porosity was studied by N_2 physisorption on a Micromeritics TriStar 3000 V6.08 apparatus. Isotherms were measured at −196 °C, using Carbon Black STSA as a reference. Prior to the measurements, the carbon samples were outgassed at 150 °C under dynamic vacuum for 14 h. Specific surface areas were calculated using the multi-point Brunauer-Emmet-Teller (BET) method, with P/P_0 between 0.05–0.25. The total pore volume was calculated as single point pore volume at P/P_0 of 0.995 and pore diameter distribution were determined using the Barrett-Joyner-Halenda (BJH) method applied to the adsorption branches of the isotherms, while the micropore surface area and volume were determined using the t-plot method.

Raman spectra of the bare carbon supports were recorded in powder form on a Renishaw inVia Raman microscope between 1,000–3,000 cm^{-1} using laser excitation at λ = 532 nm. Spectra were averaged over at least 10 different areas.

Acid−base potentiometric titrations were performed using a TitraLab pH meter. The pristine carbon (~25 mg) or surface-oxidized carbon (~8 mg) support was suspended in 65 mL of 0.1 M KCl(aq) solution. The resulting suspension was pre-treated by

degassing with N_2 flow for 5 min under vigorous stirring. Next, the titration was performed using solutions of either 0.01 M NaOH(aq) or 0.01 M HCl(aq), both in 0.1 M KCl(aq), in separate measurements. The total density of acidic and basic surface groups were calculated from the final equivalence point of the titration curves, after subtraction of a blank measurement to adjust for the presence of any dissolved CO_2.

Temperature programmed reduction (TPR) measurements were performed using a Micromeritics Autochem II ASAP 2920 apparatus, with H_2 consumption measured using a thermal conductivity detector. In a typical measurement, the sample was first dried at 120 °C for 30 min under an Ar flow (~1 L min^{-1} g^{-1}) and cooled down to room temperature. Next, the samples were heated to 250 °C (5 °C min^{-1}) under 5 vol% H_2/Ar flow (~2 mL min^{-1} g^{-1}). The onset temperature for the reduction peaks was calculated from the interception of the baseline by the slope at the first inflection point.

Transmission electron microscopy (TEM) and powder X-ray diffraction (XRD) were used as the main characterization tool to determine the Cu and $CuZnO_x$ particle size and estimate the geometric surface area. Herein, the particles were assumed to be spherical and fully accessible. These methods for particle size analysis provide greater accuracy than alternative techniques such as N_2O and H_2 chemisorption, for which the measurement of the Cu specific surface area is obscured by interaction of the chemisorption probe gasses with the ZnO_x promoter and possibly with the SiO_2 support.[71, 86, 223]

TEM imaging was performed on a Tecnai 20 (FEI), and scanning transmission electron microscopy with a high-angle annular dark-field detector (STEM-HAADF), combined with energy-dispersive X-ray spectroscopy (EDX) was performed on a FEI Talos F200X microscope. Both microscopes were operated at 200 kV. To avoid particle growth due to beam-induced sintering, TEM images were acquired with a maximum electron dose-rate of approximately 5 electrons nm^{-2} s^{-1}. Samples were prepared by grinding the catalyst into a fine powder, which was deposited directly onto a holey carbon coated Cu sample grid (Agar 300 mesh Cu) for TEM and a gold sample grid (SubstratekTM 300 mesh Au) for STEM-HAADF-EDX analysis. The particle sizes were determined by measuring the diameter of the spherical approximation of the projected particle shape, for at least 200 individual particles on 10 different sample areas. A small number of very large (>50 nm) particles was detected in some samples, which likely results from slight over-impregnation, and was hence not included in the particle size analysis. The number-averaged particle size (d_n) and corresponding standard error in the particle size (σ_{dn}) were calculated using: $d_{\mathrm{n}} \pm \sigma_{\mathrm{dn}} = \frac{1}{N}\sum_{\mathrm{i}=1}^{N} d_{\mathrm{i}} \pm \frac{d_{\mathrm{n}}}{\sqrt{N}}$. The surface-averaged particle size (d_s) and corresponding standard error in the particle size (σ_{ds}) were calculated using: $d_s \pm \sigma_{ds} = \frac{\sum_{i=1}^{N} d_i^3}{\sum_{i=1}^{N} d_i^2} \pm \frac{d_n}{\sqrt{N}}$. The standard deviations in particle size distributions ($\sigma_{PSD,dn}$ and

$\sigma_{\mathrm{PSD,ds}}$) were calculated as $\sigma_{\mathrm{PSD,dn}} = \sqrt{\frac{1}{N}\sum_{\mathrm{i}=1}^{N}(d_{\mathrm{n}} - d_{\mathrm{i}})^2}$ and $\sigma_{\mathrm{PSD,ds}} = \sqrt{\frac{1}{N}\sum_{\mathrm{i}=1}^{N}(d_{\mathrm{s}} - d_{\mathrm{i}})^2}$. Herein, d_i is the diameter of the ith particle and N the number of counted particles. EDX spectra were processed using Esprit software (Bruker AXS).

Powder XRD analysis was performed on a Bruker D8 powder X-ray diffractometer equipped with a Lynxeye detector, using a Co-$K_{\alpha 1,2}$ (λ = 1.79026 Å) radiation source, operated at 30 kV, 45 mA and a V20 variable slit. Diffractograms were collected both on the reduced and passivated catalysts. Diffractograms for the Cu and $CuZnO_x$ catalysts prepared using pristine carbon, were first measured for the passivated samples in air and later for the reduced samples after an additional step. Herein, the samples were heated to 250 °C (2 °C min^{-1}) with 1 h isothermal hold at 250 °C under 5 vol% H_2/N_2 (250 mL min^{-1} g^{-1}). Diffractograms for the Cu and $CuZnO_x$ catalysts prepared using surface-oxidized carbon, were taken directly after the final reduction step in the synthesis. The reduced samples were transferred in an air-tight container to a Ar-filled glovebox (Mbraun LABmaster; <1 ppm H_2O; <1 ppm O_2), where a XRD specimen holder was loaded and sealed with an air-tight transparent dome-like cap (A100B33, Bruker AXS) to measure the XRD under inert atmosphere. All diffractograms were collected at room temperature from 5–95° 2θ, with 0.1° increment and normalized to the intensity of the (002) diffraction peak for graphitic carbon at 30.9° 2θ. Cu crystallite sizes were calculated using peak deconvolution software (Topas V5, Bruker AXS), applying the Scherrer equation with a shape factor k = 0.89 and line broadening = 0.1 to the Cu^0 (111) diffraction at (50.7° 2θ) and the Cu^0 (200) diffraction at (59.3° 2θ). No background corrections or smoothing was applied to the displayed diffractograms.

Catalysis

All catalytic experiments were performed on a high-throughput fixed-bed reactor system, equipped with 16 parallel channels (Flowrence®, Avantium N. V.). The catalysts were pelletized (2 cm diameter) using a hydraulic press at 1,500 kgf, equivalent to 460 bar pressure, ground and sieved to obtain a granulate size of 75–150 μm. The catalyst (10–160 mg) was diluted with SiC granules (212–425 μm; purified by a HNO_3 treatment at room temperature and calcination at 800 °C) to a total catalyst bed volume of 0.3 mL. The diluted catalyst was loaded into a stainless-steel reactor (2.6 mm inner diameter) which was pre-loaded with an aliquot of SiC granules (0.5 mL) onto a stainless-steel frit. The Cu mass per reactor was approximately 10.0 mg for all un-promoted Cu catalyst, while 0.77 mg of Cu was used for the $CuZnO_x$ catalysts. The GHSV based on the packed bed volume without dilution with SiC varied between approximately 600–7,000 h^{-1}. The WHSV was kept constant at 5.8 g_{CO+CO2} g_{Cu}^{-1} h^{-1} for the Cu/C catalysts, and 66 g_{CO+CO2} g_{Cu}^{-1} h^{-1} for the $CuZnO_x$/C catalysts.

The Cu catalysts were reduced *in situ* by heating to 200 °C (2 °C min^{-1}), while the $CuZnO_x$ catalysts were heated to 250 °C, both with 120 min hold at the final temperature, under a flow of 20 vol% H_2/Ar at 3.1 mL min^{-1} per reactor. After that, the temperature was lowered to 150 °C and the reactor was purged with the reaction gas mixture (H_2:CO:He:CO_2 = 60:23:10:7 vol%) under a total gas flow of 2.2–2.5 mL min^{-1} per reactor. After 4 h purging, the pressure was gradually increased during 2 h to 40 bar(g). Finally, the temperature was increased from 150 to 260 °C (2 °C min^{-1}) and kept at this temperature during the reaction. The effluent gas composition was analysed every 15 min using a three-channel gas chromatograph. After 48 h, the catalyst was left to cool down to 90 °C and passivated by exposure to air at 90 °C.

The CO and CO_2 gas feeds were purified using carbonyl traps composed of HY zeolite in the protonated form (USY, Zeolyst) in 0.6–1 micrometer grains, mixed with grains of activated carbon (Norrit RB3). The trap for the CO_2 feed was maintained at a constant temperature of 50 °C, to keep the CO_2 adsorption stable. The effluent gas composition was analyzed every 15 min using an on-line three-channel gas chromatograph (GC, Agilent 7890B). H_2, CO, He and CO_2 were separated on a MolSieve 5A column (2.4 meter x 1/8 inch inner diameter) and quantified using a thermal conductivity detector. Alcohols and alkanes were separated using a GS-GasPro column (GS-Gaspro 30 m x 0.32 mm ID) and a HP-Innowax column (6 m x 0.32 mm ID), and analyzed by flame ionization detectors. Gas phase compositions were calculated from the integrated peak areas, using He as internal standard.

To validate that the reaction was not mass transfer limited, we performed measurements with several Cu/C catalysts of using granulate sizes of 75–150 µm, 150–425 µm and 425–630 µm. No substantial difference in the conversion profiles was observed, indicating that the reaction was not hindered by internal or external mass transfer limitations. Three reference measurements using the pristine carbon support, surface-oxidized carbon support and SiC diluent, showed no conversion at 260 °C. Several catalytic experiments were performed in multifold to ensure reproducibility.

The standard deviation in CO+CO_2 conversion ($\sigma_{conversion}$) was defined as the typical distance of a data point (χ) from the mean value (μ) and calculated by the formula $\sigma_{\mathrm{conversion}} = \sqrt{\left(\frac{1}{\mathrm{N}-1}\right)\sum_{\mathrm{i}=1}^{\mathrm{N}}(\chi_{\mathrm{i}} - \mu)^2}$. A general value for $\sigma_{conversion}$ of approximately 5 % was obtained from an experiment using 12 reactors with an equal loading of a commercial Cu/ZnO/Al_2O_3 methanol synthesis catalyst (Alfa Aesar). The CO+CO_2 conversion was calculated from the CO and CO_2 inlet and outlet molar flows (mol_{CO+CO2} min^{-1}), using the formula $\mathrm{CO} + \mathrm{CO_2}\ \mathrm{conversion} = \frac{(\mathrm{CO+CO_2\ Inlet\ flow} - \mathrm{CO+CO_2\ Outlet\ flow})}{\mathrm{CO+CO_2\ Inlet\ flow}}$. The methanol product selectivity was calculated based on the analyte concentrations in the effluent gas and corresponding carbon

numbers (#), using the formula $\mathrm{Selectivity}_{\mathrm{MeOH}} = \frac{\mathrm{Concentration}_{\mathrm{methanol}}}{\sum_1^{\mathrm{N}}(\#*\mathrm{Concentration}_{\mathrm{analyte}})}$. The standard deviation in TOF (σ_{TOF}) was calculated from $\sigma_{\mathrm{TOF}} = \sqrt{\sigma^2_{\mathrm{conversion}} + \sigma^2_{\mathrm{PSD\ dn}}}$. Curves for the TOF trends were fitted by applying an exponential model using the equation $y = a(1 - \mathrm{e}^{-bx})^c$ for the measured Cu/C catalysts and TOF values from Cu/SiO_2 from literature,[86] with *a*, *b* and *c* values of 1.98±0.33, 0.44±0.28 and 6.43±8.61 for Cu/C and 2.31±0.48, 0.34±0.46 and 1.90±2.98 for Cu/SiO_2.

The turnover frequency (TOF) was calculated per surface Cu atom, using the formula $\mathrm{TOF} = \mathrm{CTY} * \frac{M_{\mathrm{Cu}}}{D_{\mathrm{Cu}}}$, in which CTY was the Cu-time-yield ($\mu mol_{CO+CO2}\ s^{-1}\ g_{Cu}^{-1}$) at the maximum $CO+CO_2$ conversion (within 10 h on stream at 260 °C). M_{Cu} is the molecular weight of Cu, and D_{Cu} is the dispersion of surface Cu atoms. The value of D_{cu} is calculated from d_s, assuming fully accessible spherical particles using the formula $D_{\mathrm{Cu}} = 6 * \frac{(V_{\mathrm{Cu}} * A_{\mathrm{Cu}}^{-1})}{d_s}$. Herein, A_{Cu} is the molar area occupied by surface Cu atoms ($4.10*10^{22}$ nm^2) and V_{Cu} is molar volume occupied by Cu atoms in bulk metal ($7.09*10^{21}$ nm^3). D_{Cu} is hence calculated as $D_{\mathrm{Cu}} = \frac{1.04}{d_s}$, with d_s in nm.[172]

Results and Discussion

Tuning the Cu size on carbon. The first strategy we employed to tune the Cu size, was varying the Cu weight loading, using impregnation of a pristine graphitic carbon support, followed by thermal decomposition of the $Cu(NO_3)_2$ precursor salts.[73, 86] Representative transmission electron microscopy (TEM) images and corresponding Cu particle size distributions are displayed in Figure 3.1a,b. Well-distributed Cu particles were observed throughout the catalysts, with surface-averaged Cu particle sizes ranging from 8.6 to 13.4 nm, for 6.3 to 11.7 wt% Cu loadings. XRD studies on the reduced catalysts revealed 7.3–10.9 nm Cu^0 crystallite sizes, in good agreement with TEM analysis (Figure 3.2a,b). Moreover, XRD analysis on both the reduced and passivated catalysts showed no other crystalline phase. The dependence of particle size on the Cu weight loading is summarized in Figure 3.1c. Varying only the Cu loadings from around 6 to 12 wt% provided a suitable synthesis approach to tune the Cu particle size between 8–14 nm, with the strongest impact >10 wt%. Cu particles smaller than 8 nm were not obtained, even for Cu loadings well below 6 wt%, which likely stems from the weak interaction between the Cu (precursor) species and pristine carbon support. Resultingly, Cu species may agglomerate already during the drying procedure. To overcome this limitation and synthesize Cu particles significantly smaller than 8 nm, we proceeded to combine carbon surface modification with variation of the heat treatment conditions.

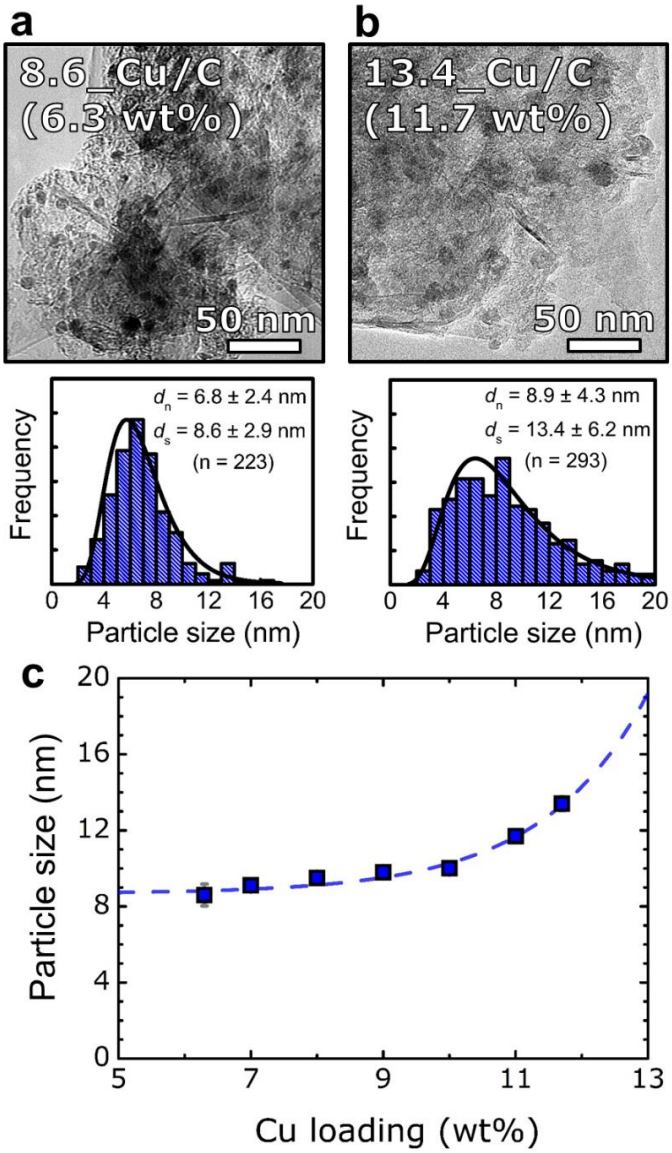

Figure 3.1: *Illustration of the influence of Cu loading on the final particle size for Cu/C catalysts. Transmission electron micrographs, Cu particle size distributions with lognormal fits, number-averaged (d_n) and surface-averaged (d_s) Cu particle sizes including standard deviations in the width of the particle size distributions, for catalysts with* ***a****) 6.3 wt% Cu and* ***b****) 12 wt% Cu;* ***c****) Dependence of surface-averaged Cu particle size on Cu weight loading, including exponential fit (dashed line), for catalysts prepared by impregnating a pristine carbon support with an aqueous $Cu(NO_3)_2$ solution and heated to 230 °C under 20 vol% H_2/N_2 flow. Error bars represent the standard error in the particle size and are generally smaller than the data markers.*

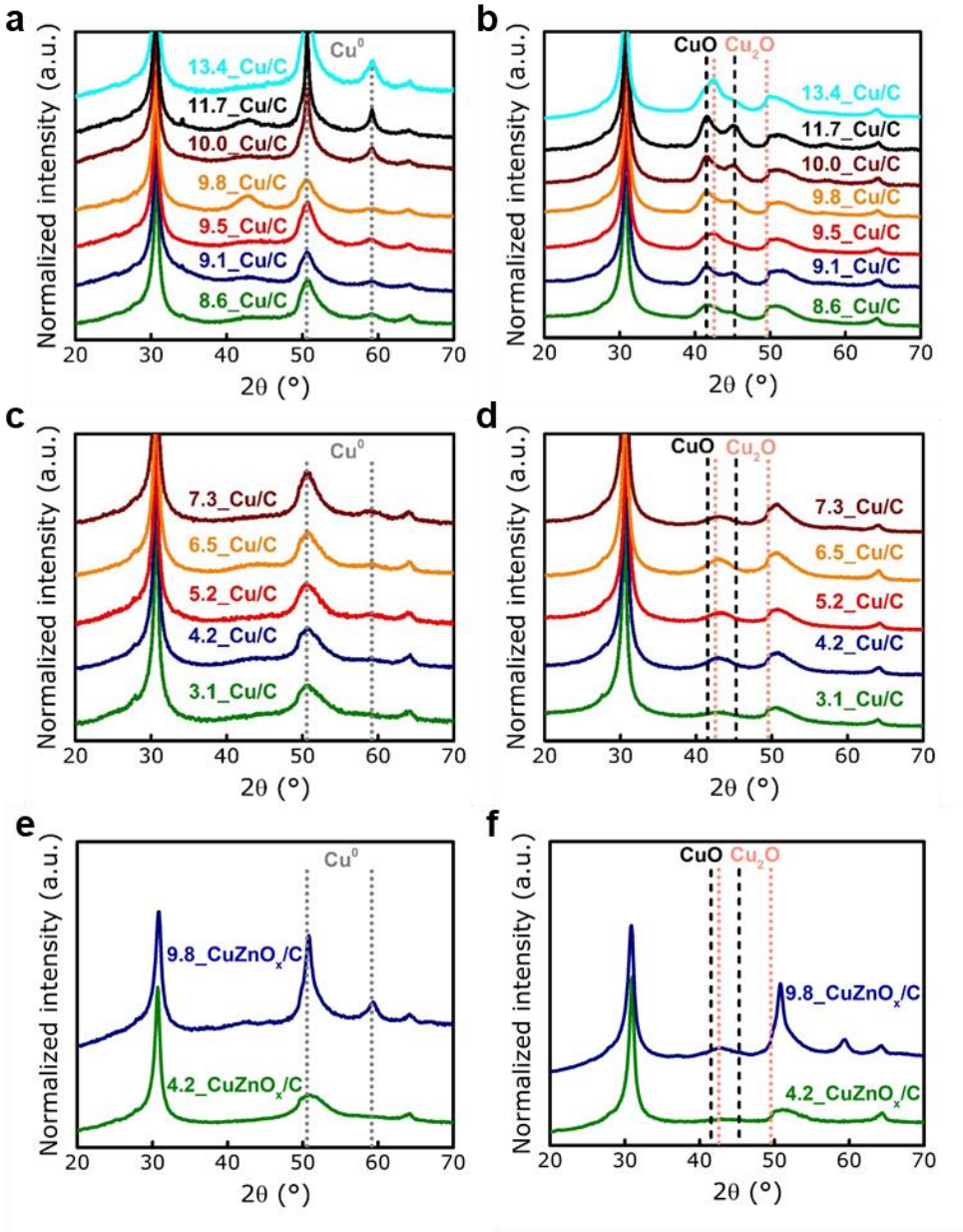

Figure 3.2: *X-ray diffractograms for Cu/C and $CuZnO_x$/C catalysts, normalized to the graphitic carbon (002) diffraction peak intensity around 30.9° 2θ and stacked with individual offset for visual clarity.* ***a****) Reduced and* ***b****) Passivated Cu/C catalysts prepared using pristine carbon and variation of the Cu loading;* ***c****) Reduced and* ***d****) Passivated Cu/C catalysts prepared using surface-oxidized carbon and variation of the final heat treatment temperature;* ***e****) Reduced and* ***f****) Passivated $CuZnO_x$/C catalysts prepared using either pristine or surface-oxidized carbon.*

To enhance the interaction of the Cu (precursor) species with the carbon support, liquid-phase HNO_3 oxidation was applied to functionalize the carbon surface, which is known to mainly introduce carboxylic groups.[22, 211] The surface-oxidation treatment slightly reduced the BET surface area from 505 m^2 g^{-1} to 440 m^2 g^{-1}, while the total pore volume decreased from 0.70 mL g^{-1} to 0.62 mL g^{-1} (Figure 3.3a). Analysis of the pore diameter distributions show that the largest number of pores was present below 20 nm for both the pristine and surface-oxidized carbon support, and that most of the pore volume is present within the mesopores of the plate-like turbostratic graphite structure (Figure 3.3b). No significant structural changes were observed by XRD analysis (Figure 3.3c), with both carbon materials exhibiting the characteristic diffraction peaks of graphitic carbon include the intense (002) peak at 30.9° 2θ, broad (100) peak at 49.6° 2θ, overlapping (100) and (101) peaks at 52.2 °2θ and minor (004) peak at 64.3°2θ.

Raman spectroscopy was applied to determine the degree of graphitization (Figure 3.3d). Three well-defined peaks were observed for the pristine and surface-oxidized carbon supports, corresponding to the graphitic peak (G band; around 1,570 cm^{-1}), the first disorder peak (D band; around 1,340 cm^{-1}) and the second disorder peak (2D; around 2,700 cm^{-1}).[224] The G band is assigned to sp^2 hybridized carbon, while the D band is attributed to defects, lattice disorder and graphite sheet curvature. Finally, the 2D band is typical for bulk graphite. The intensity ratio between D and G bands (I_D/I_G) indicates the degree of graphitization. The pristine carbon support exhibited a I_D/I_G ratio of 0.28, indicating high graphitization. The surface-oxidized carbon support showed a I_D/I_G ratio of 0.66, which suggested that although some defects were introduced, the carbon structure retaining most graphitic characteristics.

Notably, the oxidation treatment increased the density of acidic surface groups, from 0.14 nm^{-2} to 0.63 nm^{-2}, as quantified by potentiometric titration (Figure 3.3e). The amount of basic surface groups was negligible, both before and after the oxidation treatment (Figure 3.3f). A large density of acidic surface groups was hence introduced onto the carbon support, with main retention of the graphitic carbon morphology.

A catalyst batch was prepared by impregnation of the surface-oxidized carbon support with an aqueous $Cu(NO_3)_2$ solution. The dried impregnate was subsequently heated to 230 °C under flowing N_2 to decompose $Cu(NO_3)_2$, left to cool down to room temperature, and subsequently heated to 250 °C under a flow of 5 vol% H_2/N_2. TEM analysis revealed a Cu particle size of 3.1±0.2 nm, using 6.3 wt% Cu. Fractions of the same batch of dried impregnate were used as a starting point to increase the particle size by applying thermal sintering.

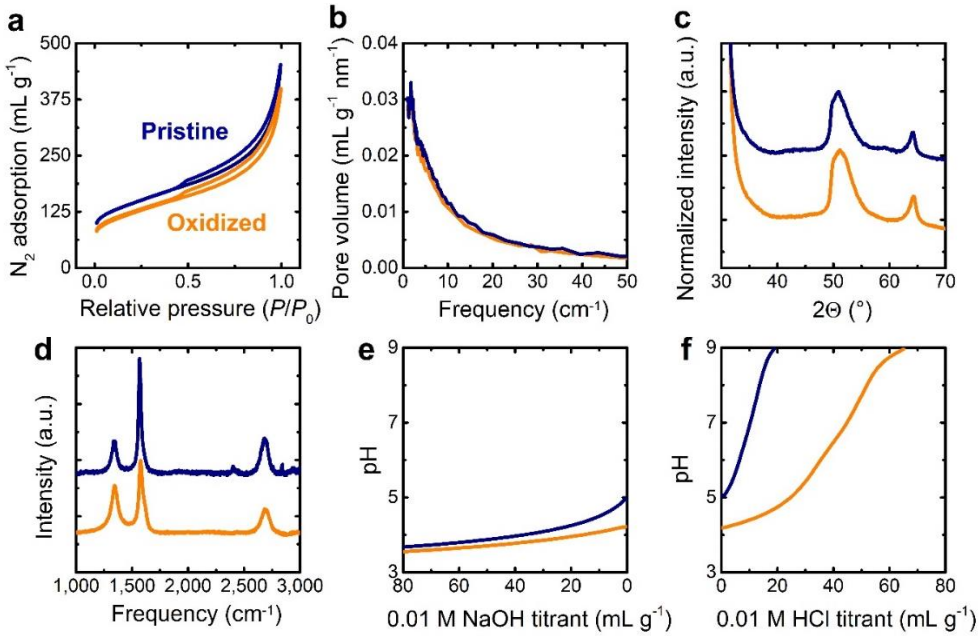

Figure 3.3: *Physicochemical characterization for the bare pristine (blue) and bare surface-oxidized (orange) carbon support materials.* ***a****) N_2 physisorption isotherms;* ***b****) Pore diameter distribution curves, as determined from the isotherm adsorption branch using the Barrett-Joyner-Halenda (BJH) method;* ***c****) Normalized X-ray diffractograms, stacked with individual offset;* ***d****) Raman spectra, stacked with individual offset; Potentiometric titration curves using titrant solutions in 0.1 M KCl $_{(aq)}$ containing* ***e****) 0.01 M NaOH $_{(aq)}$ and* ***f****) 0.01 M HCl $_{(aq)}$.*

Varying the final heat treatment temperature between 250–400 °C, yielded 3.1–7.3 nm Cu particles, all using 6.3 wt% Cu. Representative TEM images and Cu particle size distributions are displayed in Figure 3.4a,b. XRD analysis revealed 2.0–6.3 nm Cu^0 crystallite sizes, in good agreement with TEM analysis (Figure 3.3c,d). The oxygen-containing surface groups decomposed during the heat treatment under H_2-containing flow.[22] The support functionalization was hence only used as a synthesis tool and the carbon surface in the final Cu/C catalysts was similar to that of the pristine carbon support. Varying only the heat treatment temperature between 250–400 °C provided a suitable method to prepare Cu particles between 3–7 nm on carbon (Figure 3.4c). Combining the synthesis approaches of Cu loading variation, support functionalization and controlled thermal sintering, uniquely allowed us to tune the carbon-supported Cu particle size from 3 to 14 nm.

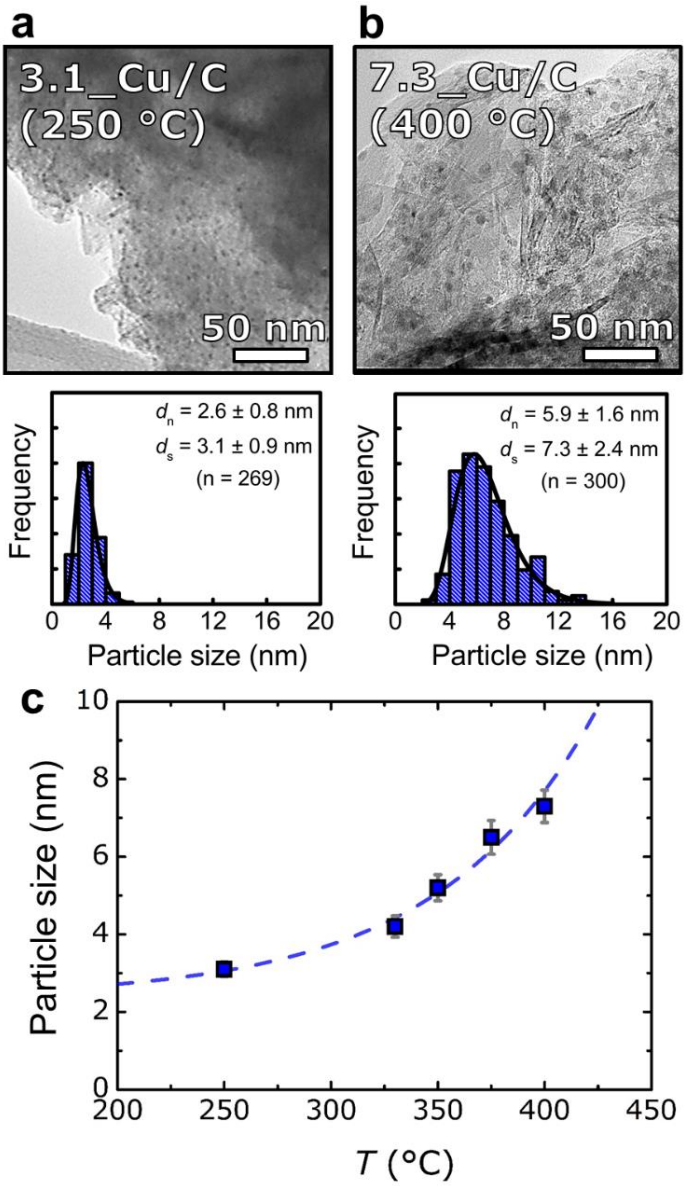

Figure 3.4: *Illustration of the influence of final heat treatment temperatures on the final particle size, for Cu/C catalysts prepared with 6.3 wt% Cu. Transmission electron micrographs, Cu particle size distributions with lognormal fits, number-averaged (d_n) and surface-averaged (d_s) Cu particle sizes including standard deviations in the width of the particle size distributions, for catalysts sintered at* ***a****) 250 °C and* ***b****) 400 °C;* ***c****) Dependence of surface-averaged Cu particle size on the final heat treatment temperature, including exponential fit (dashed line), for catalysts prepared by impregnating an surface-oxidized carbon support with an aqueous $Cu(NO_3)_2$ solution and heated between 250–400 °C under 5 vol% H_2/N_2 flow. Error bars represent the standard error in the particle size (σ_{ds}).*

To place the performance for the Cu/C catalyst in a broader perspective and allow a direct comparison to literature results, we prepared two ZnO_x-decorated Cu/C catalysts and one un-promoted Cu/SiO_2 catalyst. The $CuZnO_x$ catalysts were prepared with an approximate molar ratio Cu/Zn of 2, which is sufficiently high to induce a strong promoter effect for Cu on carbon.[86] The first $CuZnO_x$ catalyst was prepared with 7.7 wt% Cu using the pristine carbon support and exhibited 9.8±0.6 nm particles (Figure 3.5). The second $CuZnO_x$ catalyst was prepared with 6.3 wt% Cu using the surface-oxidized carbon support, and contained 4.2±0.3 nm particles. STEM-HAADF-EDX studies revealed uniformly distributed $CuZnO_x$ particles over both carbon supports, with ZnO_x localized in proximity of Cu.

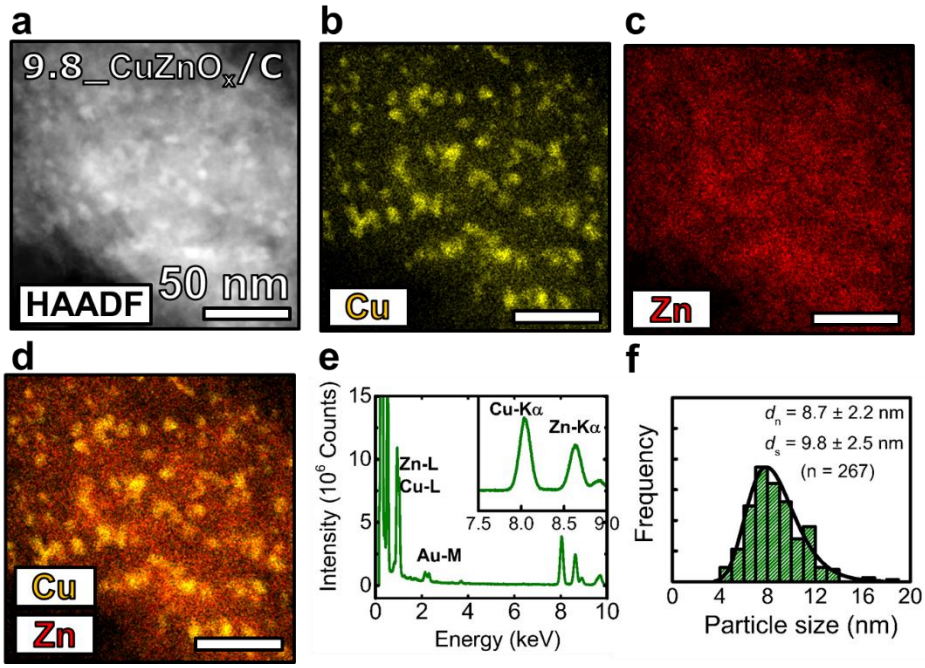

Figure 3.5: *Scanning transmission electron microscopy (STEM) analysis for the 9.8_$CuZnO_x$/C catalyst.* ***a****) high angular annular dark field (HAADF) micrograph; elemental distribution maps by energy dispersive X-ray spectroscopy (EDX) for* ***c****) Cu;* ***d****) Zn;* ***e****) Cu and Zn;* ***f****) EDX spectrum after background correction and element specific normalization;* ***f****) $CuZnO_x$ particle size distribution with a lognormal fit, number-averaged (d_n) and surface-averaged (d_s) particle sizes including standard deviations in the width of the particle size distributions*

Quantification of the elemental composition at the nanometer scale for 9.8_$CuZnO_x$/C, demonstrated a 66:34 atomic Cu:Zn ratio, in excellent agreement with the bulk Cu:Zn ratio of 65:35 (Figure 3.5e). Cu^0 crystallite sizes of 1.9 and 8.0 nm were observed for the reduced and 9.8_$CuZnO_x$/C catalysts, respectively, and no crystalline ZnO was detected. Finally, 2.7±0.1 nm particle and 2.4 nm

crystallite sizes were measured for the Cu/SiO_2 catalyst, hence allowing a direct comparison between carbon and SiO_2 as catalysts supports. The catalysts in this study were denoted as *X*_Cu/*Y* and X_$CuZnO_x$/*Y*, where *X* represents the Cu or $CuZnO_x$ surface-averaged particle size in nm, and *Y* indicates the support material. All catalyst designations, compositions and textural properties are summarized in Table 3.1.

Table 3.1: Physicochemical properties of the supported Cu and $CuZnO_x$ catalysts.

Catalyst	Cu/Zn (wt%)[a]	*T* (°C)[b]	$d_{Cu,\ XRD}$ (nm)[c]	$d_n \pm \sigma_{dn}$ (nm)[d]	$d_s \pm \sigma_{ds}$ (nm)[d]	$\sigma_{PSD,\ dn}$ (nm)[d]	$\sigma_{PSD,\ ds}$ (nm)[d]	D_{Cu} (%)[e]
3.1_Cu/C	6.3/-	250	2.0	2.6±0.2	3.1±0.2	0.8	0.9	34
4.2_Cu/C	6.3/-	330	2.6	3.7±0.2	4.2±0.3	1.0	1.1	25
5.2_Cu/C	6.3/-	350	4.2	4.3±0.3	5.2±0.3	1.4	1.6	20
6.5_Cu/C	6.3/-	375	5.1	5.8±0.4	6.5±0.4	1.5	1.5	16
7.3_Cu/C	6.3/-	400	6.0	5.9±0.3	7.3±0.4	1.6	2.4	14
8.6_Cu/C	6.3/-	230	7.3	6.8±0.4	8.6±0.5	2.4	2.9	12
9.1_Cu/C	7.0/-	230	7.3	6.5±0.2	9.1±0.2	2.9	3.8	11
9.5_Cu/C	8.0/-	230	5.5	6.5±0.2	9.5±0.3	3.9	4.7	11
9.8_Cu/C	9.0/-	230	6.0	6.8±0.2	9.8±0.3	4.0	5.0	11
10.0_Cu/C	10.0/-	230	8.9	7.8±0.2	10.0±0.2	3.2	3.8	10
11.7_Cu/C	11.0/-	230	10.2	8.5±0.3	11.7±0.3	3.9	5.1	8.8
13.4_Cu/C	11.7/-	230	10.9	8.9±0.3	13.4±0.4	4.3	6.2	7.8
4.2_$CuZnO_x$/C	6.3/3.6	250	1.9	2.3±0.1	4.2±0.3	1.3	2.3	25
9.8_$CuZnO_x$/C	7.7/4.3	230	8.0	8.7±0.5	9.8±0.6	2.2	2.5	11
2.7_Cu/SiO_2	13.5/-	250	2.4	2.3±0.1	2.7±0.1	0.7	0.8	39

***a**) Nominal Cu and Zn weight loadings for the final catalyst; **b**) Temperature of the final heat treatment under H_2/N_2 atmosphere during catalyst assembly; **c**) Cu^0 crystallite size as determined by XRD, applying the Scherrer equation to the Cu^0 (111) and Cu^0 (200) diffraction peaks; **d**) Number-averaged particle size (d_n) calculated as ($d_n = \sum_{i=1}^{N} d_i / \sum_{i=1}^{N}$) with standard error in the particle size (σ_{dn}), and surface-averaged particle size (d_s) calculated as ($d_s = \sum_{i=1}^{N} d_i^3 / \sum_{i=1}^{N} d_i^2$) with standard error in the particle size (σ_{ds}), as determined by TEM wherein d_i indicates the diameter of the ith particle and N stands for the total amount of measured particles. **e**) Cu dispersion calculated from d_s, by assuming fully accessible spherical particles.*

Activity and selectivity in methanol synthesis. The performance of the Cu and $CuZnO_x$ catalysts was investigated at 260 °C and 40 bar, with a gas feed consisting of 60:23:7 vol% H_2:CO:CO_2. An example of a typical reaction profile is displayed in Figure 3.6, for the 5.2_Cu/C catalyst. The CO+CO_2 conversion slightly increased during the first 6 h, while the selectivity towards methanol increased from 93 to >98 % and was maintained at this high value afterwards, with methane as the main by-product. Such an induction period is commonly observed in Cu-based hydrogenation catalysis and is generally attributed to nanoparticle restructuring and/or oxidation state changes.[99, 109, 112, 225] The induction period for 5.2_Cu/C was

followed by a gradual decrease in conversion of 26 % between 6–48 h. This deactivation was only slightly larger than most literature values under similar reaction conditions, *e.g.* 6 nm Cu/SiO_2 (3–13 %),[56] 6 nm $CuZnO_x/SiO_2$ (29 %)[86] and 10 nm $Cu/ZnO/Al_2O_3$ (3–14 %),[225] thus showing that the un-promoted Cu catalysts on carbon were relatively stable.

Particle growth is a well-known cause of activity loss in methanol synthesis.[109] Therefore, we compared the Cu particle sizes of representative catalysts before and after 48 h catalysis. The Cu sizes increased from 5.2±0.3 to 6.3±0.3 nm, 10.0±0.2 to 10.3±0.5 nm and 13.4±0.4 to 13.7±0.6 nm. The initial smallest Cu particles grew the most, which was ascribed to shorter interparticle distances and larger driving forces towards sintering.[56, 225] To evaluate the effect of catalyst deactivation, we calculated the surface-normalized turn-over frequencies (TOF; mol_{CO+CO2} $mol_{Surface\ Cu}^{-1}$ s^{-1}) for the 5.2_Cu/C catalyst, at both the maximum and final $CO+CO_2$ conversion, correlated to the initial and final Cu particle size, respectively. The TOF was approximately $0.8*10^{-3}$ s^{-1} for both the initial and final Cu particle sizes, indicating that particle growth was indeed the main cause of activity loss over time. This allowed us to compare the TOF values for the Cu/C catalysts with different initial Cu particle sizes, based on the maximum $CO+CO_2$ conversion within 10 h on stream.

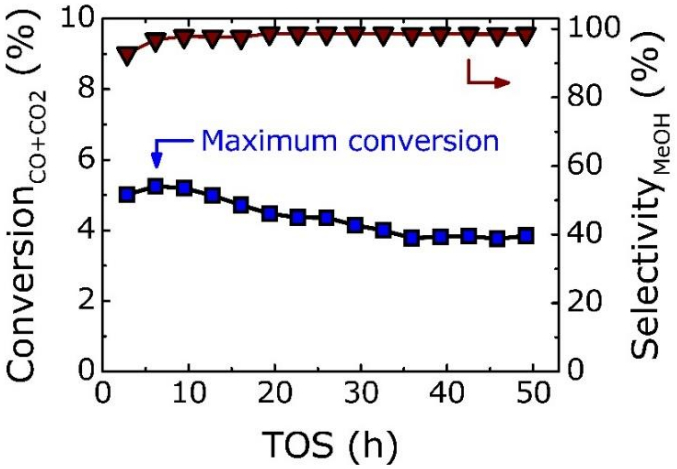

Figure 3.6: *Characteristic profiles for $CO+CO_2$ conversion (blue squares) and selectivity towards methanol (red triangles) for Cu/C catalysts as a function of time on stream (TOS, t=0 at 260 °C), the displayed example is for the 5.2_Cu/C catalyst. The relative standard deviation in $CO+CO_2$ conversion was approximately 5 %. Reaction conditions: H_2:CO:He:CO_2=60:23:10:7 vol%, 260 °C and 40 bar*.

Intrinsic Cu particle size effects. An important un-resolved question in literature is whether particle size effects in methanol synthesis are intrinsic and/or originate from a particle size-dependent coverage of the ZnO_x promoter.[86, 108] The TOF for

Cu/C increased approximately 4-fold with increasing Cu particle size from 3 to 10 nm ($0.5*10^{-3}$ s^{-1} to $1.9*10^{-3}$ s^{-1}), and became size-independent above 10 nm (Figure 3.7). This is the first time that this Cu particle size range was investigated, using carbon support materials. The size-dependence in activity unequivocally demonstrates that the methanol synthesis reaction rate is intrinsically sensitive to the Cu particle size below 10 nm, in absence of ZnO_x as promoter. However, the particle size effect is moderate as compared to that in other systems such as Co for Fischer Tropsch synthesis (~10-fold increase TOF between 2 and 6 nm),[187] or Ag for ethylene epoxidation (~10-fold increase TOF between 20 and 90 nm).[226]

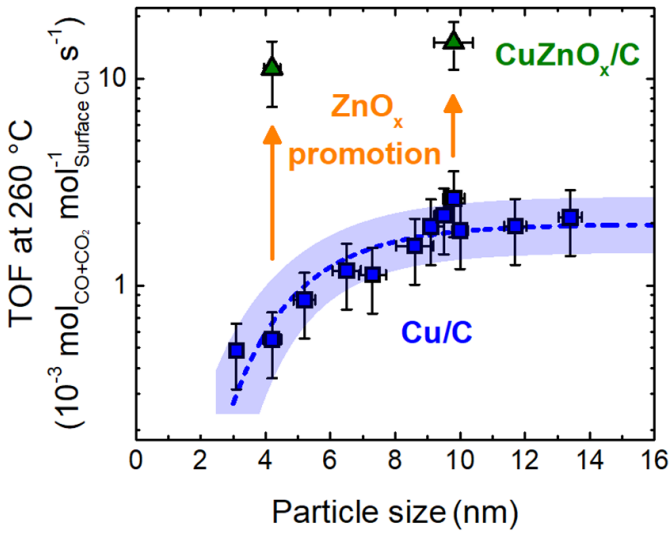

Figure 3.7: *Particle size-activity relationships for Cu/C (blue squares) and $CuZnO_x/C$ (green triangles) for the methanol synthesis, including exponential fit (dashed line). TOF values were calculated from the maximum $CO+CO_2$ conversion within the first 10 h on stream and the initial surface-averaged Cu or $CuZnO_x$ particle size. Horizontal error bars represent the standard error in the particle size and vertical error bars display the relative standard deviation in TOF. The TOF evidently increased with increasing Cu size up to 10 nm, and became constant above 10 nm. The ZnO_x promoter effect was illustrated by the strongly enhanced TOF for the $CuZnO_x/C$ catalysts compared to Cu/C. Reaction conditions: H_2:CO:He:CO_2 = 60:23:10:7 vol%, 260 °C and 40 bar.*

The reaction rate towards methanol depends on the activation energy of the rate determining step, the amount and nature of the active sites and the site coverage with reaction intermediates. Higher adsorption strengths were reported for oxygenate intermediates on a stepped Cu (211) surface, compared to the more densely packed Cu (111) surface.[105, 117, 186] The defect-rich stepped surfaces contain Cu atoms of an intermediate coordination saturation, compared to highly coordinated terrace sites on flat surfaces.[196] DFT calculations by Behrens *et al*. proposed that the higher binding energy at step sites, lowered the energy barrier for the surface

hydrogenation of the formate intermediate, which is commonly recognized as the rate determining step towards methanol from CO_2-enriched synthesis gas.[86, 97, 99, 105, 108, 222] If formate is too strongly adsorbed, for example at corner and edge sites with a low coordination saturation, the high formate surface coverage can lead to active site poisoning.[110, 186] In line with the Sabatier principle, adsorption sites with intermediate binding strength, such as step and kink sites, were proposed to give the highest activity.[99, 105, 172, 222] DFT studies by Rensburg *et al*. predicted that Cu size effects predominantly originate from the surface-specific amount of defect sites,[186] while Karelovic *et al*. reported that the activation energy for CO_2 hydrogenation did not dependent on the Cu particle size.[106] The nature of the active site is therefore likely size-independent, while the abundance of the active site increases with increasing Cu particle size up to 10 nm.

The surface structure of metal nanoparticles is known to be size-dependent.[185, 188, 227] Wulff constructions models by Van Hardeveld and Van Helden showed that the surface of face centered cubic (fcc) metals primarily consists of (111) and (100) facets with exposed terrace sites, while edge and corner sites terminate the facets. The fraction of extended facets increased with increasing particle size, while the relative amount of corners and edges decreased. At the facet interfaces, unique atomic arrangements represent stepped (211), (221) and (321) facets, which expose step and kink sites. Each of these sites exhibits a different local electron density, due to the varying degree of coordination saturation. Interestingly, the fraction of the step and kink sites gradually increases up to 10 nm.[185, 188] Recent studies propose that the defects at extended Cu facets, such as step sites, are the active sites in methanol synthesis from CO_2-enriched synthesis gas.[105, 108, 110, 194-197] The current Cu particle size-activity relationship is therefore attributed to structure sensitivity, *i.e.* the size-dependence of the fraction of surface sites that is catalytically most active. The fact that the particle size dependence is only moderate can be coined to the prevailing hydrogenation reactions and the absence of CO dissociation in methanol synthesis.[13]

ZnO_x promoter effects. The activity enhancement by ZnO_x was compared for Cu catalysts supported on carbon and SiO_2 (Table 2). Clearly and irrespective of using SiO_2 or carbon as the support material, ZnO_x was an efficient promotor for methanol synthesis. Moreover, the activity increased with increasing $CuZnO_x$ particle size on both supports, demonstrating that particle size effects are present both in the absence and presence of ZnO_x. The TOF for the $CuZnO_x$/C catalysts (11–15*10^{-3} s^{-1}) in this study, were in line with previously reported values for carbon-supported $CuZnO_x$ catalysts (11–31*10^{-3} s^{-1}) under similar reaction temperature and pressure.[86] Interestingly, the measured copper-normalized productivity was 0.12 mol_{CO+CO2} g_{Cu} h^{-1} for the 4.2_$CuZnO_x$/C catalyst, and thus higher than 0.07 mol_{CO+CO2} g_{Cu} h^{-1} for a measured commercial Cu/ZnO/Al_2O_3 methanol synthesis catalyst (Alfa Aesar). Moreover, the presence of ZnO_x enhanced the TOF significantly stronger on carbon

(8–20 fold) than on SiO_2 (3–7 fold). The activities for $CuZnO_x/SiO_2$ and Cu/ZnO_x catalysts with particle size around 9–10 nm, were previously reported to be $10*10^{-3}\,s^{-1}$ and $15*10^{-3}\,s^{-1}$, respectively. The lower TOF for the SiO_2-supported $CuZnO_x$ catalyst suggested an unfavorable effect of the SiO_2 support on the promoter efficacy. In contrast, the presence of carbon allowed for maximum ZnO_x promotion ($15*10^{-3}\,s^{-1}$).

Table 3.2: ZnO_x promoter effect, for representative Cu catalysts on carbon, SiO_2 and ZnO_x.

Particle size (nm)[a]	Support[b]	TOF Cu ($10^{-3}\,s^{-1}$)	TOF $CuZnO_x$ ($10^{-3}\,s^{-1}$)	Promoter enhancement factor[c]
4	C	0.5	11	20
10	C	1.9	15	8.1
4	SiO_2	1.2	3.9	3.3
10	SiO_2	1.5	10	6.7
9	ZnO_x	-	15	-

***a**) Representative examples of catalysts with surface-averaged particle sizes of approximately 4 and 10 nm; **b**) Catalyst support type indicating carbon (C), silica (SiO_2) and zinc oxide (ZnO_x). TOF values for Cu/SiO_2, $CuZnO_x/SiO_2$ and Cu/ZnO_x catalysts were included for direct comparison, as measured by Van den Berg et al. under similar reaction conditions;[86] **c**) Promotion expressed as the ratio between TOF for Cu catalysts of similar particle size, with and without ZnO_x. Reaction conditions: H_2:CO:He:CO_2 = 60:23:10:7 vol%, 260 °C and 40 bar.*

It is generally believed that part of the ZnO_x promoter is reduced to Zn^0 under reaction conditions and that Zn species diffuse to the Cu particle surface.[105, 108, 228-229] The efficacy of the ZnO_x promoter may therefore depend on the thermodynamic stability, and the high stability of zinc-silicates may limit the efficient ZnO_x coverage onto Cu under reaction conditions. The stronger promoter effect of ZnO_x for the inert carbon support compared to SiO_2 may be explained by a higher ZnO_x coverage of the Cu nanoparticles, due to the preference for ZnO_x to situate on top of the Cu particle rather than on the weakly interacting carbon surface.[108] Considering the slightly lower activity of un-promoted Cu on carbon than SiO_2, it is likely that the presence of ZnO_x creates additional active sites or affects the Cu particle morphology.[222] We propose that the size-dependent $CuZnO_x$ activity originates from a combination of intrinsic Cu particle size effects and effective coverage of ZnO_x onto the Cu particles.

Carbon and SiO_2 support effects. An intriguing observation was the difference in activity for Cu/C compared to Cu/SiO_2 observed in this study and reported in literature (Figure 3.8).[56, 72, 86] A consistently lower TOF was observed for Cu particles below 10 nm on carbon compared to SiO_2, while the TOF was similar above 10 nm.

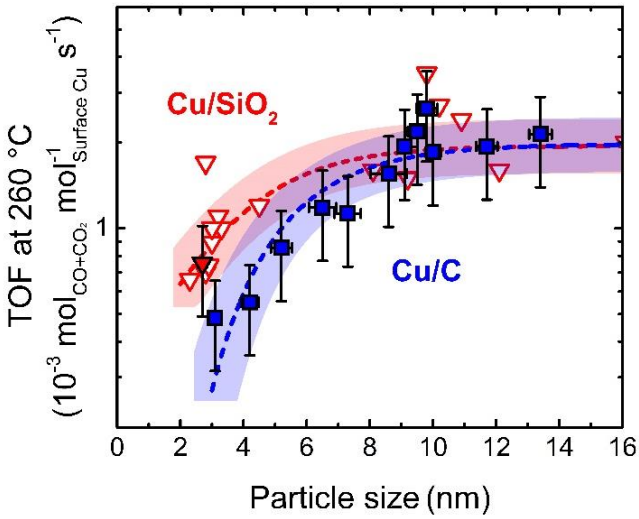

Figure 3.8: *Particle size-activity relationships for measured Cu/C (blue squares, this work) and Cu/SiO_2 (fully red triangle, this work) catalysts, and previously reported values for Cu/SiO_2 (empty red triangles, as measured by Van den Berg et al. under similar reaction conditions). TOF values were calculated from the maximum CO+CO_2 conversion within the first 10 h on stream and the initial surface-averaged Cu particle size. Horizontal error bars represent the standard error in the particle size and vertical error bars show the standard deviation in TOF. The activity increased with increasing Cu size up to 10 nm on both supports, while the TOF were lower for Cu particles below 10 nm on carbon compared to SiO_2. Exponential fits (dashed lines with highlighted areas) were added to guide the eye. Reaction conditions: H_2:CO:He:CO_2 = 60:23:10:7 vol%, 260 °C and 40 bar.*

Possible origins include electronic effects, changes in the Cu particle shape and structure, and metal-support interactions.[15, 71, 230-231] To elucidate possible electronic support effects, we applied H_2 temperature-programmed reduction to several representative passivated Cu and $CuZnO_x$ catalysts, both on carbon and SiO_2, with particle sizes around 3–4 nm (Figure 3.9). Interestingly, the support did not significantly affect the onset temperature for H_2 reductions, yet the rate of CuO reduction was significantly lower for the catalysts on SiO_2 compared to carbon. The higher hydrophilicity of SiO_2 may lead to a stronger retention of the *in situ* generated water, both during the TPR experiment and catalysis. A higher local water concentration may result in a more oxidizing local environment and partial oxidation of the Cu^0 surface. Enhanced activity of Cu^+ sites compared to Cu^0 sites was previously reported.[99, 121, 222] The smallest Cu particles are likely most susceptible towards oxidation, which potentially explains the higher TOF for Cu on SiO_2 compared to carbon.

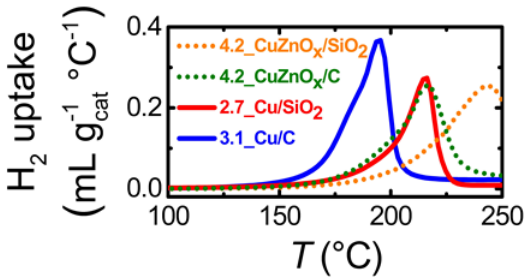

Catalyst	Onset T^a (°C)	Peak T^b (°C)
3.1_Cu/C	165	195
2.7_Cu/SiO_2	174	216
4.2_$CuZnO_x$/C	178	216
4.2_$CuZnO_x$/SiO_2	176	243

Figure 3.9: *Temperature-dependent H_2 reduction profiles for Cu and $CuZnO_x$ catalysts with particles of around 3–4 nm in size, supported on carbon and SiO_2, with H_2 uptake as a function of temperature, under a flow of 5 vol% H_2/Ar. Measurements performed with equal Cu mass per measurement;* ***Above****) Overview of onset temperatures for the reduction peak, calculated from the slope at the first inflection point in the reduction profile;* ***Below****) Overview of the onset and peak temperatures.*

Alternatively, differences in support surface energies can affect the Cu–support interaction strength. This may influence the Cu-support contact angle, which alters the particle shape and thereby the nature of the exposed surface facets.[231] Previous studies on pristine and amine-functionalized SiO_2 supports indicated that the support can alter the Cu–support contact angle (125–135 °) and TOF (0.7–0.9*10^{-3} s^{-1}).[72] Although the effects might seem small, the metal-support interaction may affect the particle shape and lead to a different abundance of the catalytically active surface sites. However, proving this by measuring the contact angles under industrially relevant reaction conditions is very challenging.

Interestingly, while the un-promoted Cu catalysts showed a higher activity on SiO_2 than on carbon, this trend was reversed in the presence of ZnO_x. It might be related to, as mentioned before, the fact that a different fraction of the ZnO_x promoter is actually present on the active Cu particles under reaction conditions. This suggested that also the nature of the support plays a subtle role in the catalytic activity, and the dependency on particle size and promoters, which showed that one has to be careful to investigate structure-performance relationships using different support materials. Using a series of catalysts all prepared on the same carbon support allowed us to distinguish the intrinsic Cu particle size effects from support and promoter effects in the methanol synthesis reaction.

3.4 Conclusions

In this chapter, we reported the assembly of carbon-supported Cu and $CuZnO_x$ catalysts with particle sizes between 3–14 nm, which was achieved by combining the synthesis approaches of Cu loading variation, support functionalization and controlled thermal sintering. The accurate control over the carbon-supported Cu particle size unequivocally demonstrated that the methanol synthesis reaction is intrinsically sensitive, though weakly, to the Cu particle size below 10 nm. The 4-fold increase in TOF with increasing Cu particle size was attributed to the size-dependent surface structure of the Cu particles. A consistently higher activity was observed for un-promoted Cu below 10 nm, when supported on SiO_2 compared to carbon. However, the ZnO_x promoter boosted the TOF around 20 times for Cu on carbon, and outperformed the $CuZnO_x$ catalysts on SiO_2, which suggested that the chemically inert nature of the carbon support provided the highest ZnO_x promoter efficacy. We demonstrated that the $CuZnO_x$ particle size effects in methanol synthesis originate from a combination of intrinsic Cu particle size effects and the effective coverage of ZnO_x onto the Cu particles, and that the nature of the support also plays a significant role in determining the activity of these methanol synthesis catalysts.

Acknowledgements

Mariosol Tapia Rosales is acknowledged for performing the Raman spectroscopy, Nynke Krans for STEM-HAADF-EDX imaging, Miguel Rivera Torrente for measuring N_2 physisorption, Lennart Weber and Jan Willem de Rijk for providing technical support in catalytic experiments.

Chapter 4

Cu Particle Size Effects in Ethyl Acetate Hydrogenation

This chapter is based on the publication: "*Particle Size Effects in Copper-Catalyzed Hydrogenation of Ethyl Acetate to Ethanol"* by R. Beerthuis, J. W. de Rijk, J. M. S. Deeley, G. J. Sunley, K. P. de Jong and P. E. de Jongh,, Journal of Catalysis, Accepted.

Abstract

In this chapter, we discuss the role of the Cu particle size in the hydrogenation of ethyl acetate, using a series of carbon-supported Cu catalysts with Cu particle sizes tuned between 3 to 14 nm. At temperatures of 180 to 210 °C and a pressure of 30 bar, the surface-normalized activity increased around 4-fold with increasing Cu particle size from 2 to 10 nm, yet became constant above 10 nm, hence showing that the Cu-catalyzed hydrogenation reaction is weakly sensitive to the Cu surface structure. The apparent activation energy for the reaction was around 94 kJ mol^{-1} and similar for all Cu particle sizes, which suggests that the nature of the active sites was size-independent, whereas the abundance of the active surface sites increased with increasing Cu particle size between 2 to 10 nm. A maximal weight-normalized activity was achieved with Cu particles of around 6 nm, providing an optimal balance between intrinsic activity and available surface area. These findings may guide optimization strategies for catalysts in reactions where the hydrogenation of relatively stable intermediates is rate-limiting.

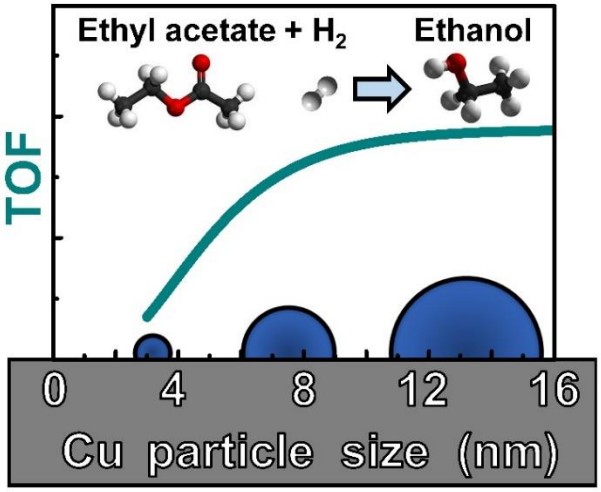

4.1 Introduction

The catalytic performance for a range of important industrial processes strongly depends on the metal particle size, such as for Co and Fe catalysts in Fischer-Tropsch synthesis,[187-189] Pd and Pt for hydrogenation catalysis,[192-193] and Ag for ethylene epoxidation.[226] The catalyst activity is often influenced by the size and structure of metal particles below ~20 nm.[13] In the Cu-catalyzed methanol synthesis reaction, a weak but significant particle size effect has been reported by Van den Berg *et al.*[86] and was further discussed in Chapter 3 of this thesis. However, the role of the Cu particle size in hydrogenation catalysis is still not fully understood. This partly originates from the complexity of the methanol synthesis reaction, which proceeds *via* concurrent CO hydrogenation, CO_2 hydrogenation and (reverse) water gas shift reactions.

The establishment of structure-performance relationships is facilitated by using well-defined supported metal catalysts and model reactions. The hydrogenation of short chain alkyl esters, such as ethyl acetate (EtOAc) to ethanol is a promising reaction, since the reaction mechanism is relatively simple and well understood (Eq. 1.4 in Chapter 1 of this thesis).[133, 141, 232] Moreover, the reaction typically proceed with high selectivity towards ethanol (~95 %),[125, 133, 136, 233] To rationally design optimization strategies for Cu-based hydrogenation catalysts in general, it is crucial to understand how activity, selectivity and stability are affected by varying Cu particle sizes for various reactions.

In this chapter, we investigate the effect of varying Cu particle size on activity and stability in the hydrogenation of ethyl acetate, under industrially-relevant temperatures (180 to 210 °C) and pressure (30 bar), as a model reaction for Cu-based hydrogenation catalysis. A series of Cu catalysts with Cu particle sizes between 3 and 14 nm was used, to determine whether the hydrogenation of EtOAc was sensitive to the Cu particle size. Additionally, the influence of the initial Cu particle size, poly-dispersity and interparticle Cu distance was evaluated on the extend of particle growth. High surface area graphite was used as the support material, to minimize the metal–support interactions[22] and reveal the intrinsic Cu particle size effects.

4.2 Experimental methods

Cu/C catalyst preparation

A series of carbon-supported Cu (Cu/C) catalysts was prepared by incipient wetness impregnation using 2.0–3.3 M aqueous $Cu(NO_3)_2$ solutions, followed by drying and thermal treatment to decompose the Cu precursor. The Cu particle size was tuned by adaptation of the synthesis methods as reported in Chapter 3. As an example of a typical synthesis procedure, a Cu/C catalyst containing 16.4 wt% Cu was prepared by impregnating around 2 g of a dried powdered carbon support to incipient wetness,

in a three-necked round-bottom flask. An aqueous solution of 5.0 M $Cu(NO_3)_2$ in 0.1 M HNO_3 (pH ~1) was added drop-wise using a syringe through a septum, while stirring under vacuum. The impregnate was stirred for 24 h to advance the uniform distribution of the metal precursor throughout the support. Subsequently, the sample was dried overnight at room temperature, while stirring under dynamic vacuum. The dried sample was transferred to an Ar-filled glovebox and loaded into a tubular flow reactor. Next, the sample was heated with 0.5 °C min^{-1} to 230 °C with 1 h hold with 230 °C under a flow of 5 vol% H_2/N_2 flow (~100 mL min^{-1} g^{-1}; GSHV ~4,000 h^{-1}), resulting in decomposition of the nitrate precursor and formation of Cu nanoparticles. Finally, the catalyst was passivated by exposing it overnight to air at room temperature. The Cu weight loading in the final catalyst was calculated as $\mathrm{Cu\ wt\%} = \left(\frac{\mathrm{mass\ Cu}}{\mathrm{mass\ CuO + mass\ support}}\right) * 100\ \%$. The Cu/C catalysts in this chapter were denoted as *X*_Cu/*Y*, in which *X* represents the surface-averaged Cu particle size in nm by TEM analysis, and *Y* indicates the carbon support material.

Catalyst characterization

Transmission electron microscopy (TEM) was performed on an FEI Tecnai 20 microscope, operated at 200 kV. Samples were prepared by dispersing the dry catalyst powder onto a Ni sample grid, coated with holey carbon (Agar 300 mesh Ni). The Cu particle size was determined by measuring the diameter of the spherical approximation of the projected particle shape, for at least 200 individual particles on 10 different sample areas. A small number of large (>50 nm) particles was detected in some samples, which likely results from slight over-impregnation and were hence not included in the particle size analysis.The number-averaged Cu particle size (d_n, also referred to as *d* [1,0]) and surface-averaged Cu particle size (d_s, also referred to as *d* [3,2]), including the standard deviation in the particle size distribution (σ), were calculated using the formulas $d_\mathrm{n} \pm \sigma_{d\mathrm{n}} = \frac{1}{N}\sum_{\mathrm{i}=1}^{N} d_\mathrm{i} \pm \sqrt{\frac{1}{N}\sum_{i=1}^{N}(d_n - d_i)^2}$ and $d_\mathrm{s} \pm \sigma_{ds} = \frac{\sum_{\mathrm{i}=1}^{N} d_\mathrm{i}^3}{\sum_{\mathrm{i}=1}^{N} d_\mathrm{i}^2} \pm \sqrt{\frac{1}{N}\sum_{i=1}^{N}(d_s - d_i)^2}$, in which d_i indicates the diameter of the ith particle and *N* stands for the total number of measured particles.

The Cu–Cu interparticle distance ($d_{\mathrm{Cu–Cu}}$) was estimated from the catalyst surface area and surface-averaged Cu particle size. Herein, only the mesoporous surface area (by BET analysis of N_2 physisorption isotherms) was assumed to be accessible for Cu particles >2 nm. The Cu nanoparticles were consistently located on the edge locations of the graphite nanosheets. Previous investigations on the structure of similar high surface area graphite supports, suggest that roughly 75 % of the carbon structure contained graphitic carbon, while the remained was comprised of disordered carbon. To account for the higher density of Cu particles on the edge positions, the carbon surface area (*SA*carbon) where the Cu particles were located, was assumed to be comprised of disordered carbon. The total volume of all Cu content (V_{Cu}) was calculated based on the specific mass of Cu per catalyst and the

bulk density of Cu (ρ_{Cu}; 8.96 g mL^{-1}) according to $V_{Cu}=m_{Cu}/\rho_{Cu}$. To calculate the volume of an individual Cu particle, we used the surface-averaged Cu particle size (d_s) and assumed the particle shape to be hemispherical, calculated as $V_{Cu\ particle}$ = 0.5*4/3*π*r^3. Next, the total number of Cu particles ($\#_{Cu\ particles}$) was calculated using $\#_{Cu\ particles}=V_{Cu\ total}/V_{Cu\ particle}$. To determine the distribution of Cu particles on the graphite support, we adjusted for the mass of the carbon support (m_{carbon}) within the mass of the final catalyst ($m_{catalyst}$), as $m_{carbon} = m_{catalyst} - m_{Cu}$. The averaged surface area per Cu particle ($SA_{carbon\ Cu\ particle}$) was calculated as $SA_{carbon\ Cu\ particle}=SA_{carbon}/\#_{Cu\ particles}$. By taking the square root of $SA_{carbon\ Cu\ particle}$, the distance between the center of each Cu particle ($d_{Cu-Cu\ center}$). Finally, we subtracted d_s from $d_{Cu-Cu\ center}$, to estimate the distance between the periphery of each individual Cu particle (d_{Cu-Cu}).

Powder X-ray diffractometry (XRD) was performed on a Bruker D8 powder X-ray diffractometer equipped with a Co-$K_{\alpha1,2}$ radiation source (λ = 1.79026 Å) and a Lynxeye detector. Diffractograms were taken directly after the final step in the synthesis under reductive atmosphere, or after an additional reduction treatment (1 h at 250 °C in 20 vol% H_2/N_2, ~100 mL min^{-1} g^{-1}), without exposure to air. The reduced catalyst was loaded into an airtight XRD specimen holder (A100B33, Bruker AXS) inside an Ar-filled glovebox (Mbraun LABmaster, <0.1 ppm H_2O, <0.1 ppm O_2). Diffractograms were continuously acquired with 0.1 °2θ increment between 5–95 °2θ, in approximately 2–3 h. The diffractograms were normalized to the peak intensity of the graphitic (002) diffraction peak at 30.9 °2θ and carbon baseline subtracted. The Cu^0 crystallite size was determined by applying the Scherrer equation to the main Cu^0 (200) diffraction peak at (59.3 °2θ), with a shape factor k of 0.1.[234]

Temperature-programmed reduction (TPR) profiles were measured on a Micromeritics Autochem II ASAP 2920 apparatus, with H_2 consumption detected by a thermal conductivity detector. Prior to the measurement, the passivated catalysts were dried at 120 °C for 30 min under Ar flow (~1 mL min^{-1} mg$_{cat}^{-1}$) and left to cool down to 50 °C. Next, the reduction profiles were determined by heating the catalyst with 2 °C min^{-1} to 400 °C, in a flow of 5 vol% H_2/Ar (~1 mL min^{-1} mg$_{cat}^{-1}$). The reduction profiles were base-line corrected and normalized to the amount of Cu. The onset temperature was estimated from the intercept of the slope at the first inflection point of the peak with the baseline.

Catalysis

Catalytic experiments were performed on a high-throughput fixed-bed reactor system, equipped with 16 parallel channels (Flowrence®, Avantium N. V.). The catalysts were pelletized (2 cm diameter) using a hydraulic press at 1,500 kgf, equivalent to 460 bar pressure, ground and sieved to obtain a granulate size of 75–150 μm. All experiments were done using ~6.0 mg of Cu mass per reactor. The

required amount of catalyst (30–100 mg) was calculated from the Cu weight loading. The Cu/C catalysts were physically diluted with SiC granulates (212–425 μm). The SiC diluent was pre-treated by washing with HNO_3(aq) (68 %; 10 mL g_{SiC}^{-1}) and calcining at 800 °C, to remove any metal or organic contaminants. The volume of the diluted catalyst bed was kept constant at 0.3 mL. The catalyst was loaded into a stainless-steel reactor tube (2.6 mm inner diameter) on top of SiC granules (0.5 mL), which were pre-loaded onto a stainless-steel frit. A hollow glass wool fibre was placed on top of the catalyst bed, up to the entrance of the reactor, to ensure constant vaporization of the liquid reactant.

The Cu/C catalysts were re-reduced *in situ* by heating with 2 °C min^{-1} to 200 °C, with 2 h hold at 200 °C, under a flow of 20 vol% H_2/Ar (2 mL min^{-1} per reactor). Subsequently, the temperature was lowered to 140 °C and the reactor was purged for 2 h using a mixture of H_2:He in a 10:1 molar ratio (6.2 mL min^{-1} per reactor). Next, the EtOAc feed was introduced in the gas phase (0.6 mL min^{-1} per reactor). The reaction mixture consisted of H_2:He:EtOAc in a 10:1:1 molar ratio (6.8 mL min^{-1} total flow per reactor). The GHSV based on the packing density of the diluted catalyst and the total flow per reactor was approximately 1,350 h^{-1}, and the WHSV was around 325 g_{EtOAc} g_{Cu}^{-1} h^{-1}. Next, the pressure was gradually increased during 75 min to 30 bar(g). Finally, the temperature was increased to 180 °C with 2 °C min^{-1} to start the catalytic experiment. Between isothermal stages, the temperature was increased with 1 °C min^{-1}. After the reaction, the catalysts were left to cool down to 90 °C and passivated by exposure to air.

The effluent gas composition was analysed every 19 min by on-line gas chromatography (GC, Agilent 7890B). H_2 and He were separated on a MolSieve 5A column (2.4 meter x 1/8 inch inner diameter) and quantified using a thermal conductivity detector. Oxygenates and hydrocarbons were separated using a GS-GasPro column (GS-Gaspro 30 m x 0.32 mm ID) and a HP-Innowax column (6 m x 0.32 mm ID), and analyzed by separate flame ionization detectors. The gas phase composition was calculated from the integrated peak areas, using He as the internal standard.

The Cu-normalized time yield (CTY, mol_{EtOAc} g_{Cu}^{-1} h^{-1}) was used to calculate the turn-over frequency (TOF, mol_{EtOAc} $mol_{surface\ Cu}$ s^{-1}) using the formula: CTY*M_{Cu}/D_{Cu}, in which M_{Cu} stands for the molecular weight of Cu and D_{Cu} the fraction of surface Cu atoms. The value of D_{cu} is calculated from the Cu d_s, assuming fully accessible and spherical particles using the formula $6*(V_{Cu}\ A_{Cu}^{-1})/d_s$. Herein, A_{Cu} is the molar area occupied by surface Cu atoms ($4.10*10^{22}$ nm^2) and V_{Cu} is the molar volume occupied by bulk Cu atoms ($7.09*10^{21}$ nm^3). D_{Cu} is thus calculated as $1.04/d_s$, with d_s in nm.[172] The initial TOF at 180 °C was determined after around 30 h on stream, and calculated from the Cu d_s of the fresh Cu/C catalyst. The final TOF at 180 °C was calculated after around 150 h on steam, and calculated from the Cu d_s after catalysis.

To be concise, the initial reaction times will be referred to as 30 and 50 h on stream, yet precise reaction times may vary ±2.5 h depending on moment of GC sampling. The standard deviation in TOF (σ_{TOF}) was determined from an experiment using 12 reactors with an equal loading of a commercial co-precipitated $CuZnMgO_x/Al_2O_3$ catalyst (Alfa Aesar). Herein, σ_{TOF} was defined as the typical distance of a data point (χ) from the mean value (μ) and calculated by the formula $\sigma_{\mathrm{TOF}} = \sqrt{\left(\frac{1}{N-1}\right)\sum_{i=1}^{N}(\chi_{\mathrm{i}} - \mu)^2}$ and found to be approximately 8 %.

To validate that the reaction was not mass transfer limited, we performed measurements with Cu/C catalysts of granulate size ranges of 75–150 µm, 150–425 µm and 425–630 µm. No substantial differences in conversions were observed, indicating that the reaction was not hindered by internal or external mass transfer limitations. Three reference measurements using the pristine and surface-oxidized carbon supports and SiC, showed no EtOAc conversion at 210 °C.

The E_a and A values in the Arrhenius model were obtained from the slope of a linear fit line through the ln(r) values and the intercept with the y-axis, respectively. Herein, the rate r was either defined as the weight-normalized CTY ($mmol_{EtOH}\ g_{Cu}^{-1}\ h^{-1}$) or surface-normalized CTY ($mmol_{EtOH}\ m_{Cu}^{-2}\ h^{-1}$), at conversions of ethyl acetate <25 %. In the Arrhenius model, the CTY at 180 °C was determined from the final isothermal stage, to minimize the influence of initial activation during the first 30 h on stream.

4.3 Results & Discussion

Tuning the Cu particle size. A series of carbon-supported Cu (Cu/C) catalysts was prepared, by variation of the synthesis method as reported in Chapter 3 of this thesis. Here, we prepared three Cu/C catalysts with the same Cu particle size, but using different Cu loadings (6.3 or 16.4 wt%) and/or support materials (pristine or surface-oxidized carbon). The first sample was prepared using 6.3 wt% Cu and pristine carbon as the support. After heating to 230 °C in 20 vol% H_2/N_2, Cu particles of 8.6 nm were obtained (8.6_Cu/PC; Figure 4.1a). The second sample was prepared using the same Cu loading (6.3 wt%), but using surface-oxidized carbon as the support. In general, oxidizing the carbon support leads to smaller particles. To obtain the same Cu particle size of around 8 nm, the second sample had to be heated to 400 °C in a flow of 5 vol% H_2/N_2, which resulted in Cu particles of 7.3 nm (7.3_Cu/OC; Figure 4.1b). The third sample was prepared using a higher Cu loading (16.4 %) on the surface-oxidized carbon support. This sample was heated to only 230 °C, yielding 8.0 nm Cu particles (8.0_Cu/OC; Figure 4.1c). The Cu particle size was ~8 nm for the three different Cu/C catalysts, with similar particle size distributions (Figure 4.1d) and poly-dispersity indexes (PDI) or around 33–34 % (Table 1). However, the estimated interparticle Cu distance (d_{Cu-Cu}) was significantly

higher for the Cu/C catalysts with the lowest Cu loading, for example 38 nm for the 8.6_Cu/PC catalyst with 6.3 wt% Cu, compared to 16 nm for the 8.0_Cu/OC catalyst with 16.1 wt% Cu. XRD studies on the reduced Cu/C catalysts (Figure 4.1e), showed similar Cu^0 crystallite sizes between 6.0 and 7.3 nm. The Cu/C catalyst with 16.4 wt% Cu exhibited the most intense Cu^0 (200) diffraction peak, which was expected since it contains the highest Cu loading. These examples illustrate how we can control the Cu particle size by tuning the synthesis parameters, and allowed us to assess the influence of the carbon pre-treatment and interparticle distance on stability during catalysis.The Cu/C catalysts were denoted as *X*_Cu/*Y*, in which *X* shows the surface-averaged Cu particle size in nm and *Y* indicates the type of carbon support material. The physicochemical properties for the full series of Cu/C catalysts were summarized in Table 4.1.

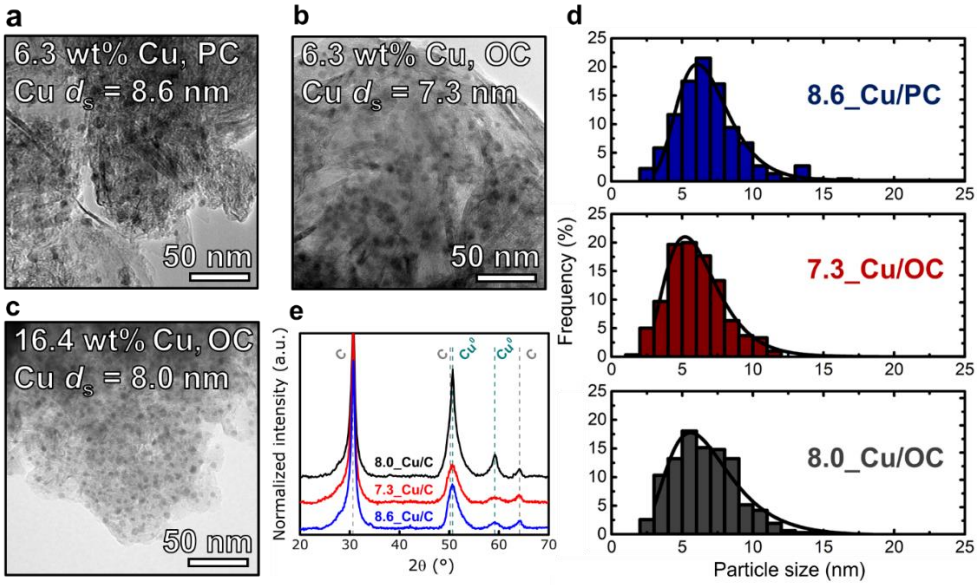

Figure 4.1: *Characterization of the carbon-supported Cu catalysts with Cu particle size around 8 nm, displaying transmission electron micrographs for* ***a****) 6.3 wt% Cu on pristine carbon (PC);* ***b****) 6.3 wt% Cu on surface-oxidized carbon (OC) and* ***c****) 16.4 wt% Cu on surface-oxidized carbon (OC);* ***d****) Cu particle size distributions by TEM, with lognormal fits;* ***e****) X-ray diffractograms, normalized to the intensity of the carbon (002) diffraction peak, carbon baseline subtracted and stacked with individual offset for visual clarity.*

Table 4.1: Physicochemical properties of Cu/C catalysts with varying Cu particle size.

Catalyst[a]	Cu loading (wt%)	T^b (°C)	$d_{Cu^0, XRD}$ (nm)	$d_n \pm \sigma_{dn}$ (nm)[c]	$d_s \pm \sigma_{ds}$ (nm)[d]	PDI (%)[e]	Estimated $d_{Cu\text{-}Cu}$ (nm)[f]
3.1_Cu/OC	6.3	250	2.0	2.6±0.8	3.1±0.9	29	7
4.2_Cu/OC	6.3	330	2.6	3.7±1.0	4.2±1.1	26	12
5.2_Cu/OC	6.3	350	4.2	4.3±1.4	5.2±1.6	31	17
7.3_Cu/OC	6.3	400	6.0	5.9±1.6	7.3±2.4	33	29
8.0_Cu/OC	16.4	230	7.1	6.6±2.2	8.0±2.7	34	16
8.6_Cu/PC	6.3	230	7.3	6.8±2.4	8.6±2.9	34	38
9.1_Cu/PC	7.0	230	7.3	6.5±2.9	9.1±3.8	42	39
9.5_Cu/PC	8.0	230	5.5	6.5±3.9	9.5±4.7	49	38
9.8_Cu/PC	9.0	230	6.0	6.8±4.0	9.8±5.0	51	37
10.0_Cu/PC	10.0	230	8.9	7.8±3.2	10.0±3.8	38	35
11.7_Cu/PC	11.0	230	10.2	8.5±3.9	11.7±5.1	44	43
13.4_Cu/PC	11.7	230	10.9	8.9±4.3	13.4±6.2	46	51

***a**) Carbon-supported Cu catalysts denoted as X_Cu/Y, in which X indicates the surface-averaged Cu particle size in nm by TEM, and Y denotes the type of carbon support material, i.e. either pristine carbon (PC) or surface-oxidized carbon (OC); **b**) Heat treatment temperature for reduction during catalyst synthesis; **c**) Cu number-averaged particle size (d_n) calculated as $\sum_{i=1}^{N} d_i / \sum_{i=1}^{N}$ and **d**) Surface-averaged particle size (d_s) calculated as $\sum_{i=1}^{N} d_i^3 / \sum_{i=1}^{N} d_i^2$ where d_i indicates the particle diameter by TEM, including standard deviations in the width of the particle size distributions (σ_{dn} and σ_{ds}); **e**) Poly-dispersity index (PDI) calculated as σ_{ds}/d_s ; **f**) Estimated average interparticle distance between the surface of individual Cu nanoparticles, assuming a hemispherical Cu particle shape.*

Impact of Cu particle size on catalyst performance. Figure 4.2 shows the EtOAc conversion and Cu-normalized time yield (CTY) for several representative Cu/C catalysts at 180–210 °C. In all cases, the conversion increased during the first 30 h on stream (Figure 4.2a). This activation behavior is common for Cu-catalyzed hydrogenation reactions and is generally believed to be caused by catalyst restructuring.[109, 112, 225] Catalyst stability was evaluated by comparing the conversions after 30 and 150 h on stream, both at 180 °C. Only minor changes in conversion were observed during catalysis. Overall, the highest conversion was observed for Cu particles of around 6 nm. Remarkably, the selectivity towards ethanol was >99.5 % for all Cu/C catalysts, with ethane and acetaldehyde as the main by-products. It was significantly higher than reported values in literature for supported Cu-based catalysts, which are typically ~95 % in the same temperature and conversion range.[125, 133, 136, 233] The superior selectivity for the Cu/C catalysts are ascribed to the chemically inert nature of the carbon support.[22, 235]

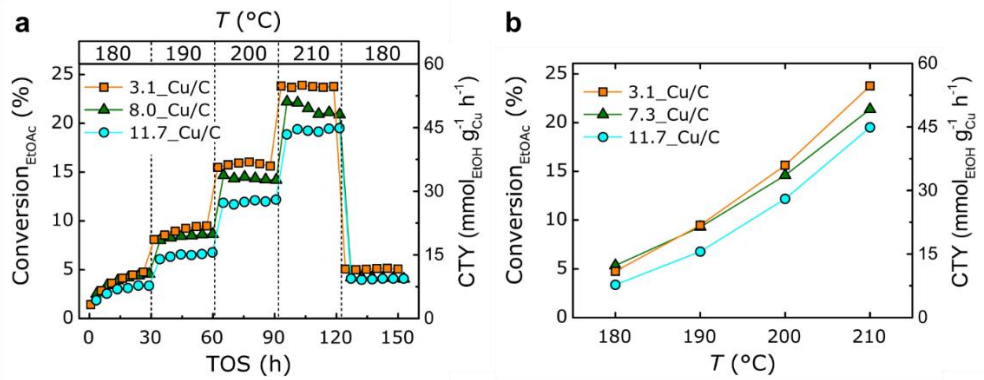

Figure 4.2: *EtOAc conversion and Cu-normalized time yield (CTY), for three representative Cu/C catalysts of various Cu particle sizes. Conversion shown as:* ***a****) a function of time on stream (TOS) at different temperatures;* ***b****) over different temperature, at the end of the isothermal stage (30, 60, 90 and 120 h on stream). Reaction conditions:* H_2*:EtOAc:He = 10:1:1 molar ratio, 180–210 °C and 30 bar(g).*

Next, we assessed the Cu particle growth during catalysis. Particle growth is known to be a main deactivation mechanism for Cu-based catalysts, and can be affected by the Cu particle size, the poly-dispersity in particle size distribution, the interparticle distance, and hence the Cu loading.[10, 19, 56, 93, 236] Here, we discern the influence of two main mechanisms for particles growth, *i.e.* particle diffusion followed by coalescence, and Ostwald ripening, as schematically depicted in Figure 4.3a. We compared the Cu particle size for the fresh and used Cu/C catalysts after 150 h on stream (Figure 4.3b). No significant influence of the carbon support oxidation treatment was observed. However, the smallest Cu particles grew consistently more than the larger Cu particles. For example, the 3.1 nm particles grew to 7.0 nm after 150 h catalysis, while the 13.4 nm particles did not significantly grow. The faster growth of the smallest Cu particles is possibly due to the typically shorter interparticle distances for the smallest Cu particles, *e.g.* 7 nm for 3.1_Cu/C and 51 nm for 13.4_Cu/C (Table 1).

The stability for the three Cu/C catalysts with particle size ~8 nm (7.3_Cu/OC, 8.0_Cu/OC and 8.6_Cu/PC) was compared. Of these catalysts, the interparticle distance was the largest for the 8.6_Cu/PC catalyst, which also showed the most stable conversion over time and least particle growth. The poly-dispersity index increased with increasing particle size, *e.g.* 29 % for 3.1_Cu/OC and 46 % for 13.4_Cu/PC (Table 1). Considering the fact that the largest particles with the largest poly-dispersity were the most stable in size, Ostwald ripening was excluded as a main growth mechanism as it is strongly enhanced by high poly-dispersities.[56] Coalescence was therefore assumed to be the main pathway for particle growth, as it strongly depends on the interparticle distance.[93, 237]

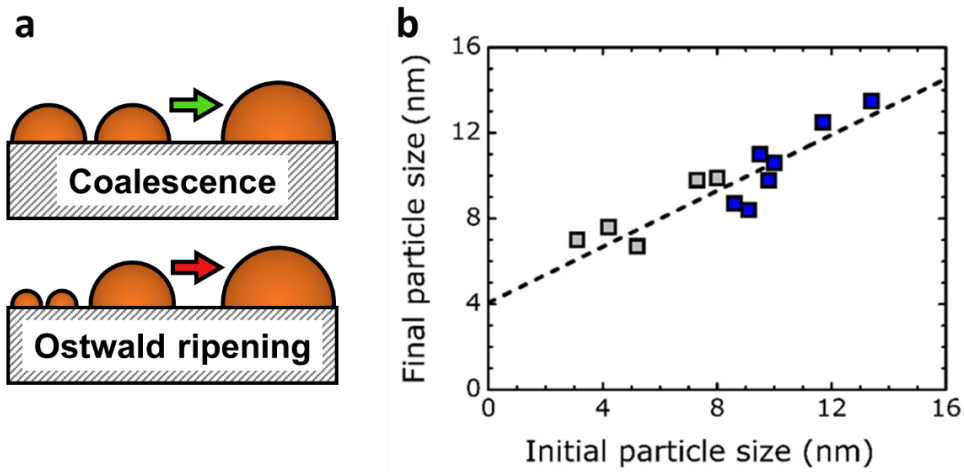

***Figure 4.3: a**) Schematic illustration of the two main mechanisms for particle growth, through coalescence and Ostwald ripening; **b**) Correlation between the initial and final Cu surface-averaged particle sizes after 150 h on stream, for the Cu/C catalysts prepared using pristine carbon (blue) or surface-oxidized carbon (gray) as the support.*

The relationship between turn-over frequency (TOF) and Cu particle size is displayed in Figure 4.4. Both the initial and final Cu particle sizes were correlated to the activities after the 30 and 150 h on stream, respectively. Limited particle growth is expected during the initial activation period of 30 h at 180 °C, since particle growth is known to be accelerated at elevated temperatures. The good correlation between initial and final TOF values around the same Cu particle same validate our approach, and allow us to determine the TOF from 3 to 14 nm. The TOF increased around 4-fold for increasing Cu particle size from 3 to 10 nm, *i.e.* $0.6*10^{-3}$ s^{-1} for the 3 nm Cu particles, up to $2.0*10^{-3}$ s^{-1} for 10 nm Cu particles. For Cu particles above 10 nm, the TOF was size-independent. This is the first report on the Cu particle size effects for EtOAc hydrogenation, and it demonstrates that the reaction is sensitive to the Cu particle size below 10 nm. A similar 4-fold increase in activity with increasing Cu particle size below 10 nm was observed in Chapter 3 for the Cu-catalyzed methanol synthesis reaction. Even though the EtOAc, CO and CO_2 reactants are distinctly different in chemical nature, the proposed rate-determining steps are quite similar, *i.e*. hydrogenation of the acyl intermediate for EtOAc hydrogenation[99, 105] and formate hydrogenation in methanol synthesis.[125] These similar trends suggest a common active site for both reactions. Interestingly, the Cu particle size effects are moderate compared to the ~10-fold increase in Fischer-Tropsch activity for increasing Co particle size from 2 to 6 nm,[187] and ~10-fold increase in ammonia synthesis activity for Ru particles increasing from 1 to 6 nm.[13, 238] For the Fischer Tropsch and ammonia synthesis reactions, the rate-determining steps are not surface hydrogenation reactions, but rather the dissociation of CO and N_2, respectively. These findings show that the chemical reactivity does not only depend on the nature

of the active site, but is also correlated to the nature of the intermediates for the rate-determining step.[13]

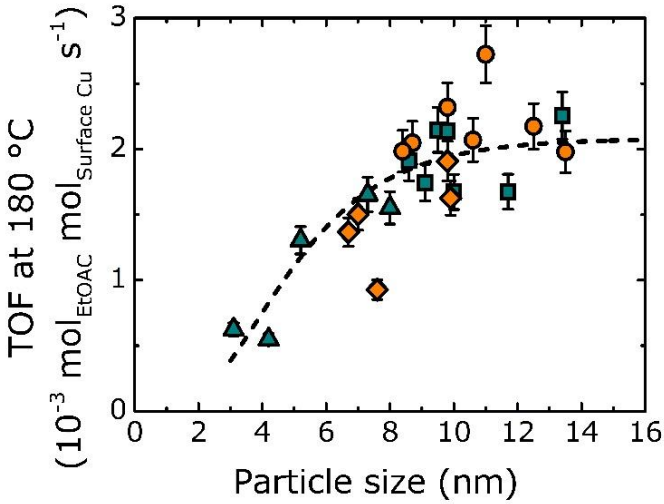

Figure 4.4: *Turn-over frequencies (TOF) 180°C and 30 bar(g), as a function of the surface-averaged Cu particle size. Both TOF after 30 h on stream (cyan symbols) and after 150 h on stream (orange symbols) are displayed as independent data points, which were correlated to the Cu particle size of the fresh and used catalysts, respectively. The Cu catalysts were prepared using either pristine graphite (circle and square symbols) or surface-oxidized graphite (triangle and diamond symbols) as the support material. An exponential curve was fitted as a trendline for the TOF values. The error bars represent the relative standard deviation in TOF, which was only 8 % and therefore error bars may lie behind the data markers. Reaction gas mixture as H_2:EtOAc:He in 10:1:1 molar ratio.*

The Cu/C catalysts were significantly more active than previously reported un-promoted Cu catalysts. For example, Lu and co-workers described TOF values of just $0.8*10^{-3}$ s^{-1} at 280 °C, for 13–23 nm Cu catalysts supported on SiO_2, Al_2O_3 and ZrO_2,[136] while we measured TOF between $0.2–2.2*10^{-3}$ s^{-1} at 180 °C. The different synthesis methods may play a crucial role. The Cu catalysts on SiO_2, Al_2O_3 and ZrO_2 were prepared using Na_2SiO_3 and Na_2CO_3 reagents,[136] whilst it is known that Na^+ may poison the Cu surface in hydrogenation reactions.[239] Another explanation for the higher TOF in this study may be the water content in the EtOAc reactant. Karl Fischer titration showed that the water concentration in our study was less than 50 ppm. The purity of the EtOAc feed can have a strong influence on the catalytic performance,[19, 146] and may explain the superior activity of the Cu/C catalysts under our experimental conditions.

Origin of Cu particle size effect. In general, particle size effects may be caused by size-dependent changes in the electronic nature, metal-support interactions and the particle surface structure. All Cu/C catalyst contained Cu particles of 2 nm or larger, for which electronic support effects are expected to be negligible.[15] Moreover, carbon only weakly interacts with the Cu particles. Therefore, metal-support interaction is an unlikely origin of the observed particle size effects. We evaluated the catalyst reducibility, by H_2 temperature-dependent reduction analysis on the passivated Cu/C catalysts (Figure 4.5a). All catalysts were completely reduced to Cu^0/C at 200 °C under a flow of 5 vol% H_2/Ar. The largest change in the reduction temperatures was observed for increasing Cu particle size from 3 to 5 nm (Figure 4.5b). Above 5 nm, the reduction temperatures did not strongly change. Hence, it is unlikely that the reducibility explains the observed Cu particle size effect.

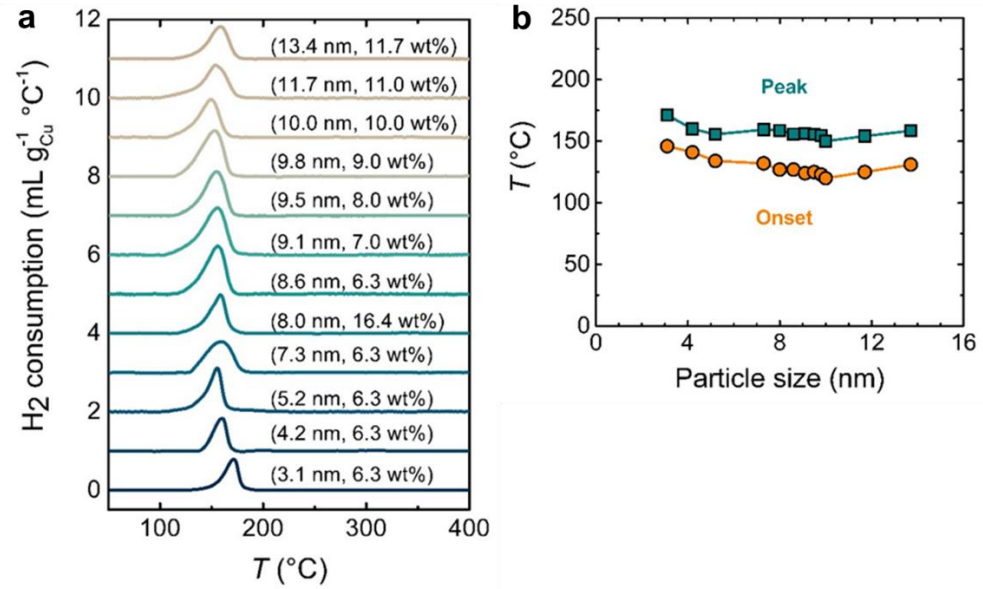

***Figure 4.5: a**) Temperature-dependent H_2 reduction profiles for the Cu/C catalysts with Cu particle size between 3 and 13 nm; **b**) Overview of onset and peak temperatures. The reduction profiles were normalized to the amount of Cu per measurement and acquired at 2 °C min^{-1} under a flow of 5 vol% H_2/Ar.*

Next, we examined the role of water. In our experiments, the formation of ethane (<0.5 % product selectivity) coincided with water production (<100 ppm in the gas-phase). The ratio between the partial pressures of water and H_2 was hence less than 0.001. Oxidation of the Cu^0 catalyst to CuO may lead to deactivation.[10, 19] We simulated the thermodynamically equilibria of Cu oxidation states under reactions conditions, *i.e.* at 30 bar(g) and 180 °C. First we assuming a molar reactant ratio in Cu:H_2:EtOAc:H_2O:He of $1:10^3:10^2:10^{-2}:10^2$ to calculate thermodynamic equilibria compositions regarding Cu^0:Cu_2O:CuO. These conditions were applied to mimic the

reaction conditions. Accordingly, the Cu^0:Cu_2O:CuO composition was found to be of the order 1: 10^{-5}: 10^{-6}. The Cu catalysts will thus be predominantly present in the Cu^0 oxidation state, with less than 1 in 10^5 Cu atoms present as Cu^+ or Cu^{2+}. Although the fraction is likely higher for nanoparticulate Cu, the results suggest that electronic effects are unlikely to explain the particle size dependence in catalytic activity.

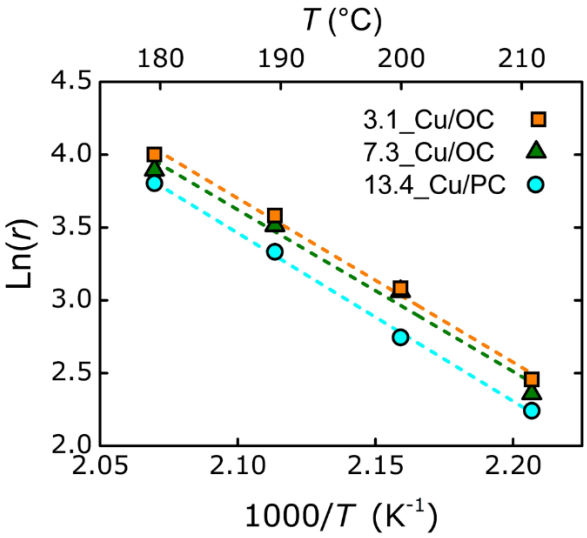

Figure 4.6: *Arrhenius plot for three representative Cu/C catalysts of varying Cu particle size, with r expressed as the weight-normalized CTY in* $mmol_{EtOH}\ g_{Cu}^{-1}\ h^{-1}$.

The apparent activation energy (E_a) was calculated using the Arrhenius model (Figure 4.6). In order to determine the E_a, it is important to consider the reaction kinetics. From literature it is known that for a 10-fold excess of H_2 over EtOAc, between 190–300 °C, the reaction orders with respect to both H_2 and EtOAc were close to zero, indicating a saturated surface coverage.[125, 133, 141, 232] Accordingly, a zeroth order dependency of the EtOAc concentration on the reaction rate was assumed. The E_a was determined from rates (rather than rate constants) over the temperature range of 180–210 °C. We used the EtOAc conversion at the final stage at 180 °C (after 150 h) to minimize the influence of the catalyst activation behavior. The E_a was calculated independently as a function of both the initial and final particle sizes (Figure 4.7a). The apparent E_a ranged between 89–103 kJ mol^{-1}, with an average value of 94 kJ mol^{-1}. Fascinatingly, the E_a for the Cu/C catalyst was hence found to be independent of the Cu particle size. Although the exact value of E_a depends on specific reaction conditions such as temperature and pressure, the results for Cu/C are in good agreement with reported values of 74 kJ mol^{-1} for Cu/ZrO_2,[139] 107 kJ mol^{-1} for Cu/SiO_2 ,[141] 88 kJ mol^{-1} for Raney Cu [232] kJ mol^{-1} and 119 kJ mol^{-1} for macroscopic Cu.[133] This confirms that electronic effects scaling with

size are not the cause of the Cu particle size effects, but that they must rather be due to an increase in relative abundance of the active sites with increasing size.

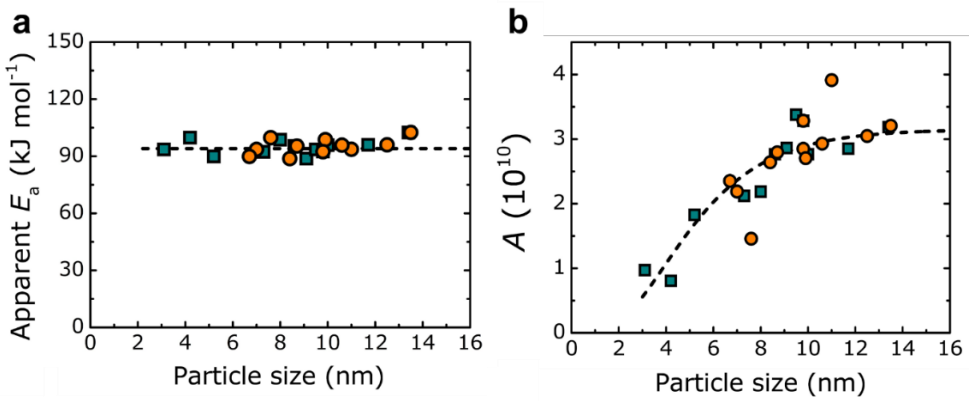

***Figure 4.7: a**) Apparent activation energy (E_a) and **b**) pre-exponential factor (A) displayed as a function of the surface-averaged Cu particle size. The A values were derived from the Arrhenius model using r as the surface-normalized reaction rate, i.e. $mmol_{EtOH}\ m_{Cu}^{-2}\ h^{-1}$. The E_a and A values were displayed both after 30 h on stream (cyan squares) and after 150 h on stream (orange circles), as independent data points. Reaction conditions: H_2:EtOAc:He = 10:1:1 molar ratio, 180–210 °C and 30 bar(g).*

We also calculated the pre-exponential factor (*A*), which can be correlated to the number of active sites for catalysis, assuming that their nature does not change with size (Figure 4.7b). The value of *A* was derived from the Arrhenius model using the surface-normalized CTY, defined as $mmol_{EtOH}\ m_{Cu}^{-2}\ h^{-1}$ and using an averaged E_a of 94 kJ mol^{-1}. An approximate 4-fold increase in *A* was observed for Cu particles from 3 to 10 nm ($0.8*10^{10}$ to $3.2*10^{10}$), correlating to the 4-fold increase in TOF for the same particle size range. This indicates the presence of a well-defined and size-independent active Cu site responsible for EtOAc conversion, for which the abundance increased with increasing particle size up to around 10 nm.

Nature of the active site. To evaluate the nature of the catalytic site, we need to consider the Cu surface structure. The particle shape and surface structure of face centered cubic metal nanoparticles are known to be size-dependent.[185, 188, 227] To describe the complete surface nature of Cu particles up to 16 nm, we extrapolated the models by Van Hardeveld[185] and Van Helden[188] for front facing cubic metal structures. The Cu surface mainly consists of (111) and (100) facets with exposed terrace sites, but also exhibits different defects sites with lower coordination numbers such as corner, edge, step and kink sites. In general, the surface sites with the lowest coordination numbers exhibit the highest adsorption strengths.[197] The different surface sites therefore may have distinctly different chemical reactivities.

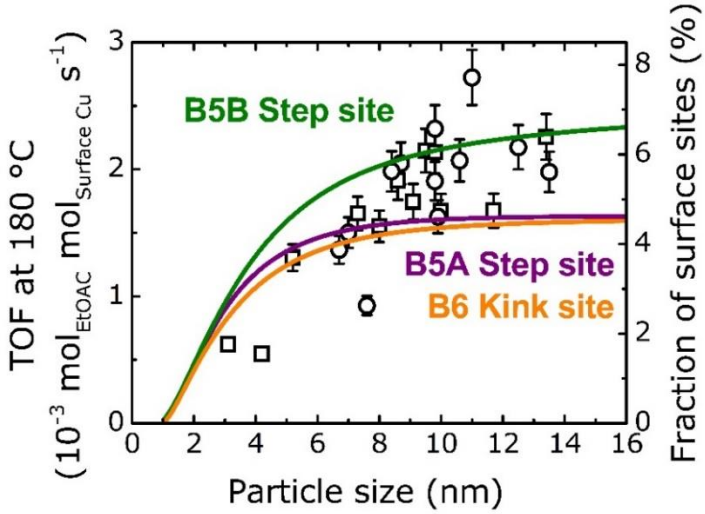

Figure 4.8: *Turn-over frequencies (TOF) and the theoretical fraction of Cu step and kink surface sites, as a function of the surface-averaged Cu particle size. Both TOF after 30 h on stream (empty squares) and after 150 h on stream (empty circles) are displayed as independent data points, which were correlated to the Cu particle size of the fresh and used catalysts, respectively. The error bars represent the relative standard deviation in TOF, which was only 8 % and therefore error bars may lie behind the data markers. Reaction gas mixture as H_2:EtOAc:He in 10:1:1 molar ratio. The fractions of the different Cu surface sites were calculated by extrapolation of the particle models by Van Hardeveld[185] and Van Helden[188] for fcc metals.*

We compared the size-dependence of the TOF with the abundance of each type of surface site. The fractions of corner and edge sites decreased with increasing Cu particle size above 2 nm, and were therefore excluded as the active site for the hydrogenation reaction. The corner and edge sites are likely too small to accommodate both dissociated hydrogen and the oxygenate intermediates.[13, 15, 240-241] The fractions of Cu (111) and Cu (110) terrace sites steeply increased with increasing Cu particle size up to around 6 nm, and are hence unlikely to strongly contribute to the catalytic activity. Interestingly, the fraction of step and kink sites gradually increases up to around 8 to 10 nm, thus closely matching the experimental TOF values. (Figure 4.8). The B5A step, B5B step and B6 kink sites can be found at the interface of different Cu (111) and Cu (100) planes, which represent the geometrical equivalent of higher Miller index Cu (311), Cu (221) and Cu (321) surfaces, respectively.[185, 188] The differences between the theoretical fraction of step and kink sites and experimental TOF values may originate from structural deviations between the free-standing particle models and actual supported Cu particles under reaction conditions. In line with Sabatier's Principle, we propose that these sites with intermediate coordination saturation and adsorption strength are responsible for activity in Cu-based hydrogenation catalysis.

This is the first systematic investigation of the impact and origin of Cu particle size effects for the hydrogenation of EtOAc. Investigating the nature of the active site for the Cu-catalyzed hydrogenation reaction, was greatly facilitated here by using carbon as a support material. We showed that the relative abundance of step sites scales with both our measured pre-exponential factor in the Arrhenius model and TOF values, and therefore propose structure sensitivity as the origin of the observed Cu particle size-activity relationships. A maximum conversion was obtained with Cu particles of around 6 nm, which may guide optimization strategies for Cu-based catalysts in a plethora of hydrogenation reactions.

4.4 Conclusions

In this chapter, the effects of Cu particle size between 3 and 14 nm were investigated for the hydrogenation of ethyl acetate. High surface area graphite was used as an inert catalyst support, to investigate the intrinsic Cu particle size effects. The catalysts with Cu particles of 8 nm or larger were the most stable in this study. The TOF increased approximately 4-fold when increasing the Cu particle size from 3 to 10 nm, and became size-independent for particles above 10 nm. The apparent activation energy was independent of the Cu particle size, suggesting that the nature of the active site did not change with Cu particle size. However, the pre-exponential factor in the Arrhenius model suggested that relative abundance of the active site increased with Cu particle size up to 10 nm, which was ascribed to a size-dependent increase in the fraction of step and kink surface sites. A maximal yield was obtained with Cu particles of around 6 nm, giving an optimal balance between intrinsic activity and available surface area as a function of Cu particle size.

Acknowledgements

Lennart Weber, Remco Dalebout, Jan Willem de Rijk, Neil Sainty and Roy Partington are acknowledged for providing technical support in the catalytic experiments.

Chapter 5
Manganese Oxide Promoter Effects in Ethyl Acetate Hydrogenation

This chapter is based on the publication: "*Manganese Promoter Effects in Copper-Catalyzed Hydrogenation of Ethyl Acetate"* by R. Beerthuis, N. L. Visser, J. E. S. van der Hoeven, J. M. S. Deeley, G. J. Sunley, K. P. de Jong and P. E. de Jongh, Under review.

Abstract

In this chapter, manganese oxide is discussed as an efficient promoter for the Cu-based hydrogenation of ethyl acetate. A series of nanoparticulate MnO_x-Cu catalysts was prepared by incipient wetness impregnation of a high surface area graphitic carbon support. Tuning the synthesis parameters allowed us to keep the MnO_x-Cu particle size constant around 6 nm, while varying the Mn loading between 0 and 33 mol% Mn(Cu+Mn), without changing the Cu loading or support structure. Under industrially-relevant temperatures (180–210 °C) and pressure (30 bar), the presence of 11 mol% Mn to Cu gave a 7-fold enhancement in activity, while also boosting catalyst stability and maintaining high selectivity towards ethanol as compared to an un-promoted Cu catalyst. The MnO_x promoter effect on Cu-based activity was attributed to a lower energy barrier of the rate-determining step at the MnO–Cu interface, as apparent from a drop in the apparent activation energy from ~100 to 50 kJ mol^{-1}. Varying the water concentration in the ethyl acetate feed showed that the MnO_x promoter significantly enhanced the resistant against water-induced deactivation. Below 11 mol% Mn loading, the activity increased during catalysis, due to the diffusion of mobile Mn species as evidenced by HAADF-STEM. However, higher Mn loadings led to higher Mn oxidation states as evidenced by XANES and to catalyst deactivation over time, which was attributed to Mn diffusion and partial coverage of the Cu particles. An intermediate Mn loading (11 mol%) provided an exceptional combination of high activity, selectivity and stability.

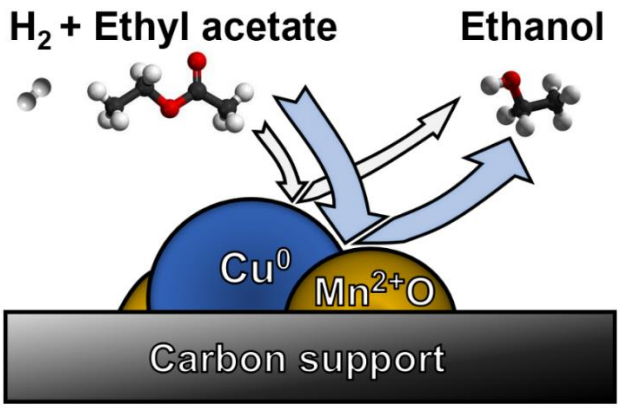

5.1 Introduction

Supported metal catalysts are widely applied for industrial hydrogenation reactions, with added metal oxide promoters to boost the performance.[59, 134, 137, 177] Promoters are defined as species that exhibit little or no activity alone, but that improve the catalytic performance when added to a catalytically active phase.[172] Copper chromite catalysts are heavily used for industrial hydrogenation reactions.[137, 242-243] However, carcinogenic Cr^{5+} and Cr^{6+} species may form during catalyst manufacturing and regeneration,[244] and environmental legislation therefore enforces the implementation of more environmentally-friendly alternatives. Early studies by Brands *et al*. indicated manganese oxide (MnO_x) as a promising promoter in the hydrogenation of alkyl esters, yet the MnO_x promoter effects for Cu are still poorly understood.[133, 137, 176]

In this chapter, we investigated the impact of the structural and electronic properties of MnO_x-promoted Cu catalysts on the activity, selectivity and stability in the hydrogenation of ethyl acetate towards ethanol (Eq. 1.4 in Chapter 1 of this thesis). High surface area graphitic carbon was applied as a chemically inert support material to investigate the intrinsic promoter effects and optimal loading for MnO_x. The catalyst performance is evaluated under industrially relevant temperatures and pressure (180–210 °C and 30 bar).[133, 139, 141, 232] In Chapter 4, the Cu particle size effects for the hydrogenation of ethyl acetate were discussed, which showed that the highest conversion was obtained using Cu particles around 6 nm.[86] Therefore, a MnO_x-Cu particle size of 6 nm was targeted, while systematically varying the Mn loading. The developed methodologies for catalyst preparation and combination of state-of-the-art characterization techniques allowed us to study the promoter effects in-depth, which is important in guiding the rational design of promoted catalysts for a broad range of reactions.

5.2 Experimental methods

Catalyst preparation

A series of manganese oxide-promoted carbon-supported copper (MnO_x-Cu/C) catalysts was prepared, using high surface area graphitic carbon as the catalyst support (Graphene nanoplatelets (GNP-500 from XG Sciences), with ~500 m^2 g^{-1} BET surface area and 0.84 mL g^{-1} total pore volume). First, the support was dried in a round-bottom flask for 90 min at 170 °C, while stirring under dynamic vacuum, and subsequently stored in an Ar-filled glovebox (Mbraun LABmaster, <0.1 ppm H_2O, <0.1 ppm O_2) until further use.

Aqueous precursor solutions of $Cu(NO_3)_2$ and/or $Mn(NO_3)_2$ were prepared by dissolving the copper nitrate ($Cu(NO_3)_2$•$3H_2O$, Acros Organics, ≥99 %) and manganese nitrate ($Mn(NO_3)_2$•$4H_2O$, Sigma Aldrich, ≥97.0 %) precursor salts in de-ionized water. The solutions were acidified using 0.10 M nitric acid ($HNO_{3\,(aq)}$, Merck,

65 %) to ensure a pH ≤1. The concentrations of $Cu(NO_3)_2$ and $Mn(NO_3)_2$ in the precursor solution were adjusted to control the Cu and Mn loadings in the final catalyst. In a typical synthesis procedure, ~2 g of dried carbon powder was impregnated to incipient wetness, in a round-bottom flask under static vacuum. The volume of the impregnation solution was approximately 95 % of the total pore volume by N_2 physisorption analysis. The solution was added dropwise by syringe through a rubber septum, under vigorous stirring. The Cu loading was kept constant around 8 wt%, while varying the Mn loading between 0 and 3.4 wt%, resulting in a mol/mol ratio of Mn/(Cu+Mn) between 0 and 33 mol% Mn/(Cu+Mn). A Cu-free MnO_x/C sample was prepared using the same synthesis method.

The impregnated sample was stirred for 24 h to homogenize the Cu and Mn content. Next, the impregnated sample was dried during 24 h at room temperature, while stirring and under dynamic vacuum. The dried catalyst precursor was transferred to an Ar-filled glovebox, and subsequently loaded into a plug-flow reactor, without exposure to air. The dried sample was heated to 230 °C (0.5 °C min^{-1}) with 1 h isothermal hold at 230 °C, under a flow of N_2 (0.1 mL min^{-1} mg^{-1}). Thermogravimetric analysis indicated the complete removal of the nitrate residues at this temperature, as observed from the disappearance of the nitric oxide (NO, M/Z = 30) signal as followed by mass spectrometry. After letting the sample cool down to room temperature, it was purged for 3 h with a flow of 10 vol% O_2/N_2 (0.1 mL min^{-1} mg^{-1}). Subsequently, the sample was purged for 30 min with N_2 to remove any residual O_2 and heated to 170 °C (2 °C min^{-1}), with 2 h isothermal hold at 170 °C, under a flow of 10 vol% H_2/N_2 (0.1 mL min^{-1} mg^{-1}) and finally heated to 400 °C (2 °C min^{-1}), with 1 h isothermal hold at 400 °C. After letting the catalyst cool down to room temperature, it was transferred to an Ar-filled glovebox, without exposure to air, to allow for XRD characterization of the reduced catalysts. Finally, the catalyst was collected by slowly passivating it in air.

Catalyst characterization

Transmission electron microscopy (TEM) was performed on an FEI Tecnai 20 microscope, operated at 200 kV. The catalysts sample was dispersed as a dry catalyst powder, onto a Cu sample grid coated with holey carbon (Agar 300 mesh Cu). The particle size was measured for at least 250 individual particles and on 10 different sample areas. The number-averaged Cu particle sizes (d_n) and surface-averaged Cu particle sizes (d_s), including the standard deviations in the widths of the particle size distributions (σ_{dn} and σ_{ds}), were calculated using the formulas $d_{\mathrm{n}} \pm \sigma_{d\mathrm{n}} = \frac{1}{N}\sum_{\mathrm{i}=1}^{N} d_{\mathrm{i}} \pm \sqrt{\frac{1}{N}\sum_{i=1}^{N}(d_n - d_i)^2}$ and $d_{\mathrm{s}} \pm \sigma_{ds} = \frac{\sum_{\mathrm{i}=1}^{N} d_{\mathrm{i}}^3}{\sum_{\mathrm{i}=1}^{N} d_{\mathrm{i}}^2} \pm \sqrt{\frac{1}{N}\sum_{i=1}^{N}(d_s - d_i)^2}$, in which d_i indicates the diameter of the ith particle and N stands for the total count of measured particles.

Scanning transmission electron microscopy (STEM) was carried out at an FEI Talos F200X operated at 200 kV. The catalysts sample was dispersed as a dry catalyst powder, onto a Ni sample grid coated with holey carbon (Agar 300 mesh Ni). The images were acquired in high-angle annular dark-field (HAADF) mode. Energy-dispersive X-ray spectroscopy (EDX) mapping was performed to analyse the distribution and amount of the Mn, Cu and C content in the catalyst before and after catalysis. The Mn and Cu distribution was analysed by acquiring high resolution EDX maps at high magnification (910,000–1,300,000 times) using a probe current of around 700 pA and total map acquisition time of 800–1,000 s to obtain sufficient EDX signals for Cu and Mn. To determine the average metal composition, EDX maps were acquired at a much lower magnification (40,000–60,000 times) and concentrations quantified using the Cliff-Lorimer method. The high resolution EDX intensity maps were used to characterize the distribution of Mn and Cu in the samples. To this end, the EDX intensity maps were analysed as line scans in the direction perpendicular to the Cu-Mn interface.

X-ray diffractometry was performed on a Bruker D8 powder X-ray diffractometer equipped with a Co-$K_{\alpha 1,2}$ radiation source (λ = 1.79026 Å) and a Lynxeye detector. Diffractograms were taken directly after the final step in the synthesis under reductive atmosphere, without exposure to air. The reduced catalyst was loaded into an airtight XRD specimen holder (A100B33, Bruker AXS) inside an Ar-filled glovebox (Mbraun LABmaster, <0.1 ppm H_2O, <0.1 ppm O_2). Diffractograms were continuously acquired with 0.1 °2θ increment between 5 and 95 °2θ, in approximately 2 to 3 h. The diffractograms were normalized to the peak intensity of the graphitic (002) diffraction peak at 30.9 °2θ and carbon baseline subtracted. A bi-modal Cu crystallite size distribution was observed for several MnO_x-Cu/C catalysts. The presence of larger Cu crystallites (>20 nm) was attributed to slight over-impregnation during catalysts synthesis. Since no bulk particles were observed by TEM analysis, any particles >20 nm were neglected in the Cu size analysis. The Cu^0 crystallite size was determined by applying the Scherrer equation to the Cu^0 (200) diffraction peak at (59.3 °2θ), with a shape factor *k* of 0.1.[234]

Thermogravimetric analysis was performed on a PerkinElmer Pyris 1 balance, coupled to a Pfeiffer mass spectrometer. The sample (5–10 mg) was first purged for 30 min at 50 °C and subsequently heated to 600 °C (5 °C min^{-1}), under a flow of Ar (20 mL min^{-1}).

Temperature-programmed reduction profiles were measured on a Micromeritics Autochem II ASAP 2920 apparatus, with H_2 consumption quantified using a thermal conductivity detector. Prior to the measurement, the catalysts were dried for 30 min at 120 °C under Ar flow (~1 mL min^{-1} mg^{-1}) and afterwards the temperature was lowered to 50 °C. Next, the reduction profiles were determined by heating the catalyst to 400 °C (2 °C min^{-1}), in a flow of 5 vol% H_2/Ar (~1 mL min^{-1} mg^{-1}). The

reduction profiles were base-line corrected and normalized to the amount of Cu per measurement.

X-ray absorption spectroscopy (XAS) data was acquired in transmission mode at the XAFS (BM26A) Dubble beamline at ESRF. The passivated sample was pelleted and placed inside a stainless-steel *in situ* cell, equipped with Kapton foil windows. The sample was surrounded by a tubular furnace for temperature control. The measurement cell was connected to a gas manifold to control the gas flow and composition. The XAS data were recorded near the Mn K-edge (6,340–7,890 eV) or Cu K-edge (8,779–9,629 eV) during separate experiments, using fresh pellets for each measurement. All data were acquired under continuous gas flow of either pure He or 4 vol% H_2/He (~1 mL min^{-1} mg), at ambient pressure. The sample was initially purged with He at room temperature for 15 min, before acquiring XAS data to analyze the passivated sample. Next, the gas flow was exchanged for 4 vol% H_2/He and purged for 15 min at room temperature. Subsequently, the temperature was increased to 250 °C (5 °C min^{-1}), with 1 h isothermal hold at 250 °C, and a final XAS spectrum of the reduced catalysts was recorded. Reference spectra were recorded using commercial Cu foil, Cu_2O, CuO, MnO, Mn_2O_3 and MnO_2 standards. The XAS data was analyzed using Athena data processing software.[245] The average Cu oxidation state was calculated by linear combination fitting of the XANES between 8,790–9,010 eV. The Cu–Cu coordination number ($CN_{Cu–Cu}$) was calculated by fitting the first shell Cu–Cu scattering from the EXAFS spectra after *in situ* reduction. The average Mn oxidation states were calculated using the method developed by Johnson *et al*., which uses a linear correlation between Mn oxidation state values and the energy of the pre-edge feature.[174]

The collected EXAFS spectra were background corrected and analyzed using the Athena software package. The Cu coordination number ($CN_{Cu–Cu}$), the difference of the Debye−Waller factor with respect to the reference ($\Delta\sigma^2$), the correction of the threshold energy (ΔE_0) and the Cu−Cu distance (R) were treated as free parameters during the fitting. The amplitude reduction factor (S_0^2) of 0.855 for Cu was obtained by fitting the EXAFS data of the Cu foil reference, with $CN_{Cu–Cu}$ defined as 12.0 for bulk Cu. The structural parameters were determined by multiple *k*-weight fitting within a distance fit range between 1.4-3.0 Å. The quality of the fit was evaluated by visual comparison of the magnitude and imaginary part of the Fourier transform, which indicated good agreement between experimental and fitted data for samples. An overview of the EXAFS fitting parameters is given in Table 5.1.

Table 5.1: EXAFS fitting parameters for several representative MnO_x-Cu/C catalysts, after reduction at 250 °C under 4 vol% H_2/He flow.

Sample	CN_{Cu-Cu}	$\Delta\sigma^2$ (*10^{-3})	E_0 (eV)	R (Å)
Cu foil (ref.)	12.0	8.44	4.16	2.54
0_MnO_x-Cu/C	11.3	9.60	3.56	2.54
4.8_MnO_x-Cu/C	10.4	10.20	3.17	2.53
11_MnO_x-Cu/C	10.8	9.80	3.35	2.53
20_MnO_x-Cu/C	10.2	10.46	3.18	2.53

Catalysis

Catalytic experiments were performed using a gas-phase fixed-bed reactor system, equipped with 16 parallel channels (Flowrence®, Avantium N. V.). The catalysts were pelletized (2 cm diameter) using a hydraulic press at 1,500 kgf, equivalent to 460 bar pressure, ground and sieved to obtain a granulate size of 75–150 μm. The catalysts were diluted with SiC granulates (212–425 μm), to maintain the volume of the diluted catalyst bed constant (~3.0 mL). The SiC diluent was pre-treated by washing with HNO_3(aq) (68%; 10 mL g_{SiC}^{-1}) and calcined at 800 °C, to remove organic and metal impurities. The diluted catalyst was loaded into a stainless-steel tubular reactor (2.6 mm inner diameter) on top of SiC granules (0.5 mL), which were pre-loaded onto a stainless-steel frit. A hollow glass wool filament (~ 10 cm) was placed in the head space above the catalyst bed, up to the entrance of the reactor, to ensure continuous evaporation of the EtOAc reactant. The GHSV, as calculated by using the packing density of the undiluted catalyst, was varied between 2,000 to 17,000 h^{-1}.

The MnO_x-Cu/C catalysts were purged for 1 h with pure He (2 mL min^{-1} per reactor) and subsequently re-reduced *in situ* by heating to either 200 °C (for the Mn-free 0.0_MnO_x_Cu/C catalyst) or to 250 °C (2 °C min^{-1}), with 2 h isothermal hold at the final temperature, under a flow of 20 vol% H_2/He (2 mL min^{-1} per reactor). Afterwards, the temperature was lowered to 140 °C and the reactor was purged for 2 h with 9 vol% H_2/He (6.2 mL min^{-1} per reactor). Next, the EtOAc feed was introduced (0.6 mL min^{-1} per reactor). The concentration of water in the EtOAc feed was determined by Karl Fischer titration, using standard method ASTM D 1364. The reaction gas mixture consisted of H_2:He:EtOAc in a 10:1:1 molar ratio (6.8 mL min^{-1} per reactor). Next, the pressure was gradually increased during 75 min to 30 bar(g). Finally, the reactor temperature was increased to either 180 °C or 200 °C (2 °C min^{-1}), to start the catalytic experiment. Between isothermal stages at 180–210 °C, the temperature was increased with 1 °C min^{-1}. After the reaction, the temperature was lowered to 90 °C and the catalysts were passivated by overnight exposure to air at this temperature. The effluent gas composition was analysed by on-line gas

chromatography at 19 min intervals (GC, Agilent 7890B). He and H_2 were separated on a MolSieve 5A column (2.4 meter x 1/8 inch inner diameter) and quantified analyzed using a thermal conductivity detector. Hydrocarbons and oxygenates were separated on a HP-Innowax column (6 m x 0.32 mm ID) and GS-GasPro column (GS-Gaspro 30 m x 0.32 mm ID), and quantified by two separate flame ionization detectors. The analyte concentrations were calculated from the peak areas, using He as the internal standard.

The Cu weight-normalized time yield (CTY, $mol_{EtOAc}\ g_{Cu}^{-1}\ h^{-1}$) was used to calculate the turn-over frequency (TOF, $mol_{EtOAc}\ mol_{surface\ Cu}\ s^{-1}$) using the formula: CTY*M_{Cu}/D_{Cu}, in which M_{Cu} stands for the molecular weight of Cu and D_{Cu} the fraction of surface Cu atoms. The value of D_{cu} is calculated from the Cu d_s, assuming fully accessible and spherical particles using the formula $6*(V_{Cu}\ A_{Cu}^{-1})/d_s$. Herein, A_{Cu} is the molar area occupied by surface Cu atoms ($4.10*10^{22}$ nm^2) and V_{Cu} is the molar volume occupied by bulk Cu atoms ($7.09*10^{21}$ nm^3). D_{Cu} is thus calculated as $1.04/d_s$, with d_s in nm.[172] Herein, we relied on TEM to calculate the surface-averaged particle size and determine the Cu surface area. TEM is considered a reliable technique to determine the Cu particle size and estimate the Cu surface area.[86] Other characterization techniques, such as N_2O and H_2 chemisorption, were found to also probe metal oxide defect sites,[223] thus rendering them unsuitable for the MnO_x-promoted catalysts. The initial TOF at 180 °C was determined after around 30 h on stream, and calculated from the Cu d_s of the fresh Cu/C catalyst. The final TOF at 180 °C was calculated after 150 h on steam, and calculated from the Cu d_s of the used catalyst. To be concise, the initial reaction times are referred to as 30 and 150 h on stream, yet precise reaction times may vary ±2.5 h depending on GC sampling time.

The activation energies (E_a) were determined from the slope of a linearly fit line through the ln(r) values in the Arrhenius plot. Herein, the reation rate r was defined as CTY ($mmol_{EtOH}\ g_{Cu}^{-1}\ h^{-1}$), at conversions of ethyl acetate <25 %. In the Arrhenius model, the CTY at 180 °C was determined from the final isothermal stage, to minimize the influence of initial activation during the first 30 h on stream. In our calculations, a zero order dependency of CTY on EtOAc concentration was assumed, based on the 10:1 molar excess of H_2 over EtOAc.

The relative standard deviation in TOF (σ_{TOF}) was determined by testing 12 reactors with the same loading of a commercial co-precipitated $CuZnMgO_x/Al_2O_3$ catalyst (Alfa Aesar). Herein, σ_{TOF} was defined as the typical distance of a data point (χ) from the mean value (μ) and calculated by the formula $\sigma_{\mathrm{TOF}} = \sqrt{\left(\frac{1}{N-1}\right)\sum_{i=1}^{N}(\chi_{\mathrm{i}} - \mu)^2}$ and found to be approximately 8 %. To corroborate that the reaction was not mass transfer limited, we performed measurements with Cu/C catalysts of different granulate size ranges, *i.e.* 75–150 µm, 150–425 µm and 425–630 µm. No significant

differences in conversions were observed, indicating that the reaction was not hindered by internal or external mass transfer limitations. Two measurements using the bare carbon support and SiC diluent showed no conversion at 210 °C.

5.3 Results and Discussion

Structural properties of MnO_x-Cu catalysts. Transmission electron micrographs (TEM) and particle size distributions for two representative MnO_x-Cu/C catalysts are shown in Figure 5.1a and 1b. In all cases, bright-field TEM analysis showed highly dispersed nanoparticles, mainly situated on the edge positions of the graphitic carbon sheets. This is further supported by the broad Cu^0 diffraction peaks in the powder X-ray diffractograms for all reduced MnO_x-Cu/C catalysts (Figure 5.1c). Moreover, the absence of diffraction peaks between 40 and 45 ° 2Θ indicates that no crystalline manganese oxide phases were present for any MnO_x-Cu/C catalyst. Table 5.2 shows that the MnO_x-Cu particle size and Cu^0 crystallite size consistently remained around 5 to 6 nm, even upon increasing the Mn loading from 0 to 3.4 wt%, while keeping the Cu loading around 8 wt%. The catalysts were denoted in this chapter as *X*_MnO_x-Cu/C, in which *X* represents the Mn loading as mol% Mn/(Cu+Mn).

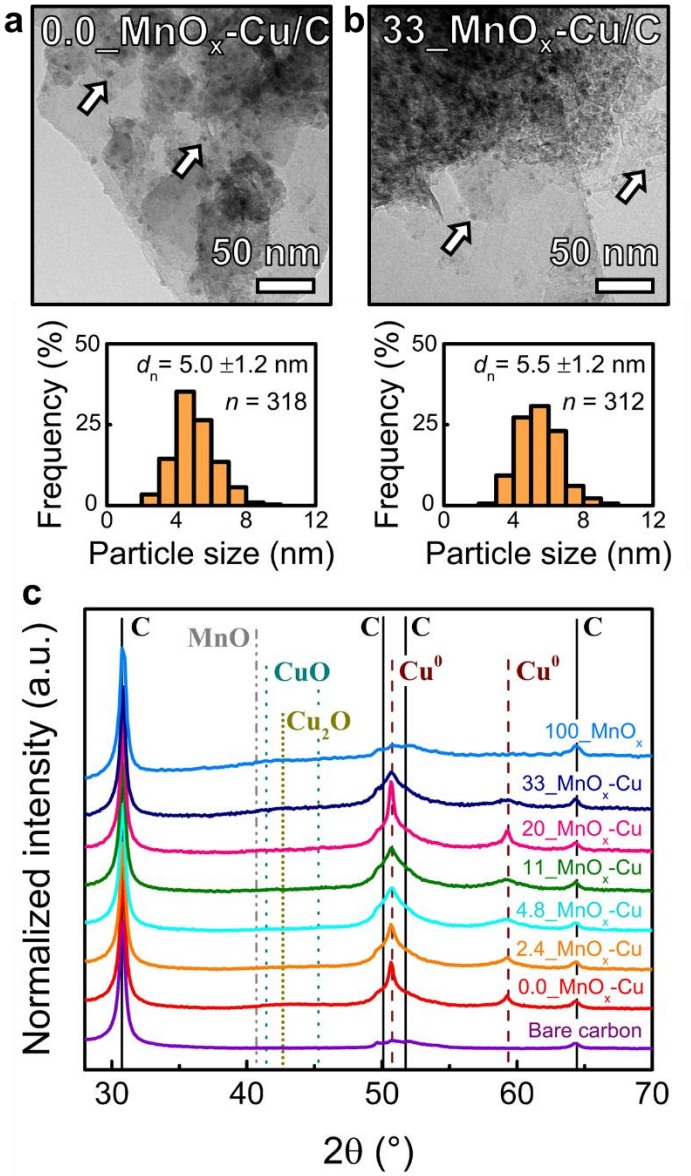

Figure 5.1: *Transmission electron micrographs with arrows indicating some representative MnO_x-Cu nanoparticles, with corresponding particle size distributions and number-averaged MnO_x-Cu particle sizes (d_n), as determined by counting n number of particles, displayed for* ***a)*** *0.0_MnO_x-Cu/C and* ***b)*** *33_MnO_x-Cu/C catalysts;* ***c)*** *Powder X-ray diffractograms of the reduced MnO_x-Cu/C catalysts, the Cu-free (100_MnO_x/C) sample and bare graphitic carbon, stacked with individual offset for visual clarity.*

The size and location of the MnO_x promoter was investigated by energy-dispersive X-ray (EDX) analysis, since Mn and Cu have similar Z-contrast and cannot be distinguished by bright-field TEM analysis. All catalyst showed the presence of distinct Cu nanoparticles of around 5 nm. With increasing Mn loadings, the MnO_X promoter appeared to accumulate as small MnO_x islands in close proximity to the Cu nanoparticles. Additionally, MnO_x was also detected in sub-nanometer species dispersed over the carbon support. The MnO_x islands were smaller than the Cu nanoparticles and therefore gave only a minor contribution to the MnO_x-Cu particle size analysis by bright-field TEM. Quantification of the elemental composition at the nanometer scale indicated 32 mol% Mn for 33_MnO_x-Cu/C and 10 mol% Mn for 11_MnO_x-Cu/C. The local compositions hence corroborated the bulk loadings, and showed homogeneous Cu and Mn distributions throughout the catalysts.

To also study the supported MnO_x promoter, we prepared a Cu-free sample with 7.3 wt% Mn (100_MnO_x/C). TEM showed MnO_x particles of approximately 2.3 nm in size, while XRD analysis did not show any crystalline manganese oxide phases (Figure 5.1c). Hence, a series of well-defined MnO_x-Cu catalysts was synthesized *via* co-impregnation of an inert carbon support with mixed Cu and Mn nitrate solutions. Fine-tuning the synthesis parameters uniquely allowed to prepare similar MnO_x-Cu particle sizes over a wide range of Mn promoter loadings.

Table 5.2: Structural properties for the full series of carbon-supported MnO_x and/or Cu samples.

Catalyst[a]	Cu (wt%)[b]	Mn (wt%)[b]	XRD d_{Cu^0} (nm)[c]	TEM $d_n \pm \sigma_{dn}$ (nm)[d]	TEM $d_s \pm \sigma_{ds}$ (nm)[d]
0_MnO_x-Cu/C	8.7	0	6.9	5.0 ± 1.2	5.6 ± 1.3
2.4_MnO_x-Cu/C	8.7	0.2	6.3	5.3 ± 1.2	5.8 ± 1.3
4.8_MnO_x-Cu/C	8.4	0.4	6.3	5.1 ± 1.3	5.7 ± 1.4
11_MnO_x-Cu/C	8.5	0.9	5.6	5.6 ± 1.3	6.2 ± 1.5
20_MnO_x-Cu/C	8.4	1.8	5.4	5.5 ± 1.7	6.7 ± 2.0
33_MnO_x-Cu/C	7.9	3.4	6.3	5.5 ± 1.2	6.0 ± 1.3
100_MnO_x/C	0	7.3	-	2.3 ± 1.0	3.4 ± 1.6

***a**) Catalysts denoted as X_MnO_x-Cu/C, with X indicating the Mn loading in mol% Mn/(Cu+Mn); **b**) Nominal Cu and Mn weight loadings for the final catalyst; **c**) Cu^0 crystallite size as determined by XRD on the reduced MnO_x-Cu/C catalysts; **d**) Number-averaged MnO_x-Cu particle size ($d_n = \sum_{i=1}^{N} d_i / \sum_{i=1}^{N}$), surface-averaged MnO_x-Cu particle size ($d_s = \sum_{i=1}^{N} d_i^3 / \sum_{i=1}^{N} d_i^2$) and standard deviations in the width of the particle size distributions (σ_{dn} and σ_{ds}), wherein d_i indicates the diameter of the ith particle and N stands for the total count of measured particles.*

Impact of Mn loading on catalyst performance. An overview of the EtOAc conversion as a function of time and at different temperatures, is given for the MnO_x-Cu/C catalysts in Figure 5.2a,b. The conversion typically increased during the first 30 h on stream (at 180 °C). Similar activation periods were previously reported to originate from Cu nanoparticle restructuring and oxidation state changes.[109, 112, 225] The Cu-free 100_MnO_x/C sample showed no significant EtOAc conversion, but the presence of MnO_x increased the EtOAc conversion for all Cu-based catalysts. For example, the EtOAc conversion after 30 h at 180 °C increased from 2.3 % for un-promoted 0.0_MnO_x-Cu/C up to 12.7 % for 11_MnO_x-Cu/C. The temperature was increased at 30 h intervals from 180 to 210 °C, and finally lowered again to 180 °C to evaluate the catalysts stabilities. Interestingly, the conversion for 4.8_MnO_x-Cu/C continuously increased throughout the experiment. However, the conversion decreased after 60 h for catalysts with ≥11 mol% Mn, reflecting a combination of activation and deactivation behavior. The presence of MnO_x hence greatly affected both the activity and stability.

To investigate how the presence of MnO_x affected the Cu-based activity, the apparent activation energy (E_a, Figure 5.2c) for the MnO_x-Cu/C catalysts was calculated from the slope of the Arrhenius plot. It is known from literature that this reaction is close to zero order with respect to both H_2 and EtOAc, when applying a 10-fold excess of H_2 over EtOAc, under similar reaction conditions.[133, 139, 141, 232] A zero order dependency of the EtOAc concentration on the conversion was therefore assumed. The presence of MnO_x decreased the E_a, from 102 kJ mol^{-1} for 0.0_MnO_x-Cu/C to 52 kJ mol^{-1} for 11_MnO_x-Cu/C. For Mn loadings above 11 mol%, the E_a remained approximately constant, *i.e.* 54 kJ mol^{-1} for 20_MnO_x-Cu/C and 58 kJ mol^{-1} for 33_MnO_x-Cu/C. This suggests that a relatively small amount of MnO_x efficiently lowered the E_a, while excess of MnO_x accumulated as spectator species or possibly passivated part of the Cu surface as related to the lower activities for higher Mn loading, as observed in Figure 5.2b. The E_a values in this chapter are in good agreement with reported values of 119 kJ mol^{-1} for macroscopic Cu,[133] 94–107 kJ mol^{-1} for un-promoted supported Cu [141] and 74 kJ mol^{-1} for ZrO_2-promoted Cu.[139] The lowered E_a indicate that the MnO_x promoter altered the nature of the active catalytic site. Close proximity between the MnO_x promoter and the Cu^0 phase is hence present in our catalysts, which is essential to effectively boost the catalytic performance.

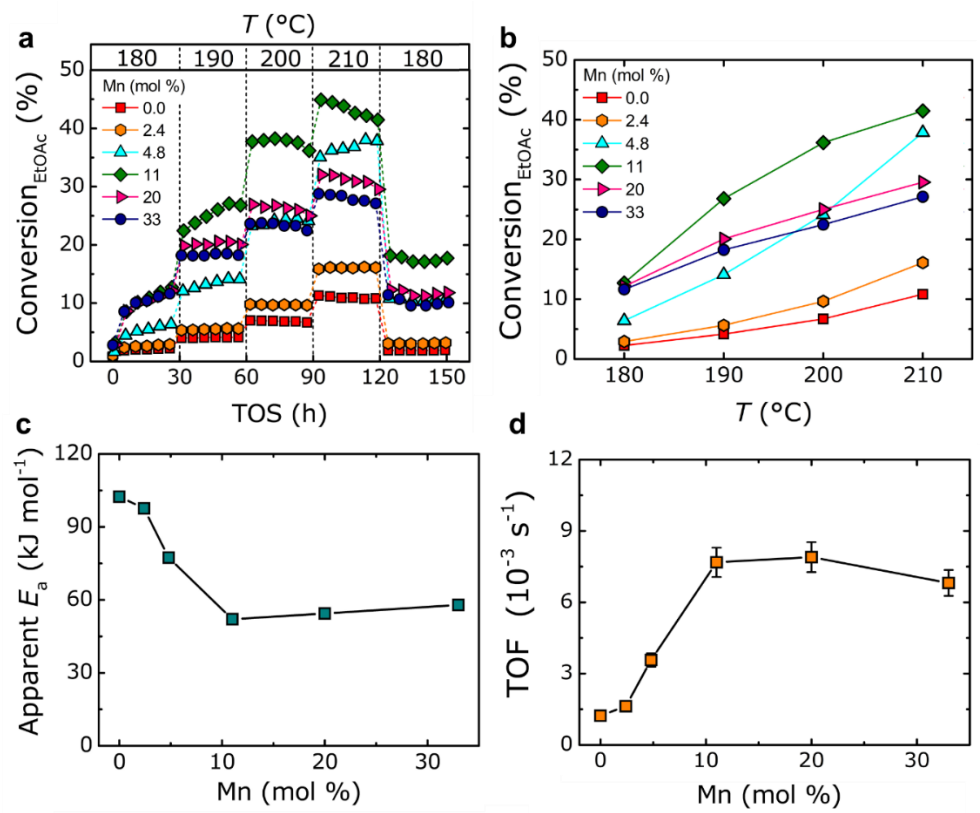

Figure 5.2: *Catalytic performance for MnO_x-Cu/C catalysts with varying Mn loading between 0–33 mol% Mn/(Cu+Mn), prepared using high surface area graphitic carbon as support. EtOAc conversions as a function of* ***a****) time on stream (TOS) at different temperatures, and* ***b****) after 30 h at each temperature stage between 180–210 °C;* ***c****; Apparent activation energy (E_a) as a function of Mn loading;* ***d****) Turn-over frequencies (TOF) at 180 °C, at t = 30 h and correlated to the particle size of the fresh catalyst after synthesis. Error bars indicate the relative standard deviation in TOF, which was around 8 % and may therefore lie behind data markers. Reaction conditions: H_2:He:EtOAc = 10:1:1 vol%, 50 ppm water in EtOAc, 180–210 °C, 30 bar and GHSV between 6,200–7,200 h^{-1}.*

The relationship between Mn loading and turn-over frequency (TOF; at 180 °C) is displayed Figure 5.2d. Herein, we calculated the initial TOF after 30 h and correlated to the MnO_x-Cu particle size after catalyst synthesis. The presence of 11 mol% Mn increased the initial TOF approximately 7-fold, from $1.2*10^{-3}$ s^{-1} for 0.0_MnO_x-Cu/C up to $7.7*10^{-3}$ s^{-1} for 11_MnO_x-Cu/C. However, further increasing the Mn loading did not enhance the initial TOF but even slightly lowered it, consistent to the decrease in E_a up to 11 mol% Mn. By comparison, Wang *et al.* reported that a maximum TOF for MeOAc hydrogenation was obtained using around 10 mol% Zn/(Cu+Zn) for SiO_2-supported Cu catalysts.[246] Van den Berg *et al.* previously demonstrated that a

maximum TOF in methanol synthesis was achieved using around 5 mol% Zn/(Cu+Zn) promoter, giving a 6-fold enhancement of TOF compared to un-promoted Cu.[86] The MnO_x and ZnO_x promoter effects are hence most pronounced at loadings around 5–10 mol%.

The MnO_xCu/C catalysts were significantly more active than (promoted) Cu catalysts in literature. For example, Santiago *et al*. reported a TOF of $2.7*10^{-3}$ s^{-1} at 250 °C for Cu/SiO_2,[125] and Lu *et al.* reported TOF values around $1.1*10^{-3}$ s^{-1} at 280 °C for Zn-promoted Cu catalysts supported on SiO_2, Al_2O_3 and ZrO_2,[136] while we measured TOF between 1.2 and $7.7*10^{-3}$ s^{-1} at a significantly lower temperature of 180 °C. An explanation for our higher TOF may be the use of a high purity EtOAc reactant, with approximately 50 ppm of water, as determined by Karl Fischer titration. To investigate the influence of water in the EtOAc feed, we incrementally increased the concentration during an experiment at 200 °C and 30 bar (Figure 5.3). A concentration of 400 ppm lead to a 3-fold lower activity for the 11_MnO_xCu/C catalyst and no significant activity for the unpromoted Cu/C catalyst, compared to the initial 50 ppm concentration. The promoted catalysts were consistently more active than the un-promoted Cu catalysts, indicating that the MnO_x promoter enhanced the stability against water-induced deactivation.

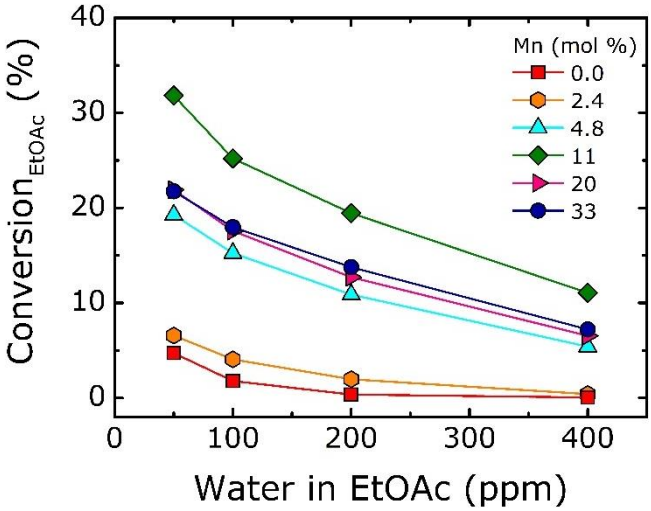

Figure 5.3*: EtOAc conversion as a function of water concentration in the EtOAc feed. Conversions were determined after 45 h on stream for each water concentration between 50 and 400 ppm. Reaction conditions: H_2:He:EtOAc = 10:1:1 vol%, 50–400 ppm water in EtOAc, 200 °C, 30 bar and GHSV between 6,200–7,200 h^{-1}.*

Remarkably, the selectivity towards ethanol was larger than 99.5 % for all MnO_x-Cu/C catalysts (Figure 5.4). The selectivity decreased with increasing EtOAc conversion in all cases. However, the presence of Mn improved the ethanol selectivity when comparing at similar EtOAc conversions, with >99.9 % for the

11_MnO_x-Cu/C catalyst even at 25 % EtOAc conversion. Ethane was observed as the main by-product, with traces of acetic acid and acetaldehyde. The selectivity for MnO_x-Cu/C was significantly higher than reported in literature for supported Cu-based catalysts, which were typically <95 % under similar reaction conditions.[59, 125, 136, 139, 233] The lower literature values were probably caused by acidic or basic surface groups on the metal oxide supports,[139] which were absent on our carbon support.

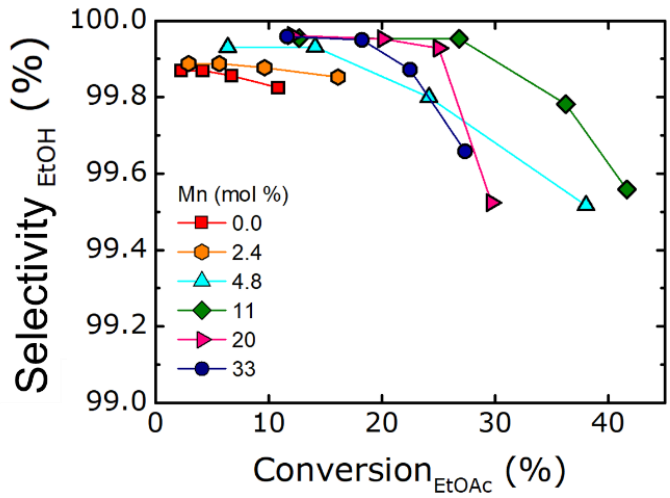

***Figure 5.4**: Ethanol selectivity as a function of EtOAc conversion, for MnO_x-Cu/C catalysts with Mn loading between 0–33 mol% Mn/(Cu+Mn), prepared using high surface area graphitic carbon as support. Reaction conditions: H_2:He:EtOAc = 10:1:1 vol%, 50 ppm water in EtOAc, 180–210 °C, 30 bar and GHSV between 6,200–7,200 h^{-1}.*

Origin of MnO_x promoter effects. The observed phenomena raise the questions which MnO_x species are responsible for the enhanced activity, and how the nature of the Cu particles is affected under reaction conditions (H_2 flow, 180–210 °C). To address these questions, we studied the Cu and Mn oxidation states before and after *in situ* reduction at 250 °C. First of all, temperature-programmed reduction analysis showed H_2 consumption between 100–250 °C, corresponding to the reduction of CuO to Cu_2O and subsequently to Cu^0 (Figure 5.5).[56, 72-73, 86, 88] The H_2 consumption was larger than H_2:Cu=1:1 mol/mol for all MnO_x-promoted catalysts. A broad reduction peak between 300–600 °C was observed for all MnO_x-promoted catalysts, which was ascribed to MnO_x reduction.[247] The intensity was weaker for the MnO_x-Cu/C catalysts than for the Cu-free 100_MnO_x/C sample, which likely results from the higher Mn loading and/or higher average Mn oxidation state for the Cu-free MnO_x/C sample. These results suggest that the close proximity of Cu^0 facilitated the partial reduction of MnO below 250 °C.[137, 176, 184 136, 248] No consistent variation in the CuO_x reduction temperature was observed upon increasing the Mn loading, indicating that MnO_x did not significantly affect the electronic nature of the Cu particles.

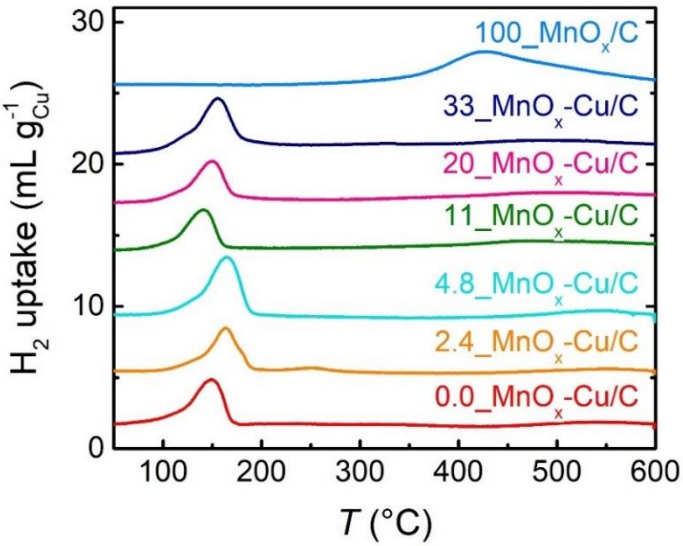

Figure 5.5: *Temperature-programmed H_2 reduction profiles for the MnO_x-Cu/C catalysts, during heating to 600 °C (2°C min^{-1}), under 5 vol% H_2/Ar flow. Profiles stacked with individual offset for visual clarity.*

In situ X-ray absorption (XAS) spectroscopy was applied to investigate the Cu and Mn oxidation states contributions under reaction conditions. The Cu K-edge absorption energies for the catalysts after synthesis (passivated) were consistently located between the Cu^+ and Cu^{2+} references within 8,970 to 9,010 eV (representative example for 33_MnO_x-Cu/C shown in Figure 5.6a), corresponding to average Cu oxidation states between 1.3–1.6. After *in situ* reduction (1 h at 250 °C, 4 vol% H_2/He flow) all spectra were similar to the Cu foil reference, thus showing complete reduction to Cu^0, irrespective of the Mn loading (Figure 5.6a). The Cu–Cu coordination number ($CN_{Cu–Cu}$) was calculated from the EXAFS (Figure 5.6b), and ranged from 10.2 to 11.3 for all MnO_x-Cu/C catalysts. The $CN_{Cu–Cu}$ were close to the bulk $CN_{Cu–Cu}$ of 12, and thereby corroborated the size range of 5–6 nm as detected by TEM and XRD analysis.[215, 249-250] The $CN_{Cu–Cu}$ was slightly higher for the un-promoted Cu/C catalyst (11.3) compared to MnO_x-Cu/C catalysts (10.2–10.8), suggesting a larger Cu particle size, in agreement with the Cu crystallite analysis by XRD. Moreover, the close overlap between the fitted and measured spectra indicate that no significant amounts of Cu oxides or mixed CuMn oxides were present, hence confirming the complete reduction of CuO_x to Cu^0 at 250 °C.

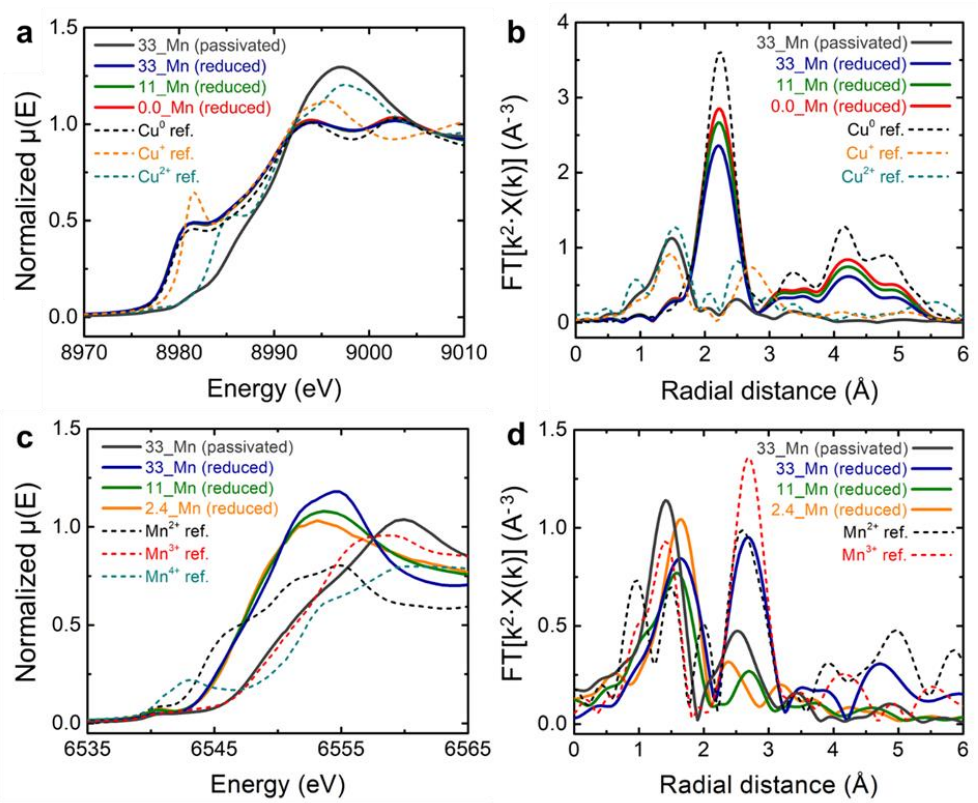

Figure 5.6: *X-ray absorption spectroscopy for several representative MnO_x-Cu/C catalysts after synthesis (passivated) and after in situ reduction for 1 h at 250 °C under 4 vol% H_2/He flow (reduced), including spectra for Cu^0, Cu^+, Cu^{2+}, Mn^{2+}, Mn^{3+} and Mn^{4+} references (dashed lines);* ***a****) near Cu K-edge normalized XANES;* ***b****) k^2-weighted EXAFS in R-space for Cu;* ***c****) near Mn K-edge normalized XANES;* ***d****) k^2-weighted EXAFS in R-space for Mn.*

The Mn K-edge absorption energies for both the MnO_x-Cu/C catalysts after synthesis (passivated) and after *in situ* reduction were consistently located between the Mn^{2+} and Mn^{3+} references within 6,535 to 6,565 eV (Figure 5.6c). EXAFS analysis for the passivated catalysts showed that both the Mn–O (R= 1.0–1.5 Å) and Mn–Mn (R= 2.5–3.0 Å) scattering increase with increasing Mn loadings, suggesting Mn accumulation as MnO_x particles. However, the MnO_x particle size analysis was hampered due to overlapping signals for Mn^{2+} and Mn^{3+} oxides (Figure 5.6d). Upon reduction at 250 °C, all Mn (pre-)edge absorption energies shifted to lower values. The Mn oxidation state decreased from 2.3–2.9 to 2.2–2.5, supporting the partial reduction of MnO_x as observed by H_2-TPR. Interestingly, the Mn oxidation state for the MnO_x-Cu/C catalysts increased from 2.2 to 2.5 with increasing Mn loading from 2.4 to 11 mol%, yet remained approximately 2.5 when further increasing in the Mn loading (Figure 5.7). This indicates that the active promoter species are Mn^{2+} oxides, for instance the MnO islands in close proximity to the Cu^0 nanoparticles as observed

by EDX analysis. Upon increasing the Mn loading, additional MnO_x accumulates as Mn oxide nanoparticles dispersed over the inert carbon support, with a higher averaged Mn oxidation state. MnO_x promoters have been reported to polarize reactants *via* Lewis acid sites and the electron lone pairs on the oxygen atoms.[174, 179, 182, 251] The Lewis acid sites in MnO_x can facilitate the initial C–O ester bond cleavage and stabilize the resulting ethoxy and acyl reaction intermediates.[173-175] The close proximity of MnO next to Cu^0 hence lowered the activation barrier for the rate-determining step in the reaction, *i.e.* hydrogenation of the acyl intermediate.[125, 135, 139, 174]

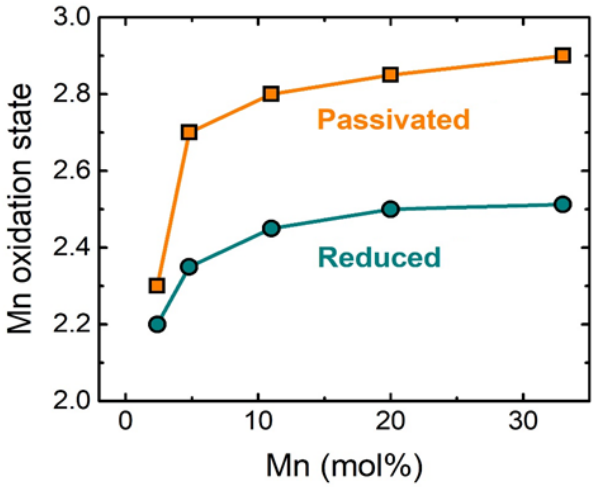

Figure 5.7: *Average Mn oxidation state as a function of Mn loading, for MnO_x-Cu/C catalysts after synthesis (passivated) and after in situ reduction (1 h at 250 °C, 4 vol% H_2/He flow), as determined from the linear correlation between Mn oxidation state values and the energy of the pre-edge feature between 6,535 to 6,545 eV in the XANES.*

Evolution of catalyst structure and activity. We investigated the influence of MnO_x on the structure during catalysis. Particle growth is a major deactivation mechanism for nanoparticulate Cu catalysts, but it is also known that promoters may enhance the stability.[19, 74, 252-253] The MnO_x-Cu particle sizes by TEM were compared for the fresh catalysts after synthesis and used catalyst after 150 h on stream at 180–210 °C (Figure 5.8a). The Cu particle size of the un-promoted 0.0_MnO_x-Cu/C catalyst increased from 5.0 nm to 9.7 nm. The presence of MnO_x limited the particle growth, *e.g.* from 5.1 nm to 5.5 nm for the 4.8_MnO_x-Cu/C catalyst. The MnO_x promoter hence not only enhanced the conversion and selectivity, but also limited Cu particle growth, again with an optimal efficiency at ≥11 mol% Mn.

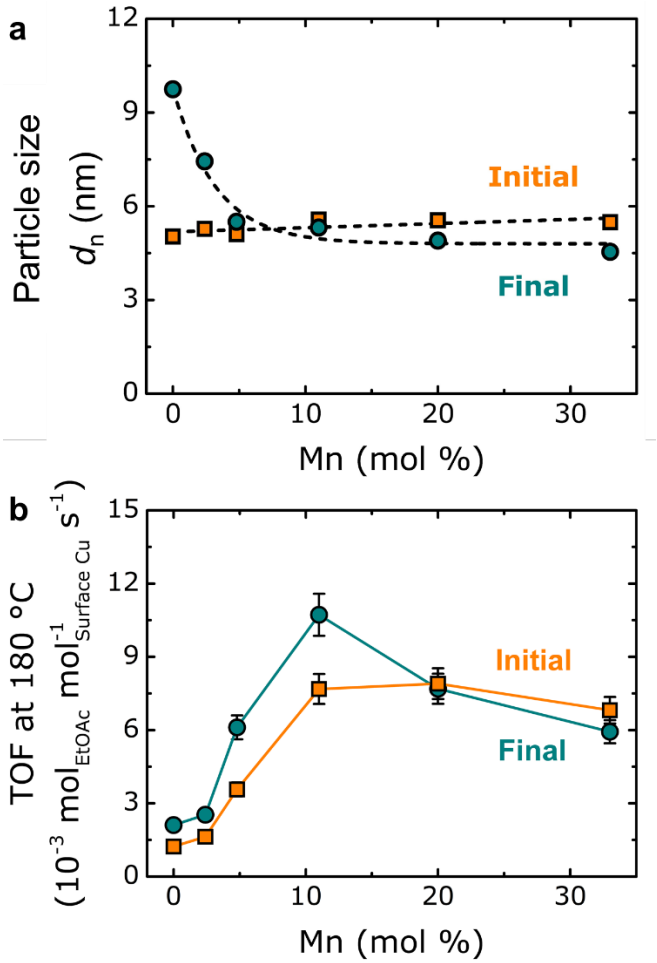

Figure 5.8: a) *TEM particle size analysis for the fresh MnO_x-Cu/C catalysts after synthesis (initial, orange squares) and used catalysts after 150 h catalysis at 180–210 °C (final, cyan circles);* ***b****) Turn-over frequencies (TOF, at 180 °C) are given both after 30 h and correlated to the initial particle size (orange squares) and after 150 h and correlated to the final particle size (cyan circles). Error bars indicate the relative standard deviation in TOF, which was around 8 % and may therefore lie behind data markers. Reaction conditions: H_2:He:EtOAc = 10:1:1 vol%, 50 ppm water in EtOAc feed, 180–210 °C, 30 bar and GHSV between 6,200–7,200 h^{-1}.*

The evolution of activity during catalysis was evaluated by comparing the initial and final TOF values (Figure 5.8b). In absence of Mn, the TOF for the un-promoted 0.0_MnO_x-Cu/C catalyst increased 2-fold from 1.2*10^{-3} s^{-1} to 2.1*10^{-3} s^{-1}, while the Cu particle size increased from 5.0 to 9.7 nm. The increase in TOF was ascribed to a Cu particle size-dependence in hydrogenation activity, in agreement with previous studies.[86] In presence of 2.4–11 mol% Mn, the TOF significantly increased during the reaction (from 1.6–7.7*10^{-3} s^{-1} to 2.5–10.7 *10^{-3} s^{-1}). This increase in TOF was

not caused by particle growth, which was limited in the presence of MnO_x (Figure 5.8a). Alternatively, changes in the oxidation state or distribution of the MnO_x promoter during catalysis likely lead to enhanced activity.[174-177, 180] However, the TOF slightly decreased for catalysts with ≥20 mol% Mn (from 6.8–7.9*10^{-3} s^{-1} to 5.9–7.7*10^{-3} s^{-1}). The final TOF therefore showed a maximum activity of around 10.7*10^{-3} s^{-1} for the Cu catalyst with 11 mol% Mn promoter. Moreover, the catalyst stability was also studied under isothermal reaction conditions, *i.e.* during 225 h at 200 °C (Figure 5.9). The isothermal experiments confirm that the conversion increased over time at low Mn loadings, while deactivation was accelerated at too high Mn loadings. The catalysts with an intermediate Mn loading (5–11 mol%) were both the most active and stable.

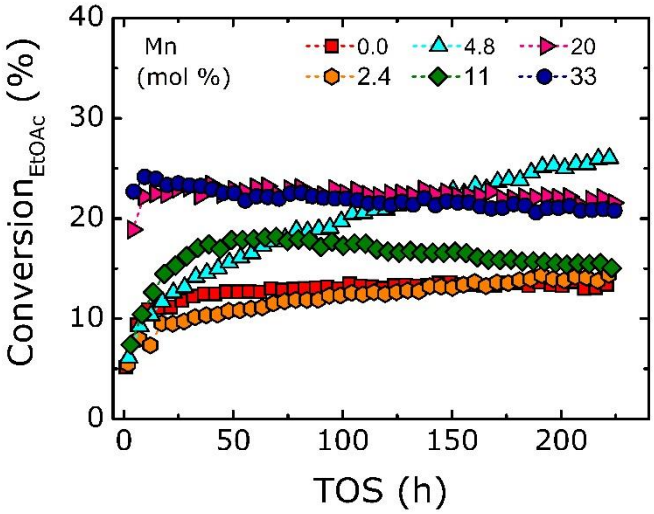

Figure 5.9: *EtOAc conversion profiles under isothermal conditions, for the MnO_x-Cu/C catalysts with varying Mn loadings between 0–33 mol% Mn/(Cu+Mn), prepared using high surface area graphitic carbon as support. Reaction conditions: H_2:He:EtOAc = 10:1:1 vol%, 50 ppm water in EtOAc feed, 225 h at 200 °C, 30 bar and GHSV tuned between 2,000–17,000 h^{-1} to achieve 15±5 % EtOAc conversion after 50 h on stream.*

To evaluate the changes in activity over time, we analyzed the Mn distribution for the fresh 33_MnO_x-Cu/C catalyst after synthesis and used catalyst after 150 h catalysis at 180–210 °C (Figure 5.10). The elemental distribution maps for Cu and Mn by energy-dispersive X-ray spectroscopy (EDX) are shown in Figure 5.10a. The plots in Figure 5.10b show Cu and Mn distributions over several representative areas in the EDX maps for the fresh and used catalysts. For the fresh catalyst, distinct MnO_x nanoparticles were observed in close proximity to the Cu nanoparticles. For the used catalyst, the MnO_x promoter was spread more evenly over the carbon support, suggesting that re-dispersion of MnO_x occurred during catalysis. Quantification of the Mn concentration showed approximately 33 mol% Mn/(Cu+Mn) before and after catalysis, indicating that no leaching occurred. The spreading of MnO_x was even more clearly seen for the Cu-free 100_MnO_x/C sample after exposure to reaction conditions. The EDX analysis showed that the used sample contained significantly smaller MnO_x particles (1.2±0.3 nm) than the fresh sample (2.3±1.0 nm). This shows that irrespective of Cu being present, the MnO_x promoter readily spreads over the catalyst support upon exposure to reaction conditions. The presence of EtOAc and traces of water (~50 ppm) likely played an important role in forming mobile Mn species at elevated temperature.

The 3-dimensional intensity plots in the EDX signal (Figure 5.10c,d) clearly show that the Mn species are closely affiliated with the Cu particles after synthesis, but upon exposure to reaction conditions spread uniformly over the support surface. The EDX analysis confirms that for 33 mol% Mn, a large part of the MnO_x content is present as a spectator. The theoretical number of Mn monolayers on the Cu particles surface was calculated to assess the Cu surface accessibility. For example, the presence of 20 mol% Mn corresponded to 1.4 monolayers. Considering that Mn is present as both MnO_x nanoparticles and spread over the carbon support, it is evident that only a fraction of the Cu surface was covered by MnO_x. The MnO_x always re-dispersed under reaction conditions, but while this leads to an increase in activity over time at ≤11 mol% Mn loadings, it decreased the activity at higher Mn loadings. These findings demonstrate the importance of a balanced Mn loading for optimum catalytic performance of the Cu nanoparticles.

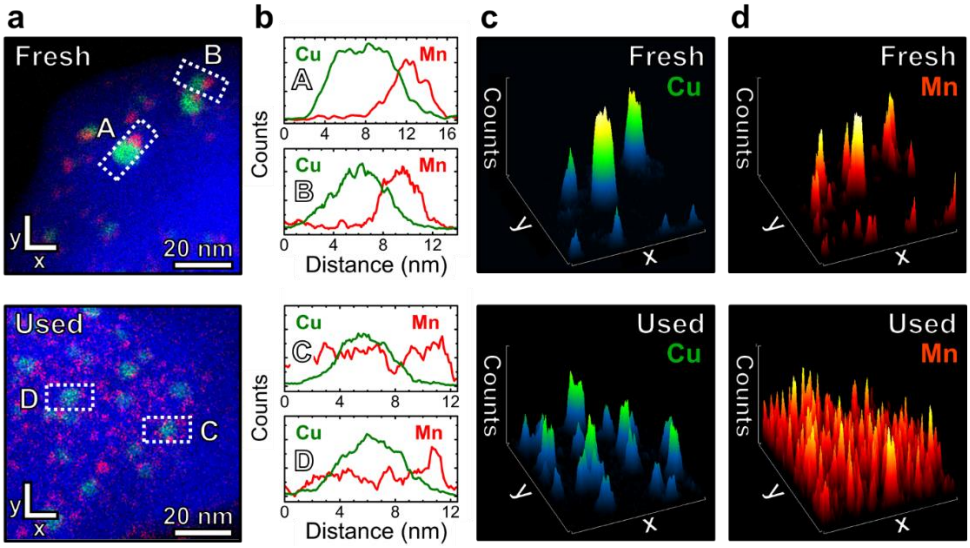

Figure 5.10: *STEM-HAADF-EDX analysis for the fresh 33_MnO$_x$-Cu/C catalyst after synthesis and used catalyst after 150 h catalysis at 180–210 °C.* ***a****) 2-dimensional EDX maps showing the elemental distributions for carbon (blue), Cu (green) and Mn (red), including regions A–D for line scan analysis (dashed white boxes);* ***b****) Cu and Mn line scan analysis, displaying EDX intensity over the length of the indicated regions (A–D);* ***c and d****) 3-dimensional intensity plots in Cu and Mn EDX signals, acquired over the x,y-planes as indicated in the EDX maps.*

5.4 Conclusions

In this chapter, the preparation of a series of well-defined MnO$_x$-Cu catalysts *via* co-impregnation was reported, using high surface area graphitic carbon as the catalyst support. Tuning the synthesis parameters allowed us to keep the MnO$_x$-Cu particle size constant around 6 nm, while varying the Mn loading between 0 and 33 mol% Mn(Cu+Mn). The methodology for catalyst preparation may be relevant for a wide range of metals and promoters. The presence of 11 mol% Mn induced a 7-fold increase in TOF, compared to the un-promoted Cu/C catalyst. This enhanced activity was correlated to a decrease in the apparent activation energy, from 102 to 52 kJ mol^{-1}, suggesting that the MnO$_x$ promoter changed the nature of the active site for catalysis. Decreasing the concentration of water in the EtOAc feed strongly increased the catalytic activity, while the MnO$_x$ promoter enhanced the stability against water-induced deactivation. The selectivity towards ethanol was >99.5 % for all catalysts, which was much higher than reported in literature. A combination of state-of-the-art electron microscopy and *in situ* X-ray absorption spectroscopy techniques revealed that the reduced MnO$_x$-Cu/C catalysts contained MnO islands in close proximity to Cu^0 nanoparticles. The origin of the promoter effect was

attributed to a lowering of the energy barrier in the rate-determining hydrogenation of the acyl reaction intermediate, at the MnO– Cu^0 interface. At low Mn loadings, the diffusion of mobile Mn species enhanced the activity over time. However at too high Mn loadings, MnO_x diffusion led to partial coverage of the Cu particles and resulting deactivation. Tuning the Mn loading to an intermediate level (11 mol%) provided an exceptional combination of high activity, selectivity and stability in hydrogenation catalysis.

Acknowledgements

This chapter was based on the MSc research project of Nienke Visser. We thank Jan Willem de Rijk, Remco Dalebout, Neil Sainty and Roy Partington for support in catalytic experiments, and Christa Oversteeg, Fei Chang, Herrick van Schaink, Ad van der Eerden and Alessandro Longo are acknowledged for their contributions to the X-ray absorption spectroscopy measurements and data processing.

Chapter 6

Carbon-Supported Copper Catalysts for Selective Hydrogenation of Butadiene

This chapter is based on the patent: *"WO2019/233961, Selective Hydrogenation of Polyunsaturates"* by R. Beerthuis, G. J. Sunley, K. P. de Jong and P. E. de Jongh, and the publication: "*Silica- and Carbon-Supported Copper Catalysts for Selective Hydrogenation of Butadiene" by G. Totarella,[#] R. Beerthuis,[#] et al. and P. E. de Jongh, In preparation ([#] authors contributed equally).*

Abstract

In this chapter, the activity, selectivity and stability of mono-metallic copper on carbon (Cu/C) catalyst are discussed in the hydrogenation of butadiene, in excess of propene. The Cu particle size was varied from 1 to 23 nm and the effects of Cu particle size on the catalyst performance were evaluated. All Cu/C catalysts gave rise to less than 0.05 % propene conversion, even at full conversion of butadiene and this selectivity did not depend on the Cu particle size. The 3 and 7 nm Cu/C catalysts retained around 90 and 50 % of the initial butadiene conversion, respectively, after 100 hours on stream at 110 °C, which is significantly more stable than other Cu catalysts in literature. Moreover, the propene conversion decreased from 0.05 to below 0.005 % during the first 20 h on stream. The high selectivity and stability for Cu/C may guide the design of efficient non-precious metal catalysts for selective hydrogenation reactions.

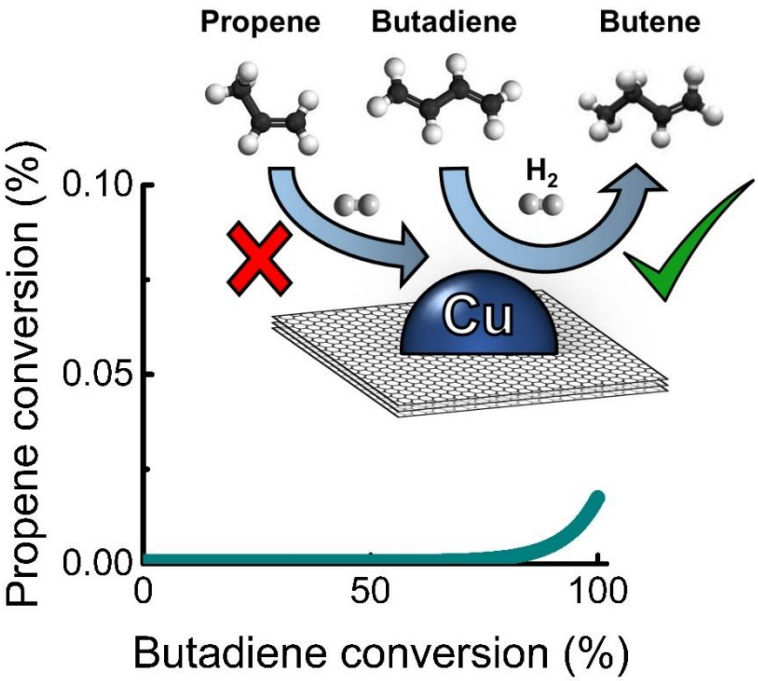

6.1 Introduction

The selective removal of alkyne and diene impurities from mono-olefin feedstocks is a crucial step in the production of high quality plastics.[142-144] Mono-olefins such as ethene, propene and butenes are mainly produced through steam cracking of naphtha and gas oil fractions, while poly-unsaturated impurities such as acetylene, propyne, butyne and butadiene are also formed in concentrations up to around 5 vol%.[142, 145] The poly-unsaturated impurities may poison the polymerization catalyst and lower the polymer quality, and hence must be selectively removed while avoiding alkane formation.[145-146] The selective hydrogenation of alkynes and dienes is typically done in industry using supported Pd-based catalysts, such as $PdAg/Al_2O_3$, $PdS/CaCO_3$ and $PdPb/CaCO_3$, at relatively low temperatures (30–150 °C) and pressures (1–30 bar).[85, 144, 148-153]

Supported Cu catalysts have been reported to be highly selective for the hydrogenation of various alkynes[162-166] and dienes.[75-76, 167-170] Nevertheless, the Cu catalysts in literature consistently showed deactivation within several hours on stream. In our research group, Masoud *et al.* recently reported that the support had a major effect on the stability of supported Au catalysts for the hydrogenation of butadiene.[171] Significantly higher stability was observed when using SiO_2 as a support compared to TiO_2, due to reduced oligomer formation on the support surface. Similarly, using carbon as an chemically inert support for mono-metallic Cu may provide catalysts with high catalyst stability.

In this chapter, we discuss the preparation of well-defined Cu catalysts supported on carbon, with variation of the Cu particle size between 1 and 23 nm. The catalytic performance of mono-metallic Cu on carbon was investigated for the gas-phase hydrogenation of butadiene at atmospheric pressure, in excess of propene as a model reaction for selective hydrogenation catalysis (Eq. 1.5 in Chapter 1 of this thesis). The Cu particle size effects were evaluated, and the carbon-supported catalyst stability was compared to metal oxide-supported Cu catalysts in literature.

6.2 Experimental methods

Catalyst assembly

A series of carbon-supported Cu (Cu/C) catalysts was prepared by adaption of the synthesis methods from Chapter 3 of this thesis. The Cu particle size was tuned by variation of the Cu loading (3–12 wt%), the final heat treatment temperature (200–500 °C) as well as applying HNO_3 surface-oxidation of the graphitic carbon support. Pristine graphitic carbon (HSAG-500, Timcal) and surface-oxidized graphitic carbon (110 min at 80 °C, concentrated HNO_3) were used as the catalyst support materials.

For the synthesis of all Cu/C catalysts, around 2 g of dried powdered carbon support was impregnated to incipient wetness, using an aqueous $Cu(NO_3)_2$ precursor solution. The $Cu(NO_3)_2$ concentration was adjusted to control the Cu weight loading on the final catalyst. The solution was added by syringe in a round-bottom flask, while stirring under vacuum. The impregnated sample was stirred for 24 h to homogenize the metal precursor throughout the support. Next, the impregnate was dried overnight at room temperature, while stirring under dynamic vacuum. Subsequently, the dried impregnate was transferred to an Ar-filled glovebox (Mbraun Labmaster dp; <1 ppm H_2O; <1 ppm O_2) and loaded into a plug-flow reactor without exposure to air.

In the case of the Cu/C catalysts prepared using surface-oxidized carbon, the dried impregnate was heated to 230 °C (0.5 °C min^{-1}), followed by 1 h isothermal hold at 230 °C, under N_2 flow (100 mL min^{-1} g^{-1}) to decompose the nitrate precursor. The sample was left to cool down to room temperature and purged with 20 vol% O_2/N_2 flow (100 mL min^{-1} g^{-1}) for 3 h at room temperature. Next, the sample was purged with pure N_2 flow (100 mL min^{-1} g^{-1}) for 30 min and subsequently reduced by heating to 150 °C (2 °C min^{-1}), with 2 h isothermal hold at 150 °C, under 5 vol% H_2/N_2 flow (100 mL min^{-1} g^{-1}). Next, the temperature was increased to either 200, 250 or 400 °C (2 °C min^{-1}), with 1 h isothermal hold at the final temperature, to obtain the 1_Cu/C, 3_Cu/C and 7_Cu/C catalysts, respectively. In the case of the 23_Cu/C catalyst, the temperature was first increased to 400 °C (2 °C min^{-1}), with 1 h isothermal hold at 400 °C, under 5 vol% H_2/N_2 flow (100 mL min^{-1} g^{-1}). Next, the gas flow was exchanged for pure N_2 (100 mL min^{-1} g^{-1}) and the sample heated to 500 °C (2 °C min^{-1}), with 1 h isothermal hold at 500 °C. After letting cool down to room temperature, the reduced catalysts were transferred to an Ar-filled glovebox, without exposure to air to allow XRD characterization of reduced Cu/C. Finally, the catalysts were collected after exposure overnight to air at room temperature.

In the case of the Cu/C catalyst prepared using pristine carbon, the dried impregnate was transferred to a plug-flow reactor and heated to 230 °C (2 °C min^{-1}) with 1 h isothermal hold at 230 °C, under 20 vol% H_2/N_2 flow (100 mL min^{-1} g^{-1}). The sample was left to cool down to room temperature and flushed with N_2 (100 mL min^{-1} g^{-1}). Next, the catalyst was heated to 200 °C (1 °C min^{-1}) with 3 h isothermal at 200 °C, under 5 vol% O_2/N_2 flow (100 mL min^{-1} g^{-1}). Still at 200 °C, the gas flow was exchanged for 15 vol% O_2/N_2 (100 mL min^{-1} g^{-1}) with 1 h isothermal hold at 200 °C. The 13_Cu/C catalyst was collected after letting it cool down to room temperature. An *ex situ* reduction treatment was done to allow XRD analysis on the reduced 13_Cu/C catalyst. Herein, around 200 mg of catalyst was loaded in a plug-flow reactor and heated to 200 °C (2 °C min^{-1}) with 1 h isothermal hold at 200 °C, under 20 vol% H_2/N_2 flow (200 mL min^{-1} g^{-1}). The catalyst was left to cool down to room temperature and was transferred to an Ar-filled glovebox, without exposure to air.

The catalysts in this study were denoted as *X*_Cu/C where *X* stands for the surface-averaged Cu particle size in nm.

Catalyst characterization

Transmission electron microscopy (TEM) was performed on either an FEI Tecnai 20 microscope and an FEI Talos F200X microscope, both operated at 200kV. The catalyst was dispersed as a fine powder directly onto a holey carbon coated Ni grid (Agar 300 mesh). The Cu Particle sizes were determined by measuring at least 200 individual particles, on 10 sample areas. The surface-averaged Cu particle size (d_s) and standard deviation in the particle size distribution (σ_{ds}) were calculated using the formula $d_s \pm \sigma_{ds} = \frac{\sum_{i=1}^{N} d_i^3}{\sum_{i=1}^{N} d_i^2} \pm \sqrt{\frac{1}{N} \sum_{i=1}^{N} (d_s - d_i)^2}$, in which d_i stands for the diameter of the ith particle and *N* the total number of counted particles.

Powder X-ray diffraction (XRD) was carried out on a Bruker D8 diffractometer equipped with a Lynxeye detector, using a Co-$K\alpha$12 radiation source (λ = 1.78897 Å). The reduced catalyst was loaded into an airtight transparent sample holder (A100B33, Bruker AXS) inside an Ar-filled glovebox. Diffractograms were acquired at room temperature from 5 to 95 °2θ, with 0.1 ° increment, and were normalized to the intensity of the graphitic (002) diffraction peak at 30.9 °2θ. The Cu^0 crystallite sizes were calculated by using the Scherrer equation with a shape factor of k = 0.1, on the Cu^0 (111) diffraction at (50.7 °2θ) and the Cu^0 (200) diffraction at (59.3 °2θ).[234]

Temperature-programmed desorption experiments were performed on the catalysis setup (see Catalysis section), coupled to a mass spectrometer (Hiden QGA) using a secondary electron multiplier detector. The gas outlet of the setup was connected to the mass spectrometer using a 6 meter nylon tube (1/18th inch inner diameter) and a 1 meter stainless-steel line. The mass spectrometer was calibrated before each individual experiment. The 7_Cu/C catalyst (250 mg) was loaded into a glass U-shaped reactor (10 mm inner diameter) fitted with a thermocouple, onto a glass frit. Glass wool plugs were placed on top of the catalyst bed to keep the bed in place. The catalyst was first purged under pure N_2 flow (120 mL min^{-1} g^{-1}) for 30 min, and subsequently reduced by heating to 200 °C (2 °C min^{-1}) under pure H_2 flow (200 mL min^{-1} g^{-1}) with 60 min isothermal hold at 200 °C. The catalyst was left to cool down to 50 °C and purged overnight at 50 °C with a flow of either butadiene/propene/H_2/He = 0.15/15/10/24.85 mL min^{-1} or butadiene/He = 0.15/49.85 mL min^{-1}. Next, the catalyst was purged under a flow of pure N_2 (200 mL min^{-1} g^{-1}) for 10 min and heated to 300 °C (10 °C min^{-1}), while monitoring the concentration of the analytes by on-line mass spectrometry.

Catalysis

The catalyst performance was measured using a gas-phase fixed-bed reactor system at atmospheric pressure, that was described in earlier studies by Masoud *et al.* in our research group.[171, 254] The as-synthesized Cu/C catalysts were pelletized (2 cm diameter) using a hydraulic press at 1,500 kgf, equivalent to 460 bar pressure, ground to a powder and sieved to obtain a granulate size of 90–212 μm. The catalyst granulates were physically mixed with SiC diluent (212–425 μm). The amount of Cu for each measurement was kept constant at 1.28 mg, with a constant catalyst bed height of 1 cm. As such, 20.0 mg of the catalysts with 6.3 wt% Cu (3_Cu/C, 7_Cu/C and 23_Cu/C) was diluted with 155 mg of SiC. The catalyst with 2.7 wt% Cu (1_Cu/C) was loaded using 47.4 mg of catalyst mixed with 85 mg of SiC, while the catalyst with 12.1 wt% Cu (13_Cu/C) was loaded using 10.6 mg of catalyst mixed with 190 mg of SiC. The diluted Cu/C catalyst was loaded into a quartz U-shaped reactor (4 mm inner diameter) onto a glass frit, with glass wool plugs placed on top of the catalyst to keep the bed in place.

The catalyst was reduced *in situ* by heating to 200 °C (2 °C min^{-1}), with 1 h isothermal hold at 200 °C under pure H_2 flow (20 mL min^{-1}; 99.999 vol% purity, Linde). The reduced catalyst was left to cool down to either 30 or 80 °C, depending on the specific experiment, and was subsequently exposed to a pre-mixed reaction gas mixture which consisted of 0.30 vol% butadiene (99.5 %, Air Liquide), 30.0 vol% propene (99.95 %, Air Liquide), 20.0 vol% H_2 (99.999 %, Linde) and balance He (99.999 %, Linde), with a total flow rate of 50.0 mL min^{-1}. The resulting gas hourly space velocity was approximately 22,500 h^{-1}, based on the catalyst bed net volume. During the temperature ramping experiments, the *in situ* reduced catalyst was allowed to cool down to 30 °C under the pure H_2 flow after the reduction treatment. Next, the catalyst was exposed to the pre-mixed reaction gas mixture to start the catalytic measurement. The catalyst was heated to 195 °C (0.5 °C min^{-1}) while gas phase samples were taken any 15 minutes (*vide infra*), subsequently left to cool down to 30 °C, and finally measured again during heated again to 195 °C (0.5 °C min^{-1}). During the isothermal experiments, the catalyst was left to cool down to 80 °C under H_2 flow, directly after the reduction treatment. Next, the catalyst was exposed to the reaction mixture. Subsequently, the temperature was increased to 110 °C (2 °C min^{-1}) to start the catalytic measurement for 100 h on stream. Finally, the catalyst was left to cool down to room temperature and passivated by overnight exposure to air at room temperature.

The composition of the effluent reaction gas mixture was analysed every 15 min by on-line gas chromatography (Interscience Trace 1300 GC, with a sebaconitrile 25 % Chromosorb PAW 80/100 Mesh column), equipped with a flame ionization detector (Perichrom PR 2100). The GC peak areas were calibrated for butadiene, *trans*-2-butene, *cis*-2-butene, 1-butene, isobutylene, butane, propene and propane using a pre-mixed calibration gas. The gas phase concentrations were calculated from the

integrated peak areas. Throughout this paper butadiene refers to buta-1,3-diene and butane to *n*-butane. Isobutylene was not observed in any catalytic experiment. It must be noted that the butadiene feed gas already contained around 0.25 vol% of *cis*-2-butene impurity, while the propene feed gas contained around 0.025 vol% propane impurity. No significant influence on reaction kinetics was expected for these trace amounts of impurities. Nevertheless, for the product analysis of *cis*-2-butene and propane, the initial concentrations were subtracted from the measured values under reaction conditions.

To corroborate that the reaction was not limited by mass transfer, the conversion was measured for several Cu/C catalysts with three different granulate sizes (38–90, 90–212 and 212–425 µm) during continuous temperature ramping experiments. No significant differences in conversion were observed, hence indicating that the reaction was not hindered by internal or external mass transfer limitations. A blank measurement was performed, using only the bare carbon support, SiC diluent and glass wool plugs, under typical reaction conditions. No butadiene or propene consumption was observed at 300 °C. Several catalytic measurements were performed multiple times to ensure reproducibility of the results. The standard deviation was determined as the averaged variation in butadiene conversion during a duplicate measurement using the 7_Cu/C catalyst at 110 °C, resulting in an relative standard deviation in conversion of 5.5 %.

The Cu weight-normalized reaction rate (CTY; $mol_{butadiene}\ g_{Cu}^{-1}\ h^{-1}$) was determined to calculate the turn-over frequency (TOF; $mol_{butadiene}\ mol_{Surface\ Cu}^{-1}\ s^{-1}$) using the formula: $CTY*M_{Cu}/D_{Cu}$, in which M_{Cu} stands for the molecular weight of Cu and D_{Cu} the fraction of surface Cu atoms of total Cu atoms. D_{cu} is calculated from the Cu particle size, assuming fully accessible and spherical particles using the formula $6*(V_{Cu}\ A_{Cu}^{-1})/d_s$. Herein, A_{Cu} is the molar area occupied by surface Cu atoms ($4.10*10^{22}$ nm^2) and V_{Cu} is the molar volume occupied by bulk Cu atoms ($7.09*10^{21}$ nm^3). D_{Cu} is hence calculated as $1.04/d_s$, with d_s in nm.[172]

6.3 Results and Discussion

Varying the Cu particle size on carbon. A series of carbon-supported Cu (Cu/C) catalysts was prepared, by adaption of the synthesis methods as described in Chapter 3 of this thesis. The Cu particle size was tuned by using a combination of carbon surface-oxidation, and variation of the Cu loadings and heat treatment temperatures, as summarized in Table 6.1. Impregnation of surface-oxidized carbon with 2.7 wt% Cu, followed by heating to 200 °C gave a surface-averaged Cu particle size of 0.9 nm. Using a Cu loading of 6.3 wt% on surface-oxidized carbon and heating to either 250, 400 or 500 °C gave surface-averaged Cu particles sizes of 3.1, 7.3 and 22.6 nm Cu particles, respectively. Using a Cu loading of 11.7 wt% on pristine carbon and heating to 230 °C gave a surface-averaged Cu particle size of

13.4 nm. The Cu^0 crystallite sizes by XRD analysis on the reduced Cu/C catalysts were in good agreement with the particle sizes by TEM. Controlling the synthesis conditions hence gave control over the Cu particle size between 1 and 23 nm. The catalysts were labelled as *X*_Cu/C, in which *X* indicates the surface-averaged Cu particle size in nm, as determined by TEM analysis.

Table 6.1. Physicochemical properties of the carbon-supported Cu catalysts.

Catalyst	Carbon support[a]	Cu loading (wt%)	T^b (°C)	$d_{Cu^0, XRD}$ (nm)	$d_s \pm \sigma_{ds}$ (nm)[c]	D_{Cu} (%)[d]
1_Cu/C	Oxidized	2.7	200	-	0.9±0.4	100
3_Cu/C	Oxidized	6.3	250	2.0	3.1±0.9	34
7_Cu/C	Oxidized	6.3	400	6.0	7.3±2.4	14
13_Cu/C	Pristine	11.7	230	10.9	13.4±6.2	8
23_Cu/C	Oxidized	6.3	500	11.6	22.6±8.1	5

***a**) Pristine graphitic carbon or surface-oxidized graphitic carbon obtained by HNO_3 oxidation (110 min at 80 °C in conc. $HNO_{3\ aq}$); **b**) Final heat treatment temperature during catalyst synthesis; **c**) Surface-averaged Cu particle size (d_s) calculated as $\sum_{i=1}^{N} d_i^3 / \sum_{i=1}^{N} d_i^2$ from TEM analysis, wherein d_i indicates the measured particle size of the ith particle for N amount of particles, including standard deviation in the width of the particle size distribution (σ_{ds}); **d**) Dispersion of Cu particles calculated from $D_{Cu}=1.04/d_s$.*

Activity in butadiene hydrogenation. The conversion of butadiene as a function of temperature is shown in Figure 6.1, for the *in situ* reduced Cu/C catalysts. In all cases, the catalysts showed no butadiene conversion below 100 °C. A steep increase in butadiene conversion was observed around 110 to 130 °C. The Cu/C catalysts with Cu particle sizes of 1 to 13 nm reached full conversion between 120 and 160 °C. However, the 23_Cu/C catalyst did not reach full conversion, even at 195 °C. The 3_Cu/C and 7_Cu/C catalysts were the most active. The surface-normalized turn-over frequencies (TOF; approximately 110 °C) were $9*10^{-3}$ s^{-1} for 3_Cu/C and $31*10^{-3}$ s^{-1} for 7_Cu/C, and hence 3-fold higher for the 7 nm Cu particles compared to 3 nm particles. The Cu particle size-dependence in hydrogenation activity was in agreement with Cu particle size effects on activity for methanol synthesis from CO and CO_2 and hydrogenation of ethyl acetate, as described in Chapters 3 and 4 of this thesis. The TOF for 7_Cu/C was similar to the TOF for 5 nm Cu supported on TiO_2, as reported in literature ($32*10^{-3}$ s^{-1} at 105 °C).[76] Interestingly, the Cu/TiO_2 were already active around 60 °C, which was attributed to enhanced activity at the Cu–TiO_2 interface.[75, 171] The Cu-based activity for butadiene hydrogenation is higher than for Au/SiO_2 ($4*10^{-3}$ s^{-1} at 120 °C)[254] and Ag/SiO_2 ($0.2*10^{-3}$ s^{-1} at 120 °C),[254] yet lower than for Pd/Al_2O_3 ($11*10^{-3}$ s^{-1} at 40 °C),[255] as measured under similar reaction conditions.

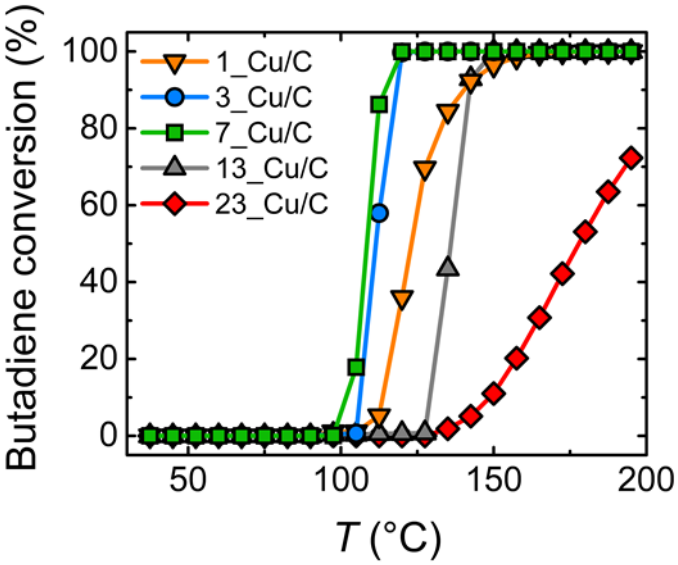

Figure 6.1: *Butadiene conversion as a function of temperature for Cu/C catalysts with Cu particle size varied between 1 and 23 nm. Reaction conditions: butadiene/propene/H_2/He = 0.15/15/10/24.85 mL min^{-1}, 30–195 °C (heating ramp 0.5 °C min^{-1}), 1 bar(a) and 1.28 mg of Cu per measurement.*

Interestingly, a steep increase in conversion between 100 and 120 °C was previously also reported for the hydrogenation of various alkynes,[163, 165] yet the origin is unknown. A possible cause for the activity onset above 100 °C is the recovery of the metallic Cu surface under reaction conditions.[256-260] The presence of trace amounts of O_2 (~50 ppm) in the reaction gas mixture may lead to Cu surface oxidation and catalyst inactivity.[217, 237, 261] We compared the activity during two consecutive heating ramps for the 7_Cu/C catalyst, either after *in situ* H_2 reduction or after N_2 pre-treatment (Figure 6.2). The non-reduced catalyst was inactive up to 135 °C during the first heating ramp, corresponding to the onset temperature for H_2 reduction of CuO_x nanoparticles, as discussed in Chapter 4 of this thesis. Trace amounts of O_2 may have hence lead to Cu surface oxidation below 100 °C, while this effect is negligible at higher temperatures when CuO_x is reduced by the H_2 in the reaction mixture. The influence of O_2 traces on the activity and selectivity of Cu-based hydrogenation catalysts is part of ongoing studies by Totarella *et al.* in our research group.

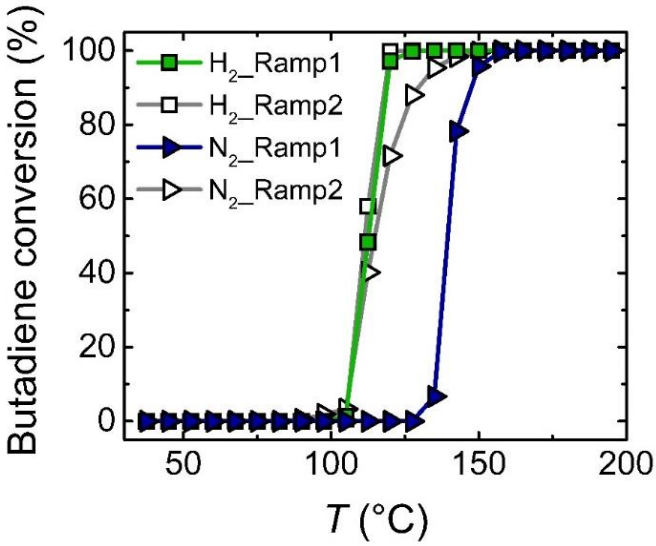

Figure 6.2: *Butadiene conversion as a function of temperature for the 7_Cu/C catalyst, either after in situ reduction (1 h at 200 °C, pure H_2 flow; square data markers) or N_2 pre-treatment (1 h at 200 °C, pure N_2 flow; triangle data markers). Two consecutive heating ramps were performed, showing the first heating ramp (solid data markers) and second heating ramp (empty data markers). Reaction conditions: butadiene/propene/H_2/He = 0.15/15/10/24.85 mL min^{-1}, 30–195 °C (heating ramp 0.5 °C min^{-1}), 1 bar(a) and 1.28 mg of Cu per measurement.*

Reactant and product selectivity. The propene conversion as a function of butadiene conversion during continuous temperature ramping (30–195 °C) is shown in Figure 6.3. The propene conversion was independent of the Cu particle size and less than 0.05 % for all Cu/C catalysts, even at full butadiene conversion. The propene conversion at full butadiene conversion was significantly lower than for Cu/TiO_2 catalysts in literature (>2 %), as measured under similar reaction conditions.[75-76, 169]. Possibly, the presence of highly active sites at the Cu–TiO_2 interface are responsible for propene hydrogenation, while such sites are absence for Cu particles supported on chemically inert carbon. The propene conversion for Cu/C was significantly lower than for Pd-based catalysts (>1 %)[148, 159, 262] and even slightly lower than for Au-based catalysts (~0.1 %).[171, 254] The high selectivity for the Cu/C catalysts was ascribed to a stronger adsorption and lower apparent activation energy for butadiene compared to butene and propene.[263-265]

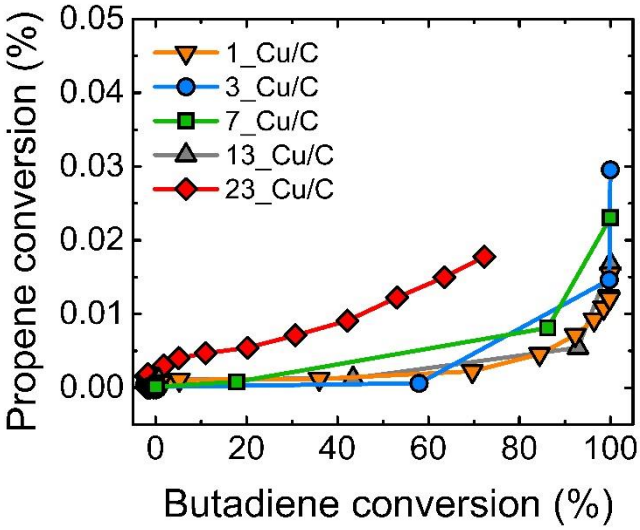

Figure 6.3: *Propene conversion as a function of butadiene conversion for Cu/C catalysts with Cu particle size varied between 1 and 23 nm. Reaction conditions: butadiene/propene/H_2/He = 0.15/15/10/24.85 mL min^{-1}, 30–195 °C, 1 bar(a) and 1.28 mg of Cu per measurement.*

It is important to also assess the product distribution, since butene isomerization typically occurs during the hydrogenation of butadiene, giving a mixture of the desired 1-butene product, and *cis*-2-butene and *trans*-2-butene isomers. All Cu/C catalysts gave around 80 % of 1-butene and less than 0.2 % butane, even at full butadiene conversion. The high product selectivity was attributed to the low isomerization activity on Cu and consistent with previous studies.[76, 163, 169-170, 266] Moreover, the butene products apparently desorbed from the Cu surface after their formation, while avoiding butane formation.[170, 263-265] The Cu/C catalysts were hence highly selective for the hydrogenation of butadiene.

Influence of support on catalyst stability. The evolution of butadiene and propene conversion during 100 h on stream is shown in Figure 6.4a,b, for the *in situ* reduced 3_Cu/C and 7_Cu/C catalysts. A temperature of 110 °C was applied to evaluate the catalyst stability at relatively high propene conversion, and to allow direct comparison with stability measurements for Cu/TiO_2 catalysts reported in literature.[75-76, 169] To evaluate the catalyst stability, a zero order dependence of the butadiene concentration on the reaction rate was assumed, based on literature reports for Cu-catalysts as measured under similar reaction conditions.[163, 266] The butadiene conversion for 3_Cu/C decreased from 91 to 46 % during the first 30 h on stream, and remained constant afterwards with 48 % after 100 h (Figure 6.4a). The 7_Cu/C catalysts showed a decrease in butadiene conversion from 99 to 95 % during the first 30 h, and retained 93 % of the initial conversion after 100 h. We compared the stability of our Cu/C catalysts to a 5 nm Cu on TiO_2 catalyst and a 2 nm ZnO_x-

promoted Cu/TiO_2 catalyst as measured under similar reaction conditions by Wang *et al*.[76, 169] The 5 nm Cu/TiO_2 catalyst lost nearly all activity after several hours on stream.[76] Interestingly, the 2 nm $CuZnO_x/TiO_2$ catalyst retained around 75 % of the initial conversion after 20 h on stream. The presence of ZnO_x as a promoter greatly improved the stability, likely by limiting oligomer formation on the TiO_2 surface.[169] Remarkably, the mono-metallic Cu catalysts on carbon were significantly more stable than the Cu catalysts supported on metal oxides as reported in literature.

Strikingly, the initial propene conversion was less than 0.05 %, but even decreased to below 0.005 % during the first 30 h on stream (Figure 6.4b). At the same time, the selectivity towards butane decreased to below 0.005 % (example for 7_Cu/C in Figure 6.4c), thus validating the use of propene as a model compound for butadiene hydrogenation in excess of a mono-olefin. After the first 30 h on stream the butene product distribution was around 80 % of 1-butene, 10 % of *cis*-2-butene and 10 % of *trans*-2-butene for 7_Cu/C and around 76 % of 1-butene, 13 % of *cis*-2-butene and 11 % of *trans*-2-butene for 3_Cu/C. Moreover, the concurrent decrease in butadiene and propene conversions suggests the presence and deactivation of an active site which is responsible for the hydrogenation of both reactants.

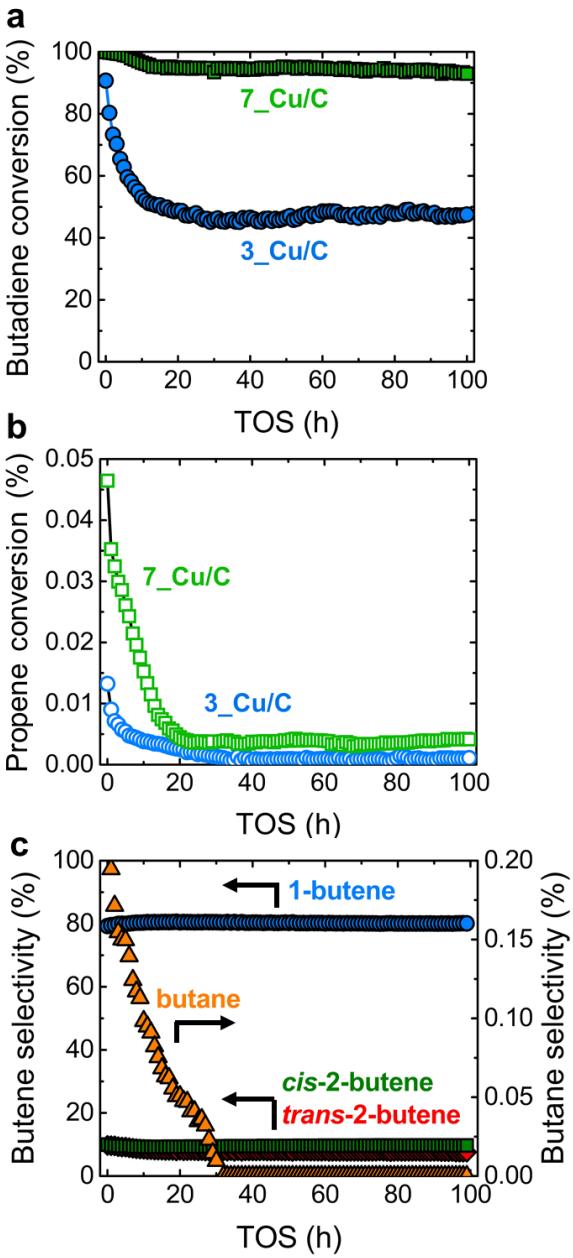

Figure 6.4: ***a****) Butadiene conversion (solid data markers) and* ***b****) propene conversion (empty data markers) as a function of time on stream (TOS) for the 3_Cu/C (green squares) and 7_Cu/C (blue circles) catalysts;* ***c****) Corresponding C_4 product distribution for 7_Cu/C, showing the selectivity to 1-butene (blue circles), cis-2-butene (green squares), trans-2-butene (red diamonds) and butane (orange triangles). Reaction conditions: butadiene/propene/H_2/He = 0.15/15/10/24.85 mL min^{-1} 110 °C, 1 bar(a) and 1.28 mg of Cu per measurement.*

To investigate the origin of the catalyst deactivation, we compared the Cu particle sizes for the as-synthesized catalysts (fresh) and after 100 h catalysis (used). While the Cu particle size increased from 3.1 to 6.5 nm for the 3_Cu/C catalyst, the 7_Cu/C catalyst did not significant grow from 7.3 to 7.4 nm (Figure 6.5). The initial TOF were $36*10^{-3}$ s^{-1} for the fresh 7_Cu/C catalyst and $14*10^{-3}$ s^{-1} for the fresh 3_Cu/C catalyst, and hence slightly higher than the TOF during the continuous temperature ramping measurements. Interestingly, the TOF for the used 3_Cu/C catalyst with 6.5 nm Cu particles ($15*10^{-3}$ s^{-1}) was significantly lower than for the used 7_Cu/C catalyst with 7.4 nm Cu particles ($34*10^{-3}$ s^{-1}), which suggests that part of the Cu surface lost activity during catalysis. We note that more extensive metal nanoparticle growth for initially smaller particles has been observed for Cu/C catalysts in hydrogenation of ethyl acetate as described in Chapter 4 of this thesis, and previously for Ni catalysts in methanation[267] and liquid-phase reforming reactions.[268]

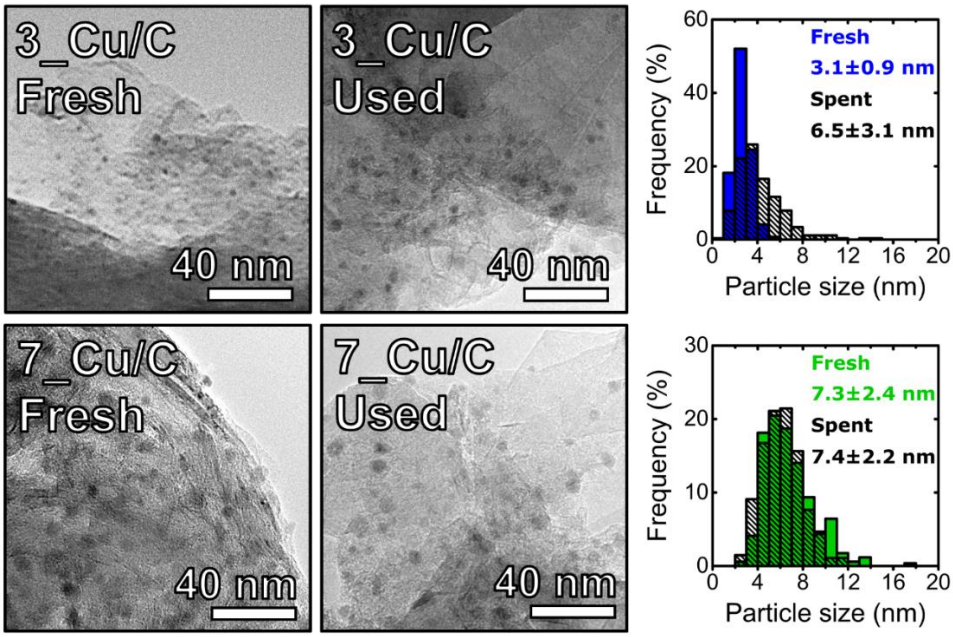

Figure 6.5: *Transmission electron micrographs for the as-synthesized 3_Cu/C and 7_Cu/C catalysts (fresh, solid bars) and after 100 h catalysis (used, striped bars), with corresponding particle size distributions and surface-averaged Cu particle sizes including standard deviations in the particle size distributions.*

A likely cause for catalyst deactivation in olefin hydrogenation reactions is surface coverage by carbonaceous residues, either from oligomerization side-reactions on the catalyst surface or from oligomer and/or aromatic impurities in the feedstock.[144, 165] However, the amount of oligomers could not be accurately determined, for

instance by thermogravimetric analysis or Raman spectroscopy, due to the difficulty to distinguish the carbonaceous residues from the carbon support material. The observation that the catalysts were stable after the first 30 h on stream suggests that the deactivation was not caused by feedstock impurities, and also that the oligomer formation likely did not occur on the carbon surface but rather on the Cu particle surface. The 3 nm Cu particles deactivated faster than the 7 nm particles, which may be due to a higher surface coverage for the 3 nm particles in combination with more extensive Cu particle growth. The nature of the active site where oligomers may be are formed is unclear, yet it is known that the fraction of different Cu surface sites depends on the Cu particle size, as discussed in Chapter 4, and it appears that the 7 nm particles are the most stable in this study. Using carbon as a chemically inert support for mono-metallic Cu gave an exceptional combination of activity, selectivity and stability in the hydrogenation of butadiene.

6.4 Conclusions

In this chapter, a series of well-defined Cu catalysts was prepared *via* incipient wetness impregnation of graphitic carbon supports. Tuning the Cu loading and heat treatment temperature gave control over the Cu particle size between 1 and 23 nm. The catalyst performance was evaluated for the hydrogenation of butadiene, in 100-fold excess of propene as a model reaction for selective hydrogenation catalysis. The catalysts with Cu particles of around 3 to 7 nm were the most active. The conversion of propene was less than 0.05 % for all carbon-supported Cu catalysts, and found to be size-independent. Remarkably, isothermal catalyst measurements showed a decrease in butadiene conversion during the first 30 h on stream, with stable conversion afterwards. At the same time, the propene conversion decreased from 0.05 to below 0.005 %. The initial deactivation behavior was tentatively ascribed to oligomer formation on the Cu surface, blocking catalytically active sites responsible for both butadiene and propene conversion. The high selectivity and stability in this study indicate the carbon-supported Cu nanoparticles as promising base metal catalysts for various selective hydrogenation reactions.

Acknowledgements

Catherine Louis, Laurent Delannoy, Nazila Masoud and Giorgio Totarella are thanked for inspiring discussions on using Cu catalysts for selective hydrogenation reactions. The authors acknowledge Nynke Krans for support in TEM imaging and Jan Willem de Rijk for support in catalytic experiments.

Chapter 7

Summary, Outlook and Nederlandse Samenvatting

Summary

Fundamental studies in catalysis rely on well-defined catalyst materials and reactions. In this thesis we focused on the synthesis, characterization and performance of carbon-supported Cu-based materials in hydrogenation catalysis. The main aim was to investigate the effects of the Cu nanoparticle size, support interactions and metal oxide promotion, on the catalytic performance in three industrially-relevant gas-phase hydrogenation reactions, namely methanol synthesis by hydrogenation of CO and CO_2, selective hydrogenation of butadiene in excess of propene, and hydrogenation of ethyl acetate to ethanol, a new reaction in our research group. In **Chapter 1**, we give a general introduction to the hydrogenation reactions, the challenges to prepare well-defined Cu catalysts on carbon supports, and the concepts of particle size effects and catalyst promotion related to the work in this thesis.

In **Chapter 2** the rational design of carbon-supported Cu catalysts is discussed. A series of highly dispersed Cu materials was prepared *via* incipient wetness impregnation of surface-oxidized carbon supports, using aqueous Cu nitrate precursor solutions. The number of deposited Cu atoms deposited was tuned with respect to the density of oxygen-containing carbon surface groups, to achieve a uniform distribution of carboxylate-coordinated Cu^{2+} ions on surface-oxidized carbon, without forming any nanoparticles. The highly dispersed Cu materials were used as a starting point for the formation of well-defined Cu nanoparticles, as monitored by *in-situ* XAS and XRD studies. The complete reduction to Cu^0 coincided with formation of Cu^0 particles of several nanometers in size. Thermal sintering was applied to gradually grow the sub-nanometer Cu clusters at room temperature to 10 nm Cu particles at 500 °C. The practical synthesis methods discussed in this chapter allowed efficient preparation of both highly dispersed Cu^{2+} ions and Cu nanoparticles of tailored size.

In **Chapter 3** we discuss the effects of Cu and $CuZnO_x$ particle size on the activity in methanol synthesis. A series of Cu catalysts with particle sizes between 3 and 14 nm was prepared, both in the absence and presence of ZnO_x as promoter. The Cu surface-specific activity increased approximately 4-fold with increasing Cu particle size from 3 to 10 nm and became size-independent for particles above 10 nm. Concurrent with the increasing activity, the specific Cu surface area decreased, which gave the highest Cu weight-normalized conversion for Cu particles of around 6 nm in size. The presence of ZnO_x enhanced the activity around 20 times compared to the un-promoted Cu nanoparticles on carbon. The activity of the ZnO_x-decorated Cu catalysts was at least 50 % higher when supported on carbon compared to silica, indicating superior ZnO_x promotion of Cu on carbon, and the activity increased with increasing particle size up to 10 nm, also in the presence of ZnO_x. We therefore

propose that the size-dependence in $CuZnO_x$ activity originates from a combination of intrinsic Cu particle size effects and effective ZnO_x coverage of the Cu particles.

In **Chapter 4** the impact of Cu particle size on the catalytic activity, selectivity and stability in the hydrogenation of ethyl acetate is discussed. Based on the synthesis methods described in Chapter 3, the Cu particle size was varied from 3 to 14 nm, using graphitic carbon as the support material. The Cu surface-specific catalytic activity increased 4-fold with increasing Cu particle size from 3 to 10 nm, and became constant above 10 nm. The correlation between Cu particle size and activity was hence similar in the hydrogenation of ethyl acetate and methanol synthesis, suggesting that a similar Cu surface site is involved in the rate-determining step in both hydrogenation reactions. The apparent activation energy was around 94 kJ mol^{-1} for all Cu catalysts and thus independent of the particle size, suggesting that the nature of the activity site did not change with Cu particle size. However, the pre-exponential factor in the Arrhenius model increased 4-fold with Cu particle size increasing from 3 to 10 nm and became constant above 10 nm, suggesting a size-dependent abundance of the active sites on the Cu particle surface. Theoretical analysis of Cu surface structure indicated step and kink sites, which represent higher Miller index surfaces, as the active sites in the gas-phase hydrogenation reaction.

Chapter 5 described a study of the effectivity of MnO_x as a promoter on the activity, selectivity and stability in the Cu-catalyzed hydrogenation of ethyl acetate. A series of MnO_x-promoted Cu catalysts was prepared *via* co-impregnation of a graphitic carbon support, using aqueous mixed Mn and Cu nitrate precursor solutions. As discussed in Chapters 3 and 4, the highest Cu weight-normalized activities for the hydrogenation reactions were obtained with Cu particles of around 6 nm in size. We therefore tuned the synthesis conditions to keep the MnO_x-Cu particle size constant around 6 nm, while systematically varying the Mn loading between 0–33 mol% Mn/(Cu+Mn). The presence of 11 mol% Mn strongly enhanced the catalytic activity, by lowering the activation energy for the rate-determining step from 102 to 54 kJ mol^{-1}. The promoter effect was attributed to the formation of highly active sites at the interface between MnO_x and Cu. Tuning the Mn loading to an intermediate level of around 11 mol% provided a combination of high catalyst activity, selectivity and stability.

In **Chapter 6** we discuss the activity, selectivity and stability of carbon-supported Cu catalysts for the selective hydrogenation of butadiene in a 100-fold excess of propene. The synthesis methods for carbon-supported Cu catalysts as described in Chapter 3, were expanded to vary the Cu particle size from 1 to 23 nm. A clear influence of the Cu size on the catalytic activity was observed, with the highest weight-normalized activity for Cu particles around 3 to 7 nm. All Cu catalysts showed more than 99.95 % reactant selectivity towards butadiene. The 7 nm Cu on carbon catalyst retained 93 % of the initial conversion after 100 hours catalysts under

isothermal reaction conditions, and thus clearly outperformed Cu catalysts on metal oxide supports reported in literature, which was attributed to limited oligomer formation. The high reactant selectivity and catalyst stability make the Cu on carbon catalysts promising candidates for a range of selective hydrogenation reactions.

In summary, the physicochemical phenomena involved in catalyst assembly were investigated on the nanometer scale for a series of carbon-supported Cu catalysts, which allowed us to prepare model catalysts with tailored structures. The work presented in this thesis showed that disentangling the effects of Cu particle size, supports and promoters, facilitated the establishment of structure-performance relationships in three important hydrogenation reactions. The advanced understanding of these relationships may assist in developing more active, selective and stable Cu-based hydrogenation catalysts, which may ultimately contribute to more efficient use of energy and materials resources.

Outlook

The methods for preparing carbon-supported Cu catalysts as described in this thesis may facilitate fundamental studies for other Cu-catalyzed reactions, such as the (electrochemical) hydrogenation of carbon dioxide or oxidation reactions. The carboxylate-coordinated Cu ions on surface-oxidized carbon are promising as catalysts with high atom efficiency and may offer unique catalytic properties as compared to conventional nanoparticulate Cu catalysts. Although our research showed that smaller Cu nanoparticles exhibit a lower intrinsic hydrogenation activity than larger particles, it may be particularly interesting to study the activity in Cu-catalyzed oxidation reactions. The systematic approaches to vary the metal particle size, and deconvolute the support, promoter and particle size effects, may be also applicable for other metals and promoters.

An interesting question in methanol synthesis is how the ZnO_x promoter interacts with both the active Cu nanoparticles, as well as the catalyst support. In the case of the industrial $Cu/ZnO/Al_2O_3$ catalyst, a potentially large amount of Zn-based spectator species can hinder the advanced understanding of the ZnO_x promoter effects. In our research, the use of graphitic carbon proved a strong tool, to investigate the intrinsic Cu-based catalyst. As reported in Chapter 3, ZnO_x-promoted Cu particles as small as 4 nm were prepared. Moreover, un-promoted Cu particles as small 1 nm were reported in Chapter 6. Well-defined and ultra-small $CuZnO_x$ nanoparticles open up possibilities from XAS analysis, in particular to monitor the changes in the Zn oxidation state and dispersion during catalysis, to elucidate the nature of the active site in ZnO_x-promoted Cu catalysts for methanol synthesis.

It is generally known that the composition of the reaction gas mixture (CO, CO_2, H_2) for methanol synthesis, can play a major role on the catalytic activity. To better understanding of the complex reaction mechanisms, it could be beneficial to elucidate the effects of Cu particle size and promoters on the activity in the (reverse) water gas shift reaction. With the increasing interest in CO_2 utilization, it would be also interesting to also investigate Cu particle size effects, promoters or bi-metallic catalysts for methanol synthesis from CO_2 in absence of CO.

MnO_x is an active, selective and stable promoter for the Cu-catalyzed hydrogenation of ethyl acetate in Chapter 5. The production of renewable short chain oxygenates warrants research into other ester reactants, such as methyl acetate and various alkyl oxalates. In addition, it could be interesting to compare the efficacy of different promoters, such as oxides of Mn, Zn, Cr, Mo, Fe and Mg, using carbon as an inert support material. Finally, the influence of catalyst poisons, such as water and chlorine species is largely neglected in academic literature, yet is crucial for efficient operation in the chemical industry. The MnO_x promoter limited the growth of Cu

particles in the presence of water, under reaction conditions. This indicates the potential of MnO_x as a promoter in other hydrogenation reactions where water is largely present, such as Co- and Fe-catalyzed Fischer Tropsch synthesis. A detailed study into poisoning of MnO_x-promoted Cu catalyst, in the hydrogenation of ethyl acetate as a model reaction, could benefit the design of more efficient promoted catalysts and reaction conditions.

Using carbon as a support material for Cu was essential to achieve high catalyst stability in the selective hydrogenation of butadiene. An unresolved question is whether Cu-based activity can be increased, while maintaining high selectivity and catalyst stability, which could be investigated for metal oxide-promoters and bi-metallic catalysts such as alloys of Cu and Ni, Co or Fe. Finally, alkynes such as acetylene and propyne are generally more reactive than dienes, and it would thus be interesting to study the general applicability of the carbon-supported Cu catalysts for the selective hydrogenation of alkynes in excess of mono-olefins.

Nederlandse samenvatting

Katalyse

Meer dan 85 % van alle chemische producten (denk hierbij aan plastics, benzine, verf en medicijnen) heeft ten minste één gekatalyseerde chemische omzetting ondergaan tijdens het productieproces.[12] Katalyse is daarom een essentieel onderdeel van de chemische industrie, welke voor 8 % van het bruto-binnenlands product bijdraagt aan de Nederlandse economie. Wat is dan eigenlijk een katalysator? Een chemische omzetting heeft doorgaans een energiebarrière, die met verhoogde temperatuur overwonnen moet worden, om de reactie plaats te laten vinden. Een katalysator is een materiaal dat de reactie versnelt of zelfs überhaupt mogelijk maakt, zonder daarbij zelf te worden verbruikt. De katalysator verlaagt de energiebarrière, door de uitgangsstoffen met elkaar in contact te brengen waardoor de reactie bij lagere temperatuur kan plaatsvinden. Een chemische reactie kan vergeleken worden met het fietsen over een berg heen (Figuur 7.1). Er is veel energie nodig om op de bergtop te komen, maar daarna volgt gemakkelijk afdalen naar het dal. Als de berg echter hoog is, duurt het erg lang of is het zelfs onmogelijk om er over heen te komen. Een katalysator verlaagt de bergtop aanzienlijk, waardoor er minder energie nodig is en het dal sneller bereikt kan worden. Het gebruik van katalysatoren leidt derhalve vaak tot een lager energieverbruik, minder afval en speelt een essentiële rol voor de overgang van fossiele naar hernieuwbare grondstoffen.

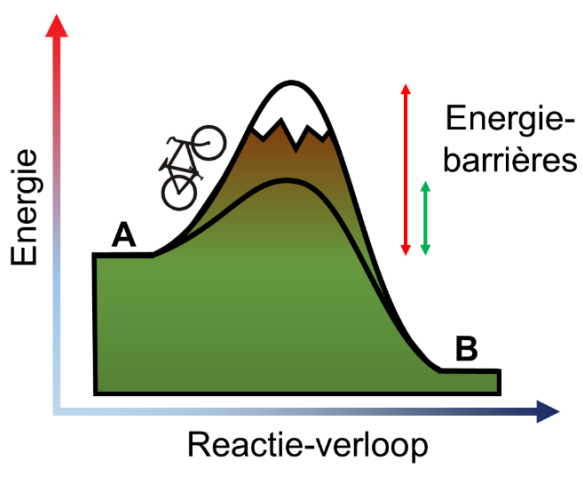

Figuur 7.1: *Schematisch energieprofiel voor een chemische reactie van uitgangsstof A naar product B over een energiebarrière. De katalysator verlaagt de benodigde temperatuur om over de berg heen te komen, door een alternatieve route te bieden.*

Het chemische element koper is een zeer interessant metaal voor katalytische toepassingen, door de grote natuurlijke aanwezigheid, lage prijs en speciale eigenschappen. In dit proefschrift worden de eigenschappen van koper-gebaseerde katalysatoren onderzocht voor het versnellen van hydrogeneringsreacties in de gasfase, dat wil zeggen het koppelen van waterstof aan verschillende uitgangsstoffen. Een praktisch voorbeeld van een hydrogeneringsreactie is de omzetting van onverzadigde plantenoliën naar margarine. Een ander interessant voorbeeld is de hydrogenering van het broeikasgas koolstofdioxide naar methanol als een waardevolle chemische bouwsteen. Wanneer waterstof bindt aan koper, kan het waterstofmolecuul uit elkaar vallen en gemakkelijk gekoppeld worden aan de uitgangsstoffen, en zodoende de hydrogeneringsreacties versnellen. De aanwezigheid van bijvoorbeeld chroomoxide, zinkoxide of mangaanoxide als promotor (een toegevoegde stof die zelf niet reactief is, maar wel de eigenschappen van koper verbetert) maken kopermaterialen tot veelgebruikte katalysatoren voor industriële reacties.

Nanodeeltjes

De meeste chemische reacties vinden alleen plaats op het oppervlak van het metaal. Het is daarom gunstig om fijn verdeelde poeders met een groot metaaloppervlak per eenheid van gewicht van het metaal te gebruiken. De meeste metalen die gebruikt worden in de katalyse bestaan derhalve uit nanodeeltjes, dat wil zeggen deeltjes met een diameter van 1 tot 100 nanometer. Het voorvoegsel nano- komt van het Latijnse woord *nanus* (dwerg) en wordt gebruikt om aan te geven dat een nanometer één miljard keer kleiner is dan een meter. De verhouding tussen de diameter van de aarde ($1{,}3*10^{7}$ m ofwel 13.000.000 meter) en een voetbal ($2{,}2*10^{-1}$ m ofwel 0,22 meter) is ongeveer dezelfde als de verhouding tussen de voetbal en een metaal nanodeeltje dat bestaat uit zo'n 500 atomen[188] ($2{,}2*10^{-9}$ m ofwel 0,000000022 meter), zoals weergegeven in Figuur 7.2.

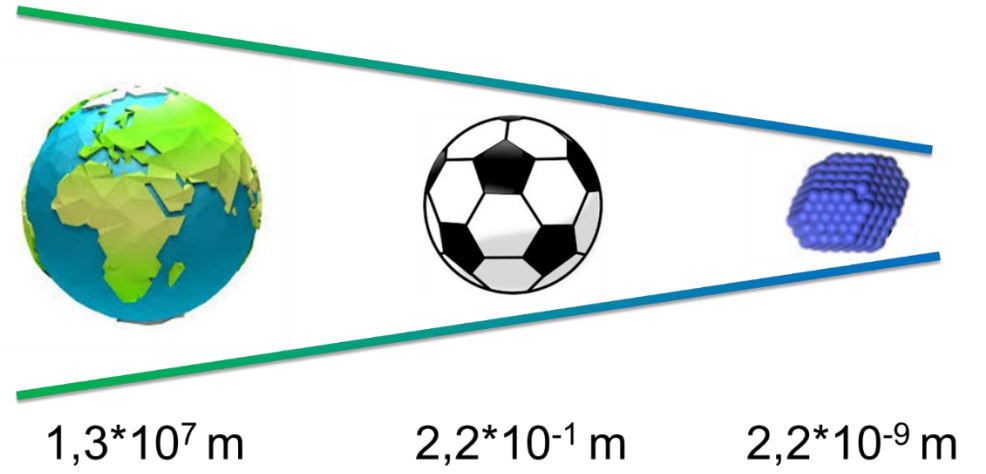

Figuur 7.2: *Verhouding tussen diameters van de aarde, een voetbal en een typisch metaalnanodeeltje.*

De eigenschappen van metalen hangen typisch sterk af van het soort metaal en hoe fijn het metaalpoeder verdeeld is. Zo worden sieraden van zilver, goud en platina gemaakt, omdat deze edelmetalen niet door de lucht aangetast worden en hun glans lang behouden, in tegenstelling tot onedele metalen zoals koper en ijzer die aan de lucht roesten. Nanodeeltjes van zowel onedele metalen als edelmetalen worden gebruikt als katalysatoren voor chemische reacties. Nanodeeltjes hebben namelijk andere eigenschappen dan grote deeltjes. Dit komt voornamelijk doordat het oppervlakte van een nanodeeltje veel reactieve atomen bevat, die de uitgangsstoffen sterker binden en gemakkelijker tot product omzetten, vergeleken met grote deeltjes. Om de reactieve metaaldeeltjes stabiel te houden, worden deze doorgaans verankerd op een poreus dragermateriaal zoals silica, titania of koolstof. Nanodeeltjes zijn niet zichtbaar met het menselijk oog en zelfs de beste optische microscopen bieden geen uitkomst om de deeltjesgrootte nauwkeurig te kunnen beschrijven. Om te nanodeeltjes te kunnen “zien”, zijn speciale microscopen nodig, die niet werken met zichtbaar licht, maar met een versnelde elektronenbundel. De transmissie of de weerkaatsing van de elektronen wordt in een elektronenmicroscoop omgezet in een digitale foto.

Doel van dit onderzoek

Om op rationele wijze betere katalysatoren te ontwerpen, in plaats van gissen en uitproberen, is het belangrijk om te begrijpen hoe de metaaleigenschappen samenhangen met de katalytische werking. Ondanks dat koperkatalysatoren al decennialang gebruikt worden op industriële schaal, resteert een aantal uitdagende wetenschappelijke vragen. Zo is het nog grotendeels onduidelijk wat de invloed is van de koperdeeltjesgrootte onder de 20 nm, op de katalytische activiteit in verschillende hydrogeneringsreacties. Daarnaast is er maar beperkte kennis over de interacties tussen de kopernanodeeltjes en het dragermateriaal en/of promotoren, en hoe deze interacties de katalytische werking beïnvloeden. Het voornaamste doel van dit onderzoek was het systematisch en van elkaar afzonderlijk bestuderen van de deeltjesgrootte-, drager- en promotor-effecten op de katalytische eigenschappen in hydrogeneringsreacties.

Fundamenteel onderzoek is gebaat bij goed gedefinieerde materialen. De katalysatoren in dit proefschrift zijn daarom ontwikkeld met specifieke deeltjesgrootten. Het gebruik van grafitisch koolstof als dragermateriaal voor kopernanodeeltjes was erg belangrijk. Elektronenmicroscopie heeft in dit onderzoek een belangrijke rol gespeeld in de karakterisering van de katalysatoren. In Hoofdstuk 2 worden het ontwerp en de bereiding van koolstof-gedragen kopermaterialen besproken. De ontwikkelde methodes leidden tot de bereiding van koper-gebaseerde katalysatoren met afgestemde deeltjesgrootten (Hoofdstukken 2, 3, 4 en 6) en verschillende promotoren (Hoofdstukken 3 en 5). De katalytische eigenschapen voor drie industrieel-relevante hydrogeneringsreacties staan beschreven in dit proefschrift, namelijk de hydrogenering van koolstofmonoxide en koolstofdioxide naar methanol, de hydrogenering van ethylacetaat naar ethanol en de selectieve hydrogenering van butadieen naar buteen. Hieronder staat in detail uitgelegd wat de belangrijkste bevindingen in ieder hoofdstuk zijn.

In **Hoofdstuk 1** wordt een inleiding over de verschillende onderwerpen gegeven die relevant zijn om dit proefschrift te begrijpen. Voor de verschillende onderwerpen worden zowel de wetenschappelijk achtergrond toegelicht als de vragen die wij willen beantwoorden.

In **Hoofdstuk 2** worden het ontwerp en de bereiding van koolstof-gedragen koperkatalysatoren besproken. De typische bereidingsmethode begint de impregnatie van een poreuze koolstof drager met waterige oplossingen van kopernitraat, gevolgd door een droogstap om het water te verdampen en uiteindelijk een hittebehandeling om het kopernitraat te ontleden. Het dragermateriaal was grafiek en stond de bereiding van koperdeeltjes kleiner dan 10 nanometer niet toe. Een oplossing om toch kleinere deeltjes te kunnen maken, was de introductie van zuurstof-bevattende oppervlaktegroepen, door middel van oppervlakte-oxidatie van het dragermateriaal met een geconcentreerde salpeterzuuroplossing (HNO_3). Door

het aantal koperatomen nauwkeurig aan te passen aan het aantal oppervlaktegroepen, zijn wij er in geslaagd om afzonderlijke koper-ionen te stabiliseren op de koolstof drager. Daaropvolgend hebben wij deze materialen gebruikt als startmateriaal, om de vorming en groei van kopernanodeeltjes te bestuderen door middel van geavanceerde röntgen-absorptie en -diffractie methodes. De volledige reductie tot metallisch koper leidde tot de vorming van koperdeeltjes met een grootte van enkele nanometers. Het geleidelijk verhogen van de temperatuur tot 500 °C stelde ons in staat de deeltjesgroei tot 10 nanometer te controleren. De praktische bereidingsmethodes die staan beschreven in dit hoofdstuk maken de weg vrij voor de bereiding van koper katalysatoren met op maat afgestemde deeltjesgrootte.

Hoofdstuk 3 beschrijft de invloed van de grootte van koper- en koperzinkoxide-deeltjes op de katalytische activiteit tijdens de hydrogenering van koolstofmonoxide en koolstofdioxide naar methanol. Met behulp van de methodes uit Hoofdstuk 1, was er voor het eerst een serie van koper- en koperzinkoxide-katalysatoren op basis van koolstof bereid met afgestemde deeltjesgrootten tussen de 3 en 14 nanometer. De oppervlakte-specifieke katalytische activiteit werd ongeveer viermaal groter voor een toenemende koperdeeltjesgrootte tussen 3 en 10 nanometer, terwijl de deze onafhankelijk was van de deeltjesgrootte boven 10 nanometer. De toenemende deeltjesgrootte ging echter ook gepaard met een afnemende hoeveelheid koperoppervlakte per gram koper, wat resulteerde in de hoogste koper gewichts-specifieke conversie voor deeltjes van ongeveer 6 nanometer in diameter. Het gebruik van koolstof als dragermateriaal was essentieel om deze intrinsieke deeltjesgrootte-effecten te onthullen. Tevens had het dragermateriaal een aanzienlijke invloed op de promotoreffecten, vermoedelijk door een verschil in de effectieve bezetting van het koperoppervlakte met zinkoxide. Deze inzichten geven een leidraad voor de ontwikkeling van meer actieve katalysatoren voor de synthese van methanol uit koolstofmonoxide, koolstofdioxide en waterstof.

In **Hoofdstuk 4** wordt de invloed van de koperdeeltjesgrootte tussen de 3 en 14 nanometer op de katalytische activiteit, selectiviteit en stabiliteit in de hydrogenering van ethylacetaat naar ethanol beschreven. De correlatie tussen koperdeeltjesgrootte en katalytische activiteit lijkt sterk op de waargenomen trends voor methanolsynthese, zoals beschreven in Hoofdstuk 3. Dit duidt op de aanwezigheid van plaatsen op het oppervlakte van de kopernanodeeltjes die actief zijn in de snelheidsbepalende stappen voor beide reacties. De activeringsenergie bleef bij benadering constant, terwijl de fractie van actieve plaatsen steeg met toenemende deeltjesgrootte. Theoretische modellen die de samenstelling van het koperoppervlakte uit verschillende oppervlakteplaatsen beschreven, duidden de oppervlakteplaatsen met gemiddelde adsorptiesterkte aan als de actieve plaats voor de hydrogeneringsreactie.

In **Hoofdstuk 5** worden de effecten van mangaanoxide als promotor gerapporteerd, op de activiteit, selectiviteit en stabiliteit in koper-gekatalyseerde hydrogenering van ethylacetaat. Een serie van koperkatalysatoren met mangaanoxide als promotor werd bereid door middel van de gelijktijdige impregnatie van grafitisch koolstof als dragermateriaal met samengestelde waterige koper- en mangaannitraatoplossingen. Zoals beschreven in Hoofdstukken 3 en 4, was de hydrogeneringsactiviteit op basis van kopergewicht het hoogste voor koperdeeltjes van 6 nanometer. Daarom hebben wij de deeltjesgrootte voor koper-mangaanoxide katalysatoren constant gehouden rond 6 nanometer, terwijl de mangaanbelading systematisch gevarieerd werd tussen 0 en 33 mol% Mn/(Cu+Mn). De aanwezigheid van 11 mol% Mn verhoogde de katalytische activiteit sterk, wat samenviel met een verlaging van de schijnbare activeringsenergie van 102 naar 54 kJ mol^{-1}. De fysische raakpunten tussen de kopernanodeeltjes en mangaanoxide nanodeeltjes speelden een grote rol voor de verbeterde katalytische werking, met de hoogste activiteit, selectiviteit en stabiliteit voor de katalysatoren met een mangaanbelading van 11 mol%.

In **Hoofdstuk 6** worden de activiteit, selectiviteit en stabiliteit van koolstof-gedragen koperkatalysatoren besproken voor de selectieve hydrogenering van butadieen in 100-voudige overmaat van propeen. In deze reactie is het essentieel dat butadieen deels gehydrogeneerd wordt naar buteen, maar dat buteen vervolgens niet gehydrogeneerd wordt naar butaan. De synthesemethodes zoals beschreven in Hoofdstuk 3 en 4, werden uitgebreid om de koperdeeltjesgrootte te variëren van 1 tot 23 nanometer. Een duidelijke invloed van de koperdeeltjesgrootte werd waargenomen, met de hoogste gewichts-specifieke activiteit voor koperdeeltjes van 3 tot 7 nanometer. Alle koperkatalysatoren waren meer dan 99.95 % selectief voor de omzetting naar buteen. De koperdeeltjes van 7 nanometer behielden 93 % van de initiële omzettingssnelheid na 100 uur bij constante temperatuur, wat een sterke verbetering betekende ten opzichte van de koperkatalysatoren op basis van metaaloxide als drager zoals gerapporteerd in de wetenschappelijke literatuur. Deze verbetering werd toegeschreven aan een aanzienlijk lagere vervuiling van het koperoppervlakte met het gebruik van de niet reagerende koolstofdrager, ten opzichte van metaaloxidedragers zoals titania. De bijzonder hoge selectiviteit en stabiliteit van de koolstof-gedragen kopernanodeeltjes, duiden dit type katalysator aan als een veelbelovende kandidaat voor verschillende selectieve hydrogeneringsreacties.

Samenvattend hebben wij de fysische en chemische fenomenen die betrokken zijn bij de katalysatorbereiding onderzocht voor koolstof-gedragen koperkatalysatoren. Dit stelde ons in staat om een serie modelkatalysatoren te bereiden met systematische variatie van de deeltjesgrootte. De methodes voor katalysatorbereiding kunnen ook algemene toepassing vinden voor andere metalen en promotoren. Het onderzoek in dit proefschrift heeft aangetoond dat zowel de

koperdeeltjesgrootte als de aard van de dragermaterialen en promotoren een sterke invloed hebben op de werking van de koperkatalysatoren in verschillende hydrogeneringsreacties. Deze nieuwe inzichten kunnen helpen bij de ontwikkeling van meer actieve, selectieve en stabiele katalysatoren, die uiteindelijk bijdragen aan een efficiënter gebruik van energie- en materiaalgrondstoffen voor de productie van essentiële chemicaliën.

References

1. Averill, B. A., *Chemistry: Principles, Patterns, and Applications*. Prentice Hall: 2007.
2. Weller, M. T.; Overton, T. L.; Rourke, J. P.; Armstrong, F. A., *Inorganic Chemistry*. Oxford University Press: 2014.
3. Emsley, J., *Nature's Building Blocks: An A-Z Guide to the Elements*. Oxford University Press: 2011.
4. Klemens, P. G.; Williams, R. K., Thermal conductivity of metals and alloys. *International Metals Reviews* **1986,** 31 (1), 197-215.
5. Constable, E. C., Evolution and understanding of the d-block elements in the periodic table. *Dalton Transactions* **2019,** 48 (26), 9408-9421.
6. Gawande, M. B.; Goswami, A.; Felpin, F.-X.; Asefa, T.; Huang, X.; Silva, R.; Zou, X.; Zboril, R.; Varma, R. S., Cu and Cu-Based Nanoparticles: Synthesis and Applications in Catalysis. *Chemical Reviews* **2016,** 116 (6), 3722-3811.
7. Dhas, N. A.; Raj, C. P.; Gedanken, A., Synthesis, Characterization, and Properties of Metallic Copper Nanoparticles. *Chemistry of Materials* **1998,** 10 (5), 1446-1452.
8. Liu, L.; Corma, A., Metal Catalysts for Heterogeneous Catalysis: From Single Atoms to Nanoclusters and Nanoparticles. *Chemical Reviews* **2018,** 118 (10), 4981-5079.
9. Watari, R.; Kayaki, Y., Copper Catalysts Unleashing the Potential for Hydrogenation of Carbon−Oxygen Bonds. *Asian Journal of Organic Chemistry* **2018,** 7 (10), 2005-2014.
10. Ye, R.-P.; Lin, L.; Li, Q.; Zhou, Z.; Wang, T.; Russell, C. K.; Adidharma, H.; Xu, Z.; Yao, Y.-G.; Fan, M., Recent progress in improving the stability of copper-based catalysts for hydrogenation of carbon–oxygen bonds. *Catalysis Science & Technology* **2018,** 8 (14), 3428-3449.
11. Berzelius, J. J., Årsberättelsen om framsteg i fysik och kemi. **1835**.
12. Barroso, M.; Bitter, J. H.; Broxterman, Q. B.; de Bruin, B.; van Buren, F. R.; Hanefeld, U.; Hensen, E. J. M.; Otto, S.; Vogt, E. T. C.; Weckhuysen, B. M., *Catalysis – Key to a Sustainable Future. Science and Technology Roadmap for Catalysis in the Netherlands*. 2015.
13. Van Santen, R. A., Complementary Structure Sensitive and Insensitive Catalytic Relationships. *Accounts of Chemical Research* **2009,** 42, 57-66.
14. Che, M.; Bennett, C. O., *Advances in Catalysis: The Influence of Particle Size on the Catalytic Properties of Supported Metals*. Academic Press: 1989.
15. Cuenya, B. R., Synthesis and catalytic properties of metal nanoparticles: Size, shape, support, composition, and oxidation state effects. *Thin Solid Films* **2010,** 518 (12), 3127-3150.
16. Reske, R.; Mistry, H.; Behafarid, F.; Roldan Cuenya, B.; Strasser, P., Particle Size Effects in the Catalytic Electroreduction of CO2 on Cu Nanoparticles. *Journal of the American Chemical Society* **2014,** 136 (19), 6978-6986.

17. Yang, X. F.; Wang, A. Q.; Qiao, B. T.; Li, J.; Liu, J. Y.; Zhang, T., Single-Atom Catalysts: A New Frontier in Heterogeneous Catalysis. *Accounts of Chemical Research* **2013,** 46 (8), 1740-1748.
18. De Jong, K. P., *Synthesis of Solid Catalysts*. Wiley: 2009.
19. Twigg, M. V.; Spencer, M. S., Deactivation of supported copper metal catalysts for hydrogenation reactions. *Applied Catalysis A: General* **2001,** 212 (1), 161-174.
20. Munnik, P.; de Jongh, P. E.; de Jong, K. P., Recent Developments in the Synthesis of Supported Catalysts. *Chemical Reviews* **2015,** 115 (14), 6687-6718.
21. James, T. E.; Hemmingson, S. L.; Campbell, C. T., Energy of Supported Metal Catalysts: From Single Atoms to Large Metal Nanoparticles. *ACS Catalysis* **2015,** 5 (10), 5673-5678.
22. Serp, P.; Figueiredo, J. L., *Carbon Materials for Catalysis*. Wiley: 2008.
23. Rodríguez-reinoso, F., The role of carbon materials in heterogeneous catalysis. *Carbon* **1998,** 36 (3), 159-175.
24. Jüntgen, H., Activated carbon as catalyst support: A review of new research results. *Fuel* **1986,** 65 (10), 1436-1446.
25. Rase, H. F., *Handbook of Commercial Catalysts: Heterogeneous Catalysts*. CRC Press: 2000.
26. Jüntgen, H.; Richter, E.; Knoblauch, K.; Hoang-Phu, T., Catalytic NOx reduction by ammonia on carbon catalysts. *Chemical Engineering Science* **1988,** 43 (3), 419-428.
27. Mochida, I.; Korai, Y.; Shirahama, M.; Kawano, S.; Hada, T.; Seo, Y.; Yoshikawa, M.; Yasutake, A., Removal of SOx and NOx over activated carbon fibers. *Carbon* **2000,** 38 (2), 227-239.
28. Bahuguna, A.; Kumar, A.; Krishnan, V., Carbon-Support-Based Heterogeneous Nanocatalysts: Synthesis and Applications in Organic Reactions. *Asian Journal of Organic Chemistry* **2019,** 8 (8), 1263-1305.
29. Fortuny, A.; Font, J.; Fabregat, A., Wet air oxidation of phenol using active carbon as catalyst. *Applied Catalysis B: Environmental* **1998,** 19 (3), 165-173.
30. Brown, D. E.; Edmonds, T.; Joyner, R. W.; McCarroll, J. J.; Tennison, S. R., The Genesis and Development of the Commercial BP Doubly Promoted Catalyst for Ammonia Synthesis. *Catalysis Letters* **2014,** 144 (4), 545-552.
31. Kowalczyk, Z.; Sentek, J.; Jodzis, S.; Mizera, E.; Góralski, J.; Paryjczak, T.; Diduszko, R., An alkali-promoted ruthenium catalyst for the synthesis of ammonia, supported on thermally modified active carbon. *Catalysis Letters* **1997,** 45 (1), 65-72.
32. Cameron, D. S.; Cooper, S. J.; Dodgson, I. L.; Harrison, B.; Jenkins, J. W., Carbons as supports for precious metal catalysts. *Catalysis Today* **1990,** 7 (2), 113-137.
33. Ramli, Z. A. C.; Kamarudin, S. K., Platinum-Based Catalysts on Various Carbon Supports and Conducting Polymers for Direct Methanol Fuel Cell Applications: a Review. *Nanoscale Research Letters* **2018,** 13 (1), 410.

34. Lamme, W. S.; Zecevic, J.; de Jong, K. P., Influence of Metal Deposition and Activation Method on the Structure and Performance of Carbon Nanotube Supported Palladium Catalysts. *Chemcatchem* **2018,** 10 (7), 1552-1555.
35. Nath Prajapati, Y.; Verma, N., Hydrodesulfurization of Thiophene on Activated Carbon Fiber Supported NiMo Catalysts. *Energy & Fuels* **2018,** 32 (2), 2183-2196.
36. Daly, F. P.; Brinen, J. S.; Schmitt, J. L., A wide pore carbon-supported hydrodesulfurization catalyst. *Applied Catalysis* **1984,** 11 (1), 161-164.
37. Moreno-Castilla, C.; Carrasco-Marin, F., Cobalt catalysts supported on activated carbons: preparation and behaviour in the hydrogenation of carbon oxides. *Journal of the Chemical Society, Faraday Transactions* **1995,** 91 (19), 3519-3524.
38. Oschatz, M.; Hofmann, J. P.; van Deelen, T. W.; Lamme, W. S.; Krans, N. A.; Hensen, E. J. M.; de Jong, K. P., Effects of the Functionalization of the Ordered Mesoporous Carbon Support Surface on Iron Catalysts for the Fischer-Tropsch Synthesis of Lower Olefins. *Chemcatchem* **2017,** 9 (4), 620-628.
39. Xie, J. X.; Galvis, H. M. T.; Koeken, A. C. J.; Kirilin, A.; Dugulan, A. I.; Ruitenbeek, M.; de Jong, K. P., Size and Promoter Effects on Stability of Carbon-Nanofiber-Supported Iron -Based Fischer-Tropsch Catalysts. *Acs Catalysis* **2016,** 6 (6), 4017-4024.
40. Figueiredo, J. L., Functionalization of porous carbons for catalytic applications. *Journal of Materials Chemistry A* **2013,** 1 (33), 9351-9364.
41. Yusuf, M.; Elfghi, F. M.; Zaidi, S. A.; Abdullah, E. C.; Khan, M. A., Applications of graphene and its derivatives as an adsorbent for heavy metal and dye removal: a systematic and comprehensive overview. *RSC Advances* **2015,** 5 (62), 50392-50420.
42. Noked, M.; Soffer, A.; Aurbach, D., The electrochemistry of activated carbonaceous materials: past, present, and future. *Journal of Solid State Electrochemistry* **2011,** 15 (7), 1563.
43. Falcao, E. H.; Wudl, F., Carbon allotropes: beyond graphite and diamond. *Journal of Chemical Technology & Biotechnology* **2007,** 82 (6), 524-531.
44. Gupta, T., *Carbon: The Black, the Gray and the Transparent*. Springer: 2018.
45. Machado, B.; Serp, P., *Nanostructured Carbon Materials for Catalysis*. The Royal Society of Chemistry: 2015.
46. Pauling, L., The nature of the chemical bond. Application of results obtained from the quantum mechanics and from a theory of paramagnetic susceptibility to the structure of molecules. *Journal of the American Chemical Society* **1931,** 53 (4), 1367-1400.
47. Busca, G., *Heterogeneous Catalytic Materials*. Elsevier: 2014.
48. Zhang, S.; Cui, Y.; Wu, B.; Song, R.; Song, H.; Zhou, J.; Chen, X.; Liu, J.; Cao, L., Control of graphitization degree and defects of carbon blacks through ball-milling. *RSC Advances* **2014,** 4 (1), 505-509.
49. Shafeeyan, M. S.; Daud, W. M. A. W.; Houshmand, A.; Shamiri, A., A review on surface modification of activated carbon for carbon dioxide adsorption. *Journal of Analytical and Applied Pyrolysis* **2010,** 89 (2), 143-151.

50. Dongil, A. B.; Bachiller-Baeza, B.; Guerrero-Ruiz, A.; Rodríguez-Ramos, I.; Martínez-Alonso, A.; Tascón, J. M. D., Surface chemical modifications induced on high surface area graphite and carbon nanofibers using different oxidation and functionalization treatments. *Journal of Colloid and Interface Science* **2011,** 355 (1), 179-189.
51. Salame, I. I.; Bandosz, T. J., Surface Chemistry of Activated Carbons: Combining the Results of Temperature-Programmed Desorption, Boehm, and Potentiometric Titrations. *Journal of Colloid and Interface Science* **2001,** 240 (1), 252-258.
52. Dimiev, A. M.; Alemany, L. B.; Tour, J. M., Graphene Oxide. Origin of Acidity, Its Instability in Water, and a New Dynamic Structural Model. *ACS Nano* **2013,** 7 (1), 576-588.
53. Dandekar, A.; Baker, R. T. K.; Vannice, M. A., Characterization of activated carbon, graphitized carbon fibers and synthetic diamond powder using TPD and DRIFTS. *Carbon* **1998,** 36 (12), 1821-1831.
54. Fuente, E.; Menéndez, J. A.; Suárez, D.; Montes-Morán, M. A., Basic Surface Oxides on Carbon Materials: A Global View. *Langmuir* **2003,** 19 (8), 3505-3511.
55. Hao, X.; Quach, L.; Korah, J.; Spieker, W. A.; Regalbuto, J. R., The control of platinum impregnation by PZC alteration of oxides and carbon. *Journal of Molecular Catalysis a-Chemical* **2004,** 219 (1), 97-107.
56. Pompe, C. E.; Slagter, M.; de Jongh, P. E.; de Jong, K. P., Impact of heterogeneities in silica-supported copper catalysts on their stability for methanol synthesis. *Journal of Catalysis* **2018,** 365, 1-9.
57. Toupance, T.; Kermarec, M.; Lambert, J.-F.; Louis, C., Conditions of Formation of Copper Phyllosilicates in Silica-Supported Copper Catalysts Prepared by Selective Adsorption. *The Journal of Physical Chemistry B* **2002,** 106 (9), 2277-2286.
58. Zhu, S.; Gao, X.; Zhu, Y.; Fan, W.; Wang, J.; Li, Y., A highly efficient and robust Cu/SiO2 catalyst prepared by the ammonia evaporation hydrothermal method for glycerol hydrogenolysis to 1,2-propanediol. *Catalysis Science & Technology* **2015,** 5 (2), 1169-1180.
59. Zhu, Y.-M.; Shi, L., Zn promoted Cu–Al catalyst for hydrogenation of ethyl acetate to alcohol. *Journal of Industrial and Engineering Chemistry* **2014,** 20 (4), 2341-2347.
60. Tangale, N. P.; Niphadkar, P. S.; Deshpande, S. S.; Joshi, P. N., Dehydrogenation of cyclohexanol over Cu/Al2O3 catalysts prepared with different precipitating agents. *Applied Catalysis A: General* **2013,** 467, 421-429.
61. Jobbágy, M.; Mariño, F.; Schönbrod, B.; Baronetti, G.; Laborde, M., Synthesis of Copper-Promoted CeO2 Catalysts. *Chemistry of Materials* **2006,** 18 (7), 1945-1950.
62. Shang, H.; Zhang, X.; Xu, J.; Han, Y., Effects of preparation methods on the activity of CuO/CeO2 catalysts for CO oxidation. *Frontiers of Chemical Science and Engineering* **2017,** 11 (4), 603-612.
63. Kawamoto, A. M.; Pardini, L. C.; Rezende, L. C., Synthesis of copper chromite catalyst. *Aerospace Science and Technology* **2004,** 8 (7), 591-598.

64. Prasad, R.; Singh, P., Applications and Preparation Methods of Copper Chromite Catalysts: A Review. *2011* **2011**, 51.
65. Mota, N.; Guil-Lopez, R.; Pawelec, B. G.; Fierro, J. L. G.; Navarro, R. M., Highly active Cu/ZnO–Al catalyst for methanol synthesis: effect of aging on its structure and activity. *RSC Advances* **2018,** 8 (37), 20619-20629.
66. Hartig, M. A. J.; Peukert, W.; Jacobsen, N.; Leuthold, A., A model-based precipitation study of copper-based catalysts. *AIChE Journal* **2015,** 61 (7), 2104-2116.
67. Bart, J. C. J.; Sneeden, R. P. A., Copper-zinc oxide-alumina methanol catalysts revisited. *Catalysis Today* **1987,** 2 (1), 1-124.
68. Tang, Q.; Gong, X.; Zhao, P.; Chen, Y.; Yang, Y., Copper–manganese oxide catalysts supported on alumina: Physicochemical features and catalytic performances in the aerobic oxidation of benzyl alcohol. *Applied Catalysis A: General* **2010,** 389 (1), 101-107.
69. Baksi, A.; Cocke, D. L.; Gomes, A.; Gossage, J.; Riggs, M.; Beall, G.; McWhinney, H. In *Characterization of Minerals, Metals, and Materials 2016*, Ikhmayies, S. J., Li, B., Carpenter, J. S., Hwang, J.-Y., Monteiro, S. N., Li, J., Firrao, D., Zhang, M., Peng, Z., Escobedo-Diaz, J. P., Bai, C., Eds. Springer International Publishing: Cham, 2016; pp 151-158.
70. Stötzel, J.; Lützenkirchen-Hecht, D.; Frahm, R.; Kimmerle, B.; Baiker, A.; Nachtegaal, M.; Beier, M. J.; Grunwaldt, J. D., Reduction and re-oxidation of Cu/Al2O3catalysts investigated with quick-scanning XANES and EXAFS. *Journal of Physics: Conference Series* **2009,** 190, 012153.
71. Chatterjee, R.; Kuld, S.; van den Berg, R.; Chen, A.; Shen, W.; Christensen, J. M.; Jensen, A. D.; Sehested, J., Mapping Support Interactions in Copper Catalysts. *Topics in Catalysis* **2019**.
72. Van den Berg, R.; Parmentier, T. E.; Elkjaer, C. F.; Gommes, C. J.; Sehested, J.; Helveg, S.; de Jongh, P. E.; de Jong, K. P., Support Functionalization To Retard Ostwald Ripening in Copper Methanol Synthesis Catalysts. *Acs Catalysis* **2015,** 5 (7), 4439-4448.
73. Wang, G.; van den Berg, R.; de Mello Donega, C.; de Jong, K. P.; de Jongh, P. E., Silica-supported Cu2O nanoparticles with tunable size for sustainable hydrogen generation. *Applied Catalysis B: Environmental* **2016,** 192, 199-207.
74. Ye, C.-L.; Guo, C.-L.; Zhang, J.-L., Highly active and stable CeO2–SiO2 supported Cu catalysts for the hydrogenation of methyl acetate to ethanol. *Fuel Processing Technology* **2016,** 143, 219-224.
75. Delannoy, L.; Thrimurthulu, G.; Reddy, P. S.; Methivier, C.; Nelayah, J.; Reddy, B. M.; Ricolleau, C.; Louis, C., Selective hydrogenation of butadiene over TiO2 supported copper, gold and gold-copper catalysts prepared by deposition-precipitation. *Physical Chemistry Chemical Physics* **2014,** 16 (48), 26514-26527.
76. Wang, Z.; Brouri, D.; Casale, S.; Delannoy, L.; Louis, C., Exploration of the preparation of Cu/TiO2 catalysts by deposition-precipitation with urea for selective hydrogenation of unsaturated hydrocarbons. *Journal of Catalysis* **2016,** 340, 95-106.

77. Eskandari, S.; Tate, G.; Leaphart, N. R.; Regalbuto, J. R., Nanoparticle Synthesis via Electrostatic Adsorption Using Incipient Wetness Impregnation. *ACS Catalysis* **2018,** 8 (11), 10383-10391.
78. Zecevic, J.; Vanbutsele, G.; de Jong, K. P.; Martens, J. A., Nanoscale intimacy in bifunctional catalysts for selective conversion of hydrocarbons. *Nature* **2015,** 528, 245.
79. Bourikas, K.; Kordulis, C.; Lycourghiotis, A., The Role of the Liquid-Solid Interface in the Preparation of Supported Catalysts. *Catalysis Reviews* **2006,** 48 (4), 363-444.
80. Brunelle, J. P., Preparation of catalysts by metallic complex adsorption on mineral oxides. *Pure and Applied Chemistry* **1978,** 50 (9-10), 1211-1229.
81. Lomelí-Rosales, D. A.; Delgado, J. A.; Díaz de los Bernardos, M.; Pérez-Rodríguez, S.; Gual, A.; Claver, C.; Godard, C., A General One-Pot Methodology for the Preparation of Mono- and Bimetallic Nanoparticles Supported on Carbon Nanotubes: Application in the Semi-hydrogenation of Alkynes and Acetylene. *Chemistry – A European Journal* **2019,** 25 (35), 8321-8331.
82. Bae, K.-L.; Kim, J.; Lim, C. K.; Nam, K. M.; Song, H., Colloidal zinc oxide-copper(I) oxide nanocatalysts for selective aqueous photocatalytic carbon dioxide conversion into methane. *Nature Communications* **2017,** 8 (1), 1156.
83. Ren, X.; Chen, D.; Tang, F., Shape-Controlled Synthesis of Copper Colloids with a Simple Chemical Route. *The Journal of Physical Chemistry B* **2005,** 109 (33), 15803-15807.
84. Calvino-Casilda, V.; López-Peinado, A. J.; Durán-Valle, C. J.; Martín-Aranda, R. M., Last Decade of Research on Activated Carbons as Catalytic Support in Chemical Processes. *Catalysis Reviews* **2010,** 52 (3), 325-380.
85. Delgado, J. A.; Benkirane, O.; Claver, C.; Curulla-Ferré, D.; Godard, C., Advances in the preparation of highly selective nanocatalysts for the semi-hydrogenation of alkynes using colloidal approaches. *Dalton Transactions* **2017,** 46 (37), 12381-12403.
86. Van den Berg, R.; Prieto, G.; Korpershoek, G.; van der Wal, L. I.; van Bunningen, A. J.; Lægsgaard-Jørgensen, S.; de Jongh, P. E.; de Jong, K. P., Structure sensitivity of Cu and CuZn catalysts relevant to industrial methanol synthesis. *Nature Communications* **2016,** 7, 13057.
87. Munnik, P.; Wolters, M.; Gabrielsson, A.; Pollington, S. D.; Headdock, G.; Bitter, J. H.; de Jongh, P. E.; de Jong, K. P., Copper Nitrate Redispersion To Arrive at Highly Active Silica-Supported Copper Catalysts. *The Journal of Physical Chemistry C* **2011,** 115 (30), 14698-14706.
88. Dandekar, A.; Baker, R. T. K.; Vannice, M. A., Carbon-Supported Copper Catalysts. *Journal of Catalysis* **1999,** 184 (2), 421-439.
89. Kvande, I.; Chen, D.; Rønning, M.; Venvik, H. J.; Holmen, A., Highly active Cu-based catalysts on carbon nanofibers for isopropanol dehydrogenation. *Catalysis Today* **2005,** 100 (3-4), 391-395.
90. Ma, J.; Park, C.; Rodriguez, N. M.; Baker, R. T. K., Characteristics of Copper Particles Supported on Various Types of Graphite Nanofibers. *The Journal of Physical Chemistry B* **2001,** 105 (48), 11994-12002.

91. Zhang, G.; Li, Z.; Zheng, H.; Fu, T.; Ju, Y.; Wang, Y., Influence of the surface oxygenated groups of activated carbon on preparation of a nano Cu/AC catalyst and heterogeneous catalysis in the oxidative carbonylation of methanol. *Applied Catalysis B: Environmental* **2015,** 179, 95-105.
92. Wang, Q.-N.; Shi, L.; Lu, A.-H., Highly Selective Copper Catalyst Supported on Mesoporous Carbon for the Dehydrogenation of Ethanol to Acetaldehyde. *ChemCatChem* **2015,** 7 (18), 2846-2852.
93. Bartholomew, C. H., Mechanisms of catalyst deactivation. *Applied Catalysis A: General* **2001,** 212 (1), 17-60.
94. Berber-Mendoza, M. S.; Leyva-Ramos, R.; Cerino-Cordoba, F. J.; Mendoza-Barron, J.; Garcia, H. J. A.; Flores-Cano, J. V., Role of Carboxylic Sites in the Adsorption of Nickel (II) and Zinc (II) onto Plain and Oxidized Activated Carbon Fibers. *Water, Air, & Soil Pollution* **2013,** 224 (7), 1604.
95. van der Lee, M. K.; van Dillen, J.; Bitter, J. H.; de Jong, K. P., Deposition Precipitation for the Preparation of Carbon Nanofiber Supported Nickel Catalysts. *Journal of the American Chemical Society* **2005,** 127 (39), 13573-13582.
96. Suh, D. J.; Tae-Jin, P.; Ihm, S.-K., Effect of surface oxygen groups of carbon supports on the characteristics of Pd/C catalysts. *Carbon* **1993,** 31 (3), 427-435.
97. Bertau, M.; Offermanns, H.; Plass, L.; Schmidt, F.; Wernicke, H.-J., *Methanol: The Basic Chemical and Energy Feedstock of the Future*. Springer: 2014.
98. Olah, G. A.; Goeppert, A.; Prakash, G. K. S., *Beyond Oil and Gas: The Methanol Economy*. Wiley: 2011.
99. Waugh, K. C., Methanol Synthesis. *Catalysis Today* **1992,** 15 (1), 51-75.
100. Sutton, D.; Kelleher, B.; Ross, J. R. H., Review of literature on catalysts for biomass gasification. *Fuel Processing Technology* **2001,** 73 (3), 155-173.
101. Arena, U., Process and technological aspects of municipal solid waste gasification. A review. *Waste Management* **2012,** 32 (4), 625-639.
102. Galadima, A.; Muraza, O., From synthesis gas production to methanol synthesis and potential upgrade to gasoline range hydrocarbons: A review. *Journal of Natural Gas Science and Engineering* **2015,** 25, 303-316.
103. Kamm, B., Production of Platform Chemicals and Synthesis Gas from Biomass. *Angewandte Chemie International Edition* **2007,** 46 (27), 5056-5058.
104. Behrens, M., Promoting the Synthesis of Methanol: Understanding the Requirements for an Industrial Catalyst for the Conversion of CO2. *Angewandte Chemie International Edition* **2016,** 55 (48), 14906-14908.
105. Behrens, M.; Studt, F.; Kasatkin, I.; Kühl, S.; Hävecker, M.; Abild-Pedersen, F.; Zander, S.; Girgsdies, F.; Kurr, P.; Kniep, B.-L.; Tovar, M.; Fischer, R. W.; Nørskov, J. K.; Schlögl, R., The Active Site of Methanol Synthesis over Cu/ZnO/Al_2O_3 Industrial Catalysts. *Science* **2012,** 336 (6083), 893-897.
106. Karelovic, A.; Galdames, G.; Medina, J. C.; Yévenes, C.; Barra, Y.; Jiménez, R., Mechanism and structure sensitivity of methanol synthesis from CO2 over SiO2-supported Cu nanoparticles. *Journal of Catalysis* **2019,** 369, 415-426.

107. Klier, K.; Chatikavanij, V.; Herman, R. G.; Simmons, G. W., Catalytic synthesis of methanol from COH2: IV. The effects of carbon dioxide. *Journal of Catalysis* **1982,** 74 (2), 343-360.
108. Kuld, S.; Thorhauge, M.; Falsig, H.; Elkjær, C. F.; Helveg, S.; Chorkendorff, I.; Sehested, J., Quantifying the promotion of Cu catalysts by ZnO for methanol synthesis. *Science* **2016,** 352 (6288), 969.
109. Kung, H. H., Deactivation of methanol synthesis catalysts - a review. *Catalysis Today* **1992,** 11 (4), 443-453.
110. Studt, F.; Behrens, M.; Kunkes, E. L.; Thomas, N.; Zander, S.; Tarasov, A.; Schumann, J.; Frei, E.; Varley, J. B.; Abild-Pedersen, F.; Nørskov, J. K.; Schlögl, R., The Mechanism of CO and CO2 Hydrogenation to Methanol over Cu-Based Catalysts. *ChemCatChem* **2015,** 7 (7), 1105-1111.
111. Prieto, G.; Meeldijk, J. D.; de Jong, K. P.; de Jongh, P. E., Interplay between pore size and nanoparticle spatial distribution: Consequences for the stability of CuZn/SiO2 methanol synthesis catalysts. *Journal of Catalysis* **2013,** 303, 31-40.
112. Prieto, G.; Zečević, J.; Friedrich, H.; de Jong, K. P.; de Jongh, P. E., Towards stable catalysts by controlling collective properties of supported metal nanoparticles. *Nat Mater* **2013,** 12 (1), 34-39.
113. Iyer, S. S.; Renganathan, T.; Pushpavanam, S.; Vasudeva Kumar, M.; Kaisare, N., Generalized thermodynamic analysis of methanol synthesis: Effect of feed composition. *Journal of CO2 Utilization* **2015,** 10, 95-104.
114. Graaf, G. H.; Sijtsema, P. J. J. M.; Stamhuis, E. J.; Joosten, G. E. H., Chemical equilibria in methanol synthesis. *Chemical Engineering Science* **1986,** 41 (11), 2883-2890.
115. Skrzypek, J.; Lachowska, M.; Grzesik, M.; Słoczyński, J.; Nowak, P., Thermodynamics and kinetics of low pressure methanol synthesis. *The Chemical Engineering Journal and the Biochemical Engineering Journal* **1995,** 58 (2), 101-108.
116. Chinchen, G. C.; Denny, P. J.; Parker, D. G.; Spencer, M. S.; Whan, D. A., Mechanism of methanol synthesis from CO2/CO/H2 mixtures over copper/zinc oxide/alumina catalysts: use of14C-labelled reactants. *Applied Catalysis* **1987,** 30 (2), 333-338.
117. Grabow, L. C.; Mavrikakis, M., Mechanism of Methanol Synthesis on Cu through CO2 and CO Hydrogenation. *ACS Catalysis* **2011,** 1 (4), 365-384.
118. Igor, K.; Patrick, K.; Benjamin, K.; Annette, T.; Robert, S., Role of Lattice Strain and Defects in Copper Particles on the Activity of Cu/ZnO/Al2O3 Catalysts for Methanol Synthesis. *Angewandte Chemie* **2007,** 119 (38), 7465-7468.
119. Kanai, Y.; Watanabe, T.; Fujitani, T.; Uchijima, T.; Nakamura, J., The synergy between Cu and ZnO in methanol synthesis catalysts. *Catalysis Letters* **1996,** 38 (3), 157-163.
120. Le Valant, A.; Comminges, C.; Tisseraud, C.; Canaff, C.; Pinard, L.; Pouilloux, Y., The Cu–ZnO synergy in methanol synthesis from CO2, Part 1: Origin of active site explained by experimental studies and a sphere contact quantification model on Cu+ZnO mechanical mixtures. *Journal of Catalysis* **2015,** 324, 41-49.

121. Nakamura, J.; Choi, Y.; Fujitani, T., On the Issue of the Active Site and the Role of ZnO in Cu/ZnO Methanol Synthesis Catalysts. *Topics in Catalysis* **2003,** 22 (3), 277-285.
122. Thomas, L.; Julia, S.; Malte, B.; Robert, S.; G., W. M., Formation of a ZnO Overlayer in Industrial Cu/ZnO/Al2O3 Catalysts Induced by Strong Metal–Support Interactions. *Angewandte Chemie International Edition* **2015,** 54 (15), 4544-4548.
123. Liu, Y.; Murata, K.; Inaba, M.; Takahara, I., Synthesis of ethanol from methanol and syngas through an indirect route containing methanol dehydrogenation, DME carbonylation, and methyl acetate hydrogenolysis. *Fuel Processing Technology* **2013,** 110, 206-213.
124. Daniel, B. J.; Deeley, J. M. S.; Gracey, B. P.; Li, C. R. WO2009063173. 2006.
125. Santiago, M. A. N.; Sanchez-Castillo, M. A.; Cortright, R. D.; Dumesic, J. A., Catalytic reduction of acetic acid, methyl acetate, and ethyl acetate over silica-supported copper. *Journal of Catalysis* **2000,** 193 (1), 16-28.
126. Wang, S.; Yin, S.; Guo, W.; Liu, Y.; Zhu, L.; Wang, X., Influence of inlet gas composition on dimethyl ether carbonylation and the subsequent hydrogenation of methyl acetate in two-stage ethanol synthesis. *New Journal of Chemistry* **2016,** 40 (7), 6460-6466.
127. Zhou, W.; Kang, J.; Cheng, K.; He, S.; Shi, J.; Zhou, C.; Zhang, Q.; Chen, J.; Peng, L.; Chen, M.; Wang, Y., Direct Conversion of Syngas into Methyl Acetate, Ethanol, and Ethylene by Relay Catalysis via the Intermediate Dimethyl Ether. *Angewandte Chemie International Edition* **2018,** 57 (37), 12012-12016.
128. Anwar Saeed, M.; Ma, H.; Yue, S.; Wang, Q.; Tu, M., Concise review on ethanol production from food waste: development and sustainability. *Environmental Science and Pollution Research* **2018,** 25 (29), 28851-28863.
129. Hoekman, S. K.; Broch, A.; Liu, X., Environmental implications of higher ethanol production and use in the U.S.: A literature review. Part I – Impacts on water, soil, and air quality. *Renewable and Sustainable Energy Reviews* **2018,** 81, 3140-3158.
130. Yue, H.; Zhao, Y.; Ma, X.; Gong, J., Ethylene glycol: properties, synthesis, and applications. *Chemical Society Reviews* **2012,** 41 (11), 4218-4244.
131. Farrell, A. E.; Plevin, R. J.; Turner, B. T.; Jones, A. D.; O'Hare, M.; Kammen, D. M., Ethanol Can Contribute to Energy and Environmental Goals. *Science* **2006,** 311 (5760), 506-508.
132. San, X.; Zhang, Y.; Shen, W.; Tsubaki, N., New Synthesis Method of Ethanol from Dimethyl Ether with a Synergic Effect between the Zeolite Catalyst and Metallic Catalyst. *Energy & Fuels* **2009,** 23 (5), 2843-2844.
133. Claus, P.; Lucas, M.; Lücke, B.; Berndt, T.; Birke, P., Selective hydrogenolysis of methyl and ethyl acetate in the gas phase on copper and supported Group VIII metal catalysts. *Applied Catalysis A: General* **1991,** 79 (1), 1-18.
134. Van de Scheur, F. T.; Staal, L. H., Effects of zinc addition to silica supported copper catalysts for the hydrogenolysis of esters. *Applied Catalysis A: General* **1994,** 108 (1), 63-83.

135. Zhao, Y.; Shan, B.; Wang, Y.; Zhou, J.; Wang, S.; Ma, X., An Effective CuZn–SiO2 Bimetallic Catalyst Prepared by Hydrolysis Precipitation Method for the Hydrogenation of Methyl Acetate to Ethanol. *Industrial & Engineering Chemistry Research* **2018,** 57 (13), 4526-4534.
136. Lu, Z.; Yin, H.; Wang, A.; Hu, J.; Xue, W.; Yin, H.; Liu, S., Hydrogenation of ethyl acetate to ethanol over Cu/ZnO/MOx (MOx=SiO2, Al2O3, and ZrO2) catalysts. *Journal of Industrial and Engineering Chemistry* **2016,** 37, 208-215.
137. Brands, D. S.; Poels, E. K.; Bliek, A., Ester hydrogenolysis over promoted Cu/SiO2 catalysts. *Applied Catalysis A: General* **1999,** 184 (2), 279-289.
138. Van de Scheur, F. T.; van der Linden, B.; Mittelmeijer-Hazeleger, M. C.; Nazloomian, J. G.; Staat, L. H., Structure-activity relation and ethane formation in the hydrogenolysis of methyl acetate on silicasupported copper catalysts. *Applied Catalysis A: General* **1994,** 111 (1), 63-77.
139. Schittkowski, J.; Tölle, K.; Anke, S.; Stürmer, S.; Muhler, M., On the bifunctional nature of Cu/ZrO2 catalysts applied in the hydrogenation of ethyl acetate. *Journal of Catalysis* **2017,** 352, 120-129.
140. Wiberg, K. B.; Crocker, L. S.; Morgan, K. M., Thermochemical studies of carbonyl compounds. 5. Enthalpies of reduction of carbonyl groups. *Journal of the American Chemical Society* **1991,** 113 (9), 3447-3450.
141. Agarwal, A. K.; Cant, N. W.; Wainwright, M. S.; Trimm, D. L., Catalytic hydrogenolysis of esters: a comparative study of the reactions of simple formates and acetates over copper on silica. *Journal of Molecular Catalysis* **1987,** 43 (1), 79-92.
142. Bender, M., An Overview of Industrial Processes for the Production of Olefins – C4 Hydrocarbons. *ChemBioEng Reviews* **2014,** 1 (4), 136-147.
143. Derrien, M. L., Chapter 18 Selective Hydrogenation Applied to the Refining of Petrochemical Raw Materials Produced by Steam Cracking. *Studies in Surface Science and Catalysis* **1986,** 27, 613-666.
144. Molnár, Á.; Sárkány, A.; Varga, M., Hydrogenation of carbon–carbon multiple bonds: chemo-, regio- and stereo-selectivity. *Journal of Molecular Catalysis A: Chemical* **2001,** 173 (1), 185-221.
145. Schulze, J.; Homan, M., *C4-Hydrocarbons and Derivatives*. Springer: 1989.
146. Argyle, M. D.; Bartholomew, C. H., Heterogeneous Catalyst Deactivation and Regeneration: A Review. *Catalysts* **2015,** 5 (1), 145-269.
147. Burger, B. J.; Thompson, M. E.; Cotter, W. D.; Bercaw, J. E., Ethylene insertion and .beta.-hydrogen elimination for permethylscandocene alkyl complexes. A study of the chain propagation and termination steps in Ziegler-Natta polymerization of ethylene. *Journal of the American Chemical Society* **1990,** 112 (4), 1566-1577.
148. Borodziński, A.; Bond, G. C., Selective Hydrogenation of Ethyne in Ethene-Rich Streams on Palladium Catalysts. Part 1. Effect of Changes to the Catalyst During Reaction. *Catalysis Reviews* **2006,** 48 (2), 91-144.
149. Chinayon, S.; Mekasuwandumrong, O.; Praserthdam, P.; Panpranot, J., Selective hydrogenation of acetylene over Pd catalysts supported on nanocrystalline alpha-Al2O3 and Zn-modified alpha-Al2O3. *Catalysis Communications* **2008,** 9 (14), 2297-2302.

150. Debras, G. L. G.; De Clippeleir, G. E. M. J.; Grootjans, J. F.; Cahen, R. M., Process for the selective hydrogenation of alkynes. CA1290354C, 1989.
151. Du, Z., Alkyne selective hydrogenation catalyst and preparation method thereof. CN102463117: 2012.
152. King, A. O.; Larsen, R. D.; Negishi, E. In *Handbook of Organopalladium Chemistry for Organic Synthesis*, pp 2719-2752.
153. Takht Ravanchi, M.; Sahebdelfar, S.; Komeili, S., Acetylene selective hydrogenation: a technical review on catalytic aspects. In *Reviews in Chemical Engineering*, 2018; Vol. 34, p 215.
154. Baerns, M., *Basic Principles in Applied Catalysis*. Springer: 2004; Vol. 75.
155. Pachulski, A.; Schödel, R.; Claus, P., Performance and regeneration studies of Pd–Ag/Al2O3 catalysts for the selective hydrogenation of acetylene. *Applied Catalysis A: General* **2011,** 400 (1), 14-24.
156. Zhang, Q.; Li, J.; Liu, X.; Zhu, Q., Synergetic effect of Pd and Ag dispersed on Al2O3 in the selective hydrogenation of acetylene. *Applied Catalysis A: General* **2000,** 197 (2), 221-228.
157. Sarkany, A.; Horvath, A.; Beck, A., Hydrogenation of acetylene over low loaded Pd and Pd-Au/SiO(2) catalysts. *Applied Catalysis a-General* **2002,** 229 (1-2), 117-125.
158. Guczi, L.; Schay, Z.; Weiss, A. H.; Nair, V.; Leviness, S., Acetylene hydrogenation selectivity control using Pd/Cu catalysts. *Reaction Kinetics and Catalysis Letters* **1985,** 27 (1), 147-151.
159. Lucci, F. R.; Liu, J.; Marcinkowski, M. D.; Yang, M.; Allard, L. F.; Flytzani-Stephanopoulos, M.; Sykes, E. C. H., Selective hydrogenation of 1,3-butadiene on platinum–copper alloys at the single-atom limit. **2015,** 6, 8550.
160. Insorn, P.; Kitiyanan, B., Selective Hydrogenation of Concentrated Vinyl Acetylene Mixed C4 by Modified Pd Catalysts: Effect of Cu. *Catalysts* **2016,** 6 (12), 12.
161. Furukawa, S.; Komatsu, T., Selective Hydrogenation of Functionalized Alkynes to (E)-Alkenes, Using Ordered Alloys as Catalysts. *ACS Catalysis* **2016,** 6 (3), 2121-2125.
162. Stammbach, M. R.; Thomas, D. J.; Trimm, D. L.; Wainwright, M. S., Hydrogenation of ethyne over an ion-exchanged copper on silica catalyst. *Applied Catalysis* **1990,** 58 (1), 209-217.
163. Koeppel, R. A.; Wehrli, J. T.; Wainwright, M. S.; Trimm, D. L.; Cant, N. W., Selective hydrogenation of C-4 alkynes over a copper on silica catalyst. *Applied Catalysis a-General* **1994,** 120 (1), 163-177.
164. Wehrli, J. T.; Thomas, D. J.; Wainwright, M. S.; Trimm, D. L.; Cant, N. W., Selective hydrogenation of propyne over an ion-exchanged copper on silica catalyst. *Applied Catalysis* **1990,** 66 (1), 199-208.
165. Setiawan, I.; Cavell, K. J., Removal of unstaturated contaminants from an industrial C4-stream using Cu/SiO2 catalysts: Subsequent testing of the purified stream with an alkyne sensitive catalyst system. *Applied Catalysis A: General* **1995,** 131 (2), 225-241.
166. Nemet-Mavrodin, M., Selective hydrogenation of acetylenic impurities in crude butadiene. US4704492: 1987.
167. Frevel, L. K.; Kressley, L. J. Dealkynation of olefin and diolefin streams. US3912789, 1975.

168. Phillipson, J. J.; Wells, P. B.; Wilson, G. R., Hydrogenation of alkadienes. 3. Hydrogenation of buta-1,3-diene catalysed by iron cobalt nickel and copper. *Journal of the Chemical Society a -Inorganic Physical Theoretical* **1969,** (9), 1351-+.
169. Wang, Z.; Wang, G.; Louis, C.; Delannoy, L., Novel non-noble bimetallic Cu-Zn/TiO2 catalysts for selective hydrogenation of butadiene. *Journal of Catalysis* **2017,** 347, 185-196.
170. Nishimura, E.; Inoue, Y.; Yasumori, I., Mechanism of selective hydrogenation of 1,3-butadiene on copper surfaces. *Bulletin of the Chemical Society of Japan* **1975,** 48 (3), 803-807.
171. Masoud, N.; Delannoy, L.; Schaink, H.; van der Eerden, A.; de Rijk, J. W.; Silva, T. A. G.; Banerjee, D.; Meeldijk, J. D.; de Jong, K. P.; Louis, C.; de Jongh, P. E., Superior Stability of Au/SiO2 Compared to Au/TiO2 Catalysts for the Selective Hydrogenation of Butadiene. *ACS Catalysis* **2017,** 7 (9), 5594-5603.
172. Ertl, G.; Knözinger, H.; Weitkamp, J., *Handbook of Heterogeneous Catalysis*. Wiley: 2008.
173. Yin, A.; Guo, X.; Dai, W.-L.; Fan, K., The Nature of Active Copper Species in Cu-HMS Catalyst for Hydrogenation of Dimethyl Oxalate to Ethylene Glycol: New Insights on the Synergetic Effect between Cu0 and Cu+. *The Journal of Physical Chemistry C* **2009,** 113 (25), 11003-11013.
174. Johnson, G. R.; Werner, S.; Bell, A. T., An Investigation into the Effects of Mn Promotion on the Activity and Selectivity of Co/SiO2 for Fischer–Tropsch Synthesis: Evidence for Enhanced CO Adsorption and Dissociation. *ACS Catalysis* **2015,** 5 (10), 5888-5903.
175. Morales, F.; Grandjean, D.; Mens, A.; de Groot, F. M. F.; Weckhuysen, B. M., X-ray Absorption Spectroscopy of Mn/Co/TiO2 Fischer−Tropsch Catalysts: Relationships between Preparation Method, Molecular Structure, and Catalyst Performance. *The Journal of Physical Chemistry B* **2006,** 110 (17), 8626-8639.
176. Brands, D. S.; Poels, E. K.; Bliek, A. In *Studies in Surface Science and Catalysis*, Hightower, J. W., Nicholas Delgass, W., Iglesia, E., Bell, A. T., Eds. Elsevier: 1996; Vol. 101, pp 1085-1094.
177. Ye, C.; Guo, C.; Sun, C.; Zhang, Y., Effect of Mn doping on the activity and stability of Cu–SiO2 catalysts for the hydrogenation of methyl acetate to ethanol. *RSC Advances* **2016,** 6 (114), 113796-113802.
178. Tian, J.; Hu, J.; Shan, W.; Wu, P.; Li, X., Cu9-Alx-Mgy catalysts for hydrogenation of ethyl acetate to ethanol. *Applied Catalysis A: General* **2017,** 544, 108-115.
179. Xiang, Y.; Kruse, N., Tuning the catalytic CO hydrogenation to straight- and long-chain aldehydes/alcohols and olefins/paraffins. *Nature Communications* **2016,** 7, 13058.
180. Bezemer, G. L.; Radstake, P. B.; Falke, U.; Oosterbeek, H.; Kuipers, H. P. C. E.; van Dillen, A. J.; de Jong, K. P., Investigation of promoter effects of manganese oxide on carbon nanofiber-supported cobalt catalysts for Fischer–Tropsch synthesis. *Journal of Catalysis* **2006,** 237 (1), 152-161.

181. Xie, Z.; Frank, B.; Huang, X.; Schlögl, R.; Trunschke, A., Higher Alcohol Synthesis Over Rh Catalysts: Conditioning of Rh/N-CNTs by Co and Mn Entrapped in the Support. *Catalysis Letters* **2016,** 146 (12), 2417-2424.
182. Yang, N.; Yoo, J. S.; Schumann, J.; Bothra, P.; Singh, J. A.; Valle, E.; Abild-Pedersen, F.; Nørskov, J. K.; Bent, S. F., Rh-MnO Interface Sites Formed by Atomic Layer Deposition Promote Syngas Conversion to Higher Oxygenates. *ACS Catalysis* **2017,** 7 (9), 5746-5757.
183. Paterson, J.; Peacock, M.; Purves, R.; Partington, R.; Sullivan, K.; Sunley, G.; Wilson, J., Manipulation of Fischer-Tropsch Synthesis for Production of Higher Alcohols Using Manganese Promoters. *ChemCatChem* **2018,** 10 (22), 5154-5163.
184. Morales, F.; de Smit, E.; de Groot, F. M. F.; Visser, T.; Weckhuysen, B. M., Effects of manganese oxide promoter on the CO and H2 adsorption properties of titania-supported cobalt Fischer–Tropsch catalysts. *Journal of Catalysis* **2007,** 246 (1), 91-99.
185. Van Hardeveld, R.; Hartog, F., The statistics of surface atoms and surface sites on metal crystals. *Surface Science* **1969,** 15 (2), 189-230.
186. Van Rensburg, W. J.; Petersen, M. A.; Datt, M. S.; van den Berg, J. A.; van Helden, P., On the Kinetic Interpretation of DFT-Derived Energy Profiles: Cu-Catalyzed Methanol Synthesis. *Catalysis Letters* **2015,** 145 (2), 559-568.
187. Den Breejen, J. P.; Radstake, P. B.; Bezemer, G. L.; Bitter, J. H.; Frøseth, V.; Holmen, A.; Jong, K. P. d., On the Origin of the Cobalt Particle Size Effects in Fischer−Tropsch Catalysis. *Journal of the American Chemical Society* **2009,** 131 (20), 7197-7203.
188. Van Helden, P.; Ciobîcă, I. M.; Coetzer, R. L. J., The size-dependent site composition of FCC cobalt nanocrystals. *Catalysis Today* **2016,** 261, 48-59.
189. Torres Galvis, H. M.; Bitter, J. H.; Davidian, T.; Ruitenbeek, M.; Dugulan, A. I.; de Jong, K. P., Iron Particle Size Effects for Direct Production of Lower Olefins from Synthesis Gas. *Journal of the American Chemical Society* **2012,** 134 (39), 16207-16215.
190. Liu, J.-X.; Wang, P.; Xu, W.; Hensen, E. J. M., Particle Size and Crystal Phase Effects in Fischer-Tropsch Catalysts. *Engineering* **2017,** 3 (4), 467-476.
191. Vogt, C.; Groeneveld, E.; Kamsma, G.; Nachtegaal, M.; Lu, L.; Kiely, C. J.; Berben, P. H.; Meirer, F.; Weckhuysen, B. M., Unravelling structure sensitivity in CO2 hydrogenation over nickel. *Nature Catalysis* **2018,** 1 (2), 127-134.
192. Van Hardeveld, R.; van Montfoort, A., The influence of crystallite size on the adsorption of molecular nitrogen on nickel, palladium and platinum: An infrared and electron-microscopic study. *Surface Science* **1966,** 4 (4), 396-430.
193. Durndell, L. J.; Parlett, C. M. A.; Hondow, N. S.; Isaacs, M. A.; Wilson, K.; Lee, A. F., Selectivity control in Pt-catalyzed cinnamaldehyde hydrogenation. *Scientific Reports* **2015,** 5, 9425.
194. Gregory, A. R.; Silbey, R., Dissociative adsorption of hydrogen on copper: Stepped versus unstepped surfaces. *Chemical Physics Letters* **1977,** 50 (3), 500-502.

195. Kopač, D.; Likozar, B.; Huš, M., Catalysis of Material Surface Defects: Multiscale Modeling of Methanol Synthesis by CO2 Reduction on Copper. *Applied Surface Science* **2019**, 143783.
196. Calle-Vallejo, F.; Loffreda, D.; KoperMarc, T. M.; Sautet, P., Introducing structural sensitivity into adsorption–energy scaling relations by means of coordination numbers. *Nat Chem* **2015,** 7 (5), 403-410.
197. Liu, Z.-P.; Hu, P., General Rules for Predicting Where a Catalytic Reaction Should Occur on Metal Surfaces: A Density Functional Theory Study of C−H and C−O Bond Breaking/Making on Flat, Stepped, and Kinked Metal Surfaces. *Journal of the American Chemical Society* **2003,** 125 (7), 1958-1967.
198. Li, X.; Yang, X.; Zhang, J.; Huang, Y.; Liu, B., In Situ/Operando Techniques for Characterization of Single-Atom Catalysts. *ACS Catalysis* **2019,** 9 (3), 2521-2531.
199. Böhme, D. K.; Schwarz, H., Gas-Phase Catalysis by Atomic and Cluster Metal Ions: The Ultimate Single-Site Catalysts. *Angewandte Chemie International Edition* **2005,** 44 (16), 2336-2354.
200. Snyder, B. E. R.; Bols, M. L.; Schoonheydt, R. A.; Sels, B. F.; Solomon, E. I., Iron and Copper Active Sites in Zeolites and Their Correlation to Metalloenzymes. *Chemical Reviews* **2018,** 118 (5), 2718-2768.
201. Tomkins, P.; Ranocchiari, M.; van Bokhoven, J. A., Direct Conversion of Methane to Methanol under Mild Conditions over Cu-Zeolites and beyond. *Accounts of Chemical Research* **2017,** 50 (2), 418-425.
202. Dinh, K. T.; Sullivan, M. M.; Serna, P.; Meyer, R. J.; Dincă, M.; Román-Leshkov, Y., Viewpoint on the Partial Oxidation of Methane to Methanol Using Cu- and Fe-Exchanged Zeolites. *ACS Catalysis* **2018,** 8 (9), 8306-8313.
203. Paolucci, C.; Khurana, I.; Parekh, A. A.; Li, S.; Shih, A. J.; Li, H.; Di Iorio, J. R.; Albarracin-Caballero, J. D.; Yezerets, A.; Miller, J. T.; Delgass, W. N.; Ribeiro, F. H.; Schneider, W. F.; Gounder, R., Dynamic multinuclear sites formed by mobilized copper ions in NOx selective catalytic reduction. *Science* **2017,** 357 (6354), 898.
204. Ambrosi, A.; Chua, C. K.; Bonanni, A.; Pumera, M., Electrochemistry of Graphene and Related Materials. *Chemical Reviews* **2014,** 114 (14), 7150-7188.
205. Song, Y.; Peng, R.; Hensley, D. K.; Bonnesen, P. V.; Liang, L.; Wu, Z.; Meyer, H. M.; Chi, M.; Ma, C.; Sumpter, B. G.; Rondinone, A. J., High-Selectivity Electrochemical Conversion of CO2 to Ethanol using a Copper Nanoparticle/N-Doped Graphene Electrode. *ChemistrySelect* **2016,** 1 (19), 6055-6061.
206. Unwin, P. R.; Güell, A. G.; Zhang, G., Nanoscale Electrochemistry of sp2 Carbon Materials: From Graphite and Graphene to Carbon Nanotubes. *Accounts of Chemical Research* **2016,** 49 (9), 2041-2048.
207. Brownson, D. A. C.; Banks, C. E., Graphene electrochemistry: an overview of potential applications. *Analyst* **2010,** 135 (11), 2768-2778.

208. Li, F.; Han, G.-F.; Noh, H.-J.; Kim, S.-J.; Lu, Y.; Jeong, H. Y.; Fu, Z.; Baek, J.-B., Boosting oxygen reduction catalysis with abundant copper single atom active sites. *Energy & Environmental Science* **2018,** 11 (8), 2263-2269.
209. Yang, H.; Wu, Y.; Li, G.; Lin, Q.; Hu, Q.; Zhang, Q.; Liu, J.; He, C., Scalable Production of Efficient Single-Atom Copper Decorated Carbon Membranes for CO2 Electroreduction to Methanol. *Journal of the American Chemical Society* **2019**.
210. Dandekar, A.; Vannice, M. A., Determination of the Dispersion and Surface Oxidation States of Supported Cu Catalysts. *Journal of Catalysis* **1998,** 178 (2), 621-639.
211. Donoeva, B.; Masoud, N.; de Jongh, P. E., Carbon Support Surface Effects in the Gold-Catalyzed Oxidation of 5-Hydroxymethylfurfural. *ACS Catalysis* **2017,** 7 (7), 4581-4591.
212. Pekala, R. W., Organic aerogels from the polycondensation of resorcinol with formaldehyde. *Journal of Materials Science* **1989,** 24 (9), 3221-3227.
213. Segre, C. U.; Leyarovska, N. E.; Chapman, L. D.; Lavender, W. M.; Plag, P. W.; King, A. S.; Kropf, A. J.; Bunker, B. A.; Kemner, K. M.; Dutta, P.; Duran, R. S.; Kaduk, J., The MRCAT insertion device beamline at the Advanced Photon Source. *AIP Conference Proceedings* **2000,** 521 (1), 419-422.
214. Sano, M.; Komorita, S.; Yamatera, H., XANES spectra of copper(II) complexes: correlation of the intensity of the 1s .fwdarw. 3d transition and the shape of the complex. *Inorganic Chemistry* **1992,** 31 (3), 459-463.
215. Miller, J. T.; Kropf, A. J.; Zha, Y.; Regalbuto, J. R.; Delannoy, L.; Louis, C.; Bus, E.; van Bokhoven, J. A., The effect of gold particle size on AuAu bond length and reactivity toward oxygen in supported catalysts. *Journal of Catalysis* **2006,** 240 (2), 222-234.
216. Toupance, T.; Kermarec, M.; Louis, C., Metal Particle Size in Silica-Supported Copper Catalysts. Influence of the Conditions of Preparation and of Thermal Pretreatments. *The Journal of Physical Chemistry B* **2000,** 104 (5), 965-972.
217. Smith, M. L.; Campos, A.; Spivey, J. J., Reduction processes in Cu/SiO2, Co/SiO2, and CuCo/SiO2 catalysts. *Catalysis Today* **2012,** 182 (1), 60-66.
218. Iyemperumal, S. K.; Fenton, T. G.; Gillingham, S. L.; Carl, A. D.; Grimm, R. L.; Li, G.; Deskins, N. A., The stability and oxidation of supported atomic-size Cu catalysts in reactive environments. *The Journal of Chemical Physics* **2019,** 151 (5), 054702.
219. Li, C.-G.; Shen, Z.-G.; Hu, Y.-F.; Tang, Y.-N.; Chen, W.-G.; Ren, B.-Z., Insights into the structures and electronic properties of Cun+1μand CunSμ(n = 1–12; μ = 0, ±1) clusters. *Scientific Reports* **2017,** 7 (1), 1345.
220. Rasmussen, D. B.; Janssens, T. V. W.; Temel, B.; Bligaard, T.; Hinnemann, B.; Helveg, S.; Sehested, J., The energies of formation and mobilities of Cu surface species on Cu and ZnO in methanol and water gas shift atmospheres studied by DFT. *Journal of Catalysis* **2012,** 293, 205-214.
221. van den Berg, R.; Elkjaer, C. F.; Gommes, C. J.; Chorkendorff, I.; Sehested, J.; de Jongh, P. E.; de Jong, K. P.; Helveg, S., Revealing the Formation of Copper Nanoparticles from a Homogeneous Solid Precursor by Electron Microscopy. *Journal of the American Chemical Society* **2016,** 138 (10), 3433-3442.

222. Klier, K., *Advances in Catalysis: Methanol Synthesis*. Academic Press: 1982.
223. Fichtl, M. B.; Schumann, J.; Kasatkin, I.; Jacobsen, N.; Behrens, M.; Schlögl, R.; Muhler, M.; Hinrichsen, O., Counting of Oxygen Defects versus Metal Surface Sites in Methanol Synthesis Catalysts by Different Probe Molecules. *Angewandte Chemie International Edition* **2014,** 53 (27), 7043-7047.
224. Ferrari, A. C., Raman spectroscopy of graphene and graphite: Disorder, electron–phonon coupling, doping and nonadiabatic effects. *Solid State Communications* **2007,** 143 (1), 47-57.
225. Fichtl, M. B.; Schlereth, D.; Jacobsen, N.; Kasatkin, I.; Schumann, J.; Behrens, M.; Schlögl, R.; Hinrichsen, O., Kinetics of deactivation on Cu/ZnO/Al2O3 methanol synthesis catalysts. *Applied Catalysis A: General* **2015,** 502, 262-270.
226. van den Reijen, J. E.; Kanungo, S.; Welling, T. A. J.; Versluijs-Helder, M.; Nijhuis, T. A.; de Jong, K. P.; de Jongh, P. E., Preparation and particle size effects of Ag/α-Al2O3 catalysts for ethylene epoxidation. *Journal of Catalysis* **2017,** 356, 65-74.
227. Einstein, T. L., *Equilibrium Shape of Crystals*. Elsevier: 2015.
228. Sebastian, K.; Christian, C.; Georg, M. P.; Ib, C.; Jens, S., Quantification of Zinc Atoms in a Surface Alloy on Copper in an Industrial-Type Methanol Synthesis Catalyst. *Angewandte Chemie International Edition* **2014,** 53 (23), 5941-5945.
229. Kanai, Y.; Watanabe, T.; Fujitani, T.; Saito, M.; Nakamura, J.; Uchijima, T., Evidence for the migration of ZnOx in a Cu/ZnO methanol synthesis catalyst. *Catalysis Letters* **1994,** 27 (1), 67-78.
230. Stakheev, A. Y.; Kustov, L. M., Effects of the support on the morphology and electronic properties of supported metal clusters: modern concepts and progress in 1990s. *Applied Catalysis A: General* **1999,** 188 (1), 3-35.
231. Hansen, P. L.; Wagner, J. B.; Helveg, S.; Rostrup-Nielsen, J. R.; Clausen, B. S.; Topsøe, H., Atom-Resolved Imaging of Dynamic Shape Changes in Supported Copper Nanocrystals. *Science* **2002,** 295 (5562), 2053-2055.
232. Evans, J. W.; Wainwright, M. S.; Cant, N. W.; Trimm, D. L., Structural and reactivity effects in the copper-catalyzed hydrogenolysis of aliphatic esters. *Journal of Catalysis* **1984,** 88 (1), 203-213.
233. Ma, X.; Yang, Z.; Liu, X.; Tan, X.; Ge, Q., Dynamic redox cycle of Cu0 and Cu+ over Cu/SiO2 catalyst in ester hydrogenation. *RSC Advances* **2015,** 5 (47), 37581-37584.
234. Patterson, A. L., The Scherrer Formula for X-Ray Particle Size Determination. *Physical Review* **1939,** 56 (10), 978-982.
235. Wang, Y.; Yang, W.; Yao, D.; Wang, S.; Xu, Y.; Zhao, Y.; Ma, X., Effect of surface hydroxyl group of ultra-small silica on the chemical states of copper catalyst for dimethyl oxalate hydrogenation. *Catalysis Today* **2019**.
236. Moulijn, J. A.; van Diepen, A. E.; Kapteijn, F., Catalyst deactivation: is it predictable?: What to do? *Applied Catalysis A: General* **2001,** 212 (1), 3-16.
237. Argyle, D. M.; Bartholomew, H. C., Heterogeneous Catalyst Deactivation and Regeneration: A Review. *Catalysts* **2015,** 5 (1).

238. Honkala, K.; Hellman, A.; Remediakis, I. N.; Logadottir, A.; Carlsson, A.; Dahl, S.; Christensen, C. H.; Nørskov, J. K., Ammonia Synthesis from First-Principles Calculations. *Science* **2005,** 307 (5709), 555-558.
239. Kondrat, S. A.; Smith, P. J.; Carter, J. H.; Hayward, J. S.; Pudge, G. J.; Shaw, G.; Spencer, M. S.; Bartley, J. K.; Taylor, S. H.; Hutchings, G. J., The effect of sodium species on methanol synthesis and water–gas shift Cu/ZnO catalysts: utilising high purity zincian georgeite. *Faraday Discussions* **2017,** 197 (0), 287-307.
240. Somorjai, G. A.; McCrea, K. R.; Zhu, J., Active Sites in Heterogeneous Catalysis: Development of Molecular Concepts and Future Challenges. *Topics in Catalysis* **2002,** 18 (3), 157-166.
241. Henry, C. R.; Chapon, C.; Giorgio, S.; Goyhenex, C. In *Chemisorption and Reactivity on Supported Clusters and Thin Films: Towards an Understanding of Microscopic Processes in Catalysis*, Lambert, R. M., Pacchioni, G., Eds. Springer Netherlands: Dordrecht, 1997; pp 117-152.
242. Turek, T.; Trimm, D. L.; Cant, N. W., The Catalytic Hydrogenolysis of Esters to Alcohols. *Catalysis Reviews* **1994,** 36 (4), 645-683.
243. Rao, R.; Dandekar, A.; Baker, R. T. K.; Vannice, M. A., Properties of Copper Chromite Catalysts in Hydrogenation Reactions. *Journal of Catalysis* **1997,** 171 (2), 406-419.
244. Katz, S. A.; Salem, H., The toxicology of chromium with respect to its chemical speciation: A review. *Journal of Applied Toxicology* **1993,** 13 (3), 217-224.
245. Ravel, B.; Newville, M., ATHENA, ARTEMIS, HEPHAESTUS: data analysis for X-ray absorption spectroscopy using IFEFFIT. *Journal of Synchrotron Radiation* **2005,** 12, 537-541.
246. Wang, Y.; Liao, J.; Zhang, J.; Wang, S.; Zhao, Y.; Ma, X., Hydrogenation of methyl acetate to ethanol by Cu/ZnO catalyst encapsulated in SBA-15. *AIChE Journal* **2017,** 63 (7), 2839-2849.
247. Stobbe, E. R.; de Boer, B. A.; Geus, J. W., The reduction and oxidation behaviour of manganese oxides. *Catalysis Today* **1999,** 47 (1), 161-167.
248. Lomate, S.; Sultana, A.; Fujitani, T., Effect of SiO2 support properties on the performance of Cu-SiO2 catalysts for the hydrogenation of levulinic acid to gamma valerolactone using formic acid as a hydrogen source. *Catalysis Science & Technology* **2017,** 7 (14), 3073-3083.
249. Frenkel, A. I.; Hills, C. W.; Nuzzo, R. G., A View from the Inside: Complexity in the Atomic Scale Ordering of Supported Metal Nanoparticles. *The Journal of Physical Chemistry B* **2001,** 105 (51), 12689-12703.
250. de Graaf, J.; van Dillen, A. J.; de Jong, K. P.; Koningsberger, D. C., Preparation of Highly Dispersed Pt Particles in Zeolite Y with a Narrow Particle Size Distribution: Characterization by Hydrogen Chemisorption, TEM, EXAFS Spectroscopy, and Particle Modeling. *Journal of Catalysis* **2001,** 203 (2), 307-321.
251. Johnson, G. R.; Bell, A. T., Effects of Lewis acidity of metal oxide promoters on the activity and selectivity of Co-based Fischer–Tropsch synthesis catalysts. *Journal of Catalysis* **2016,** 338, 250-264.

252. Popa, T.; Zhang, Y.; Jin, E.; Fan, M., An environmentally benign and low-cost approach to synthesis of thermally stable industrial catalyst Cu/SiO2 for the hydrogenation of dimethyl oxalate to ethylene glycol. *Applied Catalysis A: General* **2015,** 505, 52-61.
253. He, Z.; Lin, H.; He, P.; Yuan, Y., Effect of boric oxide doping on the stability and activity of a Cu–SiO2 catalyst for vapor-phase hydrogenation of dimethyl oxalate to ethylene glycol. *Journal of Catalysis* **2011,** 277, 54-63.
254. Masoud, N.; Delannoy, L.; Calers, C.; Gallet, J.-J.; Bournel, F.; de Jong, K. P.; Louis, C.; de Jongh, P. E., Silica-Supported Au–Ag Catalysts for the Selective Hydrogenation of Butadiene. *ChemCatChem* **2017,** 9, 2418-2425.
255. Cervantes, G. G.; Aires, F.; Bertolini, J. C., Compared properties of Pd on thermo-conductor supports (SiC, Si3N4) and Pd on oxide supports (Al2O3, SiI2) for the 1,3-butadiene hydrogenation reaction. *Journal of Catalysis* **2003,** 214 (1), 26-32.
256. Hugon, A.; Delannoy, L.; Louis, C., Influence of the reactant concentration in selective hydrogenation of 1,3-butadiene over supported gold catalysts under alkene rich conditions: A consideration of reaction mechanism. *Gold Bulletin* **2009,** 42 (4), 310-320.
257. Zhang, R.; Zhang, J.; Jiang, Z.; Wang, B.; Fan, M., The cost-effective Cu-based catalysts for the efficient removal of acetylene from ethylene: The effects of Cu valence state, surface structure and surface alloying on the selectivity and activity. *Chemical Engineering Journal* **2018,** 351, 732-746.
258. Huang, W.; Wei; WeiZhao, W.; White, J. M., Two-Photon Photoemission Spectroscopy Study of 1,3-Butadiene on Cu(111): Electronic Structures and Excitation Mechanism. *The Journal of Physical Chemistry B* **2006,** 110 (11), 5547-5552.
259. Yang, M. X.; Eng, J.; Kash, P. W.; Flynn, G. W.; Bent, B. E.; Holbrook, M. T.; Bare, S. R.; Gland, J. L.; Fischer, D. A., Generation and Reaction of Vinyl Groups on a Cu(100) Surface. *The Journal of Physical Chemistry* **1996,** 100 (30), 12431-12439.
260. Morrell, C. E.; Swaney, M. W. Separating butadiene from acetylenes. US 2388928, 1945.
261. Van Wijk, R.; Görts, P. C.; Mens, A. J. M.; Gijzeman, O. L. J.; Habraken, F. H. P. M.; Geus, J. W., XPS/NRA investigations of particle size effects during the oxidation of Cu particles supported on oxidised Si (100). *Applied Surface Science* **1995,** 90 (3), 261-269.
262. *C. N. Thanh, B. Didillon, P. Sarrazin, C. Cameron, U.S. Patent 6,054,409 (2000).*
263. Studt, F.; Abild-Pedersen, F.; Bligaard, T.; Sørensen, R. Z.; Christensen, C. H.; Nørskov, J. K., Identification of Non-Precious Metal Alloy Catalysts for Selective Hydrogenation of Acetylene. *Science* **2008,** 320 (5881), 1320.
264. Bridier, B.; Karhánek, D.; Pérez-Ramírez, J.; López, N., Molecular Understanding of Enyne Hydrogenation over Palladium and Copper Catalysts. *ChemCatChem* **2012,** 4 (9), 1420-1427.

265. Bridier, B.; López, N.; Pérez-Ramírez, J., Partial hydrogenation of propyne over copper-based catalysts and comparison with nickel-based analogues. *Journal of Catalysis* **2010,** 269 (1), 80-92.
266. Furlong, B. K.; Hightower, J. W.; Chan, T. Y. L.; Sarkany, A.; Guczi, L., 1,3-Butadiene selective hydrogenation over Pd/alumina and CuPd/alumina catalysts. *Applied Catalysis A: General* **1994,** 117 (1), 41-51.
267. Munnik, P.; Velthoen, M. E. Z.; de Jongh, P. E.; de Jong, K. P.; Gommes, C. J., Nanoparticle Growth in Supported Nickel Catalysts during Methanation Reaction—Larger is Better. *Angewandte Chemie* **2014,** 126 (36), 9647-9651.
268. van Haasterecht, T.; Swart, M.; de Jong, K. P.; Bitter, J. H., Effect of initial nickel particle size on stability of nickel catalysts for aqueous phase reforming. *Journal of Energy Chemistry* **2016,** 25 (2), 289-296.

List of publications and presentations

Scientific publications and patent partly based on this thesis

R. Beerthuis, P. J. Dietrich, G. J. Sunley, K. P. de Jong and Petra E. de Jongh, *Atomically Dispersed Cu on Carbon and Growth into Cu Nanoparticles of Tailored Size,* Under review (Chapter 2)

R. Beerthuis,[#] C. E. Pompe,[#] R. Dalebout, K. P. de Jong and P. E. de Jongh, *Disentangling Promoter, Support and Particle Size Effects in Methanol Synthesis,* Submitted ([#] authors contributed equally) (Chapter 3)

R. Beerthuis, J. W. de Rijk, J. M. S. Deeley, G. J. Sunley, K. P. de Jong and P. E. de Jongh, *Particle Size Effects in Copper-Catalyzed Hydrogenation of Ethyl Acetate to Ethanol,* Journal of Catalysis, Accepted (Chapter 4)

R. Beerthuis, N. L. Visser, J. E. S. van der Hoeven, J. M. S. Deeley, G. J. Sunley, K. P. de Jong and P. E. de Jongh, *Manganese Promoter Effects in Copper-Catalyzed Hydrogenation of Ethyl Acetate, Under review* (Chapter 5)

G. Totarella,[#] **R. Beerthuis**,[#] *et al. and* P. E. de Jongh, "*Silica-* and *Carbon-Supported Copper Catalysts for Selective Hydrogenation of Butadiene,* In preparation ([#] authors contributed equally) (Chapter 6)

R. Beerthuis, G. J. Sunley, K. P. de Jong and P. E. de Jong, *Selective Hydrogenation of Polyunsaturates*, Patent WO2019/233961 (Chapter 6)

Other scientific publications

J. L. Weber, D. Martínez del Monte, **R. Beerthuis**, J. Dufour, C. Martos, K. P. de Jong, P. E. de Jongh, *Conversion of synthesis gas to aromatics at medium temperature with a Fischer Tropsch and ZSM-5 dual catalyst bed*, Submitted

R. Beerthuis, L. Huang, N. R. Shiju, G. Rothenberg, W. Shen, H. Xu, *Facile Synthesis of a Novel Hierarchical ZSM-5 Zeolite: A Stable Acid Catalyst for Dehydrating Glycerol to Acrolein,* Chem. Cat. Chem., 2018, 10, 211.

M. A. Freire, D. T. S. L. Mendes, L. S. Freitas, **R. Beerthuis**, S. F. Amarante, A. L. D. Ramos, *Acid-catalyzed liquid-phase alkylation of phenol with branched and linear olefin isomers*, Catal. Today, 2017, 289, 192.

R. Beerthuis, N. R. Shiju, G. Rothenberg, *Catalytic Routes towards Acrylic Acid, Adipic Acid and ε-Caprolactam starting from Biorenewables*, Green Chem., 2015, 17, 1341.

R. Beerthuis, M. Granollers, D. R. Brown, H. J. Salavagione, G. Rothenberg, N. R. Shiju. *Catalytic Acetoxylation of Lactic Acid to 2-Acetoxypropionic Acid, en route to Acrylic Acid*, RSC Adv., 2015, 5, 4103.

V. Gitis, **R. Beerthuis**, N. R. Shiju, G. Rothenberg, *Organosilane Oxidation by Water Catalysed by Large Gold Nanoparticles in a Membrane Reactor*, Catal. Sci. Technol., 2014, 4, 2156.

Oral presentations

R. Beerthuis, C. E. Pompe, K. P. de Jong and P. E. de Jongh, *Particle Size Effects for Carbon-Supported Cu and $CuZnO_x$ Catalysts in Methanol Synthesis*, EuropaCat XIV, August 18–23 2019, Aachen, Germany.

R. Beerthuis, G. J. Sunley, K. P. de Jong and P. E. de Jongh, *Unlocking Copper on Carbon as a Stable Catalyst for the Selective Hydrogenation of Butadiene*, EuropaCat XIV, August 18–23 2019, Aachen, Germany.

R. Beerthuis, C. E. Pompe, K. P. de Jong and P. E. de Jongh, *Disentangling Promoter, Support and Particle Size Effects in Methanol Synthesis*, Netherlands Catalysis and Chemistry Conference XX, March 4–6 2019, Noordwijkerhout, The Netherlands.

R. Beerthuis, N. L. Visser, J. M. S. Deeley, G. J. Sunley, K. P. de Jong, P. E. de Jongh, *Manganese Promoter Effects in Carbon-Supported Copper-Based Ester Hydrogenation Catalysis*, Tocat VIII, 5-10 August 2018, Yokohama, Japan.

R. Beerthuis, N. L. Visser, J. M. S. Deeley, G. J. Sunley, K. P. de Jong, P. E. de Jongh, *Manganese Promoter Effects in Carbon-Supported Copper-Based Ester Hydrogenation Catalysis*, International Symposium on Carbon for Catalysis - CarboCat VIII, 26–29 June 2018, Porto, Portugal. Combined oral and poster award.

Poster presentations

R. Beerthuis, C. E. Pompe, K. P. de Jong and **P. E. de Jongh**, *Particle Size Effects for Carbon-Supported Cu and $CuZnO_x$ Catalysts in Methanol Synthesis*, E-MRS Fall 2019, September 16–19 2019, Warsaw, Poland.

R. Beerthuis, C. E. Pompe, K. P. de Jong and P. E. de Jongh, *Particle Size Effects for Carbon-Supported Cu and $CuZnO_x$ Catalysts in Methanol Synthesis*, EuropaCat XIV, August 18–23 2019, Aachen, Germany. Poster award.

R. Beerthuis, N. L. Visser, J. M. S. Deeley, G. J. Sunley, K. P. de Jong, P. E. de Jongh, *Manganese Promoter Effects in Carbon-Supported Copper-Based Ester Hydrogenation Catalysis*, Scientific Bases for the Preparation of Heterogeneous Catalysts XII, 8–12 July 2018, Louvain-La-Neuve, Belgium.

R. Beerthuis, N. L. Visser, J. M. S. Deeley, G. J. Sunley, K. P. de Jong, P. E. de Jongh, *Manganese Promoter Effects in Carbon-Supported Copper-Based Ester Hydrogenation Catalysis*, International Symposium on Carbon for Catalysis - CarboCat VIII, 26–29 June 2018, Porto, Portugal. Combined oral and poster award.

Acknowledgements

Doing a PhD is like a journey through science, from the unknown at the start leading to the results within this thesis. During this journey I had the privilege to work with many fantastic people, who are not only very smart, but also friendly and truly inspiring. Here, I want to express my gratitude to everybody who made this thesis possible.

First of all, I want to thank my promotors **Petra** and **Krijn** for guiding me. You both have an impressive knowledge of chemistry, from an academic and industrial perspective. I have learned more in the past four years, than I could have imagined at the start. Petra, thank you for giving me the support and freedom to explore the various research topics in this project. You have taught me to focus on the key points and sharpen the skills to present a clear scientific story. Your keen knowledge of material science and your critical eye for detail surely pushed this research to a higher level. I am grateful for the support that you give your group members, especially during external meetings and conferences. Krijn, thank you for all the insightful discussions and sharing your encyclopedic knowledge of catalysis. It was truly inspiring to work with you and I will remember your philosophies on supervising students and always doing meaningful scientific research.

This research project was part of an industrial collaboration, with financial support from BP and essential scientific discussions and cooperative experiments. I want to thank the scientists at BP, including **Glenn**, **Jon**, **Paul**, **Roy**, **Neil** and **Tegan** for sharing their passion for chemistry and showing that beautiful scientific research can also be done in an industrial environment. I especially want to thank Glenn for his big impact on this research project and being part of the PhD defense committee. Our collaboration was an enlightening experience.

I would like to thank the Inorganic Chemistry and Catalysis staff members who helped throughout this project. I want to thank especially **Jan Willem** for maintaining the gas-phase reactor systems, gloveboxes and analytic equipment in excellent operating condition. I enjoyed commissioning the Flowrence II reactor unit with you and you are a very pleasant person to work with. Thank you **AdE** and **Herrick** for your valuable input in the XAS analysis for Chapter 5. Transmission electron microscopy was an important part of this research and I am very grateful to **Hans** and **Chris** for teaching me to operate the microscopes and helping me to solve problems on many different occasions. I also want to thank **AdM**, **Marjan**, **Pascal**, **Dennie**, **Ramon**, **Oscar** and **Fouad** for their technical assistance in the laboratory. I would like to acknowledge professors **Frank**, **Bert**, **Eelco**, **Pieter**, **Baira**, **PeterN**, **Jovana** and **Florian** for inspiring scientific discussions. Last but certainly not least, the ICC group is very lucky to have **Dymph**, **Iris, Monique** and **Ilonka** as their

excellent secretaries. Thank you Dymph for your help to organize the BP–UU meetings and submit this thesis.

During this research project I had the fortune to supervise the MSc literature thesis of **Iris** and MSc research projects of **Jochem** and **Nienke**. Thank you for your hard work, independent attitude and patience during long discussions that typically raised more questions than that they answered. Supervising your projects has taught me a lot personally and your efforts have contributed to Chapter 5 of this thesis and future research in our group.

Many colleagues contributed with valuable scientific input. First of all, I want to thank **Bengisu**, **Justine**, **Kang**, **Lee**, **Luc** and **Oscar** for their support during the BP–UU meetings. Even though we worked on different topics, it felt like being part of a very strong team. The work on the Flowrence II unit was a vital part of my project. I want to thank the experts of Flowrence I, **Tom**, **Lennart**, **Carlos** and **Jogchum** for their essential help. I am very glad I could learn from your expertise. I also want to thank the team of Flowrence II, **Remco**, **Nienke** and **Laura** for all your help with the high-throughput experiments, you are great colleagues and I am sure that your work will lead to many beautiful results. Remco, it was great to work with you and I really appreciate your determination and eye for detail. I want to thank **Lisette** and **Nazila** for teaching me how to measure the catalyst performance. Our nice collaborations led to Chapters 3 and 6 of this thesis. Thank you **Jessi** for the beautiful microscopy work in Chapter 5. You are a superb scientist and a fantastic neighbor. I want to thank **Giorgio** for keeping the butadiene setup in great condition. **Carlos**, you are a fantastic colleague and scientist, it is great to have you as my paranymph, thank you!

There are many people to thank for the fun times and support over the years. Thank you **Miguel**, **Lennart**, **Carlos**, **Jessi**, **Simone**, **Nazila**, **Donglong**, **Xinwei**, **Egor**, **Nastya**, **Ara**, **Martin**, **Ru-Pan**, **Iván**, **Marisol**, **Sneh**, **Stano**, **Katarina**, **Fabiane**, **Giorgio**, **Francesco**, **PetraK**, **Jogchum**, **Lisette**, **Nynke**, **Roy**, **Gang**, **PeterB**, **Jeroen**, **JX**, **Beatriz**, **Savannah**, **Ana**, **Antonio**, **Pierre**, **Wouter**, **Thomas**, **Manuel**, **Zafer**, **Özgün**, **Johan**, **Remco**, **Christa**, **Lars**, **Justine**, **Lee**, **Nienke**, **Javier**, **Sandra**, **José**, **Roozbeh**, **Sam**, **Luc**, **Mark**, **Pasi**, **Sebastiano**, **Homer**, **JochemB**, **JochemD**, **Marianna**, **Kang**, **Tom**, **Baira**, **Sang-Ho**, **Joel**, **Roxana**, **Eric**, **Francesco**, **Koen**, **Luke**, **Max**, **Silvia**, **Nikos**, **Sophie**, **Wirawan** and all the other fantastic colleagues at ICC for the fun during borrels, LIIT, 12 pubs, conferences, lunches, coffee breaks, second lunches, game nights, diners and parties. You made the PhD a wonderful time.

I want to express my gratitude to **Gadi** and **Shiju** for supervising my MSc research project at the University of Amsterdam. You have taught me the fundamentals of scientific research and sparked my passion for chemistry. Thank you Gadi for your

continued interest in my scientific career and being part of the PhD defense committee.

Ik wil mijn vrienden **Niels**, **Abel**, **Sven**, **Kasper**, **Nikki**, **Chuchu**, **Jurn**, **Stijn**, **Lukas** en **Rosa** bedanken voor de fantastische studiejaren en de mooie tijd bij het Amsterdams Chemisch Dispuut. Ik hoop jullie altijd te blijven zien. Abel, niemand zal ooit de Beste Sportcommissie Ooit kunnen vergeten, wat een glorieus team, daarom extra mooi dat jij mijn paranymph bent!

Mijn geweldige familie wil ik bedanken voor hun onvoorwaardelijke steun. Dit thesis zou onmogelijk zijn zonder mijn pap **Joost**, mam **Nens** en zus **Iris**. Jullie hebben mij altijd ondersteund, gestimuleerd om nieuwsgierig te zijn en gedreven om voor het maximaal haalbare resultaat te gaan. Pap, jouw levenskracht en voorliefde voor scheikunde hebben mij enorm geïnspireerd. De bijlessen waarin je uitlegde waarom alle koolstof–koolstof bindingen in benzeen even lang zijn (de atomen houden elkaars handen vast en trekken allemaal even hard) waren geweldig leuk en hebben op school de basis gelegd voor mijn eigen passie, als derde generatie scheikundige. Mam, jij bent enorm geïnteresseerd in mijn onderzoek en ik krijg altijd nieuwe ideeën als ik mijn werk met jou bespreek. Dank je voor het controleren van de Nederlandse samenvatting, jouw kijk op taal is subliem. Ier, dank je voor alle steun en inspiratie als grote zus en de gezelligheid samen met **Martijn** in Utrecht. Eu quero também agradecer à minha familia no Brasil, por todo o apoio e amor. Muito obrigado a **Silvio**, **Socorro**, **Fernanda** e **Francisco**. Um abraço!

Als laatste en meest belangrijke wil ik **Lídia** en **Benki** bedanken. Jullie hebben samen met mij de intense vreugde en uitdagingen van dit project ervaren. Lídia, dank je voor de oneindige steun over de jaren. Jouw heldere blik helpt mij altijd om het grotere geheel te zien. Jij bent de liefste persoon dit ik ken, eu te amo muito! Mijn kleine Benki, jij bent mijn allergrootste inspiratie en dit proefschrift is voor jou. Ik hoop dat al het wetenschappelijke onderzoek de toekomst mooier maakt, ook al is het met één heel klein stapje per keer.

About the author

Rolf Beerthuis was born 5th of February 1989 in Vlaardingen, The Netherlands. After completing his high school curriculum at the VOS lyceum in 2007, he obtained his BSc degree in Chemistry at the University of Amsterdam in 2011, followed by a MSc degree with *cum laude* distinction at both the University of Amsterdam and Vrije Universiteit Amsterdam in 2014. His MSc research project focused on developing catalytic routes towards renewable bulk chemicals, under supervision of prof. dr. G. Rothenberg). Afterwards, the author spent 2 months at the Fudan University in Shanghai (China) for a research project on zeolite synthesis and catalysis, under supervision of prof. dr. H. Xu). During his MSc research projects, he contributed to 5 peer-reviewed articles, including 3 as the first author with one 1 high-impact literature review, fueling his interest to scientific research and catalysis.

From 2015 to 2019, Rolf worked as a PhD candidate in the Inorganic Chemistry and Catalysis group at Utrecht University, under the supervision of prof. dr. Petra de Jongh and prof. dr. ir. Krijn de Jong. During his research project, Rolf contributed to commissioning an advanced high-throughput reactor setup and supervised 3 MSc projects. Parts of the research were presented at several national and international conferences, where he was awarded both a Combined Oral and Poster Award (CarboCat VIII) and a Best Poster Award (EuropaCat XIV). An invention was patented based on his research, together with BP as the industrial partner. The main results of his PhD project are described in this thesis.

Since January 2020, Rolf is working as a researcher at AkzoNobel on the topic of waterborne paints and coatings.